DEVELOPMENT OF POROUS METAL-ORGANIC FRAMEWORKS FOR GAS ADSORPTION APPLICATIONS

A Dissertation
Presented to
The Academic Faculty

by

Jagadeswarareddy Karra

In Partial Fulfillment
of the Requirements for the Degree
Doctor of Philosophy in the
School of Chemical and Biomolecular Engineering

Georgia Institute of Technology
December 2011

DEVELOPMENT OF POROUS METAL-ORGANIC FRAMEWORKS FOR GAS ADSORPTION APPLICATIONS

Approved by:

Dr. Krista S.Walton, Advisor
School of Chemical and Biomolecular Engineering
Georgia Institute of Technology

Dr. David S. Sholl
School of Chemical and Biomolecular Engineering
Georgia Institute of Technology

Dr. Carson Meredith
School of Chemical and Biomolecular Engineering
Georgia Institute of Technology

Dr.Yoshiaki Kawajiri
School of Chemical and Biomolecular Engineering
Georgia Institute of Technology

Dr. Seung Soon Jang
School of Materials and Science Engineering
Georgia Institute of Technology

Date Approved: July 21, 2011

ACKNOWLEDGEMENTS

First and foremost, I would like to acknowledge my advisor Dr. Krista Walton for believing me in my research abilities and taking me in her research group at Kansas State University. I am extremely fortunate to have her as my PhD advisor. If I were not working under her, I would not have landed in Georgia Tech. I will forever be indebted to her for giving me this opportunity to get a doctoral degree from Georgia Tech and for being instrumental in fetching me a job as a Senior Research Engineer at United Technologies Research Center. She has been kind of a role model to me. She sets high standards for her students and she encourages and guides them to meet those standards. Besides training me on how to use the experimental and molecular modeling tools in adsorption field, she educated me how to write scientific papers better, how to use the English language properly, how to present well at the Conferences and more importantly, how to become a good scientific researcher. Her warm-heartedness, enthusiasm, professionalism and passion for science have deeply influenced me and undoubtedly will benefit me forever.

I would like to thank Dr.David Sholl, Dr.Carson Meredith, Dr.Yoshiaki Kawajiri and Dr.Seung Soon Jang for serving on my PhD committee. I especially would like to thank Dr.Sholl for his valuable comments and suggestions.

I owe special thanks to Dr.Yougui Huang for sharing me his experiences in crystallography, for his help in solving the single crystal x-ray diffraction data for all my new crystals and introducing me to some of the crystal software tools. I thank Dr. Kenneth Hardcastle, Emory University for his help in collecting the single crystal X-ray

data for all the materials discovered in this work. I appreciate the help of Emanuel Haldoupis (Sholl Group) in determining the pore sizes for all my new MOFs. I would like to thank Taku (Sholl Group) for his collaborative work on the molecular modeling of the materials discovered in this work. I would like to thank Nair Group for letting me use their powder x-ray diffraction equipment. I would also like to thank Dr.Mary Rezac for letting me use her gravimetric adsorption equipment for my adsorption equilibrium experiments at Kansas State University. I would like to acknowledge Paul Shoenecker for his help in making me proficient in using the Vapor Sorption Appartus and TGA-Mass Spectrometry Equipment by myself. I would also like to thank him for maintaining and managing all the Walton Group Laboratory equipments efficiently and smoothly without any hassle.

I am grateful to all the present and former members of Walton Group (Dr.Huang, Paul, Cantwell, Bin, Himanshu, Greg, Yang, Christine, Katrina, Micheal, Dr.Feng, and Dr.Bogna) for their helpful comments, discussions and encouragements during our regular group meetings. I had a wonderful time working with them and they made my experience at graduate school more enjoyable.

Most importantly, none of this would have been possible without the love and patience of my family. They have been a constant source of love, concern, support and strength all these years. I would like to express my whole-hearted regards to my family. Finally, I would like to acknowledge National Science Foundation and Army Research Office for financial support of this work.

TABLE OF CONTENTS

LIST OF TABLES

Page

LIST OF FIGURES

SUMMARY

Metal-organic frameworks are a new class of porous materials that have potential applications in gas storage, separations, catalysis, sensors, non-linear optics, displays and electroluminescent devices. They are synthesized in a "building-block" approach by self-assembly of metal or metal-oxide vertices interconnected by rigid linker molecules. The highly ordered nature of MOF materials and the ability to tailor the framework's chemical functionality by modifying the organic ligands give the materials great potential for high efficiency adsorbents. In particular, MOFs that selectively adsorb CO_2 over N_2, and CH_4 are very important because they have the potential to reduce carbon emissions from coal-fired power plants and substantially diminish the cost of natural gas production. Despite their importance, MOFs that show very high selective gas adsorption behavior are not so common.

Development of MOFs for gas adsorption applications has been hindered by the lack of fundamental understanding of the interactions between the host-guest systems. Knowledge of how adsorbates bind to the material, and if so where and through which interaction, as well as how different species in adsorbed mixture compete and interact with the adsorption sites is a prerequisite for considering MOFs for adsorptive gas separation applications. In this work, we seek to understand the role of structural features (such as pore sizes, open metal site, functionalized ligands, pore volume, electrostatics) on the adsorptive separation of CO_2, CO and N_2 in prototype MOFs with the help of molecular modeling studies (GCMC simulations). Our simulation results suggest that the

suitable MOFs for CO_2 adsorption and separation should have small size, open metal site, or large pore volume with functionalized groups.

Some of the experimental challenges in the MOF based adsorbents for CO_2 capture include designing MOFs with smaller pores with/without open metal sites. Constructing such type of porous MOFs can lead to greater CO_2 capacities and adsorption selectivities over mixtures of methane or nitrogen. Therefore, in the second project, we focused on design and development of small pore MOFs with/without open metal sites for adsorptive separation of carbon dioxide from binary mixtures of methane and nitrogen. We have synthesized and characterized several new MOFs (single ligand and mixed ligand MOFs) using different characterization techniques like single-crystal X-ray diffraction, powder X-ray diffraction, TGA, BET, gravimetric adsorption and examined their applicability in CO_2/N_2 and CO_2/CH_4 mixture separations. Our findings from this study suggest that further, rational development of new MOF compounds for CO_2 capture applications should focus on enriching open metal sites, increasing the pore volume, and minimizing the size of large pores.

Flue gas streams and natural gas streams containing CO_2 are often saturated by water and its presence greatly reduces the CO_2 adsorption capacities and selectivities. So, in the third project, we investigated the structural stability of the developed MOFs by measuring water vapor adsorption isotherms on them at different humid conditions to understand which type of coordination environment in MOFs can resist humid environments. The results of this study suggest that MOFs connected through nitrogen-bearing ligands show greater water stability than materials constructed solely through carboxylic acid groups.

CHAPTER 1

INTRODUCTION, MOTIVATION AND OVERVIEW

1.1 INTRODUCTION TO POROUS METAL-ORGANIC FRAMEWORKS

Adsorption has been one of the most important gas separation technologies in the chemical industry from the last few decades. The essential requirement of adsorption separation processes is an adsorbent that preferentially adsorbs one or more components from a feed stream. Traditional porous materials such as activated carbon and zeolites have been extensively used as adsorbents in gas industry. Activated carbons have been used since the start of nineteenth century for applications such as air and water purification.[1] Zeolites have been dominant in the adsorbent industry since the 1950s and have become a technology of choice for the petroleum and chemical industry for heterogeneously catalyzed processes, for minimizing emissions to the environment, of mainly volatile organic compounds and for removing heavy metals from industrial waste.[1] Although these materials can be applied with some success, they do not fulfill all the characteristics of an ideal adsorbent for target gas pair separations.

An ideal adsorbent should possess high surface areas, low densities, high crystallinity, uniform pore structures, and higher gas adsorption capacities and selectivities towards a specific gas component. Furthermore, their pore sizes should be easily tailored and pore structures should be easily functionalized for a target species. In addition, it should also have good adsorption/desorption rates, should be easily regenerable, and should possess hydrothermal and chemical stability. Activated carbons do not have uniform pore structures. Despite the many advances made in the zeolite field,

the control and modulation of the electronic properties of framework active sites are still limited. In addition, zeolites are not easily regenerable (for example, in the case of CO_2 adsorption) and are energy intensive to recover the strongly adsorbed component.[2] New adsorbents are still needed to optimize the gas separation processes to make them commercially more attractive.

Metal Organic Frameworks (MOFs) are a recent addition to the classes of porous materials and have the potential for providing just such a flexible platform for developing designer adsorbents. MOFs are crystalline materials with regular networks and are self-assembled from the building blocks such as metal-ions or clusters and organic ligands.[3] They can be one, two, or three-dimensional infinite networks. An example of a construction of three-dimensional porous MOF, IRMOF-1 is shown in Figure 1.1.

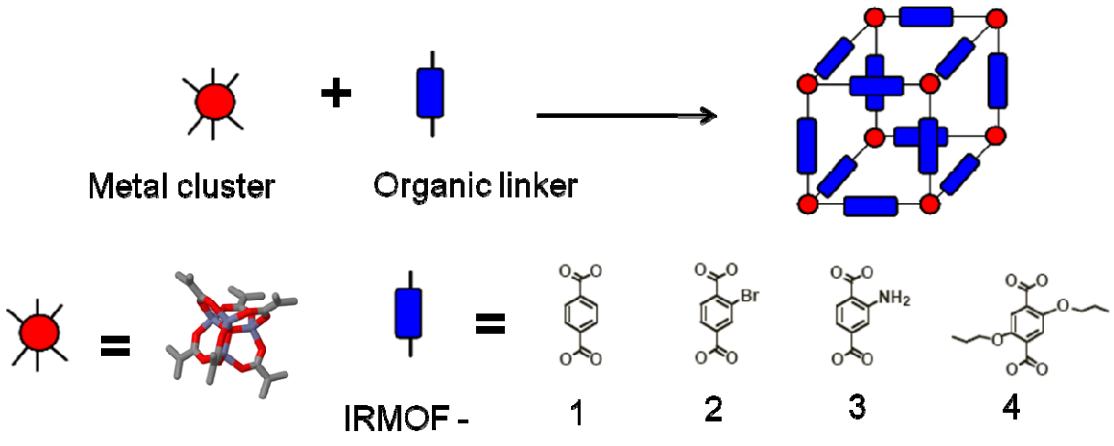

Figure 1.1 Schematic showing construction of IRMOFs (Metal cluster = $Zn_4O(COO)_6$ unit with zinc (light blue), oxygen (red), and C (gray).

The generic modular approach to synthesizing these materials allows for practically innumerable variations on the geometry and the chemical composition of these materials.[3]

MOFs possess highly crystalline nature, extraordinarily low densities (1.0 to 0.2 g/cm^3), large pore sizes (up to 29 Å), large free volumes, high surface areas (500 – 4500 m^2/g), and fascinating topologies.[4-6] They exhibit unique advantages over other traditional porous materials, due to their fine-tunable pore structures and adjustable chemical functionality. However, unlike the zeolites that are thermally stable, MOFs are subject to decomposition at high temperatures (usually above 350 ˚C). [7]

MOFs have also shown interesting flexible and dynamic behavior. These types of MOFs respond to external stimuli, such as light, electric field, guest molecules, and change their channels or pore reversibly.[8] MOFs have already shown potential in gas storage[6], separations[6], catalysis,[7] sensing, and drug delivery,[9,10] luminescent and magnetic applications.[11] Their progress in these areas can be witnessed from thousands of publications on metal organic frameworks to date.

1.2 MOTIVATION AND OBJECTIVES

Reports of gas adsorption in MOFs have shown that these materials have the potential to make a great impact in adsorption separation technologies, but MOF applications have not been truly demonstrated yet**.** Development of MOFs for gas adsorption applications has been impeded by the lack of fundamental understanding of the intermolecular interactions between the host-guest systems. Knowledge of how adsorbates bind to the material, and if so where and through which interaction, as well as how different species

in adsorbed mixture compete and interact with the adsorption sites is a prerequisite for considering MOFs for adsorptive gas separation applications.

The design of MOFs containing unsaturated metal centers has been used to prepare materials with improved adsorption capacity for gas-storage and adsorption separations. Indeed, the presence of open metal sites is of key importance for adsorption since it strongly favors the direct interaction between the metal and substrate. For instance, well-known MOFs such as Mg-DOBDC and HKUST-1 have shown good adsorption performance for carbon dioxide owing to the presence of open metal sites.[12, 13] In chapter 3, we have used atomistic grand canonical Monte Carlo (GCMC) simulations to examine the role of open copper sites of prototype MOF, Cu-BTC in affecting the separation of carbon monoxide from binary mixtures containing methane, nitrogen, or hydrogen. In chapter 4, we seek to understand the role of structural features (such as pore sizes, open metal site, functionalized ligands, pore volume, electrostatics) on the adsorptive separation of carbon dioxide, carbon monoxide and nitrogen molecules in prototype MOFs (Cu-BTC, IRMOF-1, IRMOF-3, $Zn_2(bdc)_2(dabco)$) with the help of molecular modeling studies (GCMC simulations).

Chen et al[14] previously reported a interwoven MOF (MOF-14) on a periodic minimal surface with extra-large pores. However, there have been no reports of adsorption data on this MOF. This compound has water ligands that are axially bound to copper and upon activation can generate polar Cu(II) sites. So, we hypothesized that this material might facilitate selective adsorption of quadrupolar CO_2 over nonpolar CH_4 or weakly quadrupolar N_2. In chapter 5, we report results for pure gases (CO_2, CH_4, N_2,

H_2O) and CO_2/CH_4, CO_2/N_2 mixture adsorption on this interwoven, open copper site containing MOF.

Previous works in the literature[15-17] and our conclusions from our molecular modeling and experimental work[18, 19] have shown that building MOFs with smaller pores and exposed metal sites can improve the interaction of the MOF with the gas species and could lead to greater adsorption capacities and adsorption selectivities for desired adsorptive gas separations. Furthermore, majority of the MOFs reported in the literature[6] have pore dimensions much greater than the kinetic diameter of smaller gas molecules such as CO, CO_2, CH_4, H_2, N_2, etc and hence are not highly selective towards adsorptive separations such as CO_2/N_2, CO_2/CH_4, etc. Therefore, in chapters 6, 7 and 8, we focused on design and development of small pore MOFs with/without open metal sites for adsorptive separation of carbon dioxide from binary mixtures of methane and nitrogen by utilizing (4, 4', 4'', 4'''-benzene-1, 2, 4, 5-tetrayltetrabenzoic acid (BTTB)) as a building block. We have synthesized and characterized several new MOFs (single ligand and mixed ligand MOFs) using different characterization techniques like single-crystal x-ray diffraction, powder x-ray diffraction, TGA, BET, gravimetric adsorption and examined their applicability in CO_2/N_2 and CO_2/CH_4 mixture separations. The findings from this work would enhance the understanding of relationships among MOF properties and CO_2 capture performance and would identify MOFs with the best sorption properties for CO_2.

Flue gas streams and natural gas streams containing CO_2 are often saturated by water and its presence could increase the chance of pore collapse and can greatly reduce the CO_2 adsorption capacities and selectivities.[20] However, only few reports on the effect

of water on the structural stability of MOFs have been reported in the literature.[21-23] So, in chapter 9, we investigated the structural stability of the developed MOFs by measuring water vapor adsorption isotherms on them at different humid conditions to understand which type of coordination environment in MOFs can resist humid environments.

The overall goal of my PhD research is to enhance the fundamental understanding of adsorption phenomena in the microporous metal-organic frameworks and to evaluate the potential of these materials in adsorption separations. The specific objectives of my thesis are as follows:

(1) Understand the role of structural features on the adsorptive separation of CO, CO_2, and N_2 molecules in prototype MOFs through employment of molecular modeling and experimental studies to guide the design and development of new MOFs.

(2) Design and develop novel robust MOFs with smaller pores and/or exposed open metal sites for the adsorptive separation of carbon dioxide from mixtures of methane and nitrogen.

(3) Investigate the structural stability of the developed MOFs in this study under humid conditions to determine which type of MOFs can resist humid environments.

The main contributions of this thesis are two-fold: (1) The research on modeling and simulation will advance the fundamental understanding of adsorption properties of MOFs. (2) The materials that would be developed in this work will have impact not only

on adsorption separations but also on other applications such as catalysis, sensing, drug delivery and luminescent applications.

1.3 REFERENCES

(1) Yang, R. T. *Adsorbents. Fundamentals and Applications* ; John Wiley & Sons, Inc:Hobbken, New Jersey, **2003**

(2) Ng, E. P.; Mintova, S. *Microporous Mesoporous Mater* **2008**, *114*, 1.

(3) Yaghi, O. M.; O'Keeffe, M.; Ockwig, N. W.; Chae, H. K.; Eddaoudi, M.; Kim, J. *Nature* **2003**, *423*, 705.

(4) Eddaoudi, M.; Kim, J.; Rosi, N.; Vodak, D.; Wachter, J.; O'Keeffe, M.; Yaghi, O. M. *Science* **2002**, *295*, 469.

(5) Ferey, G. *Chem. Soc. Rev.* **2008**, *37*, 191.

(6) Li, J. R.; Kuppler, R. J.; Zhou, H. C. *Chem. Soc. Rev.* **2009**, *38*, 1477.

(7) Lee, J.; Farha, O. K.; Roberts, J.; Scheidt, K. A.; Nguyen, S. T.; Hupp, J. T. *Chem. Soc. Rev.* **2009**, *38*, 1450.

(8) Kitagawa, S.; Kitaura, R.; Noro, S. *Angew. Chem. Int. Ed.* **2004**, *43*, 2334.

(9) Hinks, N. J.; McKinlay, A. C.; Xiao, B.; Wheatley, P. S.; Morris, R. E. *Microporous Mesoporous Mater* **2010**, *129*, 330.

(10) Keskin, S.; Kizilel, S. *Ind. Eng. Chem. Res* **2011**, *50*, 1799.

(11) Kuppler, R. J.; Timmons, D. J.; Fang , Q. R.; Li, J. R.; Makal, T. A.; Young, M. D.; Yuan, D. Q.; Zhao, D.; Zhuang, W. J.; Zhou, H. C. *Coordination Chemistry Reviews* **2009**, *253*, 3042.

(12) Caskey, S. R.; Wong-Foy, A. G.; Matzger, A. J. *J. Am. Chem. Soc.* **2008**, *130*, 10870.

(13) Yang, Q. Y.; Zhong, C. L. *Chemphyschem* **2006**, *7*, 1417.

(14) Chen, B. L.; Eddaoudi, M.; Hyde, S. T.; O'Keeffe, M.; Yaghi, O. M. *Science* **2001**, *291*, 1021.

(15) Chen, B. L.; Ma, S. Q.; Zapata, F.; Fronczek, F. R.; Lobkovsky, E. B.; Zhou, H. C. *Inorg. Chem* **2007**, *46*, 1233.

(16) Chen, B. L.; Xiang, S. C.; Qian, G. D. *Accounts of Chemical Research* **2010**, *43*, 1115.

(17) Liu, D. H.; Zhong, C. L. *J. Mater. Chem* **2010**, *20*, 10308.

(18) Karra, J. R.; Walton, K. S. *Langmuir* **2008**, *24*, 8620-862.

(19) Karra, J. R.; Walton, K. S. *J. Phys. Chem. C* **2010**, *114*, 15735.

(20) D'Alessandro, D. M.; Smit, B.; Long, J. R. *Angew.Chem.Int.Ed* **2010**, *49*, 6058.

(21) Kondo, A.; Daimaru, T.; Noguchi, H.; Ohba, T.; Kaneko, K.; Kanob, H. *Journal of colloid and Interface Science* **2007**, *314*, 422.

(22) Cychosz, K. A.; Matzger, A. J. *Langmuir* **2010**, *26*, 17198.

(23) Low, J. J.; Benin, A. I.; Jakubczak, P.; Abrahamian, J. F.; Faheem, S. A.; Willis, R. R. *J. Am. Chem. Soc.* **2009**, *131*, 15834.

CHAPTER 2

BACKGROUND

2.1 SYNTHESIS OF MOFS

The synthesis of MOFs is usually carried out by mixing the metal precursors and organic component in a pure solvent or suitable mixture of solvents, and heating at mild temperatures (typically between 50 and 250 ˚C) in a sealed vessels such as Teflon-lined stainless steel bombs, glass vials, or glass tubes under (hydro) solvothermal conditions. Water, alcohols, alkyl formamides (such as dimethyl formamide, diethyl formamide) or dimethyl sulfoxide (DMSO), and dioxane are generally used as solvents in the synthesis of MOFs. A large variety of metal atoms in their stable oxidation states, i.e., alkaline, alkaline-earth, transition metals, lanthanide elements are used in the synthesis of MOFs. Common choices of organic ligands include polycarboxylic aromatic molecules, bipyridines, and polyazaheterocycles (imidazoles, triazoles, tetrazoles, pyrimidines, pyrazines, etc).[1] Figure 2.1 shows the ligands such as 1,4-terepthalic acid (1,4-BDC), 1,3,5-benzene tricarboxylic acid (BTC), 1,3,5-tris(4-carboxyphenyl) benzene (BTB), 4,4',4'',4'''-benzene-1,2,4,5-tetrayltetrabenzoic acid (BTTB), 4,4'-bipyridine (BPY), 4,4'-azopyridine (AZPY), 1,4-diazabicylco[2.2.2]octane (DABCO) that are employed in this work.

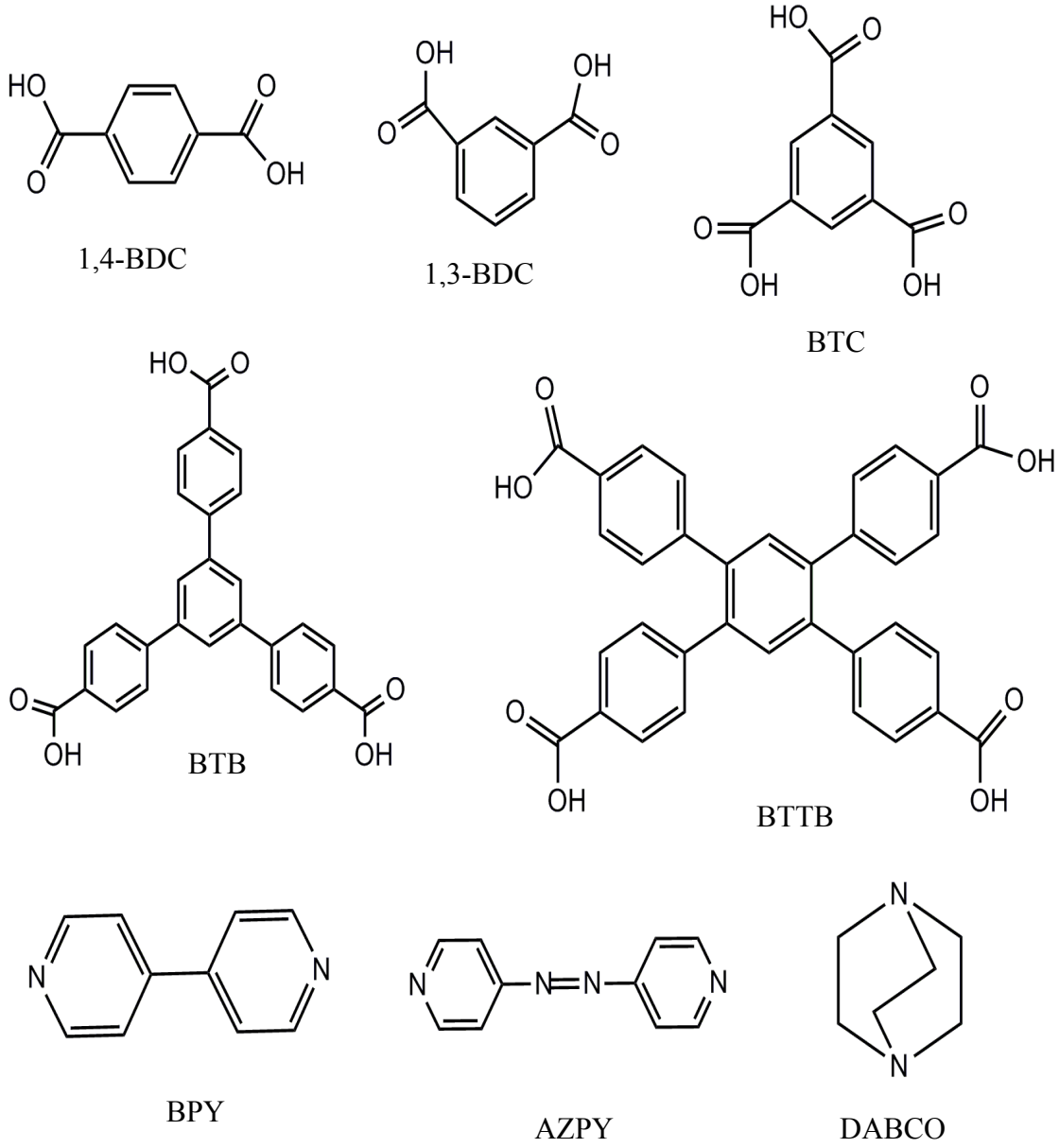

Figure 2.1 Organic ligands that are employed in this work

The synthesis parameters such as nature of the solvent, ligand/metal salt ratio, pH or temperature can have a dramatic effect on the crystal structure of the material obtained.

Thus, a given metal-ligand combination can lead to a number of different structures depending on the subtle changes on the above-mentioned synthesis parameters. For instance, the system zinc-terepthalate has resulted in several different structures, MOF-5, MOF-2, MOF-3, and MOF-69C by simply changing the solvent.[2]

2.2 CONSTRUCTION OF MOFS

MOF geometry is controlled by the secondary building unit (SBU) formed *in situ* between the metal precursor and the organic ligand.[3] Different SBU's such as tetrahedral, paddle-wheel, and octahedral metal clusters can lead to different MOF topologies from discrete chains, rods, and squares to pillared structures and cubic frameworks. An octahedral SBU and paddlewheel cluster SBU are shown in Figure 2.2.

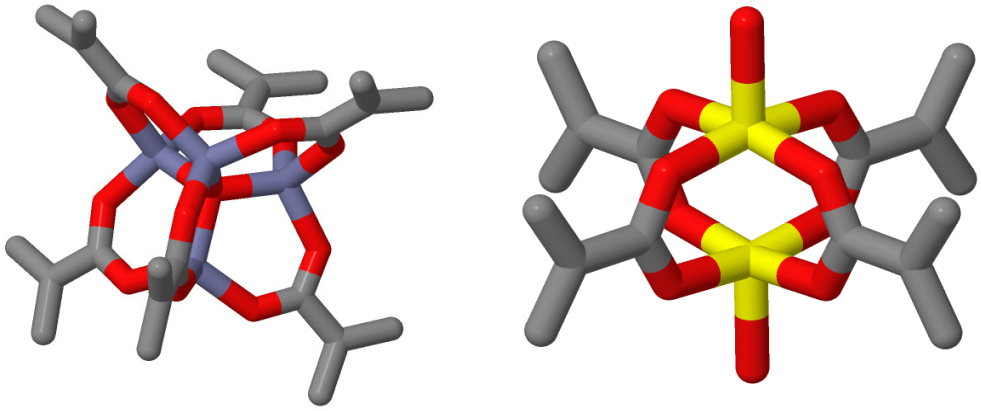

Figure 2.2 Example of secondary building units a) Octahedral SBU
b) Paddle wheel SBU

In principle, different MOFs with varying pore sizes and functionalities can be attained just by using the same metal cluster and varying the organic ligand. This principle was followed in synthesizing the IRMOF series and was first demonstrated by Yaghi's group.[3] Each of these three-dimensional cubic structures are based upon the octahedral cluster $Zn_4O(COO)_6$ SBU and a series of ditopic carboxylate linkers. As illustrated in Figure 1, the ligands in IRMOF-1, 2, 3, and 4 have the same length, and so the diameters of the channels in their structures are affected only by the functional groups on the linking phenyl ring. The characteristics of the ligand (bond angles, ligand length, bulkiness, chirality, etc.) can also play a crucial role in dictating what the resultant framework will be. For example, linking a copper-based paddle wheel with triangular SBUs, either BTB or BTC, results in MOF-14 with the Pt_3O_4 topology and HKUST-1 with the twisted boracite topology.[4] Additionally the tendency of metal ions to adopt certain geometries also influences the structure of the MOF.

2.3 CHARACTERIZATION OF POROUS MOFS

Crystal structures of newly synthesized compounds are analyzed by single-crystal X-ray diffraction technique and the framework integrity and phase purity of the samples are determined by powder X-ray diffraction technique. Once the structure is analyzed, the pore size of the porous MOF can be determined by measuring the atom-to-atom distance across the pores or channels, and the pore volume can be estimated based on the accessible solvent volume calculated using PLATON.[36] For the MOF to be permanently porous, it needs to withstand the removal of solvent molecules during evacuation. The

permanent porosity can be confirmed by using N_2 adsorption/desorption studies at 77 K. The data obtained from these isotherms can be used to quantify the surface area, pore volume, and pore size of the tested MOF. Thermogravimetric analyses (TGA) are frequently used to obtain the thermal behavior and chemical composition of solid materials. Infrared spectroscopy can be used to identify and elucidate structural details, and improve understanding of crystal chemistry of solid materials. Electron microscopy can be used to identify the morphology of the MOF particles and elemental analysis is used to confirm the chemical composition of the compound. The adsorption isotherms of different gas molecules in MOFs can be obtained using the gravimetric adsorption instrument or volumetric adsorption equipment.

2.4 MOLECULAR MODELING

Due to the predictability of MOF structure and uniformity of the frameworks, molecular modeling can be used as a complement to the experiments for studying the adsorption in these systems. In these simulations, one assumes that the interactions between each pair of atoms in a system can be described accurately using a classical force field. Once the force fields are specified, grand canonical Monte Carlo (GCMC) method can be used to compute the equilibrium properties of the simulated material. This method is analogous to the experimental procedure of specifying the temperature and external (bulk) pressure of a gas and measuring the uptake as a function of these variables. It is the chemical potential of the adsorbate that is specified in GCMC simulations, rather than bulk pressure. The chemical potential can easily be related to the bulk pressure through an equation of state or separate bulk phase simulations.[5] In the grand canonical ensemble,

the configurations of the system evolve from randomly inserting, deleting, or repositioning particles within the system at constant temperature, volume and chemical potential, μ. The new configuration is either accepted or rejected based on the Metropolis- Hastings criteria. Once the system has reached equilibrium, ensemble averages can be calculated to determine various properties of the system.[6]

GCMC simulations are usually done on a "perfect" crystal structure. Therefore, comparison with adsorption experiments can help us reveal the defects or impurities present in the experimental samples. These simulations can provide valuable information such as preferred adsorption sites, isosteric heats, effect of electrostatic interactions and evidence of monolayer or multilayer formation, but it is important that the predicted isotherms capture the basic characteristics of the experimental isotherms. Experimental measurement of multi-component adsorption in MOFs is complex and time consuming. In this context, molecular simulations can play a useful role. Once a molecular model describing single component adsorption is available, simulations can then be easily performed to probe mixture adsorption in MOF systems. These studies can give us insight into the competition between the components for the adsorption sites and can predict the properties of specific MOFs for particular separations of interest. Understanding these insights from the pure and multi-component adsorption simulations could then be used to guide synthetic efforts to design new MOFs that target certain adsorption behavior.

2.5 GAS STORAGE AND SEPARATION IN POROUS MOFS

MOFs first garnered significant attention as possible adsorbents for hydrogen or methane storage.[7] Since these early investigations, a large number of experimental and computational studies of adsorption in MOFs have been reported. The most widely studied MOFs include the MIL materials of Ferey and co-workers,[8] the IRMOF series of Yaghi and co- workers[3] and Cu-BTC or HKUST-1, which was first reported by Chui et al.[9] Among the MIL series, the MIL-53 material has been found to adsorb relatively large amounts of CH_4 and CO_2.[10] Yaghi and co-workers found high storage capacities of the IRMOFs for CH_4 and H_2. [3,11] The experimental results of Wang et al.[12] show that Cu-BTC has the potential to be used for separation of gas mixtures such as CO_2-CO, CO_2-CH_4, and ethylene-ethane. There have also been reports of multi-component adsorption experiments in MOFs including the use of MOFs for separation of xylene isomers,[13,14] ortho-substituted alkylaromatics,[15] CO_2 from N_2 and CH_4,[16,17] kinetic separation of hexane isomers,[18] liquid-phase separation of aliphatic C_5-diolefins, mono-olefins, and paraffins,[19] and removal of thiophene from CO_2/CH_4 mixtures in dry and humid conditions.[20]

Many molecular simulation studies have been performed to investigate adsorption and diffusion properties in MOFs. Grand canonical Monte Carlo (GCMC) simulations were employed to identify strategies in designing MOFs for hydrogen, methane, and carbon dioxide storage.[5,21] A recent report on water adsorption in Cu-BTC showed that water has a strong affinity for copper sites compared to molecules such as CO_2, N_2, or O_2.[22] Many of the simulation studies on MOFs have focused on separating CO_2 from

CH_4 for natural gas upgrading,[23,24] while some have focused on separation of H_2/CH_4 mixtures,[25, 26] and CO_2 from flue gas.[27-29] Other investigations include separating mixtures of alkanes,[30,31] separation of CO from CH_4, CO_2, and N_2,[25, 32] alcohol/water mixtures,[33] and olefins/paraffins.[32,34] However, only a few studies so far have considered mixtures containing carbon monoxide.[25, 32,35] Therefore, my work gives special attention to these systems.

2.6 REFERENCES

(1) Corma, A.; Garcia, H.; Xamena, F. X. L. *Chem. Rev* **2010**, *110*, 4606.

(2) Caskey, S. R.; Wong-Foy, A. G.; Matzger, A. J. *Inorg. Chem* **2008**, *47*, 7751.

(3) Eddaoudi, M.; Kim, J.; Rosi, N.; Vodak, D.; Wachter, J.; O'Keeffe, M.; Yaghi, O. M. *Science* **2002**, *295*, 469.

(4) Yaghi, O. M.; O'Keeffe, M.; Ockwig, N. W.; Chae, H. K.; Eddaoudi, M.; Kim, J. *Nature* **2003**, *423*, 705.

(5) Keskin, S.; Liu, J.; Rankin, R. B.; Johnson, J. K.; Sholl, D. S. *Ind. Eng. Chem. Res.* **2009**, *48*, 2355.

(6) Frost, H. Evaluation of metal-organic frameworks as adsorbent materials with applications in hydrogen storage and carbon dioxide separations, Ph.D. Dissertation. Northwestern University, Evanston, IL, **2007**.

(7) Ma, S.; Zhou, H. C. *Chem. Commun.* **2010**, *46*, 44-53.

(8) Ferey, G. *Chem. Soc. Rev.* **2008**, *37*, 191.

(9) Chui, S. S. Y.; Lo, S. M. F.; Charmant, J. P. H.; Orpen, A. G.; Williams, I. D. *Science* **1999**, *283*, 1148.

(10) Bourrelly, S.; Llewellyn, P. L.; Serrey, C.; Millanage, F.; Loiseau, T.; Ferey, G. *J. Am. Chem. Soc.* **2005**, *127*, 13519.

(11) Li, H.; Eddaoudi, M.; O'Keeffe, M.; Yaghi, O. M. *Nature* **1999**, *402*, 276.

(12) Wang, Q. M.; Shen, D. M.; Bulow, M.; Lau, M. L.; Deng, S.; Fitch, F. R.; Lemcoff, N. O.; Semanscin, J. *Microporous and mesoporous materials* **2002**, *55*, 217.

(13) Alaerts, L.; Kirschhock, C. E. A.; Maes, M.; van der Veen, M. A.; Finsy, V.; Depla, A.; Martens, J. A.; Baron, G. V.; Jacobs, P. A.; Denayer, J. E. M.; De Vos, D. E. *Angew. Chem. Int. Ed.* **2007**, *46*, 4293.

(14) Finsy, V.; Verelst, H.; Alaerts, L.; De Vos, D.,Dirk; Jacobs, P. A.; Baron, G. V.; Denayer, J. F. M. *J. Am. Chem. Soc.* **2008**, *130*, 7110-7118.

(15) Alaerts, L.; Maes, M.; Giebeler, L.; Jacobs, P. A.; Martens, J. A.; Denayer, J. F. M.; Kirschhock, C. E. A.; De Vos, D. E. *J. Am. Chem. Soc.* **2008**, *130*, 14170-14178.

(16) Bastin, L.; Barcia, P. S.; Hurtado, E. J.; Silva, J. A. C.; Rodrigues, A. E.; Chen, B. *J. Phys. Chem. C* **2008**, *112*, 1575.

(17) Finsy, V.; Ma, L.; Alaerts, L.; De Vos, D. E.; Baron, G. V.; Denayer, J. F. M. *Microporous Mesoporous Mater.* **2009**, *120*, 221.

(18) Bárcia, P. S.; Zapata, F.; Silva, J. A. C.; Rodrigues, A. E.; Chen, B. L. *J. Phys. Chem. B* **2007**, *111*, 6101.

(19) Maes, M.; Alaerts, L.; Vermoortele, F.; Ameloot, R.; Couck, S.; Finsy, V.; Denayer, J. F. M.; De Vos, D. E. *J. Am. Chem. Soc.* **2010**, *132*, 2284-2292.

(20) Galli, S.; Masciocchi, N.; Colombo, V.; Maspero, A.; Palmisano, G.; Lopez-Garzon, F. J.; Domingo-Garcia, M.; Fernandez-Morales, I.; Barea, E.; Navarro, J. A. R. *Chem. Mater.* **2010**, *22*, 1664-1672.

(21) Düren, T.; Bae, Y. S.; Snurr, R. Q. *Chem. Soc. Rev.* **2009**, *38*, 1237.

(22) Castillo, J. M.; Vlugt, T. J. H.; Calero, S. *J. Phys. Chem. B* **2008**, *112*, 15934.

(23) Babarao, R.; Jiang, J.; Sandler, S. I. *Langmuir* **2009**, *25*, 5239-5247.

(24) Bae, Y. S.; Farha, O. K.; Sponkoyny, A. M.; Mirkin, C. A.; Hupp, J. T.; Snurr, R. Q. *Chemical communications* **2008**, , 4135.

(25) Karra, J. R.; Walton, K. S. *Langmuir* **2008**, *24*, 8620-862.

(26) Gallo, M.; Glossman-Mitnik, D. *J. Phys. Chem. C* **2009**, *113*, 6634.

(27) Liu, B.; Yang, Q.; Xue, C.; Zhong, C.; Chen, B.; Smit, B. *J. Phys. Chem. C* **2008**, *112*, 9854.

(28) Liu, B.; Smit, B. *Langmuir* **2009**, *25*, 5918.

(29) Yazaydin, A. O.; Snurr, R. Q.; Park, T. H.; Koh, K.; Liu, J.; LeVan, M. D.; Benin, A. I.; Jakubczak, P.; Lanuza, M.; Galloway, D. B.; Low, J. J.; Willis, R. R. *J. Am. Chem. Soc.* **2009**, *131*, 18198.

(30) Babarao, R.; Tong, Y. H.; Jiang, J. *J. Phys. Chem. B.* **2009**, *113*, 9129-9136.

(31) Dubbeldam, D.; Galvin, C. J.; Walton, K. S.; Ellis, D. E.; Snurr, R. Q. *J. Am. Chem. Soc.* **2008**, *130*, 10884.

(32) Wang, S. Y.; Yang, Q. Y.; Zhong, C. L. *Sep. Purif. Technol.* **2008**, *60*, 30.

(33) Chen, Y. F.; Lee, J. Y.; Babarao, R.; Li, J.; Jiang, J. W. *J. Phys. Chem. C* **2010**, *114*, 6602.

(34) Lamia, N.; Jorge, M.; Granato, M. A.; Almeida P., F. A.; Chevreau, H.; Rodrigues, A. E. *Chem. Eng. Sci.* **2009**, *64*, 3246-3259.

(35) Karra, J. R.; Walton, K. S. *J. Phys. Chem. C* **2010**, *114*, 15735.

(36) Spek, A.L. **2005**, PLATON, A Multipurpose Crystallographic Tool, Utrecht University, Utrecht, The Netherlands.

CHAPTER 3

EFFECT OF OPEN METAL SITES ON ADSORPTION OF POLAR AND NONPOLAR MOLECULES IN METAL-ORGANIC FRAMEWORK CU-BTC

3.1 INTRODUCTION

A critical step in developing adsorption-based technologies is the identification/synthesis of adsorbents that provide the proper adsorption capacities, selectivities, or reactivities for the application. It is well known that metal sites in porous materials have a tremendous influence on the resulting adsorption properties. For example, the exchangeable cations in zeolite molecular sieves[1-5] or the metals in impregnated carbons[6-10] are known to provide catalytic sites and also impose acid/base character to the pores that can enhance separations.

The ability to design an adsorbent with a particular pore size, pore shape, and chemical functionality would provide a significant advance in areas such as adsorption separations and catalysis. Metal-organic frameworks (MOFs) are a recent addition to the classes of porous materials and have the potential for providing just such a flexible platform for developing designer adsorbents. MOFs are synthesized by self assembly of organic ligands and metal oxide clusters. The resulting crystalline materials possess regular porous structures with pore sizes and chemical functionalities that can be manipulated by modifying the metal group or organic linker.[11-20] These flexible methods have led to the synthesis of thousands of MOFs over the past decade.

Several MOFs have open metal sites (coordinatively unsaturated) that are built into the pore 'walls' in a repeating, regular fashion. These metal sites, such as those found in Cu-BTC[21] or MIL-100[22], have been shown to impart catalytic activity to the materials. The partial positive charges on the metal sites in MOFs also have the potential to enhance general adsorption properties. This has often been discussed as a strategy for increasing hydrogen adsorption in MOFs.[16, 23, 24] This strategy could also be expected to improve adsorption selectivities in separating mixtures with molecules of differing polarities.

In this work, we have used atomistic GCMC simulations to examine the role of the open metal sites of Cu-BTC in affecting the separation of carbon monoxide from mixtures containing methane, nitrogen, or hydrogen. These are important mixtures that are generated from a variety of sources such as off-gases from steel plants, synthesis gas from steam reforming, CO_2 conversion, and partial oxidation of hydrocarbons and coal gasification.[25] The selective removal of CO using MOFs has not been previously explored. From pure-component adsorption experiments,[26] it was shown that CO adsorbs in comparable amounts to methane in Cu-BTC. Thus, exploring the pure-component and binary adsorption behavior of these molecules should provide insight into the importance of electrostatic effects in adsorption separations. We first use GCMC to simulate pure-component adsorption of CO, CH_4, H_2, and N_2 in Cu-BTC and verify our model with experiments. Heats of adsorption and Henry's constants for each component are also computed. Binary mixture simulations are performed for CO with each of the three gases at 5%, 50% and 95% mixtures, and adsorption selectivities are calculated. The contribution to the adsorption mechanism of CO from electrostatic effects relative to van

der Waals interactions is determined. Simulation snapshots are used to identify preferred adsorption sites for CO and methane.

3.2 MODELS

Cu-BTC, shown in Figure 3.1, has been extensively studied both experimentally[26-29] and theoretically.[30, 31] It has a face centered cubic crystal structure and contains an intersecting 3D system of large square-shaped pores (9 x 9 Å) and is composed of paddle-wheel units assembled from two copper atoms and four benzenetricarboxylate(BTC) groups.[27] The structure of Cu-BTC has two kinds of domains: tetrahedron side pockets (~ 5 Å diameter with 3.5 Å windows), and large square-shaped channels. The unit cell has a free volume of 66 %[32] and a BET surface area ranging from 1200 – 1500 m^2/g.[26, 33]

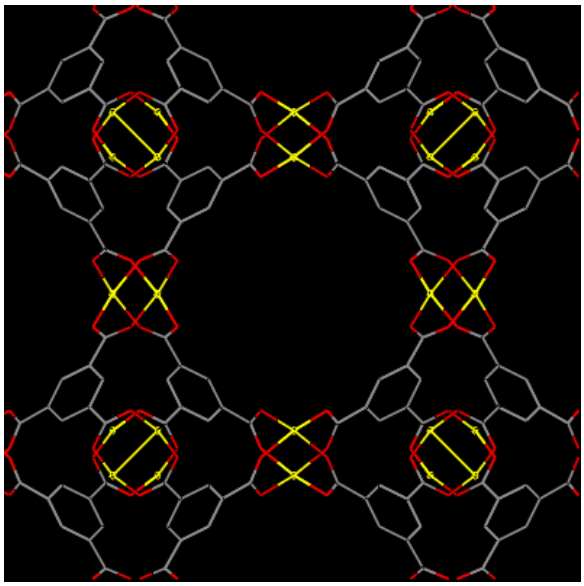

Figure 3.1 Unit cell of Cu-BTC. Red = oxygen; yellow = copper; gray = carbon.

The molecular model used in this work was constructed from the experimental X-ray diffraction crystallographic data with water molecules removed to simulate a regenerated material.[27] The atomic partial charges of Cu-BTC were taken from Yang and Zhong. The Lennard-Jones (LJ) parameters for the MOF atoms were taken from Wang et al.[34] for carbon monoxide and from Yang and Zhong[35] for methane and hydrogen. These authors used all-atom OPLS force field (OPLS-AA) of Jorgensen et al[36] in their work. For copper, they have used all-atom universal force field (UFF)[37] as it was not available in OPLS-AA force field. For the case of nitrogen, we used the same potential parameters of methane taken from literature[31] to give a good reproduction of the experimental isotherms. The numerical values for these parameters along with the partial charges on the atoms of framework Cu-BTC are listed in Table 3.1.

Hydrogen was treated as a united atom molecule and its parameters were taken from Michels et al.[38]Methane was modeled as a single-center Lennard-Jones molecule using the TraPPE force field developed by Martin and Siepmann.[39] Nitrogen was modeled as a diatomic molecule with fixed bond lengths and bond angles using the TraPPE force field developed by Potoff and Siepmann.[40] In this model, point charges were centered on each LJ site and electric neutrality was maintained by placing a point charge of +0.964 e at the center of mass (COM) of the N_2 molecule.

Table 3.1 Atomic Partial Charges and Potential Parameters of the Atoms in the Framework of Cu-BTC

Atom	Partial Charge q (e)	σ (Å)	ε/k_B (K) CO	CH_4	H_2	N_2
O	-0.665	2.96	105.7	61.29	73.98	61.29
$C_{carboxyl}$	0.778	3.75	52.84	42.27	52.84	42.27
$C_{benzene}$	-0.092	3.55	35.23	35.23	35.23	35.23
$C_{benzene}$	-0.014	3.55	35.23	35.23	35.23	35.23
$H_{benzene}$	0.109	2.42	15.1	15.1	15.1	15.1
Cu	1.098	3.11	2.52	2.52	2.52	2.52

Table 3.2 LJ and Coulombic Potential Parameters

Sorbate	atom	σ (Å)	ε/k_B (K)	q(e)	l (Å)
CH_4		3.73	148.000	0	
H_2		2.958	36.7	0	
N_2	N	3.31	36	-0.482	0.55
	NCOM	0	0	0.964	
CO	C	3.385	39.89	0.831	-0.6446
	O	2.885	61.57	0	0.4836
	Site 1			-0.636	-1.0820
	Site 2			-0.195	0.3256

l is the distance from the molecular center of mass and q is the partial charge

A four-site model developed by Piper et al.[41] was used for carbon monoxide. Lennard-Jones sites are located on the carbon and oxygen atom, and point charges are used to mimic the dipole moment of the molecule. In this four-site model, one charge site is placed on the molecular axis roughly 0.42 Å to the 'left' of the carbon atom. The center of mass of the carbon atom provides the second charge site. The third charge site is located on the molecular axis between the carbon and oxygen atoms, and center of mass of oxygen provides the fourth site. The potential parameters, partial charges, and bond lengths for methane, hydrogen, nitrogen, and CO are shown in Table 3.2. For interactions of the adsorbates with Cu-BTC, cross-terms for the Lennard-Jones potentials were calculated using the Lorentz-Berthelot combining rules.[42]

3.3 METHODOLOGY

The Monte Carlo method was used to calculate adsorption equilibria for single components and mixtures. The grand canonical ensemble was employed in the simulations to mimic adsorption experiments. In grand canonical Monte Carlo (GCMC) simulations, a chemical potential is imposed on the constant volume system at constant temperature.[42] The number of molecules is then allowed to fluctuate until equilibrium at the required chemical potential has been attained. These simulations were performed using Music simulation code.[43]

Three different types of Monte Carlo trials were used in these simulations: creation of a new adsorbate molecule at random position in the adsorbent, removal of a randomly chosen adsorbate molecule from the adsorbent and translation of a randomly chosen adsorbate molecule within the adsorbent. For each trial, the energy difference between

the new and old configurations was calculated. The new configuration was accepted if the new energy was less than the old energy or if the Boltzmann factor calculated from the energy difference was less than a random number generated at each trial.

The simulation box representing Cu-BTC contained 8 (2x2x2) unit cells. The MOF atoms were treated as rigid. The single component and mixture simulations were run for at least 20 million trials. In all cases the first half of these trials was used for equilibration and was not included in the final averaging. The nonideal behavior of the bulk pure gas and gas mixtures was described by the Peng-Robinson equation of state (PR-EOS).[44] For all of the binary mixtures, the binary interaction parameter in the PR-EOS was assumed to be zero. Ewald summations were used to calculate Coulombic interactions between the sorbate and framework atoms.[45] A cutoff based on the center of mass distance was used to calculate Coulomb interactions between sorbate molecules. GCMC simulation gives the absolute number of molecules adsorbed. However, experimental data are typically reported as the excess amount adsorbed. Thus, all absolute loadings were converted to excess loadings to allow direct comparison of results with experimental data.[46]

Isosteric heats of adsorption, q_{st}, were also calculated for each component. This quantity can be calculated from simulations as the difference of the partial molar enthalpy of the sorbate in the bulk phase and the partial molar internal energy in the adsorbed phase. This is given below by Eq. 1,

$$q_{st} = RT - \left(\frac{\partial U}{\partial N_{ads}} \right)_{T,V} \qquad (1)$$

where N_{ads} is the adsorption loading and U is the internal energy of the sorbate in the adsorbed phase that includes contributions from both adsorbate-adsorbent and adsorbate-adsorbate interactions.[47]

Adsorption selectivities were calculated to examine the competitive adsorption between two components. The selectivity for component *i* over component *j* was calculated as $\alpha_{ij} = (x_i/x_j)(y_j/y_i)$, where *x* indicates the mole fraction in the adsorbed phase and *y* indicates the mole fraction in the gas phase.

3.4 RESULTS AND DISCUSSION

The isotherms computed from single component GCMC simulations for CO, CH_4, N_2, at 295K and H_2 at 298K are shown with experimental results in Figures 3.2 and 3.3. The lines are drawn for visual clarity for simulated results. As shown in the figures, there is a good agreement between experimental isotherms and simulation isotherms for all sorbates. The adsorption isotherms of CO and CH_4 are quite similar throughout this pressure range, with loadings around 0.9 mol/kg at 100 kPa. GCMC simulations for all four components over a larger pressure range are shown in Fig. 3.4. These calculations indicate that Cu-BTC has a slight adsorption preference for CO over the other three sorbates at higher pressures. CO adsorbs more strongly than methane above approximately 1 MPa and achieves a loading of 11 mol/kg at 4 MPa. It is notable that even at such high pressures, none of the isotherms appear to be completely at the saturation point.

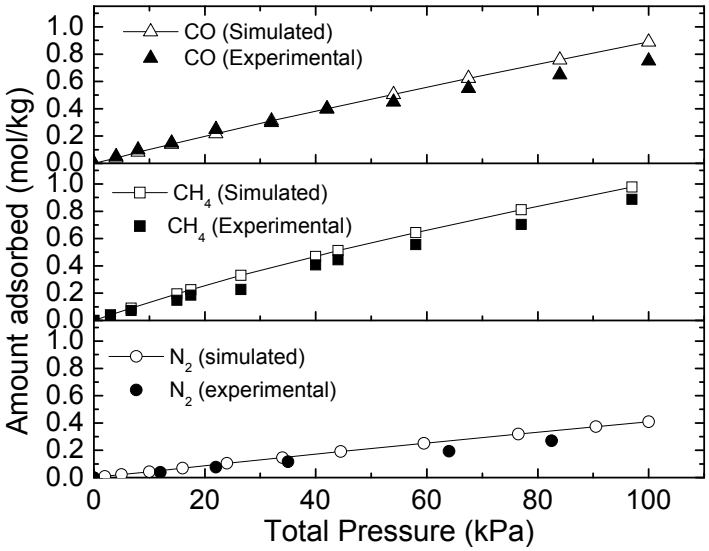

Figure 3.2 Adsorption isotherms calculated from GCMC simulations vs experimental isotherms[39] for (a) CO (b) CH_4 (c) N_2 at 295 K in Cu-BTC.

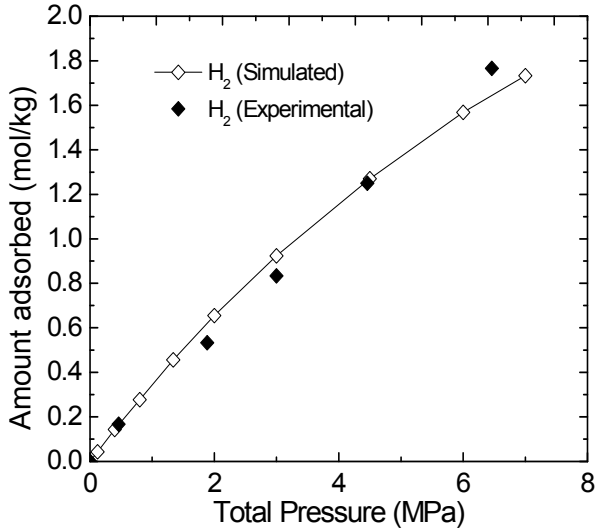

Figure 3.3 Comparison of GCMC simulations of hydrogen adsorption in Cu-BTC at 298 K with experimental data.

The isosteric heats of adsorption (q_{st}) for pure CO, CH_4, N_2, and H_2 at 298K in Cu-BTC are shown in Figure 3.5. Methane exhibits the highest heat of adsorption at low loadings, but q_{st} decreases with increasing loading until roughly 3 mol/kg, where it reaches a constant value of approximately 16 kJ/mol. The initial decrease is a consequence of the heterogeneous character of the Cu-BTC surface, in which the energetically favored side pockets of Cu-BTC are occupied first and then the less favorable sites are occupied as the loading increases. CO exhibits the highest isosteric heat of adsorption in Cu-BTC at loadings greater than 1 mol/kg but is actually lower than methane at low loadings. As expected, the trends of the isosteric heats are consistent with the trends of the adsorption isotherms in Figs. 2-4.

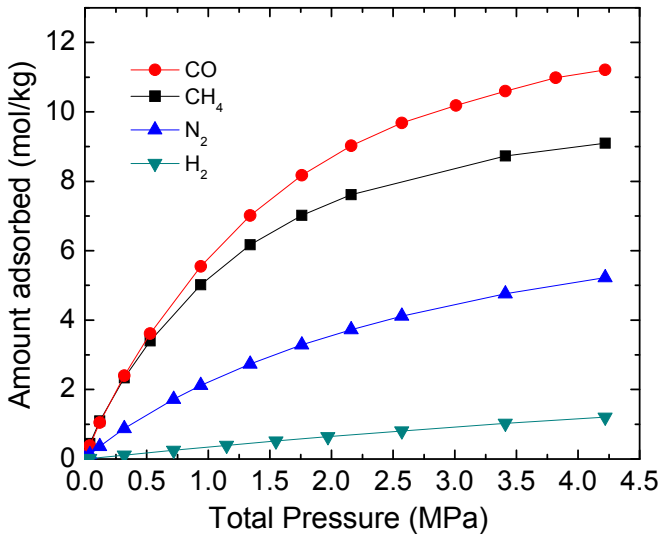

Figure 3.4 Adsorption isotherms for CO, CH_4, N_2, and H_2 in Cu-BTC at 298 K calculated from GCMC simulations.

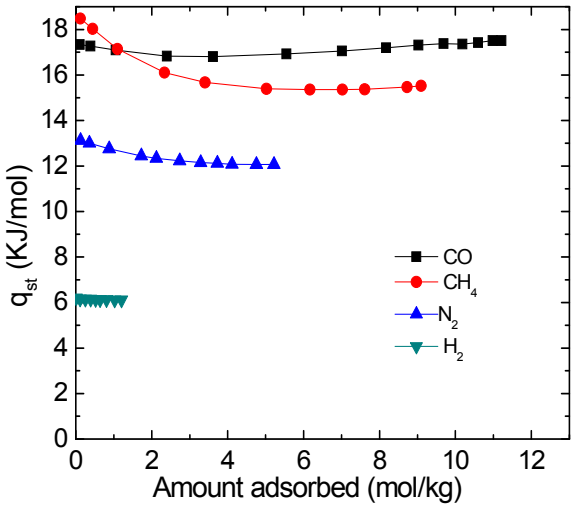

Figure 3.5 Isosteric heats of adsorption as a function of loading for CO, CH_4, N_2, and H_2 at 298 K.

Figure 3.6 shows isosteric heats for methane and CO separated into two types of contributions: sorbate-sorbent and sorbate-sorbate. For CO, the contribution of the sorbent-sorbate interaction to the total isosteric heat decreases slightly with increasing loading. This behavior is reasonable because the favorable adsorption sites begin to fill up as loadings increase. The interaction of CO with itself becomes a larger contributor to the overall isosteric heat as loading increases. The net effect is that the isosteric heat for CO remains essentially constant at loadings up to 11 mol/kg. Conversely, the isosteric heat of adsorption for CH_4 decreases sharply with loadings up to 4 mol/kg (Fig 6a). These contributions, which include only Van der Waals interactions, continue to decrease steadily, even at higher loadings. These trends are consistent with the adsorption isotherms. These results indicate that the contribution of the sorbent-sorbate interaction to

the isosteric heat of adsorption for CO leads to higher loadings compared to methane at the same pressure.

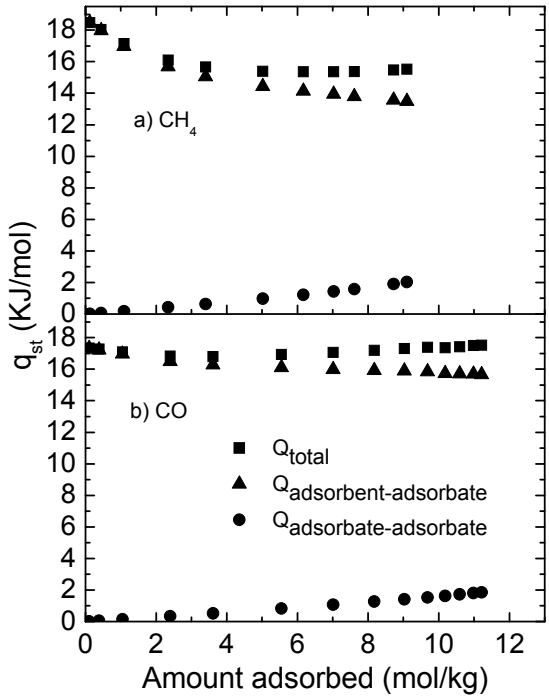

Figure 3.6 Contributions of sorbent-sorbate and sorbate-sorbate interactions to the isosteric heat for a) CH_4 and b) CO.

To further examine the effect of the electrostatic interactions, CO adsorption isotherms were calculated for three cases: a full model, which considers Van der Waals interactions and electrostatic interactions of CO with itself and with the framework; a model in which the electrostatic interaction between CO and the framework is neglected; and a model which only considers Van der Waals interactions. These results are shown in Figure 3.7. The electrostatic interactions between the framework atoms and CO molecules clearly dominate the adsorption mechanism. Sorbate-sorbent interactions typically exhibit the greatest effect on adsorption at low coverage. In this case, CO is far from saturating the

pore space of Cu-BTC. Thus, sorbate-sorbent interactions remain important at higher loadings than is traditionally observed because framework atoms are still available to interact with incoming sorbate molecules. This is quite different from behavior that was found for CO_2 adsorption in several MOFs.[48] The electrostatic interaction between CO_2 molecules (sorbate-sorbate) was found to have a great effect on the adsorption mechanism, but here we find that the CO-CO interaction has relatively no effect on the isotherm.

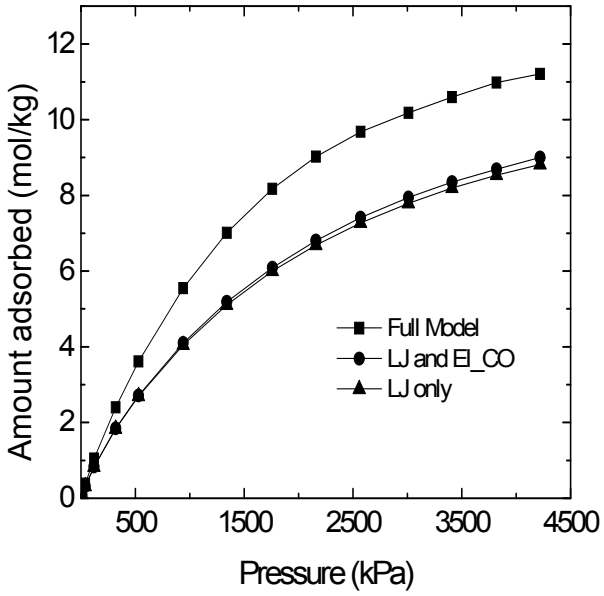

Figure 3.7 Effect of electrostatic interactions on CO adsorption in Cu-BTC at 298 K.

Henry's constants for each sorbate are shown in Table 3.3. As expected, these values follow the same trends as the isosteric heats at low coverage. The Henry's constant for methane is 35% greater than that of CO. This shows that the Van der Waals forces are relatively strong between methane and the MOF surface at low coverage. Henry's constants for CO were calculated using both the full model, and the model which neglects electrostatic interactions. The Henry's constant for the full model is slightly higher than

the LJ-only model. This indicates that the partial positive charges of the framework do enhance the adsorption interaction of CO with the MOF.

The electrostatic interactions between CO and the MOF atoms were shown in Figure 3.7 to have a significant impact on the pure-component isotherm. This was also reflected in the Henry's constants. However, at low pressures, the adsorption of methane was found to be slightly more favorable than CO as a result of the strong Van der Waals forces. Now that pure-component adsorption behavior has been established, the next relevant issue that arises is how electrostatic interactions affect adsorption selectivities. To explore this, adsorption equilibrium data and adsorption selectivities were calculated for binary mixtures of CO/H_2, CO/CH_4, and CO/N_2 at three different compositions (5, 50, and 95% CO).

Table 3.3 Henry's constants for sorbates.

Sorbate	**Henry's constants (mol/kg.kPa)**
CH_4	0.013
CO[a]	0.0095
CO[b]	0.0083
N_2	0.0043
H_2	0.0004

[a] Includes electrostatic interactions with the framework
[b] Includes Lennard-Jones interactions only

Adsorption selectivities for mixtures of CO and hydrogen are shown in Figure 3.8. The pure-component isotherms indicate that CO should be preferentially adsorbed over H_2, and the mixture simulations confirm this. The selectivity for CO remains essentially constant for all three compositions up to a pressure of about 1 MPa. At this point, the 95% mixture has the highest selectivity for CO. At such high pressures, the large number of CO molecules in the system prevents appreciable amounts of hydrogen from adsorbing; the preference for CO is too strong to allow competitive coadsorption. Selectivities for this mixture are well above 100 at these pressures. The mixture containing 5% CO exhibits the lowest selectivities, which remain approximately constant at a value of ~28 over the entire pressure range. Both components in the 5 % mixture adsorb at quantities that are roughly equal to their pure-component behavior; the quantity of CO in the mixture is too small to significantly displace hydrogen at the higher pressures. In fact, we find that an adsorbed-phase composition of 0.6 and 0.4 for CO and H_2, respectively, are maintained throughout the pressure range examined.

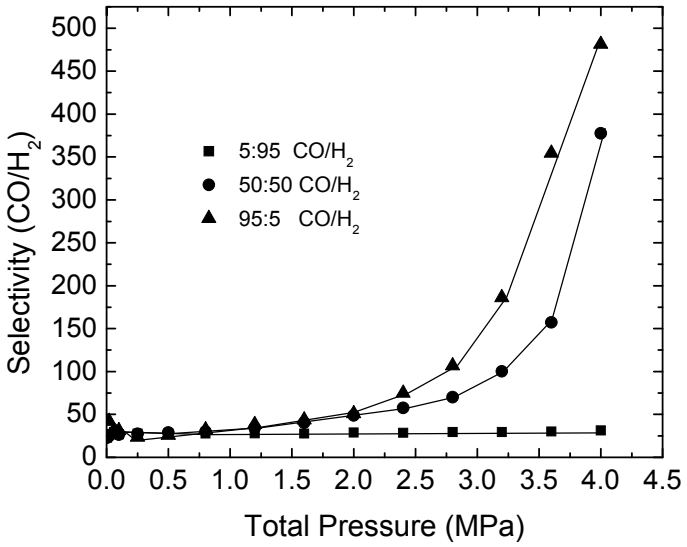

Figure 3.8 Adsorption selectivities for CO over H_2 in mixtures of 5, 50, and 95 % CO at 298 K.

The binary mixture CO/N_2 provides an appropriate system to examine adsorption behavior when both molecules possess some degree of polarity. The electrostatic interaction resulting from the nitrogen quadrupole should result in more competitive adsorption with CO than H_2 according to the pure-component isotherms. As shown in Figure 3.10, Cu-BTC has a greater preference for CO over N_2 for all mixture compositions, with the equimolar mixtures displaying the highest selectivities. This is consistent with pure-component behavior and isosteric heats of adsorption. Selectivities are lowest for the 95% mixture due to the enhanced affinity of Cu-BTC for N_2 as a result of the quadrupole moment.

Figure 3.9 shows selectivities of CO/CH_4 mixtures. The dependence of selectivity on composition is opposite from that of the hydrogen mixtures. In general, Cu-BTC is slightly more selective for methane at total pressures below 0.5 MPa for all three mixture

compositions. This is consistent with the pure-component isotherms, isosteric heats, and Henry's constants. The 5% mixtures show the highest selectivities above 1 MPa, although they are generally quite low at values less than 1.5. This is a result of the electrostatic interaction of CO with the MOF. In fact, we find that when electrostatic interactions are neglected, the MOF actually becomes selective for methane over the entire pressure range. For the 95% mixture, Cu-BTC is slightly more selective for methane. This reflects the affinity that the material has for methane, and is opposite of the hydrogen/CO mixture behavior. With only 5% methane in the mixture, the methane molecules adsorb without experiencing significant displacement from coadsorbed CO.

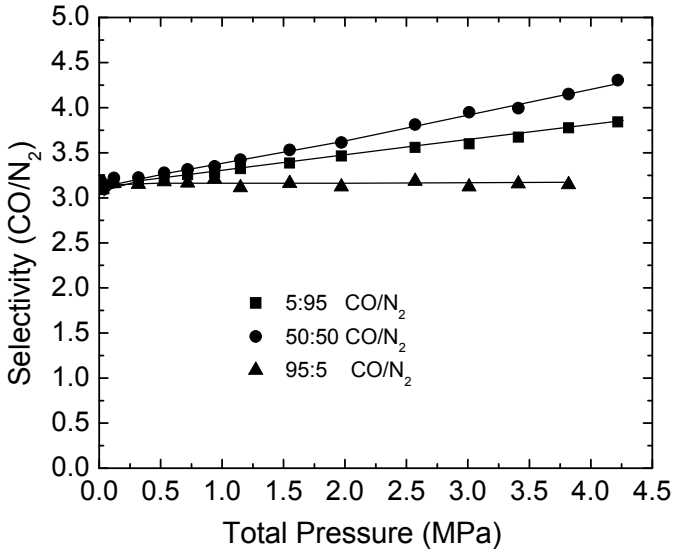

Figure 3.9 Adsorption selectivities for CO over N_2 in mixtures of 5, 50, and 95 % CO at 298 K

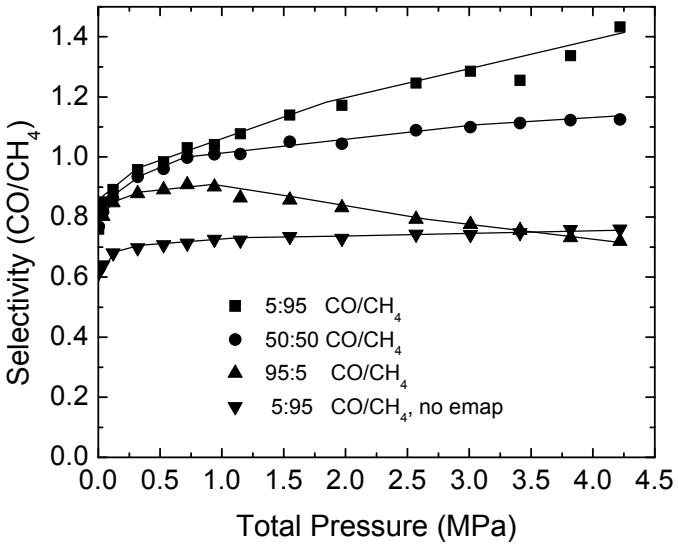

Figure 3.10 Adsorption selectivities for CO over CH_4 in mixtures of 5, 50, and 95 % CO at 298 K.

Figure 3.11 shows simulation snapshots of pure CO and pure CH_4 at 320 kPa and 298 K. From pure-component isotherms, Cu-BTC adsorbs approximately 24 molecules per unit cell at this pressure for both CO and CH_4. The snapshots show that CO molecules tend to adsorb near the copper sites in the framework, while methane molecules are somewhat more dispersed throughout. The same behavior is observed in the mixture simulations. Figure 3.12a shows a simulation snapshot for 5% CO mixture with methane at a total pressure of 3820 kPa. The CO molecules adsorb near the metal sites, and methane molecules are uniformly dispersed throughout the unit cell. This snapshot shows that even at high methane partial pressure, the MOF structure is large enough to accommodate CO molecules at the preferred adsorption sites. A snapshot of the equimolar mixture at 1550 kPa total pressure is shown in Figure 3.12b. In general, the

main pore of Cu-BTC is so large that the molecules easily coadsorb in amounts that are roughly equal to pure-component loadings.

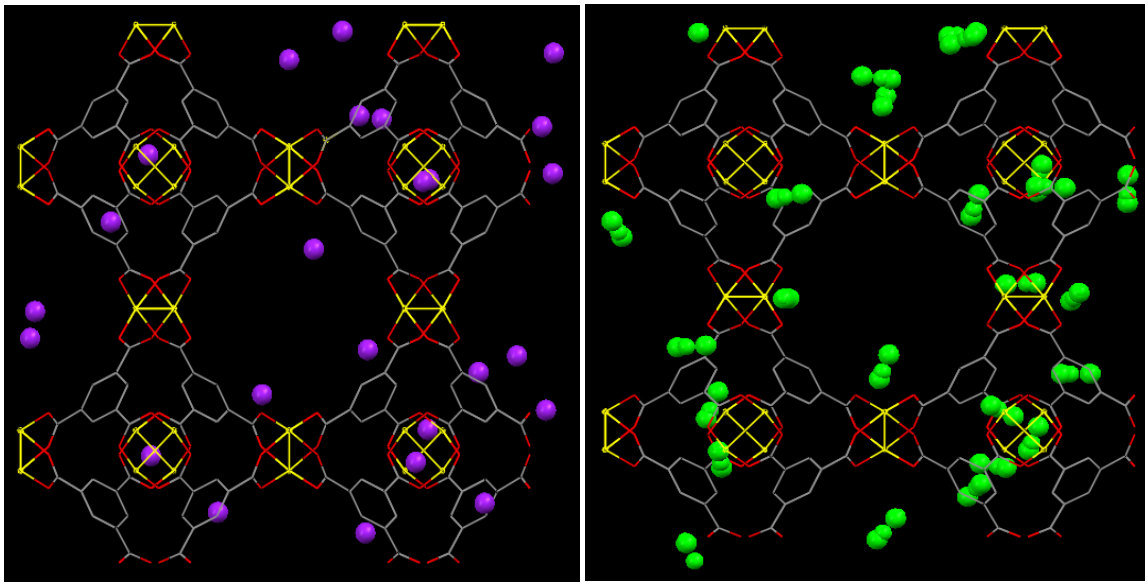

Figure 3.11 Simulation snapshots of pure components at 320 kPa and 298K a) CH_4 (violet) b) CO (green). Loading for each are 24 molecules per unit cell.

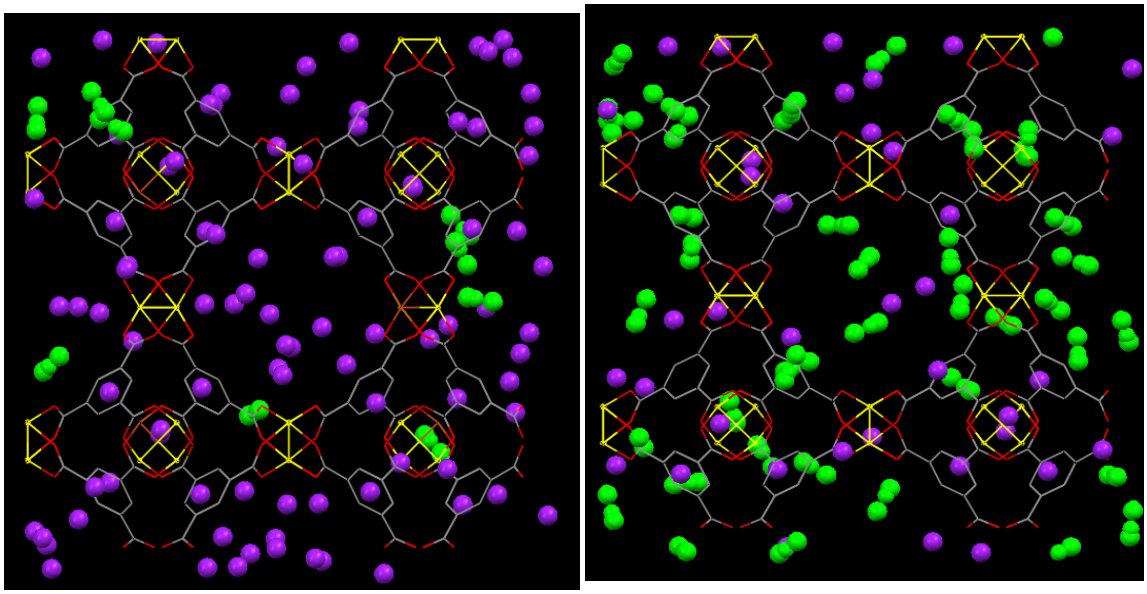

Figure 3.12 Simulation snapshots of binary mixtures of CO and CH_4 a) 5 % CO at 3820 kPa b) 50% CO at 1550 kPa.

3.5 CONCLUSIONS

GCMC simulations carried out here predict adsorption of gases like CO, CH_4, H_2, and N_2 in Cu-BTC and are in good agreement with experiment. Detailed studies of CO adsorption on Cu-BTC reveal that the electrostatic interactions between CO and Cu-BTC framework atoms dominate adsorption while CO-CO interactions are insignificant. In the case of CO/CH_4 separations, LJ interactions of methane are large enough to rival CO electrostatic interactions and the low concentration removal of CO is slightly enhanced by the electrostatic interactions with copper. Snapshots show preferential adsorption of CO near the framework; methane has no preference. This work indicates that MOFs with open metal sites have a great potential however much is unknown regarding catalytic properties. The concept of open metal sites in MOFs needs to be further examined as a strategy for selective adsorption.

3.6 REFERENCES

(1) Barthomeuf, D. *Microporous Mesoporous Mater.* **2003**, *66*, 1.

(2) Yang, R. T. *Adsorbents. Fundamentals and Applications* **2003**, .

(3) Walton, K. S.; Abney, M. B.; Levan, M. D. *Microporous Mesoporous Mater.* **2006**, *91*, 78.

(4) Velu, S.; Ma, X. L.; Song, C. S. *Ind. Eng. Chem. Res.* **2003**, *42*, 5293.

(5) Hernandez-Maldonado, A. J.; Yang, R. T. *AIChE J.* **2004**, *50*, 791.

(6) Petit, C.; Karwacki, C.; Peterson, G.; Bandosz, T. J. *J. Phys. Chem. C* **2007**, *111*, 12705.

(7) Ma, L.; Yang, R. T. *Ind. Eng. Chem. Res.* **2007**, *46*, 2760.

(8) Lopez, D.; Buitrago, R.; Sepulveda-Escribano, A.; Rodriguez-Reinoso, F.; Mondragon, F. *Langmuir* **2007**, *23*, 12131.

(9) Knoblauch, K.; Richter, E.; Juntgen, H. *Fuel* **1981**, *60*, 832.

(10) Rodriguez-Reinoso, F. *Carbon* **1998**, *36*, 159.

(11) James, S. L. *Chem. Soc. Rev.* **2003**, *32*, 276.

(12) Snurr, R. Q.; Hupp, J. T.; Nguyen, S. T. *AIChE J.* **2004**, *50*, 1090.

(13) Kitagawa, S.; Kitaura, R.; Noro, S. *Angew. Chem. Int. Ed.* **2004**, *43*, 2334.

(14) Eddaoudi, M.; Kim, J.; Rosi, N.; Vodak, D.; Wachter, J.; O'keeffe, M.; Yaghi, O. M. *Science* **2002**, *295*, 469.

(15) Fajula, F.; Galarneau, A.; Di Renzo, F. *Microporous Mesoporous Mater.* **2005**, *82*, 227.

(16) Rosseinsky, M. J. *Microporous Mesoporous Mater.* **2004**, *73*, 15.

(17) Rowsell, J. L. C.; Yaghi, O. M. *Microporous Mesoporous Mater.* **2004**, *73*, 3.

(18) Janiak, C. *Dalton Trans.* **2003**, , 2781.

(19) Ockwig, N. W.; Delgado-Friedrichs, O.; O'Keeffe, M.; Yaghi, O. M. *Acc. Chem. Res.* **2005**, *38*, 176.

(20) Ferey, G. *Chem. Soc. Rev.* **2008**, *37*, 191.

(21) Alaerts, L.; Seguin, E.; Poelman, H.; Thibault-Starzyk, F.; Jacobs, P. A.; De Vos, D. E. *Chem. Eur. J.* **2006**, *12*, 7353.

(22) Horcajada, P.; Surble, S.; Hong, D. Y.; Seo, Y. K.; Chang, J. S.; Margiolaki, I.; Ferey, G. *Chem. Commun.* **2007**, , 2820.

(23) Chen, B. L.; Ockwig, N. W. l. M., A.R.; Contreras, D. S.; Yaghi, O. M. *Angew. Chem. , Int. Ed.* **2005**, *44*, 4745.

(24) Rowsell, J. L. C.; Eckert, J.; Yaghi, O. M. *J. Am. Chem. Soc.* **2005**, *127*, 14904.

(25) Xie, Y. C.; Zhang, J. P.; Qiu, J. G.; Tong, X. Z.; Fu, J. P.; Yang, G.; Yan, H. J.; Tang, Y. Q. *Adsorption* **1996**, *3*, 27.

(26) Wang, Q. M.; Shen, D. M.; Bulow, M.; Lau, M. L. l. D., S.G.; Fitch, F. R.; Lemcoff, N. O.; Semanscin, J. *Microporous Mesoporous Mater.* **2002**, *55*, 217.

(27) Chui, S. S. Y.; Lo, S. M. F.; Charmant, J. P. H.; Orpen, A. G.; Williams, I. D. *Science* **1999**, *283*, 1148.

(28) Bordiga, S.; Regli, L.; Bonino, F.; Groppo, E.; Lamberti, C.; Xiao, B.; Wheatley, P. S.; Morris, R. E.; Zecchina, A. *Phys. Chem. Chem. Phys.* **2007**, *9*, 2676.

(29) Panella, B.; Hirscher, M.; Putter, H.; Muller, U. *Adv. Funct. Mater.* **2006**, *16*, 520.

(30) Yang, Q. Y.; Zhong, C. L. *ChemPhysChem* **2006**, *7*, 1417.

(31) Yang, Q. Y.; Zhong, C. L. *J. Phys. Chem. B* **2006**, *110*, 17776.

(32) Rowsell, J. L. C.; Yaghi, O. M. *J. Am. Chem. Soc.* **2006**, *128*, 1304.

(33) Vishnyakov, A.; Ravikovitch, P. I.; Neimark, A. V.; Bulow, M.; Wang, Q. M. *Nano Lett.* **2003**, *3*, 713.

(34) Wang, S.; Yang, Q.; Zhong, C. *J. Phys. Chem. B* **2006**, .

(35) Yang, Q. Y.; Xue, C. Y.; Zhong, C. L.; Chen, J. F. *AIChE J.* **2007**, *53*, 2832.

(36) Jorgensen, W. L.; Maxwell, D. S.; TiradoRives, J. *J. Am. Chem. Soc.* **1996**, *118*, 11225.

(37) Rappe, A. K.; Casewit, C. J.; Colwell, K. S.; Goddard, W. A.; Skiff, W. M. *J. Am. Chem. Soc.* **1992**, *114*, 10024.

(38) Michels, A.; Degraff, W.; Tenseldam, C. A. *Physica* **1960**, *26*, 393.

(39) Martin, M. G.; Siepmann, J. I. *J. Phys. Chem. B* **1998**, *102*, 2569.

(40) Potoff, J. J.; Siepmann, J. I. *AIChE J.* **2001**, *47*, 1676.

(41) Piper, J.; Morrison, J. A.; Peters, C. *Mol. Phys.* **1984**, *53*, 1463.

(42) Frenkel, D.; Smit, B. In *Understanding molecular simulation : from algorithms to applications;* Academic Press: San Diego, 1996; Vol. 18, pp 444.

(43) Gupta, A.; Chempath, S.; Sanborn, M. J.; Clark, L. A.; Snurr, R. Q. *Mol. Simul.* **2003**, *29*, 29.

(44) Elliott, J. R.; Lira, C. T. In *Introductory chemical engineering thermodynamics;* Prentice-Hall international series in the physical and chemical engineering sciences; Prentice Hall PTR: Upper Saddle River, NJ, 1999; , pp 660.

(45) Heyes, D. M. *Phys. Rev. B* **1994**, *49*, 755.

(46) Myers, A. L.; Monson, P. A. *Langmuir* **2002**, *18*, 10261.

(47) Karavias, F.; Myers, A. L. *Langmuir* **1991**, *7*, 3118.

(48) Walton, K. S.; Millward, A. R.; Dubbeldam, D.; Frost, H.; Low, J. J.; Yaghi, O. M.; Snurr, R. Q. *J. Am. Chem. Soc.* **2008**, *130*, 406.

CHAPTER 4

EXPERIMENTAL AND MOLECULAR SIMULATION STUDIES OF CO_2, CO, AND N_2 ADSORPTION IN METAL ORGANIC FRAMEWORKS

4.1 INTRODUCTION

Mixtures containing CO_2, CO, CH_4, N_2, and H_2 pose major challenges in adsorption separations due to the similarities of the molecules and lack of highly selective adsorbents. MOFs have the potential to have a significant impact here, but structure-property relationships are far behind the other classes of porous materials. In pursuing practical applications of MOFs, it is necessary to understand host-guest interactions to aid the selection of materials that have the most favorable adsorption characteristics. In previous work,[1] we studied the adsorption of CO in Cu-BTC with binary mixtures of nitrogen, hydrogen and methane with various mixture compositions using GCMC simulations and found that Cu-BTC was selective for CO to a certain degree due to the enhanced electrostatic effects induced by the open copper atoms with the CO dipole. In this work, we use GCMC simulations to study the adsorption of CO, CO_2 and N_2, both as single-component and as binary mixtures (CO/CO_2, N_2/CO_2), in three well-known MOFs: Cu-BTC,[2] IRMOF-1,[3] IRMOF-3,[3] and a relatively new MOF [$Zn_2bdc_2(dabco)$] (Zn MOF).[4-9]

CO/CO_2 mixtures are produced from a large variety of sources such as metallurgical plants, synthesis gas from steam reforming, CO_2 conversion and partial

oxidation of hydrocarbons, and coal gasification.[10] In general, the off-gases contain CO together with CO_2, N_2, CH_4, and H_2O as impurities.[11] The capture or removal of these gases is important to meet environmental regulations. As an added benefit, purified CO is a valuable raw material for the synthesis of a variety of chemicals such as phosgene for polyurethanes and polycarbonates, acetic acid, and formic acid.[10] N_2 and CO_2 are the main components in flue gas and are emitted by industrial and utility power generation plants.

A systematic study of the adsorption of CO, CO_2, and N_2, both as a single-component and as binary mixtures in these four MOFs will provide insight into the importance of pore size and open metal sites, and the role of the organic linker and electrostatic effects in adsorption separations. We have synthesized and characterized Cu-BTC and Zn MOF using powder X-ray diffraction experiments and nitrogen adsorption at 77K. Adsorption isotherms for CO_2, CO, and N_2 were measured gravimetrically at room temperature and calculated using GCMC simulations. Heats of adsorption for each component in all the three MOFs were also computed. Binary mixture simulations (CO_2/CO, CO_2/N_2) were performed for 5%, 50%, and 95% CO_2 mixtures, and adsorption selectivities were calculated. Particular attention is given to the effect of mixture composition on adsorption.

4.2 MOLECULAR MODELING

Molecular models of the metal-organic frameworks used in this work are constructed from experimental XRD crystallographic data with solvent molecules removed to simulate an activated material. The structures are shown in Figure 4.1.

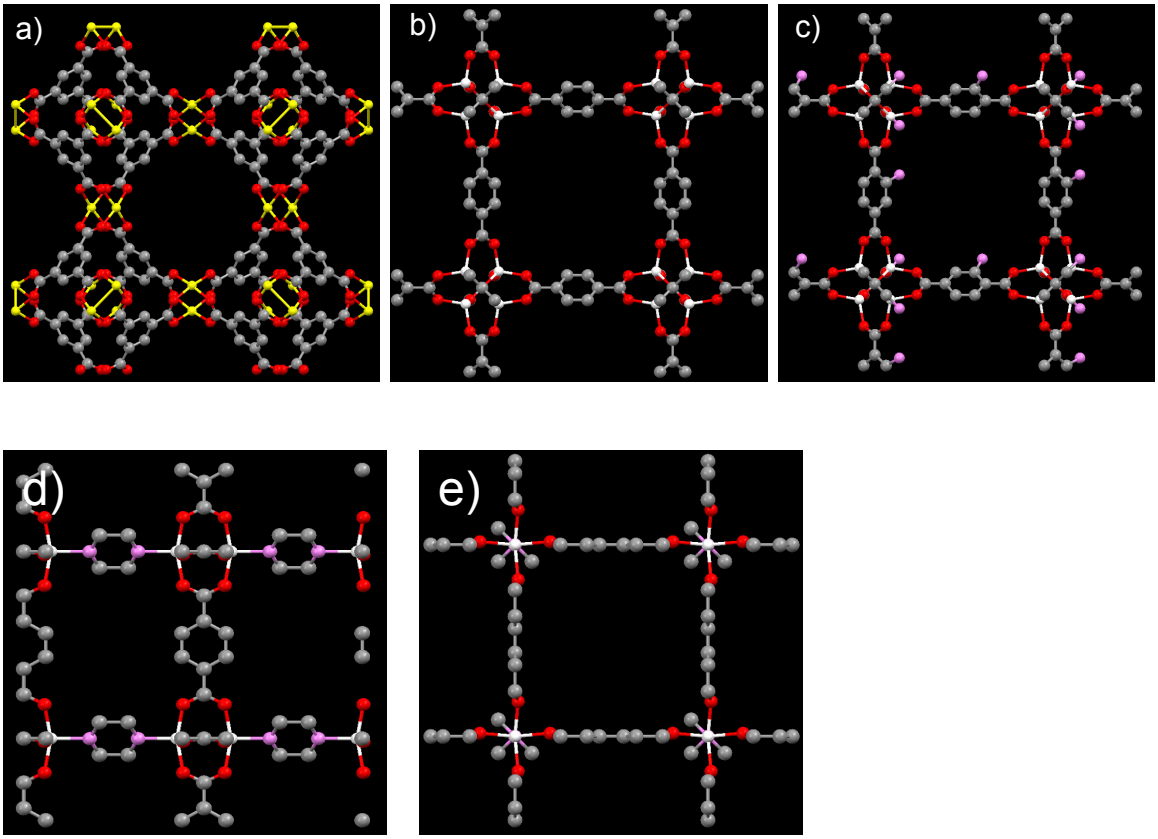

Figure 4.1 Unit-cell of MOFs. a) Cu-BTC, b) IRMOF-1, c) IRMOF-3, d), and e) Zn MOF (view along b-axis and c-axis) (Copper – yellow, oxygen – red, carbon-gray, zinc-white, nitrogen-violet)

The framework is considered rigid for all the MOFs. Various properties of the four MOFs are given in Table 4.1. Cu-BTC has a face-centered cubic crystal structure and is composed of paddle-wheel units assembled from two copper atoms and four benzenetricarboxylate (BTC) groups. Cu-BTC has two types of porous domains:

tetrahedron side pockets (~ 5Å diameter with 3.5Å windows) and large square-shaped channels (9 x 9 Å).[1] IRMOF-1 has a formula of $Zn_4O(BDC)_3$, where BDC is 1,4-benzenedicarboxylate. This MOF has an octahedral $Zn_4O(O_2C\text{-})_6$ unit, built from oxide-centered Zn_4O tetrahedron and six carboxylate linkers. These building units assemble into a three-dimensional cubic structure with benzene struts. IRMOF-1 has interconnected channels with openings of 12 and 15 Å.[3] The structure of IRMOF-3 is isoreticular to IRMOF-1 with an amino functional group ($-NH_2$) attached to the benzene linker. The pore diameters are 10 and 15 Å.[3]

Table 4.1 Physical properties of MOFs.

MOF	BET surface area (m^2/g)	Pore volume ($Å^3$)	Pore size(Å)
Cu-BTC[1]	1200-1500	12796	5/9
Zn MOF[5]	1200-1900	786	4.8x3.2/7.5
IRMOF-3[3]	1500-2160	13650	10/15
IRMOF-1[3]	2100-3362	14026	12/15

Zn MOF is formed from paddle wheel $Zn_2(COO)_4(dabco)_2$ units, built from two zinc atoms, four benzene dicarboxylate groups, and two dabco molecules. The BDC groups are linked to each paddle-wheel building unit to form a 2D net parallel to the XY plane, which is further connected by dabco molecules to form a pillared-layer 3D framework.[6, 12, 13] This MOF crystallizes in the P4/ncc space group when it is synthesized.

However it changes its phase from P4/ncc space group to P4/mmm space group upon activation.[5] The pore sizes are 7.5 x 7.5 Å in the larger channel along the c-axis and 4.8 x 3.2 Å in the smaller channels along both a- and b-axes. All zinc atoms are coordinatively saturated.

The Lennard-Jones parameters for the framework atoms were taken from the DREIDING force field[14] for IRMOF-1, IRMOF-3 and Zn MOF, and parameters for Cu-BTC were taken from previous work.[1, 15] Partial charges for the framework atoms of Cu-BTC, IRMOF-1, and IRMOF-3 are also included.[15, 16] No partial charges were considered for the framework atoms of Zn MOF because there are no open metal sites or functional groups in this MOF. Charges were included for IRMOF-1 to allow direct comparison with IRMOF-3 results. CO_2 was modeled as a triatomic molecule with charges on each atom using a TraPPE potential.[17] Nitrogen was also modeled using a TraPPE potential with charges placed on each atom and at the center of mass.[17] A four-site model developed by Piper et al[18] and employed in previous work[1] was used for carbon monoxide. Lorentz-Berthelot mixing rules were employed to calculate the sorbate/framework and sorbate/sorbate parameters. All force field parameters and charges are given in Tables 4.2 and 4.3.

Table 4.2 Potential Parameters of the Atoms in the Framework of Cu-BTC, IRMOF-1, IRMOF-3, and Zn MOF

		ε/k_B (K)		
Atom	σ (Å)	CO	CO_2	N_2
O	2.96	105.7	73.98	61.29
$C_{carboxyl}$	3.75	52.84	44.91	42.27
$C_{benzene}$	3.55	35.23	35.23	35.23
$C_{benzene}$	3.55	35.23	35.23	35.23
$H_{benzene}$	2.42	15.1	15.1	15.1
Cu	3.11	2.52	2.52	2.52
C	3.216	41.924	41.924	41.924
H	2.902	16.761	16.761	16.761
O	2.996	42.056	42.056	42.056
Zn	3.051	31.882	31.882	31.882

Table 4.3 LJ and Coulombic Potential Parameters

Sorbate	atom	σ (Å)	ε/k_B (K)	q(e)	l (Å)
CO_2	C	2.8	27	0.7	
	O	3.05	79	-0.35	1.16
N_2	N	3.31	36	-0.482	0.55
	NCOM	0	0	0.964	
CO	C	3.385	39.89	0.831	-0.6446
	O	2.885	61.57	0	0.4836
	Site 1			-0.636	-1.0820
	Site 2			-0.195	0.3256

l is the distance from the molecular center of mass and q is the partial charge

GCMC simulations were used to calculate single component and mixture adsorption.[19] The simulation box representing Zn MOF contained 3x3x3 unit cells, while 2x2x2 unit cells were adopted for the other MOFs. At least 20 million trials were used in the single-component and mixture simulations. Among these trials, the first half was used for equilibration, and the last half was used to calculate the ensemble averages. A cut-off radius of 12.8 Å was used for the LJ potential between all atoms for Cu-BTC and IRMOFs while a cut-off radius of 9.6 Å was used for the LJ potential between all atoms for Zn MOF. The simulated (absolute) adsorption data were converted to excess adsorption for comparison with experiments using the equation $N_{ex} = N_{abs} - V_g \rho_g$ where V_g is the pore volume calculated using the method of Myers and Monson[20] and ρ_g is the

density of the ambient gas-phase. Isosteric heats of adsorption, q_{st}, were calculated for each component using the method of Karavias and Myers.[21] Adsorption selectivities were calculated from binary adsorption isotherms as $\alpha_{12} = {x_1 y_2}/{x_2 y_1}$.

4.3 RESULTS AND DISCUSSION

4.3.1 Pure gas adsorption isotherms

Cu-BTC and Zn MOF were synthesized according to published methods. Details are given in the supporting information. Adsorption isotherms for pure CO, CO_2, and N_2 on activated Cu-BTC and Zn MOF samples were measured gravimetrically up to pressures of 1300, 1700, and 2500 kPa, respectively, at 298 K. Data for CO adsorption in IRMOF-1 were taken from literature.[22] Calculated adsorption isotherms for pure CO, CO_2, and N_2 were obtained by GCMC simulations.

Figure 4.2 shows the comparison between experimental and simulated single-component isotherms of CO, CO_2, and N_2 for Cu-BTC and Zn MOF at 298 K (Figure 4.2a) and CO for IRMOF-1 at 237K (Figure 4.2b). Lines are drawn between symbols for visual clarity. The GCMC simulations predict the measured and available experimental results with acceptable accuracy. The slight differences between the measured and experimental results suggest that impurities or defects were present in the samples. The impurities could have blocked some of the pores in Cu-BTC and Zn MOF that might have led to lower adsorption capacities compared to the simulated data. In addition, the empirical force fields used may not be accurate enough to describe such a small discrepancy. Experimental and simulated adsorption data for CO_2 in Zn MOF are also

compared with the data reported in the literature [4](see Appendix A, Figures A6-A.7). The simulation models used in this work for N_2 and CO_2 on IRMOF-1 and IRMOF-3 have been validated in prior work,[23, 24] but experiments and simulations for adsorption of these gases and CO in Zn MOF have not been reported previously.

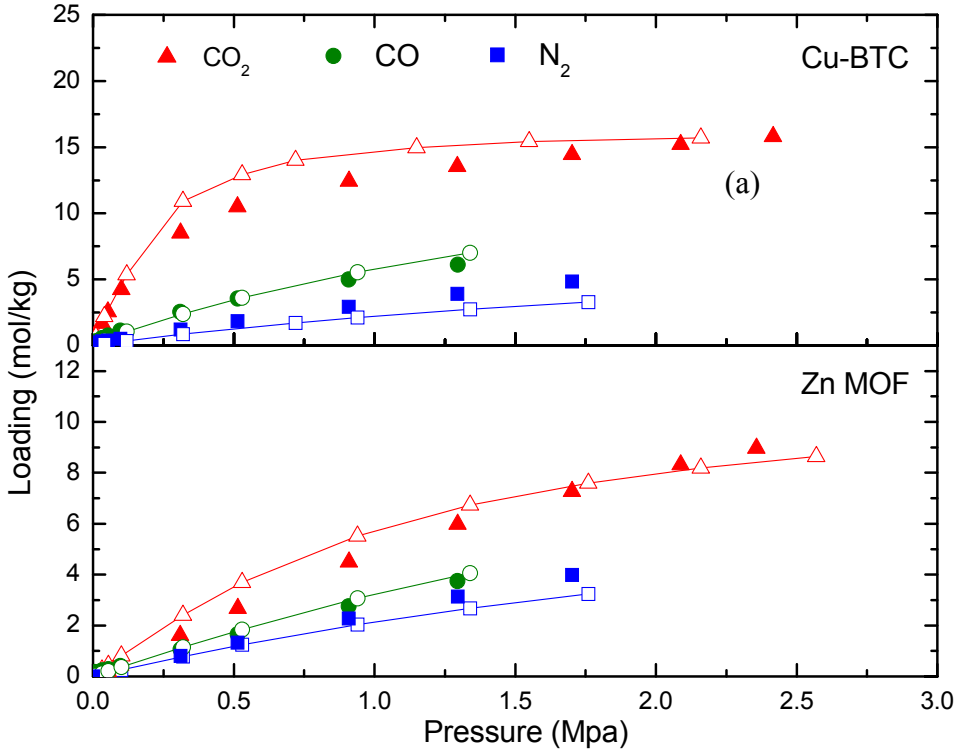

Figure 4.2 Adsorption isotherms calculated from GCMC simulations vs experimental isotherms for (a) Cu-BTC, Zn MOF, and (b) IRMOF-1. Filled symbols are experimental data; open symbols are GCMC simulations.

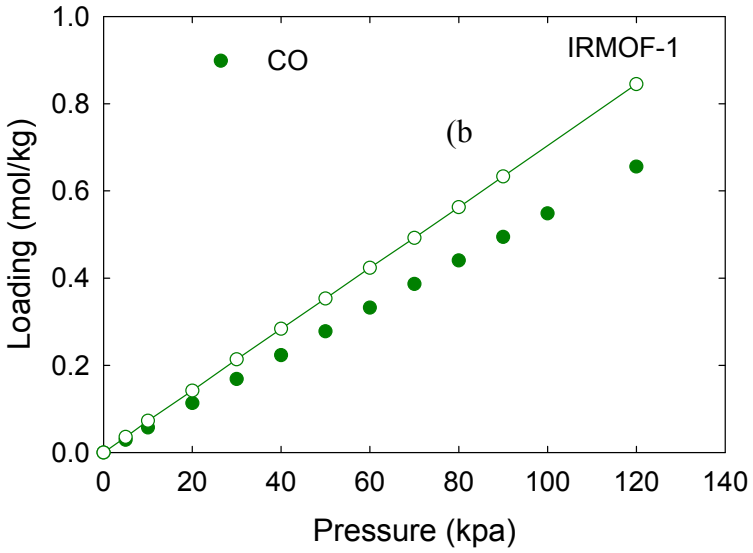

Figure 4.2 Continued

A comparison of the simulated adsorption isotherms of CO_2 for Cu-BTC, IRMOF-1, IRMOF-3, and Zn MOF is shown in Figure 4.3. According to pore size, at lower pressures Zn MOF should exhibit the highest adsorption capacities, followed by Cu-BTC, IRMOF-3, and IRMOF-1. The isotherms for Zn MOF and Cu-BTC do present the same Type I isotherm shape, but the loadings are higher in Cu-BTC, despite the pore size differences. This is because at lower pressures, the electrostatic interactions between CO_2 and the framework atoms dominate the adsorption mechanism (see Appendix A, Figure A.8). The higher adsorption loadings of CO_2 in IRMOF-3 compared to IRMOF-1 at lower pressures can be partly attributed to the amine functionalized groups, but the slightly smaller pore size of IRMOF-3 also plays a role. This confirms that CO_2 prefers interacting with itself in larger-pore MOFs at lower pressures in the absence of open

metal sites. However, presumably there will be a critical pore diameter that dictates this behavior depending on the kinetic diameter of CO_2.

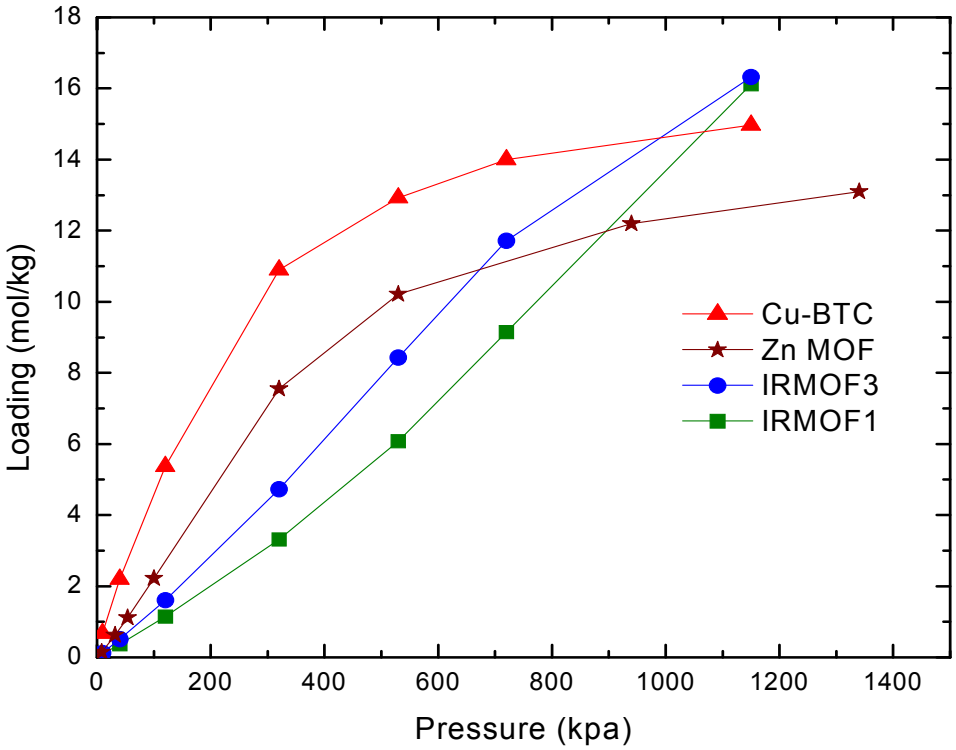

Figure 4.3 Adsorption isotherms calculated from GCMC simulations for CO_2 at 298 K in Cu-BTC, IRMOF-1 and IRMOF-3, and Zn MOF.

Simulated adsorption isotherms for Cu-BTC, IRMOF-1, IRMOF-3, and Zn MOF are shown in Figure 4.4 up to a pressure of 4.5 Mpa. The adsorption capacities for CO_2 follow the order of decreasing pore volume with IRMOF-1 > IRMOF-3 > Cu-BTC > Zn MOF. This trend is not observed for CO and N_2 adsorption at high pressure because the loadings at 4 MPa have not yet reached saturation. Within the pressure range considered, there is still much free volume in the pores of these materials while adsorbing CO and N_2.

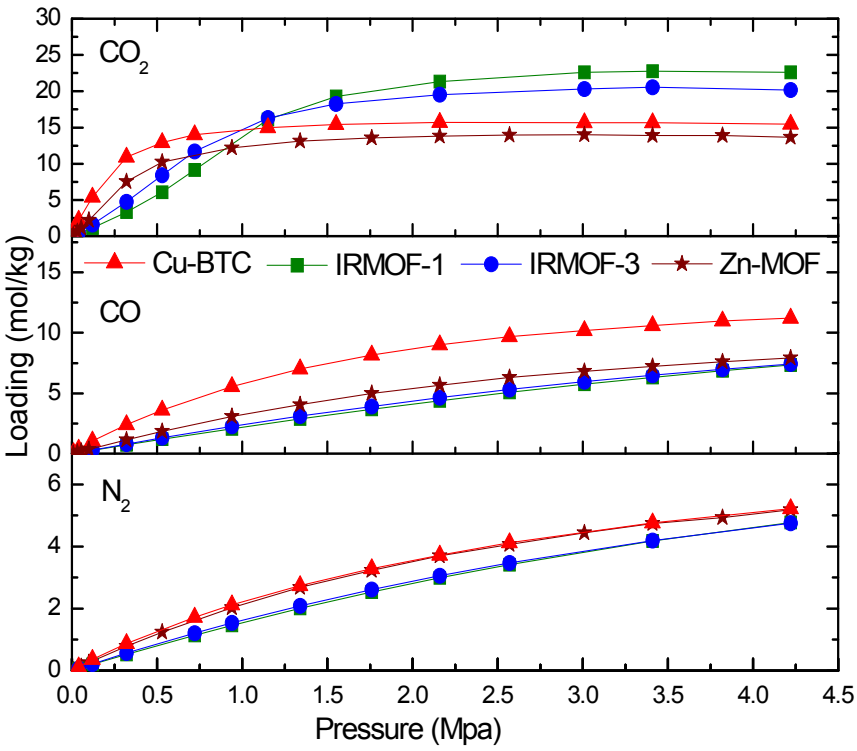

Figure 4.4 Adsorption isotherms for CO, CO_2 and N_2 in Cu-BTC, IRMOF-1 and IRMOF-3, and Zn MOF at 298 K calculated from GCMC simulations.

CO adsorption capacities are higher in Cu-BTC compared to other MOFs due largely to the electrostatic interactions between the open copper sites and CO molecules (see Appendix A, Figure A.9). Zn MOF exhibits slightly higher CO adsorption capacities compared to IRMOF-1 and IRMOF-3 due to smaller pore sizes, but clearly, open metal sites are critical for high CO uptake along the entire pressure range. N_2 adsorption capacities are greatest in Cu-BTC and Zn MOF due to the smaller pore sizes. Almost identical adsorption capacities are seen in Cu-BTC and Zn MOF because the weak electrostatic interactions between the quadrupole moment of nitrogen and the open

copper sites offset the small pore size differences (see Appendix A, Figure A.10). As expected, all MOFs studied here have a higher adsorption preference for CO_2 over the other two sorbates at all pressures.

Figure 4.5 shows simulation snapshots of CO in Cu-BTC, IRMOF-1, IRMOF-3, and Zn MOF at 298 K and 3.2 bar. The snapshots of Cu-BTC show that CO molecules are strongly associated with the framework atoms. As the pressure increases, the side pockets will become saturated, and the CO molecules then begin to occupy the main channels. For IRMOF-1, CO molecules occupy somewhat near the Zn_4O clusters, but the adsorption sites are not very specific. For IRMOF-3, CO molecules are located primarily near the NH_2 group on the organic linker at low pressures. As the pressure increases, the density of CO molecules will spread throughout the pore space. CO molecules occupy sites near the organic linkers in Zn MOF at low pressures due to the π-π interactions between CO molecules and organic linkers, and as the pressure increases, they begin to occupy the vacant spaces within the channels.

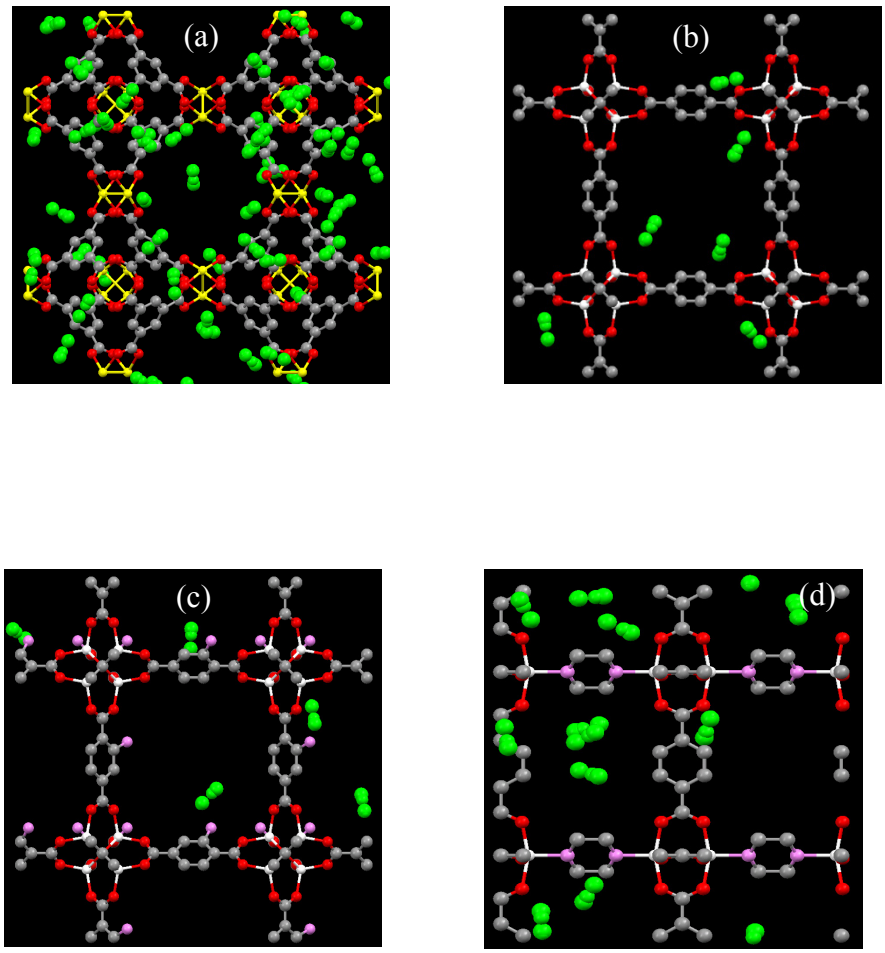

Figure 4.5 Snapshots of the structures of Cu-BTC (a), IRMOF-1 (b), IRMOF-3 (c), and Zn MOF (d) with adsorbed carbon monoxide (green) at 3.2 bar and 298 K.

4.3.2 Isosteric Heats of Adsorption

The isosteric heats of adsorption as a function of loading are shown in Figure 4.6. The isosteric heats of all sorbates in Cu-BTC show a slight decrease with increasing loading, while isosteric heats for the IRMOFs are almost constant. The isosteric heat for Zn MOF shows a slight increase with increase in loading as interaction of guest with itself becomes a larger contributor to the overall isosteric heat. Note that the IRMOFs display

the lowest heats of adsorption for all molecules. The large pore size and absence of open metal sites provide an approximately homogeneous surface, which results in constant heats of adsorption with increasing loading. Low coverage heats are given in Table 4.4. The relatively high heats of adsorption observed at low coverage in Cu-BTC are a result of the open metal sites. This behavior is observed for all three molecules. Aside from Cu-BTC, the low coverage heats decrease with increasing pore size.

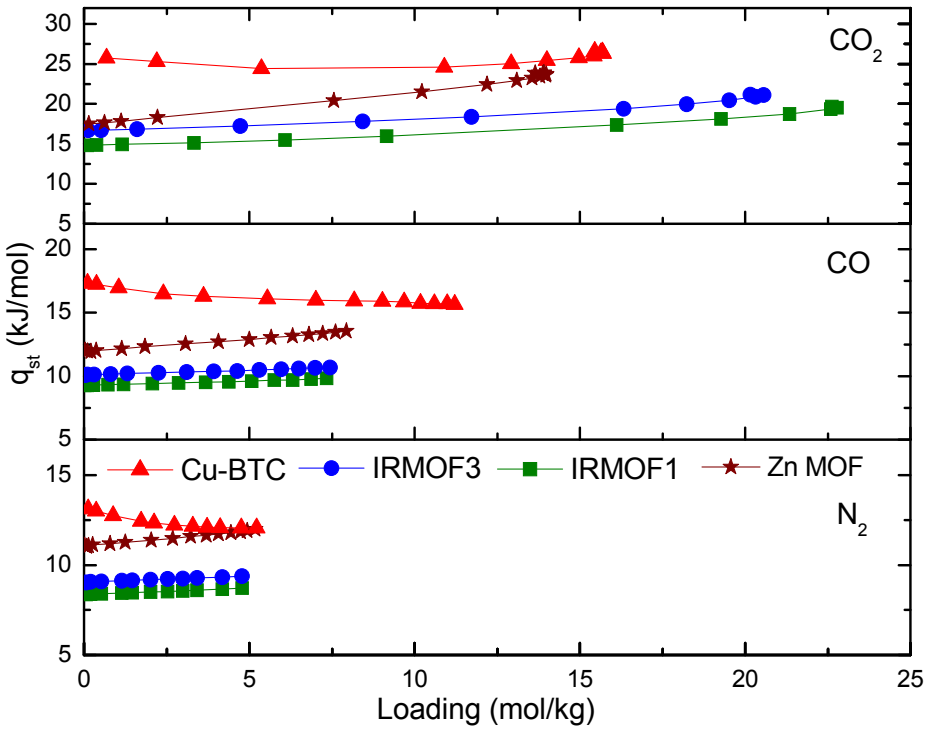

Figure 4.6 Isosteric heats of adsorption as a function of loading for CO, CO_2 and N_2 in Cu-BTC, IRMOF-1, IRMOF-3, and Zn MOF at 298 K.

Table 4.4 Low coverage values of isosteric heats of CO_2, CO and N_2 in all MOFs

MOF	$q_{st} - CO_2$ (kJ/mol)	$q_{st} - CO$ (kJ/mol)	$q_{st} - N_2$ (kJ/mol)
Cu-BTC	25.8	17.3	13.1
Zn MOF	17.4	12	11
IRMOF-3	16.7	10.1	9
IRMOF-1	14.8	9.3	8.4

4.3.3Binary Mixture Adsorption

To explore mixture behavior as a function of composition, adsorption equilibrium data and adsorption selectivities were calculated for binary mixtures of CO_2/N_2 and CO_2/CO at three different CO_2 compositions: 5%, 50%, and 95%. The selectivities for CO_2 over N_2 and CO for each mixture composition are shown in Figures 4.7 and 4.8, respectively. These results show that all three MOFs are good adsorbents for separating CO_2 from both N_2 and CO, with selectivities as high as 40 for Cu-BTC and no lower than 5 for the IRMOFs. As shown in Figure 4.6, the selectivities for CO_2/N_2 follow approximately the same trends at all three compositions. Cu-BTC exhibits the highest selectivity for CO_2 followed by Zn MOF, IRMOF-3, and IRMOF-1, which follows the order of decreasing isosteric heat of adsorption.

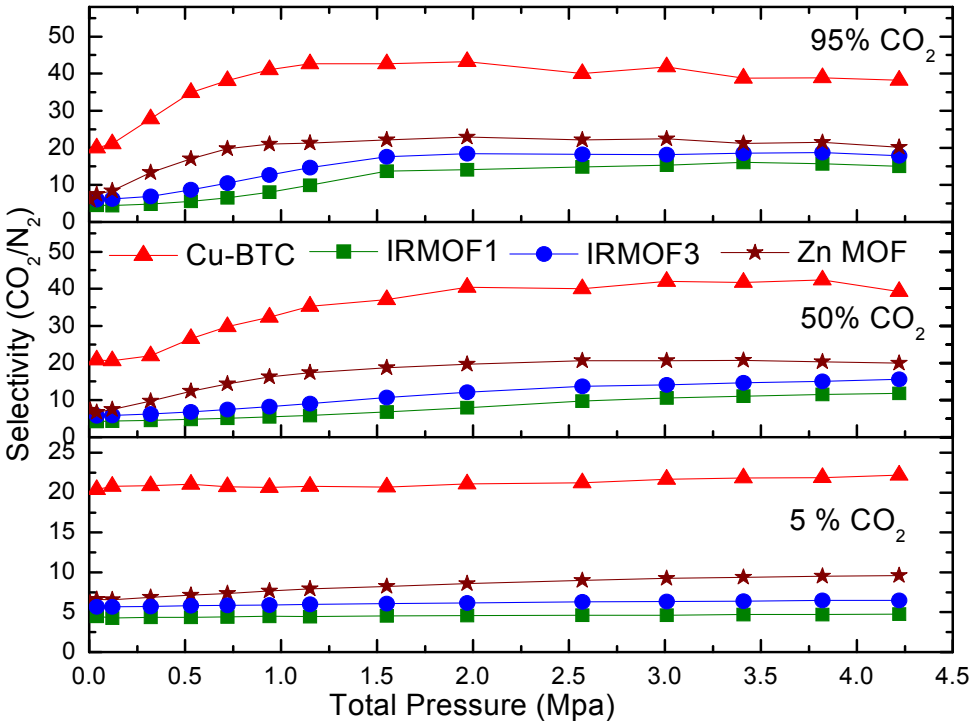

Figure 4.7 Adsorption selectivities for CO_2 over N_2 in mixtures of 5%, 50%, and 95% CO_2 in Cu-BTC, IRMOF-1, IRMOF-3, and Zn MOF at 298 K

CO_2/CO mixtures give strikingly different results. As shown in Figure 4.8, the selectivities for CO_2 in Zn MOF match Cu-BTC for the two higher mixture compositions along the entire pressure range. For total pressures up to 1 MPa, the order of selectivities is Zn MOF/Cu-BTC > IRMOF-3 > IRMOF-1, which follows the order of increasing pore size. As the pressure increases, IRMOF-3 exhibits surprisingly high selectivities compared to the other MOFs, especially for the 95% mixture. However, the same behavior is not observed for IRMOF-1. This illustrates the importance of the amino functional group in addition to pore volume. For the 5% mixture, Cu-BTC exhibits the

greatest selectivity for CO_2 over the entire pressure range. These results indicate that there is significant competition between CO and CO_2 for the open copper sites of Cu-BTC, giving much lower selectivities compared to CO_2/N_2 mixtures. (see Appendix A, Figures A11-A21).

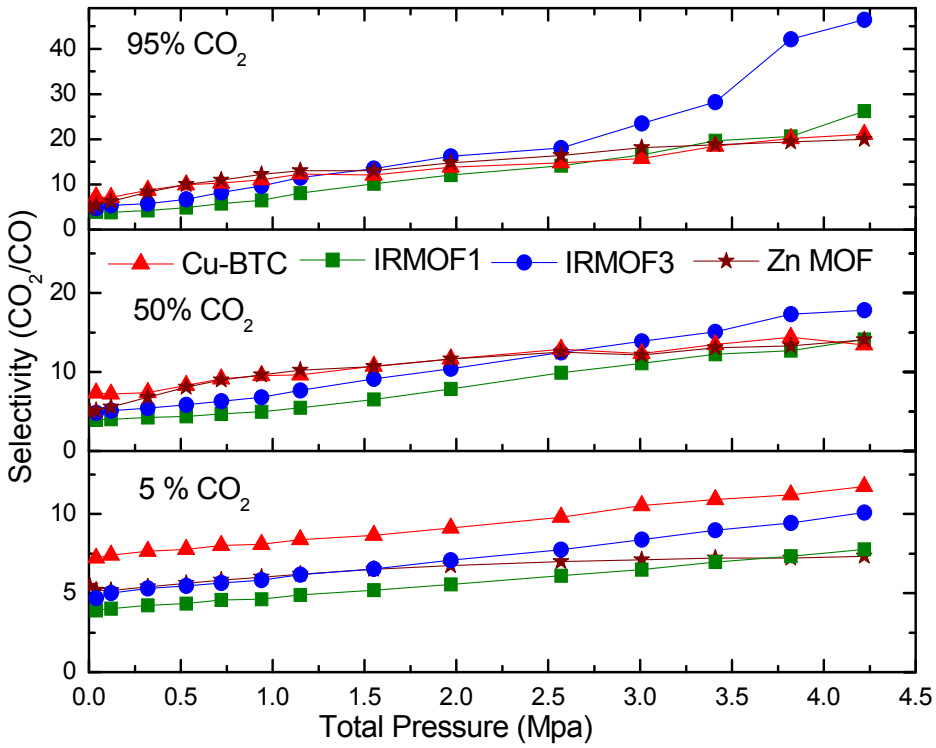

Figure 4.8 Adsorption selectivities for CO_2 over CO in mixtures of 5%, 50%, and 95% CO_2 in Cu-BTC, IRMOF-1 and IRMOF-3 at 298 K

A few studies have reported the effect of gas mixture composition on selectivity in MOFs at low pressures and found that selectivity is weakly dependent on gas composition.[16, 25] In our study, we observe that selectivities for CO_2 over CO and N_2 are independent of the bulk phase CO_2 composition at very low pressures. However, with

increasing pressure, CO_2 selectivity actually increases with increasing bulk-phase CO_2 composition as shown in Figures 4.8 and 4.9. This occurs because an increase in the number of CO_2 molecules in the mixture leads to an additional contribution to adsorption from the electrostatic interactions between CO_2 molecules. 5% CO_2 mixtures are dominated by large numbers of CO or N_2 molecules and the CO and N_2 mixture adsorption isotherms exhibit loadings close to the pure adsorption isotherms, although there is significant competition for space from the small portion of CO_2 molecules (see Appendix, Figures A.11, A.15). In the case of 50% and 95% mixtures, the CO_2 mixture adsorption loadings are close to their pure CO_2 loadings (see Appendix, Figures A.12-A.13, A.16-A.17), and the materials are filled mostly with CO_2 molecules.

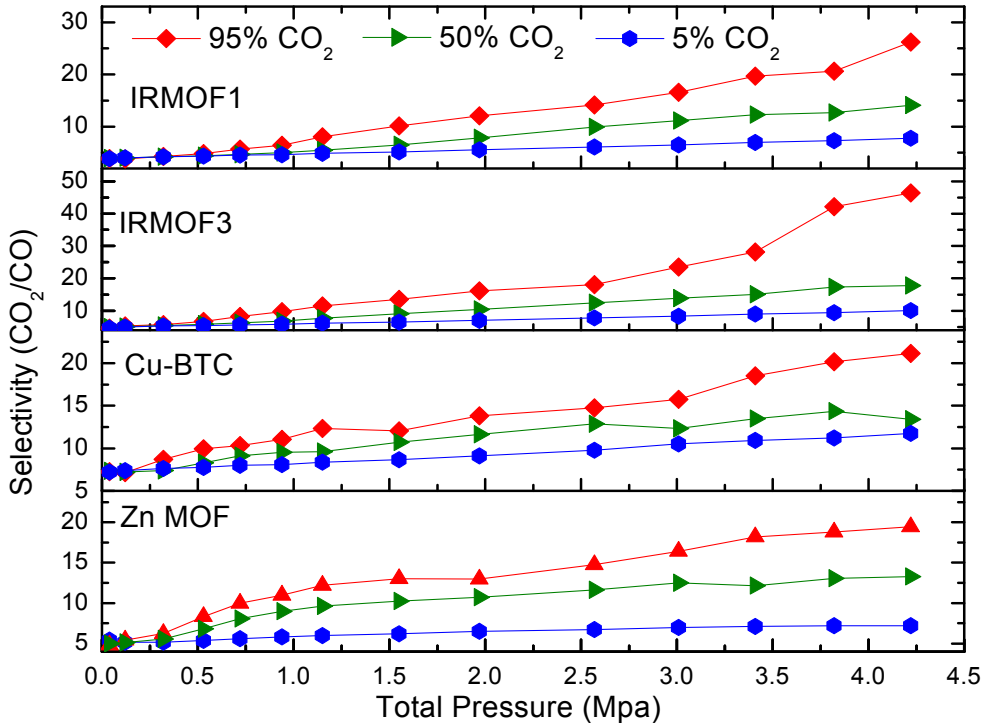

Figure 4.9 Adsorption selectivities for CO_2 over CO as a function of composition in Cu-BTC, IRMOF-1, IRMOF-3, and Zn MOF at 298 K

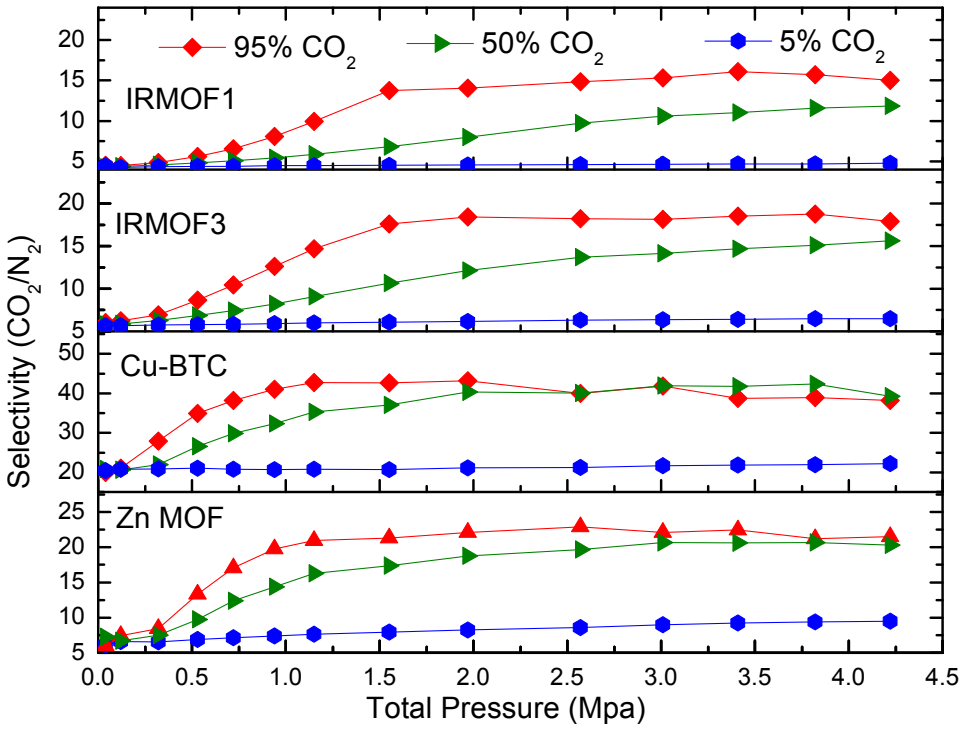

Figure 4.10 Adsorption selectivities for CO_2 over N_2 as a function of composition in Cu-BTC, IRMOF-1, IRMOF-3, and Zn MOF at 298 K

4.4. CONCLUSIONS

GCMC simulations were found to predict adsorption equilibria of CO_2, CO, and N_2 in Cu-BTC, IRMOF-1, and Zn MOF in good agreement with the measured experimental data. The simulation studies of CO_2 adsorption suggest that MOFs with smaller pores can have a similar impact on CO_2 adsorption as larger-pore MOFs with open metal sites. CO isotherms suggest that relative pore size has a much smaller impact on adsorption compared to MOFs possessing open metal sites. The binary mixture (CO_2/CO, CO_2/N_2) results show that these MOFs are actually more selective in the mixtures than the pure isotherms would suggest. Cu-BTC is more selective for CO_2 over N_2 at all concentrations of CO_2, while IRMOF-3 is surprisingly selective for CO_2 over CO at higher concentrations of CO_2. The mixture results also show that the effect of gas mixture composition on selectivity is more pronounced at higher pressures. This work shows that open metal sites and small pore diameters are important for high CO_2 selectivity at low pressure (< 5 bar). At high pressure, MOFs that maintain high pore volume while incorporating functional groups into the structure provide the greatest CO_2 selectivities.

4.5 REFERENCES

(1) Karra, J. R.; Walton, K. S. *Langmuir* **2008**, *24*, 8620-862.

(2) Wang, Q. M.; Shen, D. M.; Bulow, M.; Lau, M. L.; Deng, S. G.; Fitch, F. R.; Lemcoff, N. O.; Semanscin, J. *Microporous Mesoporous Mater.* **2002**, *55*, 217.

(3) Eddaoudi, M.; Kim, J.; Rosi, N.; Vodak, D.; Wachter, J.; O'Keeffe, M.; Yaghi, O. M. *Science* **2002**, *295*, 469.

(4) Chen, Y. F.; Lee, J. Y.; Babarao, R.; Li, J.; Jiang, J. W. *J. Phys. Chem. C* **2010**, *114*, 6602-6609.

(5) Dybtsev, D. N.; Chun, H.; Kim, K. *Angew. Chem. , Int. Ed.* **2004**, *43*, 5033.

(6) Lee, J. Y.; Olson, D. H.; Pan, L.; Emge, T. J.; Li, J. *Adv. Funct. Mater.* **2007**, *17*, 1255-1262.

(7) Liu, B.; Smit, B. *Langmuir* **2009**, *25*, 5918-5926.

(8) Uemura, K.; Yamasaki, Y.; Komagawa, Y.; Tanaka, K.; Kita, H. *Angew. Chem. Int. Ed.* **2007**, *46*, 6662.

(9) Liu, Y.; Liu, D.; Yang, Q.; Zhong, C.; Mi, J. *Ind. Eng. Chem. Res.* **2010**, *49*, 2902-2906.

(10) Xie, Y. C.; Zhang, J. P.; Qiu, J. G.; Tong, X. Z.; Fu, J. P.; Yang, G.; Yan, H. J.; Tang, Y. Q. *Adsorption* **1996**, *3*, 27.

(11) Xie, Y. C.; Zhang, J. P.; Qiu, J. G.; Tong, X. Z.; Fu, J. P.; Yang, G.; Yan, H. J.; Tang, Y. Q. *Adsorption* **1996**, *3*, 27.

(12) Krawiec, P.; Kramer, M.; Sabo, M.; Kunschke, R.; Frode, H.; Kaskel, S. *Advanced engineering materials* **2006**, *8*, 293.

(13) Senkovska, I.; Kaskel, S. *Microporous Mesoporous Mater.* **2008**, *112*, 108-115.

(14) Senkovska, I.; Kaskel, S. *Microporous Mesoporous Mater.* **2008**, *112*, 108.

(15) Yang, Q. Y.; Zhong, C. L. *ChemPhysChem* **2006**, *7*, 1417.

(16) Frost, H. Evaluation of metal-organic frameworks as adsorbent materials with applications in hydrogen storage and carbon dioxide separations, PhD.Dissertation, Northwestern University, IL, **2007**.

(17) Potoff, J. J.; Siepmann, J. I. *AIChE J.* **2001**, *47*, 1676.

(18) Piper, J.; Morrison, J. A.; Peters, C. *Mol. Phys.* **1984**, *53*, 1463.

(19) Gupta, A.; Chempath, S.; Sanborn, M. J.; Clark, L. A.; Snurr, R. Q. *Mol. Simul.* **2003**, *29*, 29.

(20) Myers, A. L.; Monson, P. A. *Langmuir* **2002**, *18*, 10261.

(21) Karavias, F.; Myers, A. L. *Langmuir* **1991**, *7*, 3118.

(22) Saha, D.; Deng, S. *J. Chem. Eng. Data.* **2009**, *54*, 2245-2250.

(23) Walton, K. S.; Snurr, R. Q. *J. Am. Chem. Soc.* **2007**, *129*, 8552-8556.

(24) Walton, K. S.; Millward, A. R.; Dubbeldam, D.; Frost, H.; Low, J. J.; Yaghi, O. M.; Snurr, R. Q. *J. Am. Chem. Soc.* **2008**, *130*, 406.

(25) Liu, B.; Yang, Q.; Xue, C.; Zhong, C.; Chen, B.; Smit, B. *J. Phys. Chem. C.* **2008**, *112*, 9854-9860.

CHAPTER 5

CO_2, CH_4, N_2, AND H_2O ADSORPTION STUDIES ON AN INTERWOVEN BTB BASED MOF (MOF-14)

5.1 INTRODUCTION

Metal-organic frameworks (MOFs) have attracted attention because of their potential applications in gas storage, separations[1] and catalysis[2]. The modular approach of MOFs allows their pore size and shape to be systematically tuned by the judicious choice of metal-containing secondary building units and/or bridging linkers and by making use of framework interpenetration or interweaving.[3] Their selective adsorption and high thermal stability make these microporous materials potentially useful for CO_2 adsorption separations from flue gas and natural gas mixtures. The separation of CO_2 from flue gas mixtures is an important process for reducing carbon emissions from coal or natural gas fired power plants, and the high CO_2 concentration in natural gas mixtures is undesirable as it reduces the heating value of natural gas and could also lead to corrosion in steel pipes.

The design of MOFs containing unsaturated metal centers has been used to develop materials with improved adsorption capacity for gas-storage and adsorption separations. Indeed, the presence of open metal sites is of key importance for adsorption since it strongly favors the direct interaction between the metal and substrate. For instance, well-known MOFs such as Mg-DOBDC and HKUST-1 have shown good adsorption performance for CO_2 owing to the presence of open metal sites.[4,5] Chen et al previously reported an interwoven MOF ({$[Cu_3(BTB)_2(H_2O)_3].(DMF)_9(H_2O)_2$ or MOF-14) on a

periodic minimal surface with extra-large pores,[6] but no adsorption data have been reported. In this study, we report results for the adsorption of pure gases (CO_2, CH_4, N_2, H_2O) and CO_2/CH_4, CO_2/N_2 mixtures on this interwoven, open copper site containing MOF (hereafter compound 1). This compound has water ligands that are axially bound to copper and upon activation can generate polar Cu(II) sites. So, we hypothesized that this material might facilitate selective adsorption of quadrupolar CO_2 over nonpolar CH_4 or weakly quadrupolar N_2.

As shown in Figure 5.1, this MOF consists of a dicopper paddlewheel secondary building unit and the BTB ligand. Each BTB is linked to three paddle wheel building units and each paddle-wheel building unit is connected to four BTB units. Such connections give rise to (3,4)-connected net with the Pt_3O_4 topology (Figure 5.2a). The overall structure is a pair of identical nets which are interwoven with each other (Figure 5.2b).

In compound 1, the rings of one net are penetrated by links of the other so that they are truly catenated. Each net is involved in numerous π-π and C-H..π interactions with those of the adjacent interpenetrated net. The pore limiting diameter and largest cavity diameter was estimated to be 5.187 and 16.363 Å, from the geometric approach algorithm.[7] The removal of the bound water molecules gives rise to open metal sites, which are important in increasing binding strengths between frameworks and guest molecules.

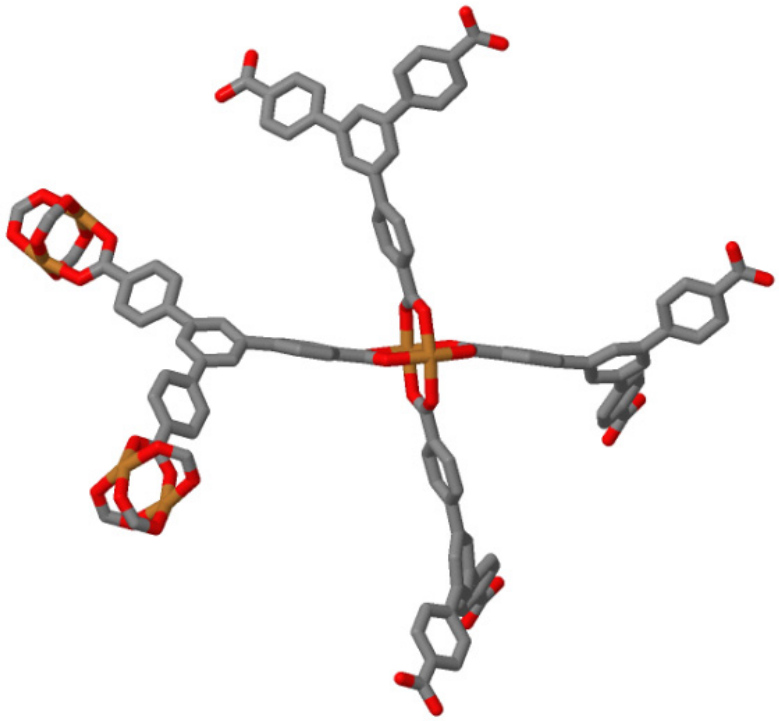

Figure 5.1 Coordination environment of compound 1

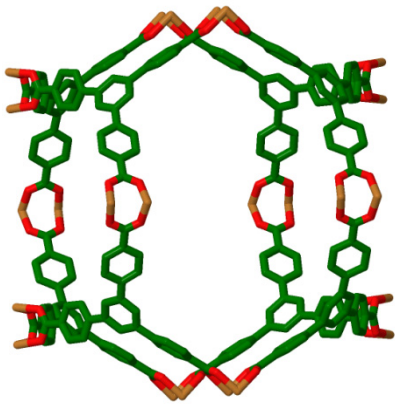

(a)

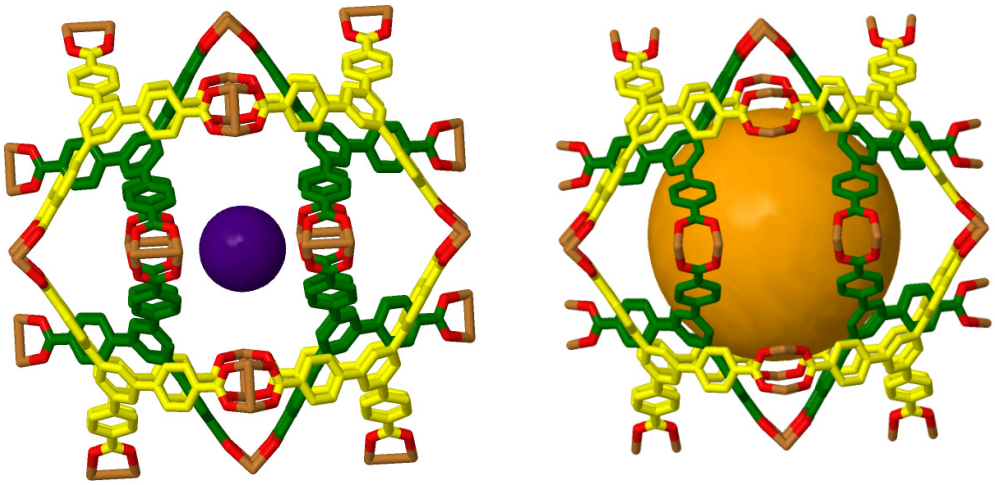

(b) (c)

Figure 5.2 Perspective view of the compound 1 showing a) single Pt_3O_4 net b) pair of interwoven Pt_3O_4 nets with cavity size of 5.187 Å c) cavity size of 16.363 Å. Color scheme: copper, brown; oxygen, red; yellow and green colors represent different frameworks.

5.2 MATERIALS SYNTHESIS AND CHARACTERIZATION

All commercially available chemicals and solvents are of reagent grade and were used as received without further purification. Elemental analysis was performed by Desert Analytics, Arizona. Note that the synthesis recipe followed here is different from that reported in the literature.[6] Despite several attempts, synthesis of MOF-14 was not successful with the reported recipe.[6] Therefore, we modified the reported synthesis procedure slightly. As a typical preparation procedure, a mixture of $Cu(NO_3)_2.3H_20$ (30.2 mg, 0.125 mmol) and BTB (54.8 mg, 0.125 mmol), pyrazine (10 mg, 0.125 mmol) was dissolved in DMF (5 mL) at room temperature. Two drops of 1N NaOH was added to the mixture and the mixture was transferred to stainless steel reactors and left undisturbed at 110 ˚C for 4 days to give green cubic crystals with molecular formula $\{[Cu_3(BTB)_2(H_2O)_3].(DMF)_9(H_2O)_2\}$. The molecular formula was confirmed from the reported crystal structure,[6] elemental analysis, and thermogravimetric analyses. Elemental analysis (%) Calcd: C 53.59 H 6.04 N 6.94 Found: C 52.69 H 5.84 N 6.64. The compound was stable in air and insoluble in water and common organic solvents. Single crystals suitable for x-ray crystallographic analysis were selected following examination under a microscope. Single crystal study performed on crystals indicated that the collected cell parameters were identical to that of MOF-14 structure reported by Chen et al.[6] The purity of the bulk phase was confirmed by comparing the experimental powder X-ray diffraction patterns with that of the simulated patterns of the reported MOF. The synthesized sample of compound 1 was solvent exchanged with chloroform for 3 days to remove the nonvolatile solvates (DMF and H_2O). After the removal of chloroform by decanting, the sample was dried under vacuum at 150 ˚C for overnight to give activated compound 1.

Thermogravimetric analyses (TGA) were carried out in the temperature range of 25-700 ˚C on a NETSZCH TG/Mass spectrometry analyzer under helium with a heating rate of 5 ˚C/min. Powder X-ray diffraction patterns (PXRD) were recorded on a X'Pert X-ray PANalytical diffractometer with an X'accelerator module using Cu Kα (λ = 1.5418 Å) radiation at room temperature, with a step size of 0.02˚ in 2θ.

Nitrogen adsorption isotherms were measured at 77 K with an Autosorb 1-MP from Quantachrome Instruments. Samples of a known weight (35-50 mg) were loaded into a sample tube and evacuated at 150 °C under 10^{-5} Torr dynamic vacuum overnight. After evacuation, the sample and tube were precisely weighed again to obtain the evacuated sample weight. The Brunauer-Emmett-Teller (BET) surface area was determined in the range $0.007 < P/P_o < 0.05$.

Carbon dioxide (CO_2), Nitrogen (N_2), and methane (CH_4) sorption experiments were carried out using a Intelligent Gravimetric Analyzer (IGA-1 series, Hiden Analytical Ltd). The same activation procedure mentioned earlier was followed when doing the gas sorption measurement. Each adsorption/desorption step was allowed to approach equilibrium over a period of 20-40 minutes. The adsorption measurement of water was carried out at 298 K using an Intelligent gravimetric Analyzer (IGA-3 series, Hiden Analytical Ltd). Each adsorption/desorption step was allowed to approach equilibrium over a period of 2- 24 hrs. Nitrogen adsorption/desorption isotherms were run at 77 K and PXRD patterns were measured after exposure to water vapor and thermal activation in order to know whether the structure of compound 1 is retained.

5.3 RESULTS AND DISCUSSION

5.3.1 Characterization

X-ray powder diffraction (PXRD) studies were performed for the as-synthesized, chloroform-exchanged, and activated samples and the results are shown in Figure 5.3. The PXRD pattern of 1 is almost coincident with the simulated pattern, indicating that the bulk sample is the same as the single crystal. Furthermore, the PXRD pattern of guest-free phase and chloroform-exchanged phase are the same as that of the as- synthesized compound 1.

TGA data indicate that compound 1 releases its guest molecules over the temperature range 25 – 250 ˚C to form the guest-free phase, which is thermally stable to 300 ˚C (Figure 5.4).

Nitrogen sorption experiments of the fully activated compound 1 sample reveals typical Type –I sorption behavior confirming the permanent porosity of compound 1 (Figure 5.5). Calculated from the nitrogen adsorption data, the estimated BET surface area of compound 1 is 1398 m^2/g, and the estimated pore volume is 0.573 cm^3/g.

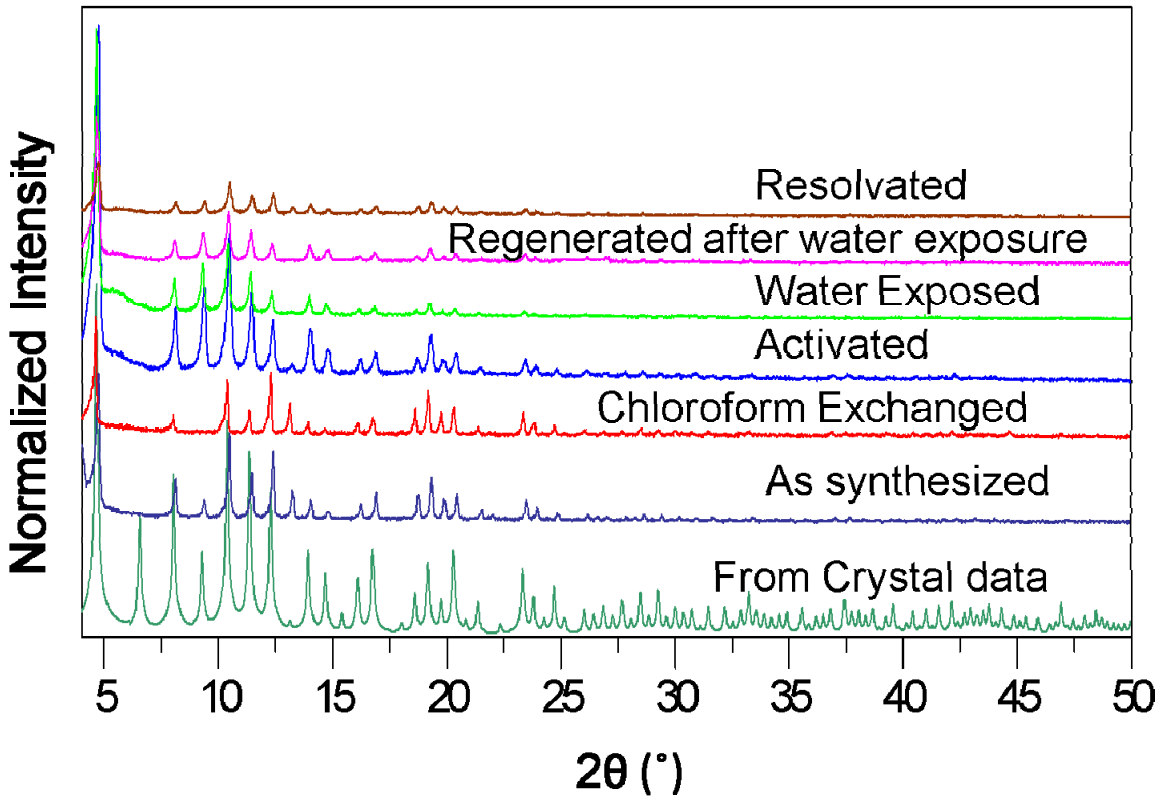

Figure 5.3 Powder X-ray diffraction patterns of as synthesized, chloroform exchanged, activated, water exposed, regenerated after water exposure and resolvated samples of compound 1

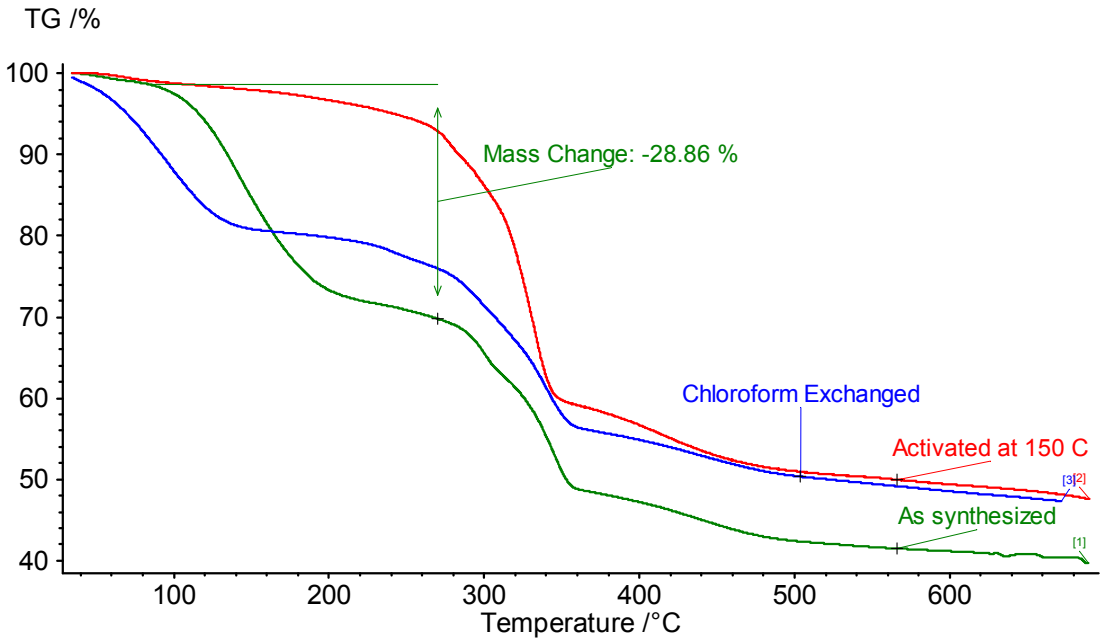

Figure 5.4 TGA trace of as synthesized, chloroform exchanged, activated samples of compound 1

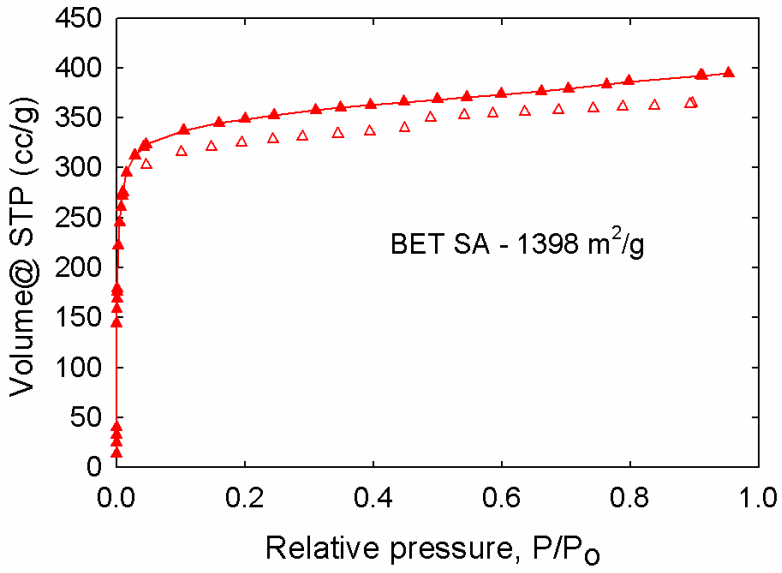

Figure 5.5 N_2 isotherms of activated compound 1 at 77 K (closed symbols, solid line – adsorption, open symbols – desorption)

5.3.2 Pure gas adsorption isotherms

Pure isotherms of CO_2, N_2 and CH_4 for compound 1 at 298 K and pressures up to 20 bar were measured. A comparison was also made for CH_4 with the simulated data reported by Gallo et al.[8] Their simulation results slightly overestimate our experimental results. The overestimation of simulated results can be attributed to the crystal defects or impurities present in the experimental samples and the inaccuracy of the force field used in their simulations. Figure 5.6 shows that the adsorption trend for compound 1 follows CO_2>CH_4>N_2. CO_2 has a significant quadrupole moment and nitrogen has a weaker quadrupole moment, whereas CH_4 is nonpolar. The electrostatic interactions between the exposed copper sites and the quadrupole moment of carbon dioxide lead to higher adsorption uptake for CO_2 compared to CH_4 and N_2. The adsorption temperature of 298 K considered here is subcritical for CO_2 (T_C = 304.4 K). Thus, CO_2 is more condensable than CH_4 and N_2 at 298 K. Compound 1 adsorbs CO_2 up to ~ 2.5 mmol/g at 1 bar and 298 K. The adsorption capacities are higher than those of some well-known MOFs, IRMOF-1 (~ 1.1 mmol/g),[9] IRMOF-3 (~ 1.3 mmol/g),[9] Cu-BTB (2 mmol/g)[10] and DMOF (~ 2.2 mmol/g)[11] under the same conditions. At higher pressures, the desolvated compound 1 adsorbs CO_2 up to ~ 11 mol/kg at 20 bar due to its large pore volume and surface area.

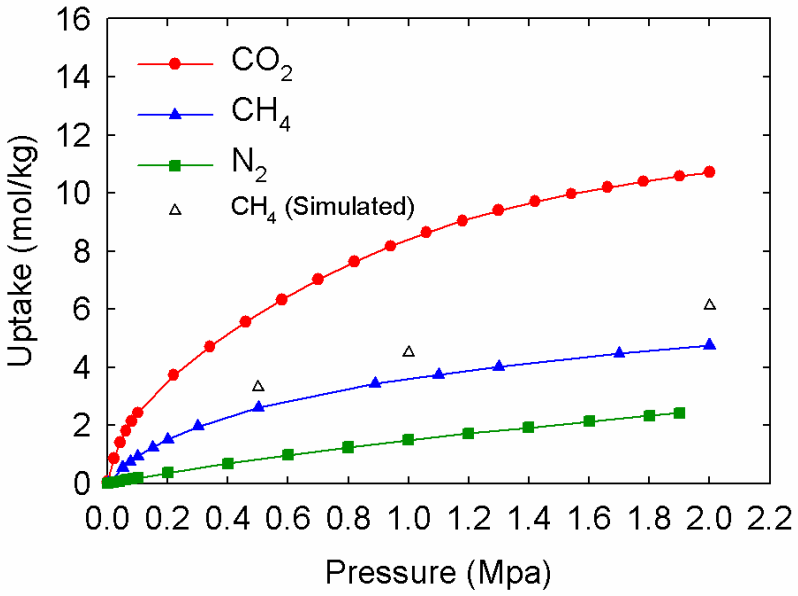

Figure 5.6 CO_2, CH_4, and N_2 sorption isotherms of desolvated compound 1 at 298 K. (Open symbols – Simulated data of CH_4 from Gallo et al. [8])

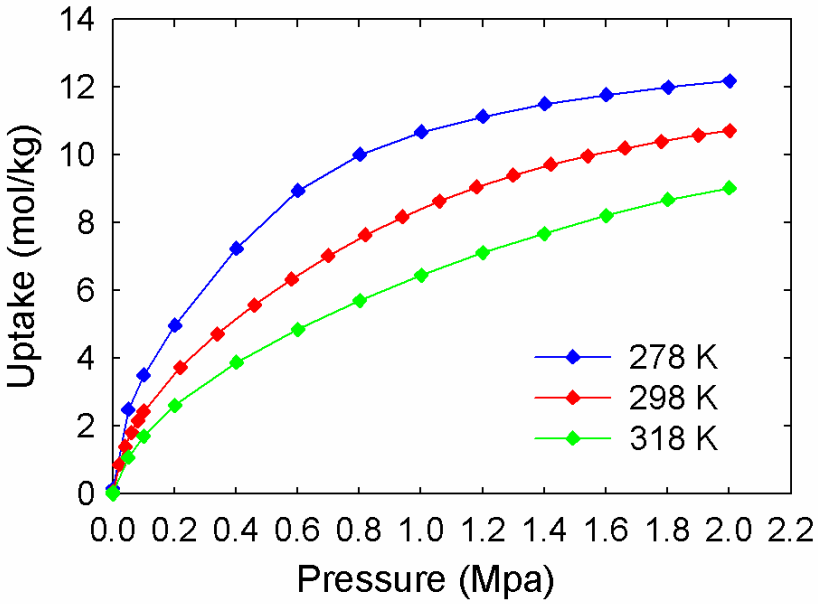

Figure 5.7 CO_2 sorption isotherms of desolvated compound 1at 278 K, 298K and 318 K.

5.3.3. Analysis of Heat of adsorption

The strength of interaction between the framework and CO_2 can be reflected by isosteric heats of adsorption Q_{st}. The isosteric heats of adsorption of CO_2 were calculated using the Clasius-Clapeyron equation $Q_{st} = -R\frac{d(lnP)}{dT}$ using isotherms taken at 278, 298, and 318 K (Figure 5.7). As shown in Figure 5.8, the Q_{st} at low loading is as high as 26 kJ/mol, revealing strong interactions between CO_2 and the framework. The Q_{st} decreases with increasing CO_2 loading. This indicates that at low concentrations of CO_2, the electrostatic interactions between quadrupole moment of CO_2 and exposed copper sites are dominant as seen in other open metal site MOF systems.[4,11-13] The high Q_{st} at low concentration CO_2 loading supports the predictions that incorporating open metal sites into the framework can lead to higher affinity of CO_2. The obtained value is similar to Cu-BTC.[11]

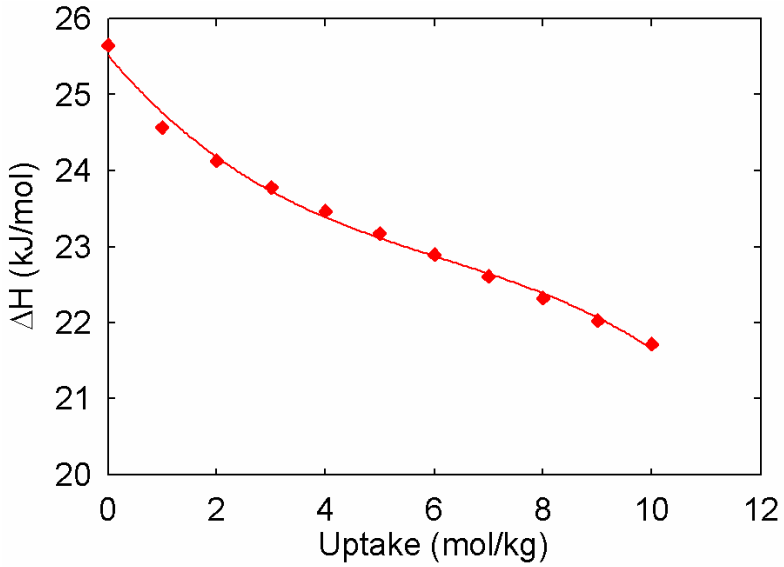

Figure 5.8 Isosteric heat of adsorption for CO_2 in compound 1

5.3.4 Water vapor adsorption

Figure 5.9 shows the water vapor adsorption isotherms at 25 ˚C for activated compound 1. The amount of water vapor adsorbed increases gradually with increase in relative humidity. The water vapor adsorption capacities at 90% relative humidity is 3 mol/kg (5.3 wt %). The water vapor isotherm is irreversible and exhibits large hysteresis. Furthermore, it can be seen that there is still some amount of water retained in the pores of the MOFs even when the stream was switched to dry air. The amount of water irreversibly bound in the MOF is about 1.45 mmol H_2O/g. This corresponds to 0.84 water molecules per formula unit that is equivalent to 0.28 water molecules per copper center. In comparison, similar experiment with Cu-BTC showed 0.69 water molecules per copper center.[14]

The XRD patterns of the sample after the water sorption experiments were compared with that of the as synthesized and activated samples (Figure 5.3). Compound 1 was not significantly degraded structurally. Minimal changes in the XRD patterns were observed after water sorption experiments and thermal activation. The N_2 sorption isotherms of the samples were measured again after water sorption and thermal activation. Surface area loss was significant. The BET surface areas reduced from 1398 to 643 m^2/g for compound 1. This suggests that after exposure to higher humidity levels and thermal regeneration, it is difficult to remove the water molecules that are irreversibly bonded to copper atoms. Also, PXRD will not show if you have small changes in crystallinity. Similar behavior was seen with Cu-BTC.[14] Cu-BTC showed 26% loss compared to 54% loss in compound 1.

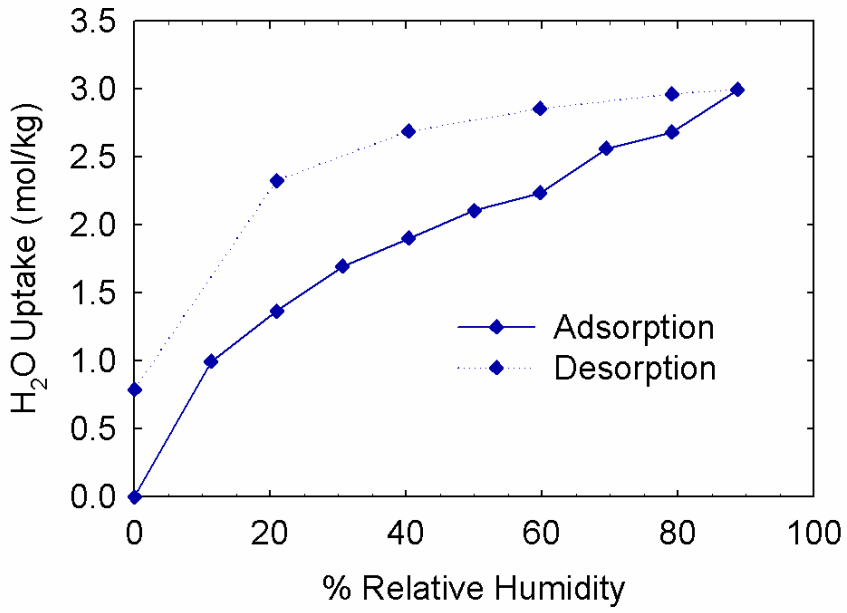

Figure 5.9 Water vapor adsorption/desorption isotherm of desolvated compound 1 at 298 K

5.3.5 Binary mixture adsorption

To explore mixture adsorption, adsorption equilibrium data and adsorption selectivities were calculated using Ideal Adsorbed Solution Theory (IAST) for binary mixtures of CO_2/CH_4 and CO_2/N_2 at 50% CO_2 composition. It has been reported that IAST can accurately predict gas mixture adsorption in many zeolites and MOFs.[15] In the calculation of adsorption selectivities for the binary mixtures through IAST method, the Toth equation was used as it provided the best fit to the single component experimental data.

The separation of the CO_2/CH_4 and CO_2/N_2 mixtures is quantified by the selectivity $S_{ij} = \left({}^{x_i}/_{x_j}\right)\left({}^{y_j}/_{y_i}\right)$, where x_i and y_i are the mole fractions of component i in the adsorbed and bulk phases, respectively.

Adsorption isotherms predicted by IAST for equimolar mixtures of CO_2/N_2 and CO_2/CH_4 in 1 as a function of total bulk pressure are shown in Figures 5.10 and 5.11 respectively. CO_2 is preferentially adsorbed over N_2 and CH_4 because of stronger interactions between CO_2 and the MOF.

In case of CO_2/N_2 mixtures, the presence of nitrogen does not significantly affect the adsorption of CO_2, but the nitrogen adsorption is much lower in the mixtures than in single-component adsorption because of competition from CO_2, which adsorbs more strongly. In the low-pressure region, the selectivity of CO_2 is 32, and the selectivity drops to 19 as pressure increases (as shown in Figure 5.12). First, the CO_2 molecules occupy the favorable exposed metal sites and then with increasing pressure, the CO_2 molecules occupy less favorable adsorption sites competing with nitrogen molecules. The selectivity for CO_2/N_2 separation at 1 bar and 298 K is 22 and is slightly higher than the reported porous materials and MOFs: Zeolite Na-4A (18.8),[16] activated carbon Norit R1(15.3)[17] , Cu-BTC (20),[11] and MOF-508b(3-6)[18] at similar conditions.

In case of CO_2/CH_4 mixtures, the presence of methane does affect the adsorption of CO_2, but the methane adsorption is lower in the mixtures than in single-component adsorption because of competition from CO_2, which adsorbs more strongly. The selectivity of CO_2 shows a weak dependency on bulk pressure (as shown in Figure 5.12). The selectivity

for CO_2/CH_4 separation at 1 bar and 298 K is 4 and is in the same range as reported for other MOFs : IRMOF-1 (2-3),[19] Cu-BTC (6-9),[19] MOF-508b (3-6)[18] at similar conditions.

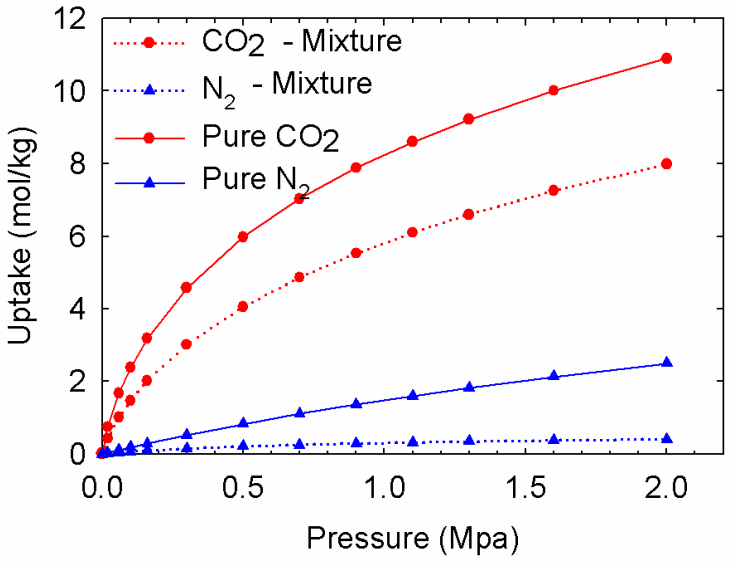

Figure 5.10 Comparison of CO_2 (red) and N_2 (blue) in pure form and in 50:50 CO_2/N_2 binary mixture (dotted line) in compound 1

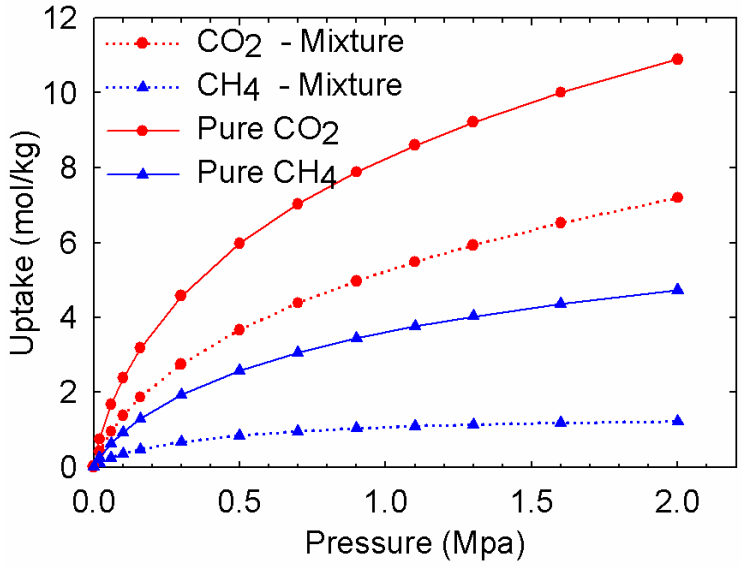

Figure 5.11 Comparison of CO_2 (red) and CH_4 (blue) in pure form and in 50:50 CO_2/CH_4 binary mixture (dotted line) in compound 1

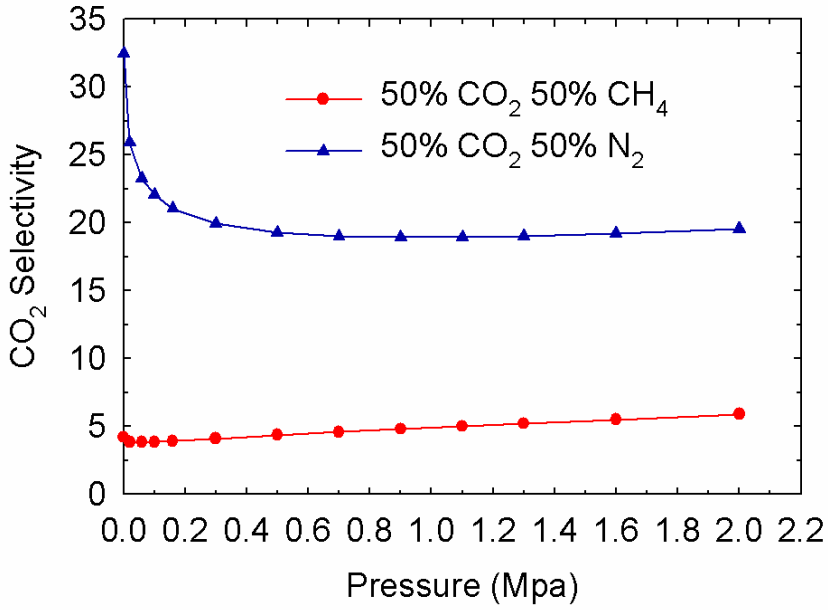

Figure 5.12 Selectivity for CO_2 over N_2 (blue) and CO_2 over CH_4 (red) in equimolar binary mixtures of CO_2/N_2 and CO_2/CH_4 in compound 1

5.4 CONCLUSIONS

MOF-14 was prepared and characterized. Its potential for application in CO_2 adsorption separation was evaluated by measuring sorption isotherms for CO_2, CH_4 and N_2. The CO_2 uptake at 1bar and 298 K is higher than that of IRMOFs and other coordination polymers.The heats of adsorption of CO_2 at low coverage was similar to that of Cu-BTC. Water vapor adsorption experiments and its subsequent structural analysis showed that this MOF is difficult to regenerate after water exposure, but PXRD patterns show that the crystalline structure is maintained. Mixture adsorption results showed that this MOF exhibited higher adsorption selectivities for CO_2 over N_2 compared to some of the well-known MOFs. This work indicates that MOF-14 is a promising nanoporous material for CO_2 adsorption separations.

5.5 REFERENCES

(1) Li, J. R.; Kuppler, R. J.; Zhou, H. C. *Chem. Soc. Rev.* **2009**, *38*, 1477.

(2) Lee, J.; Farha, O. K.; Roberts, J.; Scheidt, K. A.; Nguyen, S. T.; Hupp, J. T. *Chem. Soc. Rev.* **2009**, *38*, 1450.

(3) Chen, B. L.; Liang, C. D.; Yang, J.; Contreras, D. S.; Clancy, Y. L.; Lobkovsky, E. B.; Yaghi, O. M.; Dai, S. *Angewandte Chemie (International ed.)* **2006**, *45*, 1390.

(4) Caskey, S. R.; Wong-Foy, A. G.; Matzger, A. J. *J. Am. Chem. Soc.* **2008**, *130*, 10870.

(5) Liu, J.; Wang, Y.; Benin, A. I.; Jakubczak, P.; Willis, R. R.; LeVan , M. D. *Langmuir* **2010**, *26*, 14301.

(6) Chen, B. L.; Eddaoudi, M.; Hyde, S. T.; O'Keeffe, M.; Yaghi, O. M. *Science* **2001**, *291*, 1021.

(7) Haldoupis, E.; Nair, S.; Sholl, D. S. *J. Am. Chem. Soc.* **2010**, *132*, 7528.

(8) Gallo, M.; Glossman-Mitnik, D. *J. Phys. Chem. C* **2009**, *113*, 6634.

(9) Millward, A. R.; Yaghi, O. M. *Journal of the American Chemical Society* **2005**, *127*, 17998.

(10) Mu, B.; Li, F.; Walton, K. S. *Chem. Commun* **2009**, 18, 2493.

(11) Karra, J. R.; Walton, K. S. *J. Phys. Chem. C* **2010**, *114*, 15735.

(12) Llewellyn, P.L.; Bourelly, S.; Serre, C.; Vimont, A.; Daturi, M.; Hamon, L.; De Weireld, G.; Chang, J.S.; Hong, D.Y.; Hwang, Y.K.; Jhung, S.H.; Ferey, G. *Langmuir* **2010**, *24*, 7245.

(13) Demessence, A.; D'Alessandro, D. M.; Foo, M. L.; Long, J. R. *J. Am. Chem. Soc.* **2009**, *131*, 8784.

(14) Schoenecker, P.; Carson, C.; Walton, K. S. *Microporous Mesoporous Mater.* , under review

(15) Keskin, S.; Liu, J.; Rankin, R. B.; Johnson, J. K.; Sholl, D. S. *Ind. Eng. Chem. Res.* **2009**, *48*, 2355.

(16) Akten, E. D.; Siriwardane, R.; Sholl, D. S. *Energy & Fuels* **2003**, *17*, 977.

(17) Dreisbach, F.; Staudt, R.; Keller, J. U. *Adsorption* **1999**, *5*, 215.

(18) Bastin, L.; Barcia, P. S.; Hurtado, E. J.; Silva, J. A. C.; Rodrigues, A. E.; Chen, B. *J. Phys. Chem. C* **2008**, *112*, 1575.

(19) Yang, Q. Y.; Zhong, C. L. *J. Phys. Chem. B.* **2006**, *110*, 17776.

CHAPTER 6

SYNTHESIS AND X-RAY CRYSTAL STRUCTURES OF CADMIUM (II), MAGNESIUM (II), NICKEL (II) AND ZINC (II) COORDINATION FRAMEWORKS OF BTTB

6.1 INTRODUCTION

Porous metal-organic frameworks (MOFs) have attracted considerable research interest in the past decade, as they possess high surface areas, modifiable surfaces, and tunable pore sizes.[1] These characteristics have led to an enormous application potential for MOFs in catalysis,[2] gas storage, and adsorptive separation.[3] In particular, MOFs that selectively adsorb CO_2 over N_2, and CH_4 are very important because they have the potential to reduce carbon emissions from coal-fired power plants and substantially diminish the cost of natural gas production. Despite their importance, MOFs that show very high selective gas adsorption behavior are not so common.

Among various organic ligands, polycarboxyl compounds have been extensively used as building blocks to construct diverse frameworks ranging from one-dimensional (1D) to three-dimensional (3D) due to their ability to covalent bond and participate in supramolecular interactions (H-bonding and aromatic stacking).[4] Compared with the widely used 1,3-benzenedicarboxylic acid (1,3-BDC), 1,4-benzenedicarboxylic acid (1,4-BDC), 1,3,5-benzenetricarboxylic acid (BTC), and 4,4′,4″,-Benzene-1,3,5-triyl-tris(benzoic acid) (BTB), 4,4′,4″,4‴-benzene-1,2,4,5-tetrayltetrabenzoic acid (BTTB) is less explored. BTTB has distinctive features such as a) it contains four carboxylate groups, which can adopt different coordination modes, allowing for the formation of a

topologically diverse family of materials; b) it can act as a rigid building block to form robust MOFs with metal ions and c) its bulky structure can give rise to smaller pores through framework interpenetration, making it suitable for gas storage, separation and catalysis. In this regard, BTTB has been used to obtain some interesting coordination polymers with zinc. [5-8] However, the mixed ligand MOFs of BTTB and different carboxylic acids with different metal ions have rarely been studied. In addition, no BTTB-Ni(II) or Cd(II) or Mg(II) complexes have been found by a Cambridge Structural Database (CSD) search. So, we focus our attention on the reactions of varied metal salts with mixed ligands of BTTB and other polycarboxylic acids (shown in Figure 7.1).

We attempted to use 2,5-pyridinedicarboxylic acid (PDC), 1,4-napthalenedicarboxylic acid (1,4-NDC), 2,6-napthalenedicarboxylic acid (2,6-NDC), 1,2,4,5-benenetetracarboxylic acid (1,2,4,5-BTEC), 2,5-dihydroxyterepthalic acid (BDC-OH), 4,4'-biphenyldicarboxylic acid (BPDC), as a secondary co-ligand with the aim of obtaining a porous structure suitable for CO_2 capture applications. The secondary co-ligand should coordinate with the metal ions along with BTTB ligand in the formation of porous 3D metal-organic frameworks.

Cadmium nitrate tetrahydrate, BTTB and PDC in the relative molar ratios of 1:1:1 and DEF/Ethanol/Water (2:2:1 v/v) were sealed in a 23 mL Teflon lined stainless steel container and heated at 100 ˚C for 4 days. Upon cooling to room temperature and filtering the mother liquor, block shaped colorless crystals were obtained. Analogous reactions were carried out, replacing the cadmium salts with different metal salts (Ni, Mg, Cu, Co, Zn, Mn). High quality crystals were obtained only in the case of Mg, Zn and Ni. In the case of nickel, the mixed solvent system 1,4-dioxane/DEF/water (3:1:1) was used

to obtain the single crystals. X-ray structures of synthesized MOFs revealed that there was no involvement of PDC in the coordination modes of their respective metal ions. Subsequent synthesis without PDC produced the title compounds, thus suggesting merely a spectator role for the PDC. The same set of reactions were carried out with different metal salts and different co-ligands (1,4-NDC, BPDC, BDC-OH, 2,6-NDC, 1,2,4,5-BTEC). In most of the cases, amorphous products were obtained. In the cases where crystals were obtained, spectator role of the co-ligands in the reactions was confirmed from powder X-ray diffraction data. One notable exception here was the crystals produced from zinc nitrate salt with BTTB and 1,2,4,5-BTEC as a co-ligand. Structural analysis of this crystal revealed that only two carboxylic acid groups of 1,2,4,5-BTEC participated in the zinc(II) reaction with BTTB.

In this contribution, we will describe our recent research on the synthesis, crystal structures, and gas sorption properties of a series of MOFs synthesized from BTTB, and transition metal ions Cd(II), Zn(II), Mg(II), Ni(II) as metal centers in DEF, ethanol/1,4-dioxane and aqueous media. These MOFs are formulated as $\{[Cd_3(BTTB)_2.(H_2O)_2].(DEF)_4(H_2O)_6\}_n$(CdBTTB), $\{[Mg(BTTB).(C_2H_5OH)_2].(DEF)_4\}_n$ (MgBTTB), $\{[Ni(BTTB).(H_2O)_2].(Dioxane)_2\}_n$ (NiBTTB), $\{[Zn(BTTB)].(DEF)_3(H_2O)_2\}_n$ (ZnBTTB),and $\{[Zn_6(BTTB)_3(BDC)(H_2O)_4].(DEF)\}_n$ (ZnBTTBBDC). The structures of these MOFs have been determined by single crystal X-ray diffraction analyses and further characterized by PXRD, thermogravimetric analyses and nitrogen adsorption at 77 K.

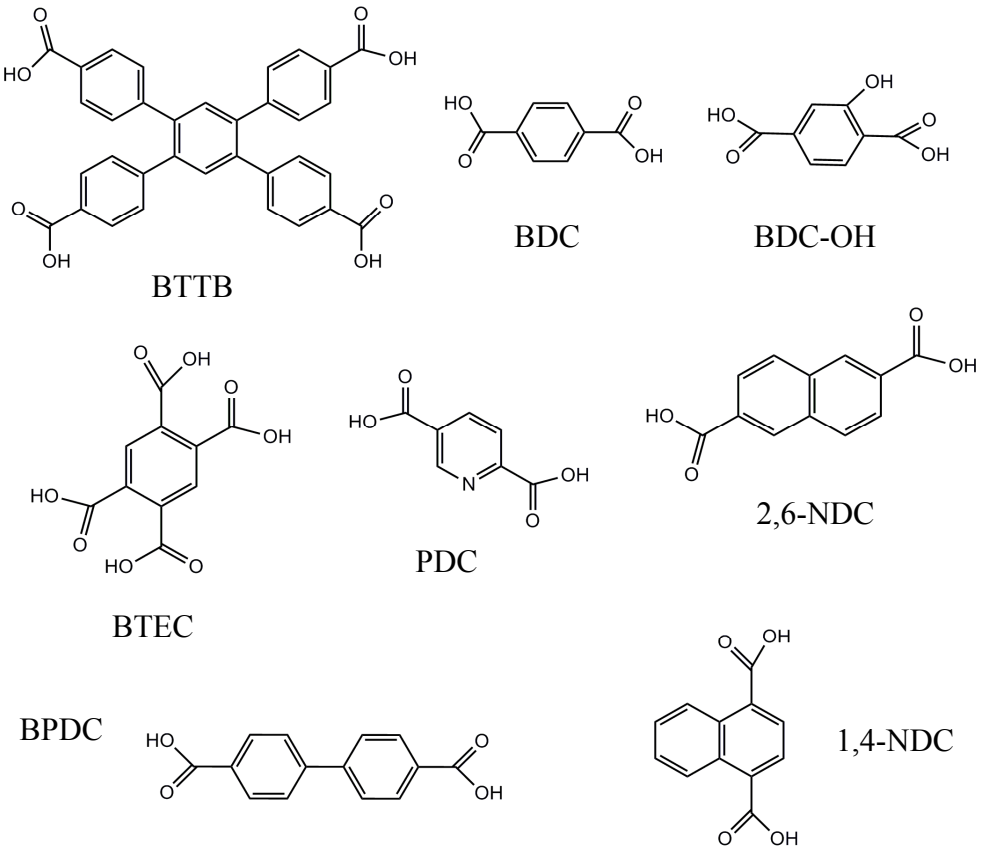

Figure 6.1 Structures of various organic struts employed in this work

6.2 EXPERIMENTAL SECTION

6.2.1 Materials and methods

All commercially available chemicals and solvents are of reagent grade and were used as received without further purification. Thermogravimetric analyses (TGA) were carried out in the temperature range of 25-700 ˚C on a NETSZCH TG/Mass spectrometry analyzer under helium with a heating rate of 5 ˚C/min. Powder X-ray diffraction patterns

(PXRD) were recorded on a X'Pert X-ray PANalytical diffractometer with an X'accelerator module using Cu Kα (λ = 1.5418 Å) radiation at room temperature, with a a step size of 0.02˚ in 2θ. Nitrogen (N_2), carbon dioxide (CO_2) and methane (CH_4) sorption experiments were carried out using a Intelligent Gravimetric Analyzer (IGA-1 series, Hiden Analytical Ltd). Elemental analysis was performed by Desert Analytics, Arizona.

Synthesis of complex $\{[Cd_3(BTTB)_2.(H_2O)_2].(DEF)_4(H_2O)_6\}_n$ (CdBTTB). A mixture containing $Cd(NO_3)_2.4H_2O$ (61.6 mg, 0.2 mmol), BTTB (55.8 mg, 0.1 mmol), PDC (16.7 mg, 0.1mmol), 2 mL DEF, 2 mL ethanol, 1 mL water, and 2 drops of 1N HCl was sealed in a 23 mL Teflon lined stainless steel container and heated at 100 ˚C for 4 days. After cooling to room temperature, colorless block shaped crystals of CdBTTB were obtained (Figure 6.2). Subsequent synthesis without PDC produced the title compound, thus suggesting merely a spectator role for the PDC. Elemental analysis (%) Calcd: C 52.76 H 5.22 N 2.79 Found : C 52.2 H 5.13 N 2.61. Yield: 57 mg (42 % based on Cd).

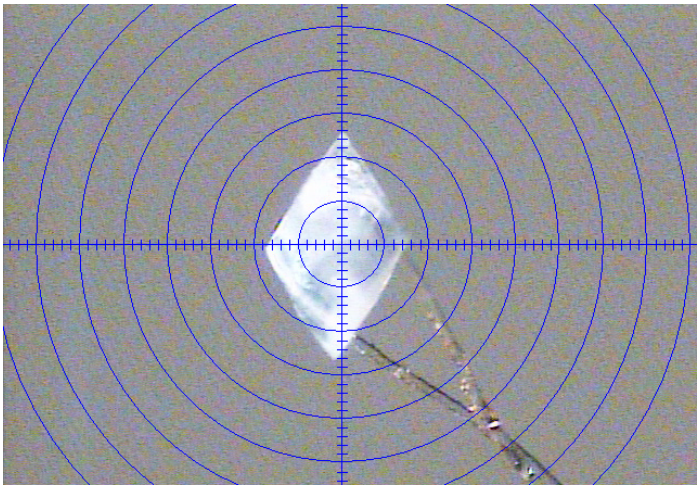

Figure 6.2 Photograph of single crystal of CdBTTB (size (mm) – 0.1 x 0.1 x 0.07)

Synthesis of complex {[Mg (BTTB).$(C_2H_5OH)_2$].$(DEF)_4$}$_n$ (MgBTTB). The preparation of MgBTTB is similar to that of CdBTTB except that $Cd(NO_3)_2.4H_2O$ was replaced by $Mg(NO_3)_2.6H_2O$ (51 mg, 0.2 mmol). After cooling to room temperature, colorless needle shaped crystals of MgBTTB were obtained (Figure 6.3). Elemental analysis (%) Calcd: C 64.53 H 7.27 N 5.19 Found : C 65.63 H 7.05 N 5.24. Yield: 47 mg (22% based on Mg).

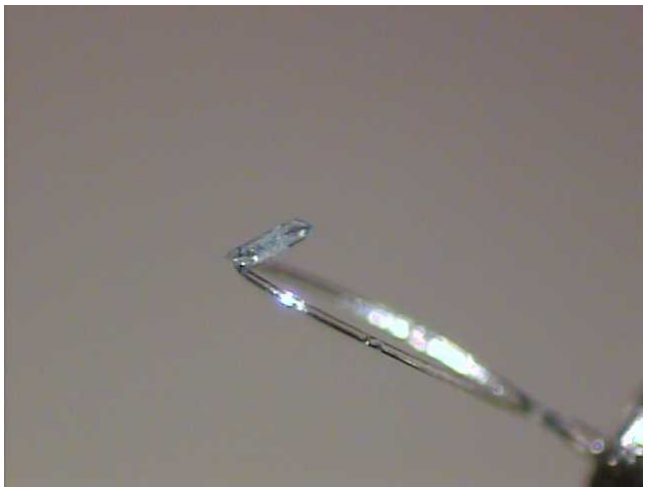

Figure 6.3 Photograph of single crystal of MgBTTB. (size (mm) – 0.12 x 0.12 x 0.1)

Synthesis of complex {[Ni (BTTB).$(H_2O)_2$].$(Dioxane)_2$}$_n$ (NiBTTB). A mixture containing $Ni(NO_3)_2.6H_2O$ (43.6 mg, 0.15 mmol), BTTB (27.9 mg, 0.05 mmol), PDC (8.35 mg, 0.05 mmol), 3 mL 1,4-dioxane, 1 mL DEF, 1 mL water, and 2 drops of 1N HCl was sealed in a 23 mL Teflon lined stainless steel container and heated at 100 ˚C for 4 days. After cooling to room temperature, green block shaped crystals of NiBTTB were obtained (Figure 6.4). Subsequent synthesis without PDC produced the title compound. Elemental analysis (%) Calcd: C 60.81 H 5.09 Found: C 60.33 H 5.67. Yield: 28.1 mg (23% yield based on Ni).

Figure 6.4 Photograph of single crystal of NiBTTB (size (mm) – 0.12 x 0.12 x 0.06)

Synthesis of complex {[Zn(BTTB)].$(DEF)_3(H_2O)_2$}$_n$ (ZnBTTB). The complex was synthesized by the same procedure used for CdBTTB except $Cd(NO_3)_2.6H_2O$ was replaced by $Zn(NO_3)_2.6H_2O$ (59.4 mg, 0.2 mmol). After cooling to room temperature, colorless block shaped crystals of ZnBTTB were obtained (Figure 6.5). Elemental analysis (%) Calcd : C: 53.92 H 5.44 N 3.85 Found: C 54.57 H 4.92 N 3.2. Yield: 58.1 mg (27% based on Zn).

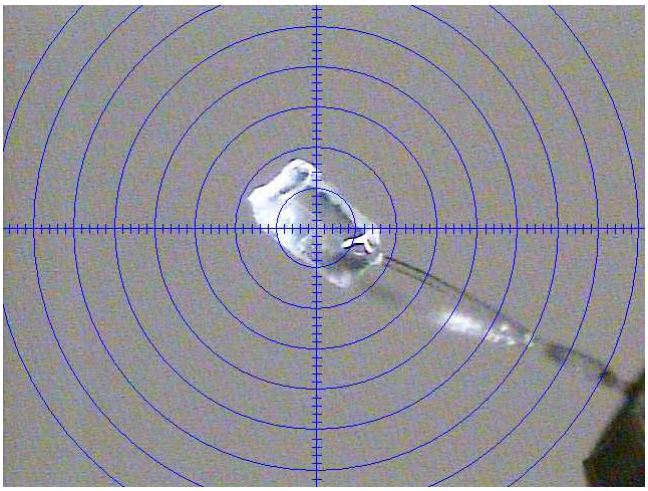

Figure 6.5 Photograph of single crystal of ZnBTTB (size (mm) – 0.14 x 0.14 x 0.08)

Synthesis of complex $\{[Zn_6(BTTB)_3(BDC)(H_2O)_4].(DEF)\}_n$ (ZnBTTBBDC). A mixture containing $Zn(NO_3)_2.6H_2O$ (59.4 mg, 0.2 mmol), BTTB (58.8 mg, 0.1 mmol), BTEC (25.4 mg, 0.1 mmol), 2 mL DEF, 2 mL ethanol, 1 mL water , and 2 drops of 1N HCl was sealed in a 23 mL Teflon lined stainless steel container and heated at 100 ˚C for 4 days. After cooling to room temperature, colorless block shaped crystals of ZnBTTBBDC were obtained (Figure 6.6). Subsequent synthesis with the same procedure by replacing BDC instead of BTEC produced the title compound. Elemental analysis (%) Calcd: C 57.6 H 4.6 N 2.06 Found : C 57.3 H 4.84 N 2.12. Yield: 35.7 mg (40% yield based on Zn).

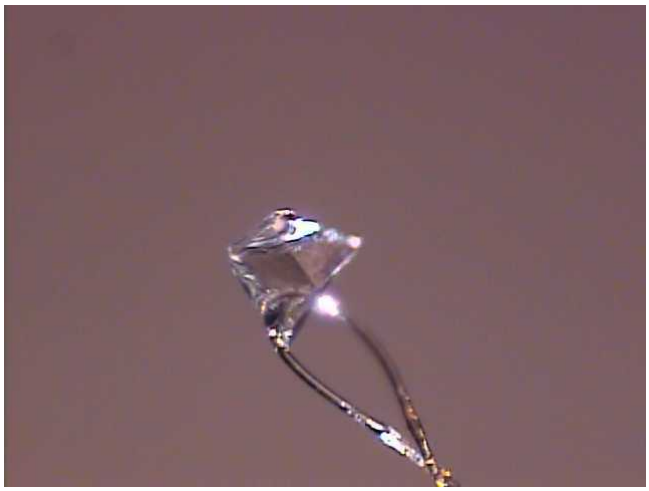

Figure 6.6 Photograph of single crystal of ZnBTTBBDC (size (mm) – 0.12 x 0.12 x 0.06)

6.2.2 X-ray crystallography

Single crystal X-ray data of CdBTTB, MgBTTB, NiBTTB and ZnBTTBBDC were collected on a Bruker APEX II CCD sealed tube diffractometer by using Cu-*K*α radiation with a graphite monochromator while for ZnBTTB, single crystal X-ray data was collected on a Bruker APEX II CCD sealed tube diffractometer by using Mo-*K*α radiation. Crystals of the MOFs were mounted on nylon CryoLoops with Paratone-N. The structure was solved by direct methods and refined using the SHELXTL-97 software suite. Anisotropic thermal parameters were refined for all nonhydrogen atoms; hydrogen

atoms were refined isotropically as riding atoms. Some of the hydrogen atoms could not be resolved, and thus were not included in the analysis.

6.3 RESULTS AND DISCUSSION

6.3.1 Crystal structure description of CdBTTB

The coordination environment around Cd(II) of CdBTTB is shown in Figure 6.7 and 6.8. Single–crystal X-ray diffraction reveals that CdBTTB crystallizes in the space group *P2221* and the asymmetric unit contains three crystallographically independent Cd centers. As shown in Figure 6.7, the cadmium atom on the left is surrounded by chelating oxygen atoms from two different BTTB ligands and two oxygen atoms from two different BTTB ligands to give a distorted octahedral coordination geometry. The central cadmium atom is ligated by four oxygen atoms from four different BTTB ligands and two water molecules to form a CdO_6 distorted octahedral geometry. The cadmium on the right is coordinated by two oxygen atoms from two different BTTB ligands and chelating oxygen atoms from two different BTTB ligands. The Cd-O distances range from 2.208 to 2.536 Å. The distances between central cadmium atom to adjacent cadmium atoms (left and right) are 4.513 and 3.618 Å respectively. The dihedral angles between the central benzene ring and two phenyl rings of BTTB ligands are in the range of 112.12–120.32˚, 58.86–68.23˚, 112.12–120.32˚, and 54.86–67.68˚ respectively. In the Cd-BTTB network, there are four types of BTTB ligands: L1 that adopts the $(\kappa^2) - (\kappa^2) - (\kappa^1 - \kappa^1) - (\kappa^1 - \kappa^1) - \mu_6$ coordination mode, L2 adopts the $(\kappa^1 - \kappa^1) - (\kappa^1 - \kappa^1) - (\kappa^1 - \kappa^1) - (\kappa^1 - \kappa^1) - \mu_8$ coordination mode, L3 adopts the $(\kappa^1) -$

$(\kappa^1)-(\kappa^2)-(\kappa^2)-\mu_4$ coordination mode and L4 adopts the $(\kappa^2)-(\kappa^2)-(\kappa^2)-(\kappa^2)-\mu_4$ coordination mode (Figure 6.8). The framework expands in three directions using the previously mentioned coordination modes, producing channels interconnected in three-dimensions with pore sizes of 5.413 Å along [1 0 0] direction, 5.413 Å along [0 1 0] direction and 7.773 Å along [0 0 1] direction (taking into account the van der Waals radii of atoms), which are available for guest accommodation and exchange (Figure 6.9). In this compound, 52 % of the void space is accessible to the solvent molecules. The channels are occupied by water, DEF, and ethanol molecules. Water molecules interact weakly with the central cadmium atom, and removal of water molecules generates exposed cadmium sites inside the pores, which can act as interaction sites between the host and guest molecules.

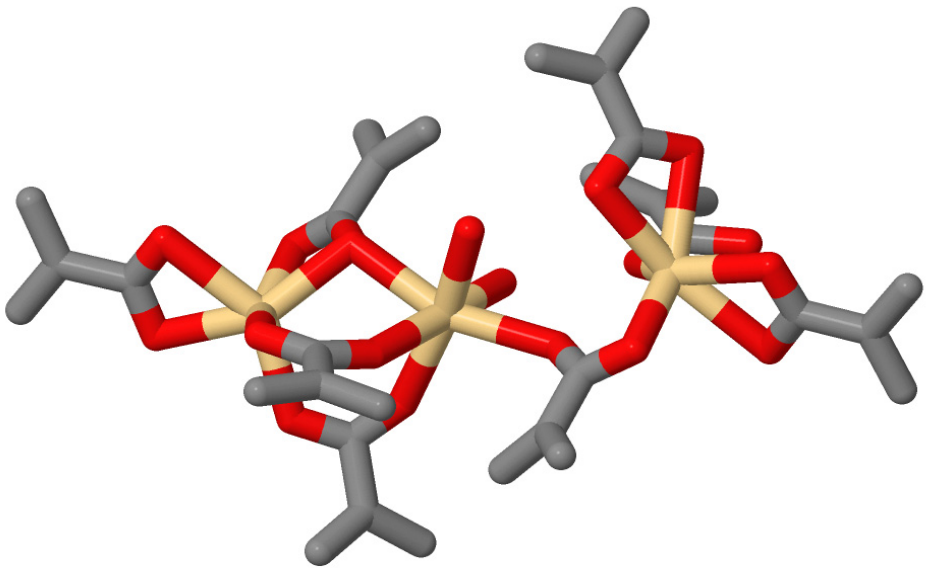

Figure 6.7 Coordination environment of the Cd (II) ion in CdBTTB. Color scheme: Cd: gold; C, grey; O, red. Hydrogen atoms are omitted for clarity

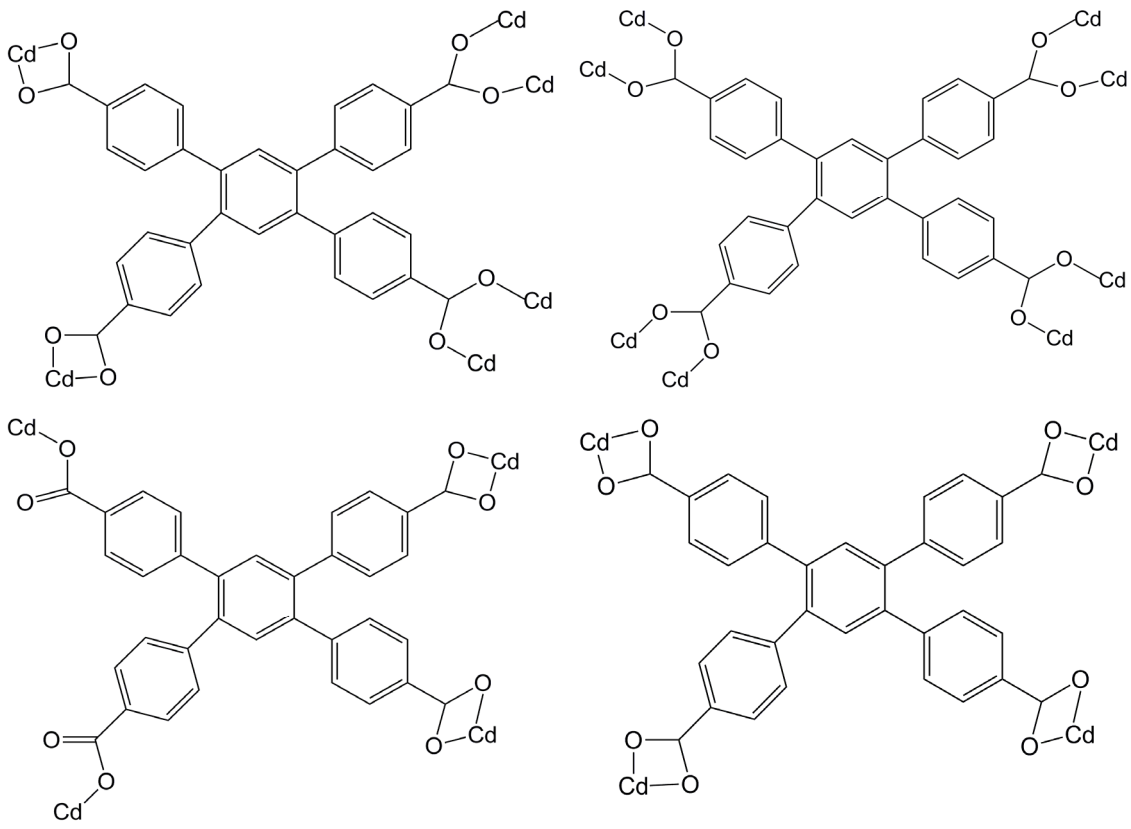

Figure 6.8 Coordination modes of BTTB ligand in CdBTTB

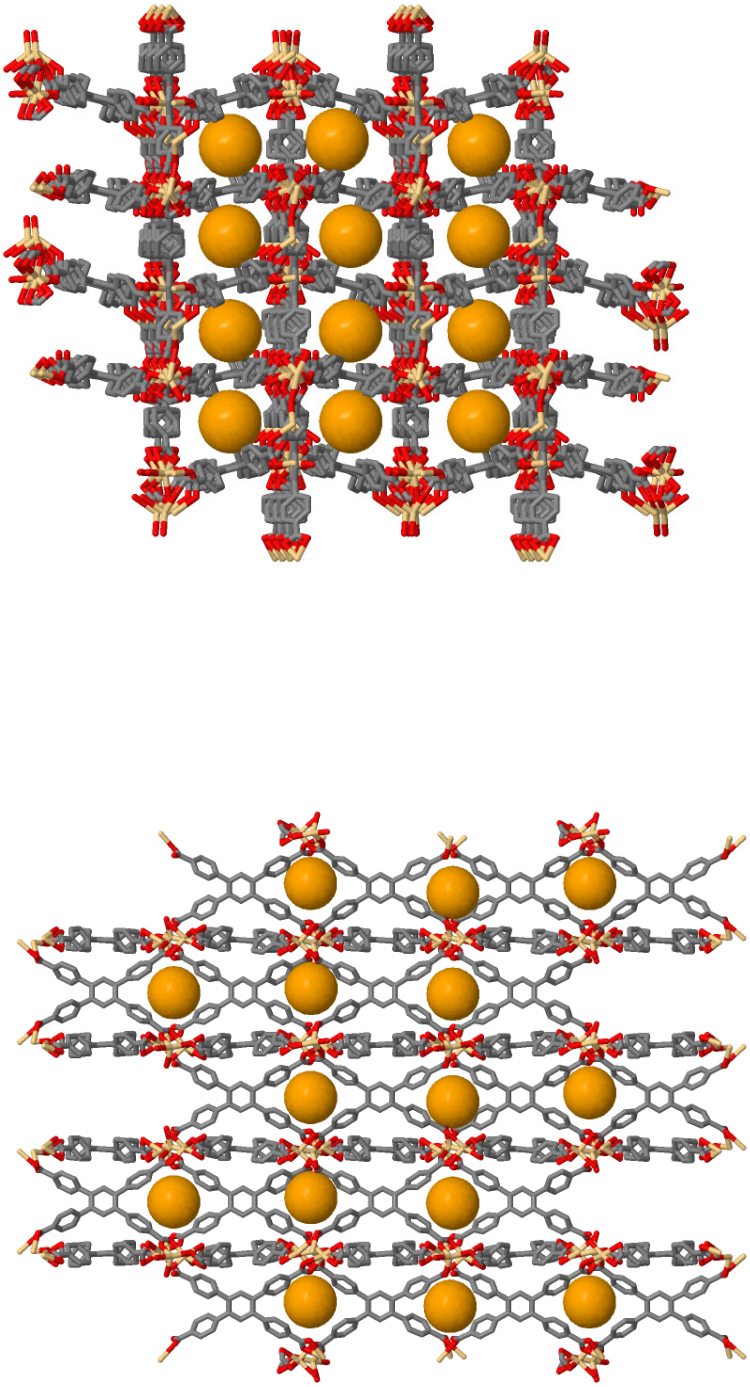

Figure 6.9 View of the 3D network of CdBTTB along the a) [1 0 0] direction b) [0 1 0] direction c) [0 0 1] direction, Color scheme: Cd: creamy white C, grey; O, red. Guest molecules and hydrogen atoms are omitted for clarity

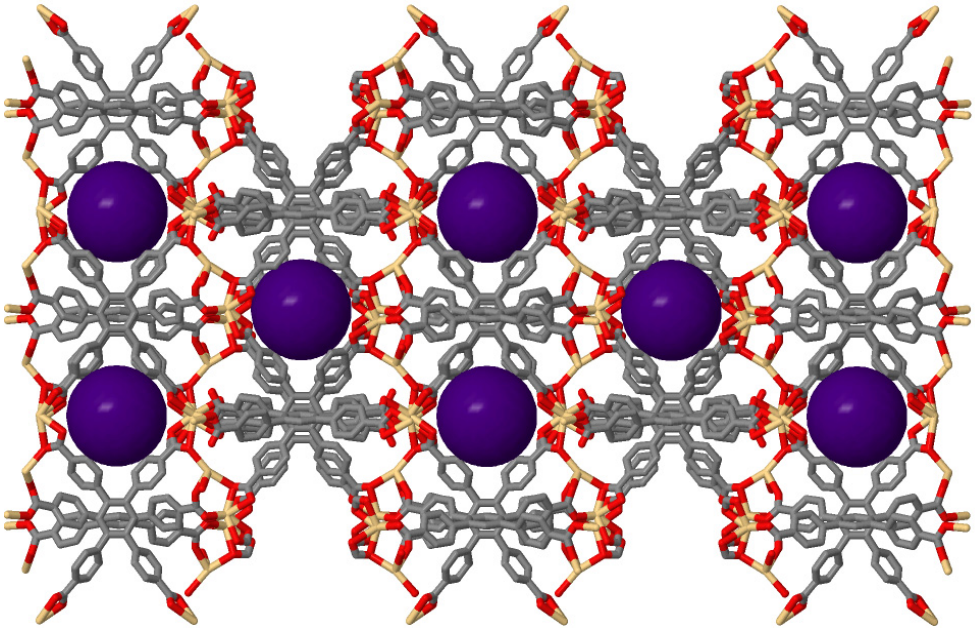

Figure 6.9 Continued

6.3.2 Crystal structure description of MgBTTB and NiBTTB

Single crystal X-ray diffraction was used to determine the structure of MgBTTB and NiBTTB. X-ray crystallography reveals that MgBTTB crystallizes in the space group *C2/c* and NiBTTB crystallizes in the space group *P-1*. The fundamental building unit of MgBTTB contains four magnesium atoms, four BTTB ligands, and four ethanol molecules, whereas the fundamental unit of NiBTTB contains four nickel ions, four BTTB ligands, and four water molecules.

In case of MgBTTB, each Mg atom has a distorted octahedral geometry and is surrounded by four oxygen atoms from four different BTTB ligands and two oxygen atoms from two different ethanol molecules (Figure 6.10). Each BTTB ligand is bound to four Mg(II) atoms in coordination mode $(\kappa^1) - (\kappa^1) - (\kappa^1) - (\kappa^1) - \mu_4$ (Figure 6.12) to give rise to a three-dimensional net with open rhomboid channels of approximately 8.555 Å along [1 1 $\bar{1}$] direction (Figure 6.13). Calculation with PLATON[9] shows that the effective volume for the inclusion is 51.1 % of the crystal volume.

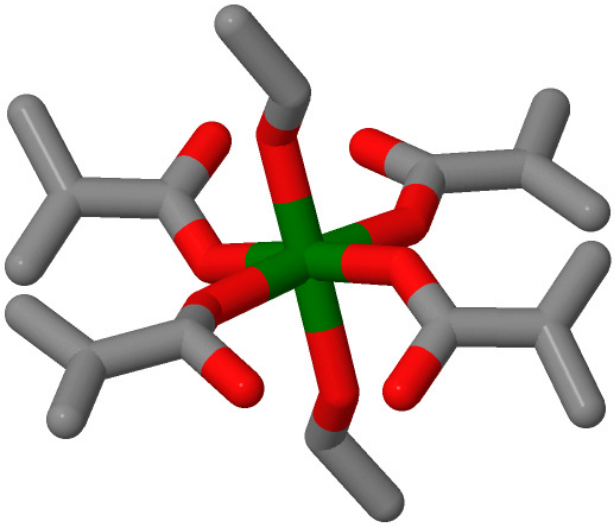

Figure 6.10 Coordination environment of Mg(II) in MgBTTB. Hydrogen atoms are omitted for clarity.

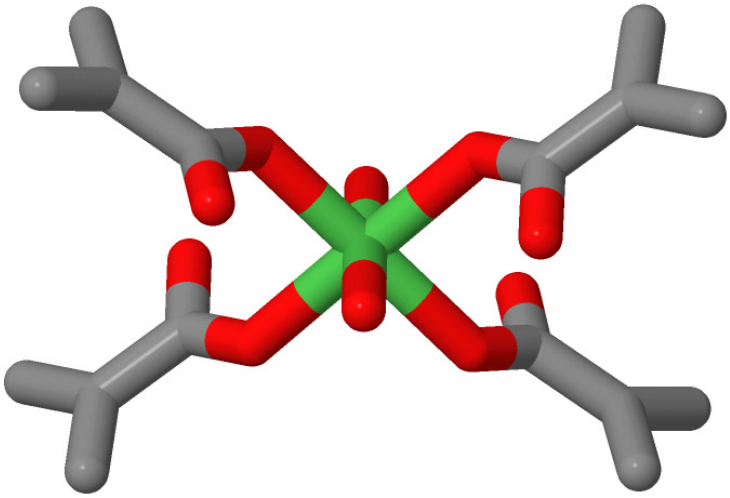

Figure 6.11 Coordination environment of Ni(II) in NiBTTB. Hydrogen atoms are omitted for clarity

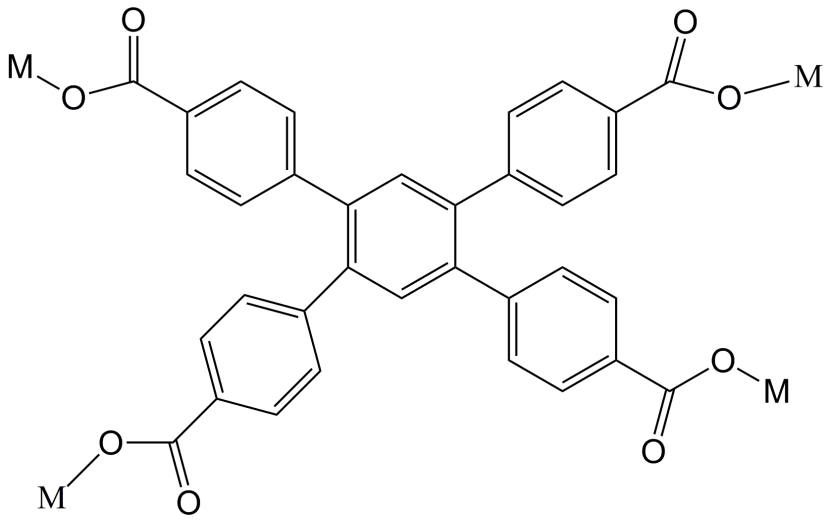

M = Mg or Ni

Figure 6.12 Coordination modes of BTTB ligand in MgBTTB and NiBTTB

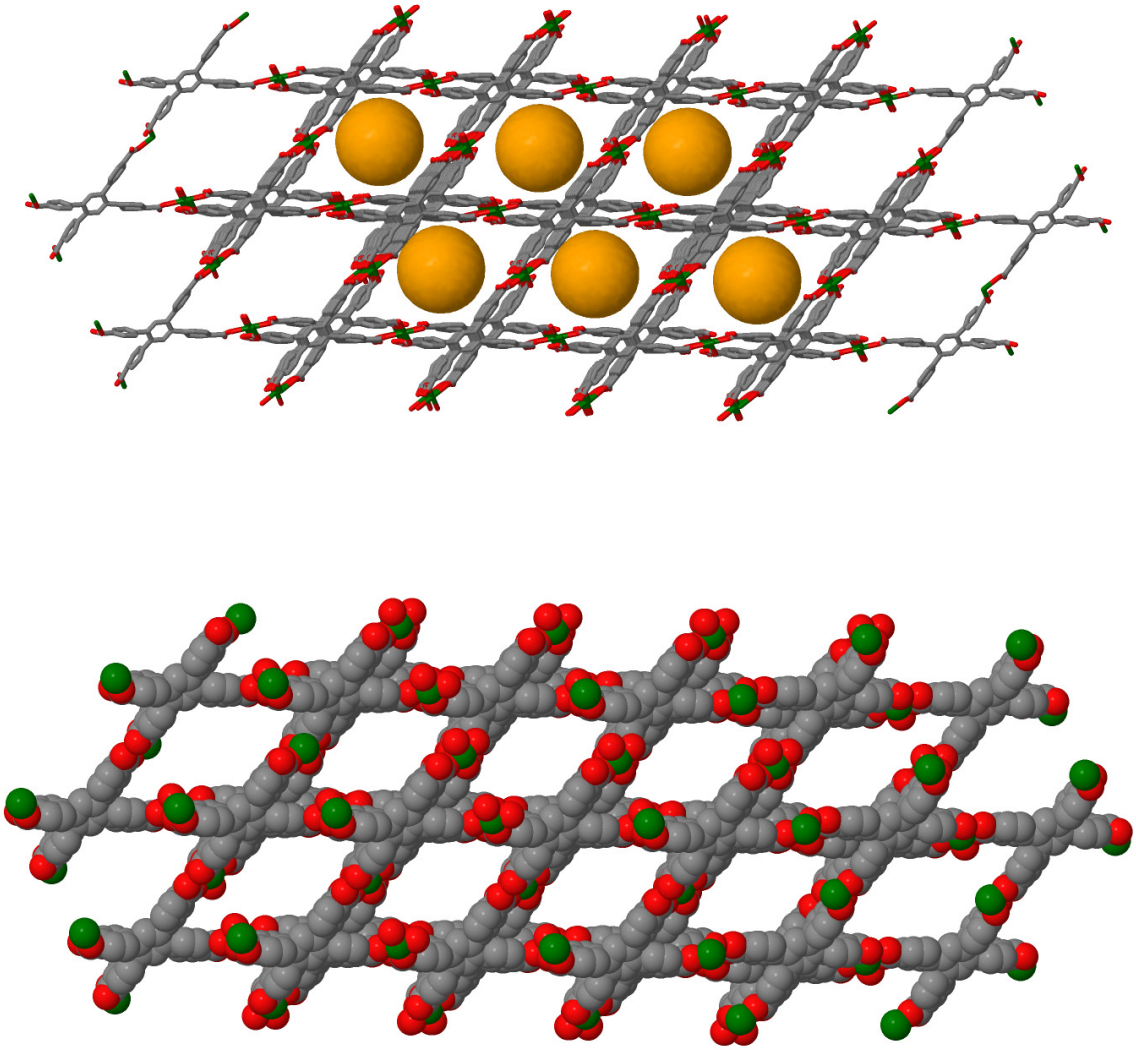

Figure 6.13 Wire frame view (top) and spacefill view (bottom) of MgBTTB showing how BTTB linkers connect the Mg atoms of the network. Yellow balls represent the pore space. Color scheme: Mg, darkgreen; C, grey; O, red. Guest molecules and hydrogen atoms are omitted for clarity

In case of NiBTTB, each Ni(II) atom is slightly octahedrally disorted and is coordinated by four oxygen atoms from four different BTTB ligands and two oxygen atoms from two different water molecules, while each BTTB ligand is bound to four Ni atoms in coordination mode $(\kappa^1)-(\kappa^1)-(\kappa^1)-(\kappa^1)-\mu_4$ (Figure 6.11 and 6.12). Such connections of Ni(II) and BTTB ligands result in the formation of a two-dimensional net with two open channels of dimensions 4.291 Å and 4.95 Å along [1 0 0] direction as shown in Figure 6.14 and 6.15. The 2D nets stack on top of each other through face to face π-π interactions to make a 3D structure. The distance between two linkers on separate layers is 3.85 Å. Calculation with PLATON[9] shows that the effective volume for the inclusion is 33.1 % of the crystal volume.

It is interesting to note that Mg(II) in MgBTTB and Ni(II) in NiBTTB have the same coordination environment and geometry, furthermore, the coordination mode of the BTTB ligand in MgBTTB and NiBTTB is also the same. However, MgBTTB and NiBTTB adopt completely different structures. In the case of MgBTTB, the strut twists sufficiently to create a true 3D framework, rather than a layered 2D framework as in the case of NiBTTB. The Ni-O and Mg-O bond distances in MgBTTB and NiBTTB are in the range of 2.022–2.072 Å and 1.958–2.117 Å, respectively, while the dihedral angles between the central benzene ring and two phenyl rings of the BTTB ligand in MgBTTB and NiBTTB are in the range of 115.41–115.93˚, 64.61–66.25˚, 115.41–116.03˚, 64.79–65.88˚ and 114.21˚, 65.79˚, 114.21˚, 65.79˚ respectively. In MgBTTB, the bond angles between O1–Mg1–O3 are in the range of 85.58–89.03˚ and in NiBTTB, bond angle between O1–Ni1–O4 is 87.30˚. Both compounds upon removal of solvent molecules possess open metal sites.

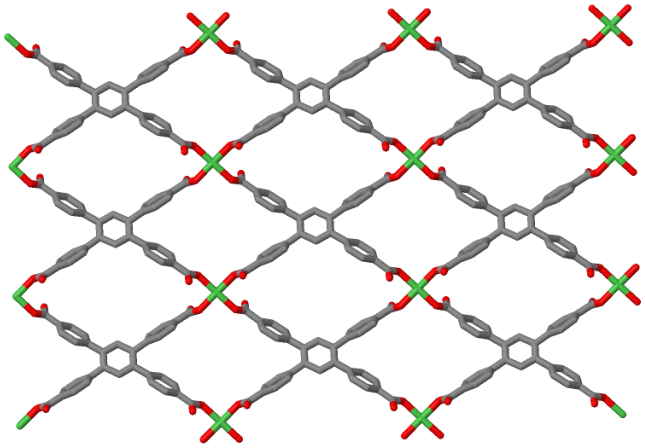

Figure 6.14 Perspective view of NiBTTB showing 2D layer with two types of open channels. Color scheme: Ni, light green; C, grey; O, red. Guest molecules and hydrogen atoms are omitted for clarity

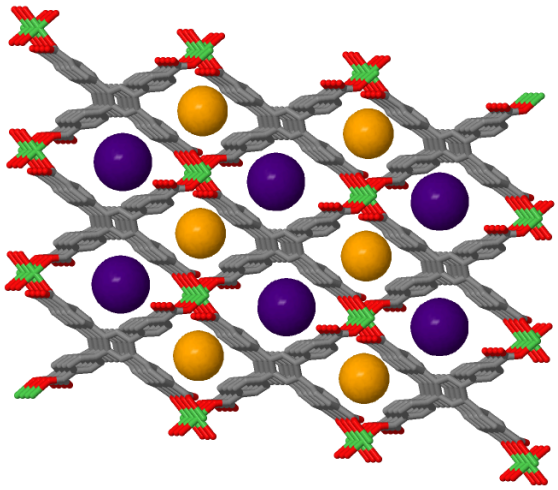

Figure 6.15 Wireframe and Spacefill view of NiBTTB showing the stacked layers along the a-axis. Yellow and Blue balls represent pore space. Color scheme: Ni, light green; C, grey; O, red. Guest molecules and hydrogen atoms are omitted for clarity

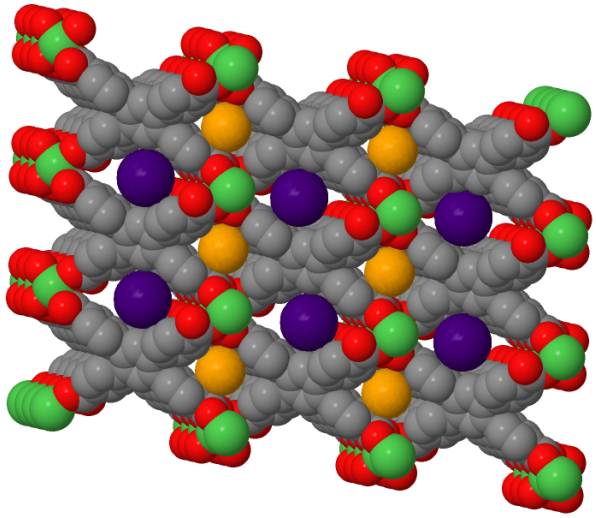

Figure 6.15 Continued

6.3.3 Crystal structure description of ZnBTTB

When $Zn(NO_3)_2.6H_2O$ was used to react with BTTB ligand, ZnBTTB was obtained. The asymmetric unit of ZnBTTB consists of two zinc atoms and two BTTB ligands. Each Zn(II) atom is four-coordinated by four oxygen atoms from four different BTTB ligands. Zn(II) atoms in the cluster are bridged by two carboxylate groups from two different BTTB ligands (Figure 6.16). Each BTTB ligand in turn coordinates with zinc metal centers in two coordination modes $(\kappa^1) - (\kappa^1 - \kappa^1) - (\kappa^1 - \kappa^1) - (\kappa^1) - \mu_6$ and $(\kappa^1) - (\kappa^1) - \mu_2$ (Figure 6.17). Interestingly, in one of the coordination modes of BTTB

ligand, two carboxyl groups do not take part in the coordination. In the dinulear zinc cluster, zinc atoms are bridged by two carboxylate groups with Zn….Zn distance of 4.303 Å and the Zn-O bond distances are in the range of 1.944-1.998 Å. Dihedral angles between central benzene ring and phenyl rings of the BTTB ligand are in the range of 112.23–113.70˚, 66.88–67.96˚, 114.15–115.19˚, 63.19–66.42˚ respectively. Therefore, the coordination interactions between the six-connecting BTTB ligand, two-connecting BTTB ligand and four-coordinated Zn(II) atom as described above make ZnBTTB a 3D framework. It is noteworthy that the void space in the single 3D framework is so large that two individual 3D frameworks interpenetrate each other to form a unique two-fold interpenetrated architecture, leaving small voids for the inclusion of guest molecules.

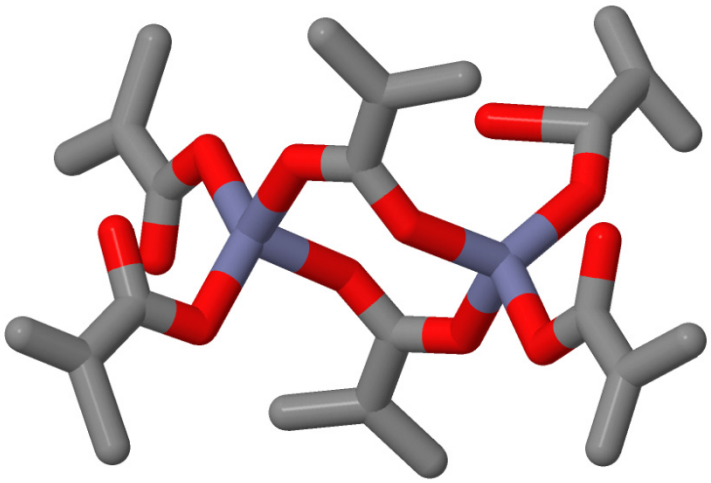

Figure 6.16 Coordination environment of Zn(II) in ZnBTTB. Hydrogen atoms are omitted for clarity, Color scheme: Zn light blue; C, grey; O, red. Guest molecules and hydrogen atoms are omitted for clarity

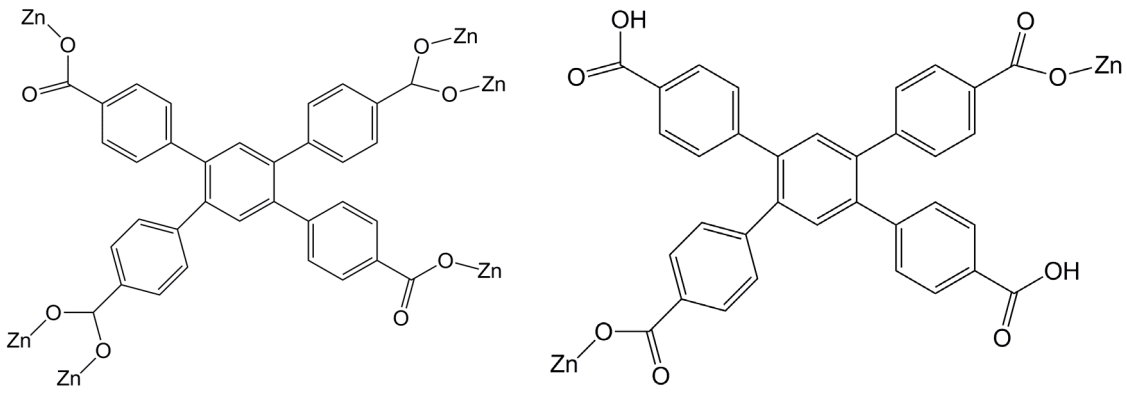

Figure 6.17 Coordination modes of BTTB ligand in ZnBTTB

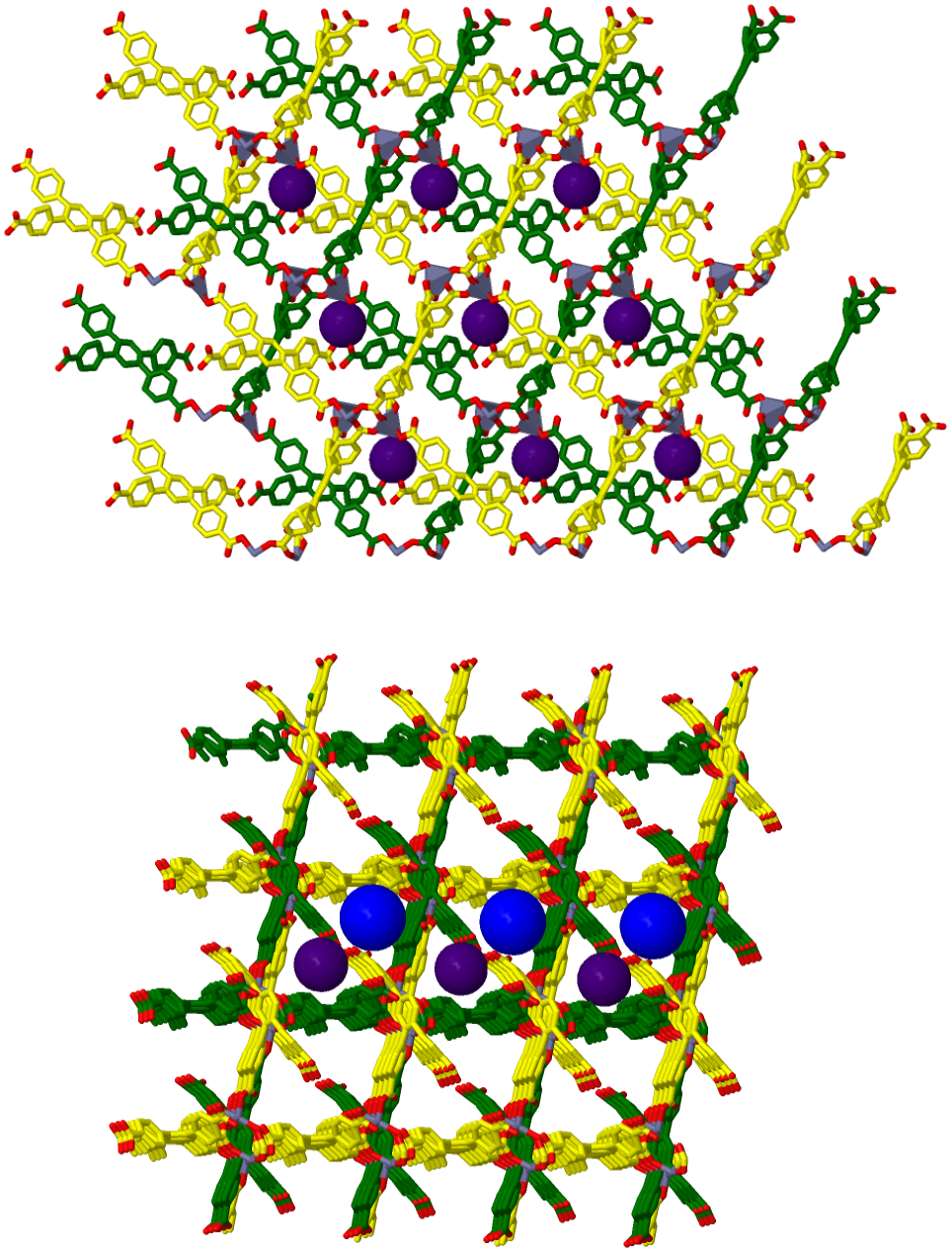

Figure 6.18 Perspective view of the 3D network of ZnBTTB along the a) [0 1 0] direction b) [0 $\bar{1}$ 1] direction c) along the [$\bar{1}$ 1 1] direction. Violet and Blue balls represent pore space. Color scheme: Yellow ang green represent different frameworks, Zn polyhedra, light blue; C, grey; O, red. Guest molecules and hydrogen atoms are omitted for clarity.

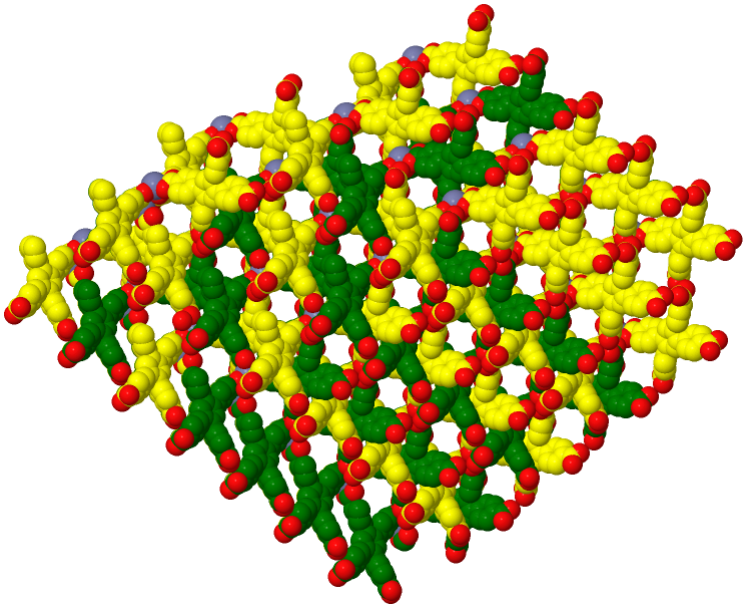

Figure 6.18 continued

The porous framework is stable up to 300 ˚C and has pore sizes of 4.468 Å in [0 1 0] direction, 4.468 Å and 5.587 Å in [0 $\bar{1}$ 1] direction, and 5.587 Å in [$\bar{1}$ 1 1] direction as shown in Figure 6.18. Framework ZnBTTB is involved in face-to-face π-π interactions with those of adjacent interpenetrated net. The calculations using PLATON[9] suggest that void space is 44.2% of the total crystal volume after removal of guest molecules.

Previously, Hupp and co-workers[8] reported porous MOF from the same metal and organic building blocks but with DMF as solvent. Despite the same reactants, the framework structure of the ZnBTTB is completely different from the previously reported structure, indicating that the change of solvent greatly affects the framework structure.

6.3.4 Crystal structure description of ZnBTTBBDC

The asymmetric unit of ZnBTTBBDC consists of six Zn(II) atoms, three BTTB ligands, one BDC ligand and four coordinated water molecules. The coordination environment of Zn(II) and ligands is shown in Figure 6.19 and 6.20. Single–crystal X-ray diffraction reveals that the compound ZnBTTBBDC crystallizes in the space group *P-1*, and the asymmetric unit contains six crystallographically independent Zn centers that can be subdivided into three binuclear zinc clusters, cluster 1 (Zn1 and Zn2 - Figure 6.19a), cluster 2 (Zn3 and Zn4 - Figure 6.19b) and cluster 3 (Zn5 and Zn6 - Figure 6.19c).

Zn1 is four-coordinated by three carboxylate oxygen atoms from three different BTTB ligands and one carboxylate oxygen atom from BDC ligand. Zn2 is six-coordinated by two carboxylate oxygen atoms in chelating bridging modes from one BTTB ligand, three carboxylate oxygen atoms in mondodentate bridging modes from three different BTTB ligands, and one water molecule. In cluster 1, Zn1 and Zn2 are bridged by three carboxylate groups from three different BTTB ligands with Zn1…Zn2 distance of 3.423 Å and Zn1-O_{BTTB} and Zn2-O_{BTTB} bond distances in the range of 1.909-1.960 Å and 1.945-2.130 Å respectively. The Zn2-O_{H2O} bond distance is 2.284 Å.

Zn3 is four-coordinated by four carboxylate oxygen atoms from four different BTTB ligands, while Zn4 is six-coordinated by two carboxylate oxygen atoms from two different BTTB ligands, two carboxylate oxygen atoms in chelating mode from one BTTB ligand, and two oxygen atoms from two water molecules. In cluster 2, Zn3 and Zn4 are connected through a chelating/bridging mode and are further bridged by two carboxylate groups from two different BTTB ligands with Zn3…Zn4 distance of 3.279 Å

and Zn3-O_{BTTB} and Zn4-O_{BTTB} bond distances in the range of 1.898-1.980 Å and 2.004-2.364 Å respectively. The Zn4-O_{H2O} bond distances are 2.034 Å and 2.141 Å.

Zn5 is six-coordinated by four carboxylate oxygen atoms in chelating bridging mode from two different BTTB ligands, one carboxylate oxygen atom from one BTTB ligand, and one carboxylate oxygen atom from one BDC ligand while Zn6 is four-coordinated by three carboxylate oxygen atoms from three different BTTB ligands and one oxygen atom from one water molecule. In cluster 3, Zn5 and Zn6 are connected through a chelating/bridging mode from two carboxylate groups from different BTTB ligands with Zn4…Zn6 distance of 3.631 Å and Zn5-O_{BTTB} and Zn6-O_{BTTB} bond distances in the range of 1.959-2.382 Å and 1.931-1.969 Å respectively. The Zn6-O_{H2O} bond distance is 2.022 Å.

It is noteworthy that the coordination modes of BTTB ligand in compound ZnBTTBBDC are different from that of compound ZnBTTB. BTTB ligands in ZnBTTBBDC adopt 3 different coordination modes $(\kappa^1-\kappa^1)-(\kappa^1)-(\kappa^1-\kappa^1)-(\kappa^1)-\mu_6$, $(\kappa^2)-(\kappa^1-\kappa^1)-(\kappa^2)-(\kappa^2-\kappa^1)-\mu_6$ and $(\kappa^1-\kappa^1)-(\kappa^1-\kappa^1)-(\kappa^2)-(\kappa^1-\kappa^1)-\mu_7$, while BDC ligand adopts coordination mode $(\kappa^1-\kappa^1)-\mu_2$ (Figure 6.20). Therefore, the connections of three zinc metal clusters and different coordination modes of BTTB ligands and BDC ligand repeats infinitely to give the 3D framework as depicted in Figure 6.21. Removal of the solvent molecules from the pores will generate unsaturated zinc sites upon evacuation.

The pores of ZnBTTBBDC are 4.243 Å along [0 0 2] direction and 6.507 Å along [0 1 0] direction and are filled with guest solvent molecules (Figure 6.21). However activation of these frameworks can yield a fully evacuated MOF with accessible metal sites to which gases can bind. Calculation with PLATON[9] shows that the effective volume for the inclusion is 44% of the crystal volume.

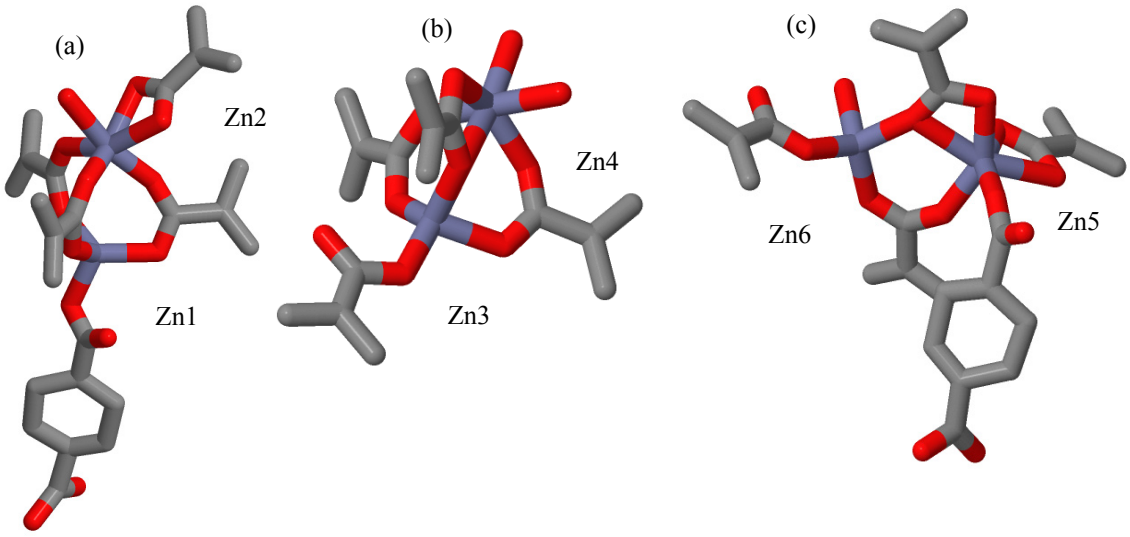

Figure 6.19 Coordination environment of Zn(II) in ZnBTTBBDC. (a) Cluster 1 (b) Cluster 2 (c) Cluster 3. Hydrogen atoms are omitted for clarity, Color scheme: Zn light blue; C, grey; O, red. hydrogen atoms are omitted for clarity

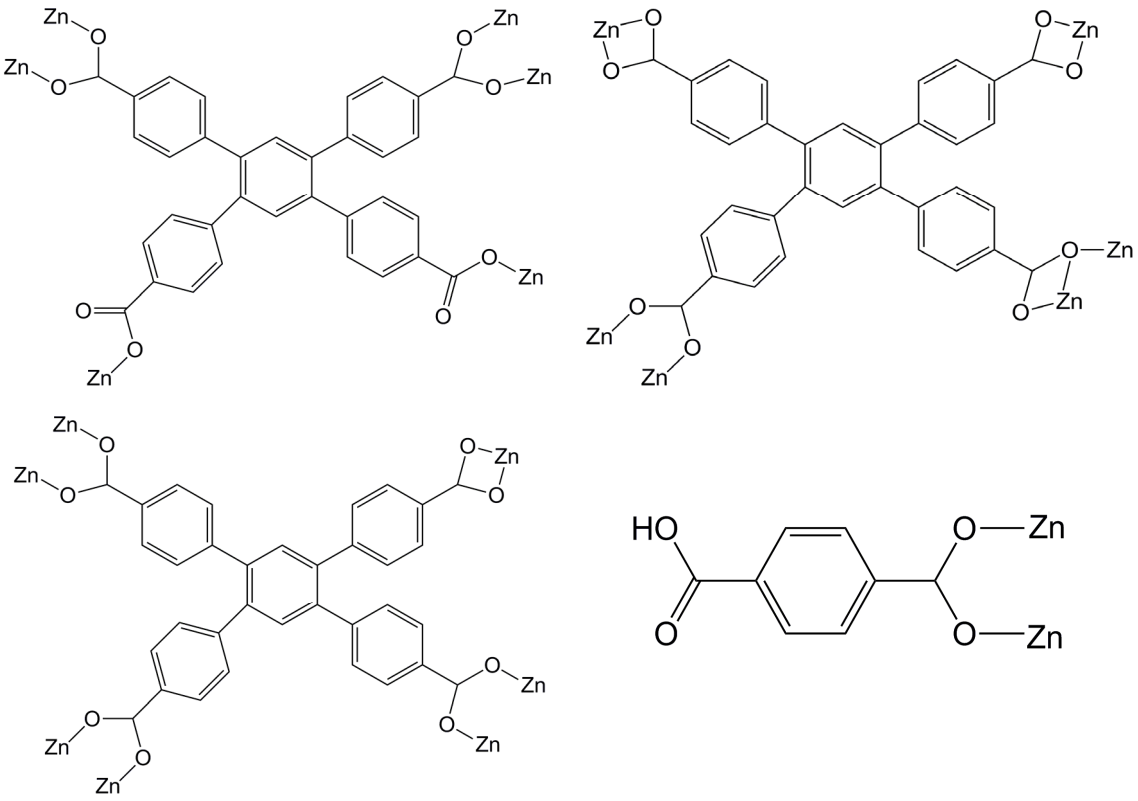

Figure 6.20 Coordination modes of BTTB and BDC ligands in ZnBTTBBDC

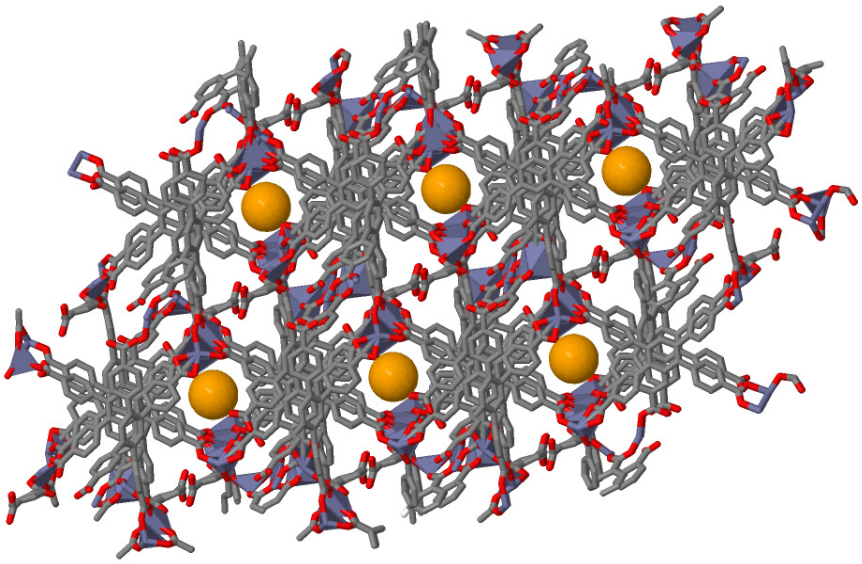

Figure 6.21 a) Perspective view of the 3D network of ZnBTTBBDC along the [0 0 2] direction b) along the [0 1 0] direction c) Space filling model view along [0 1 0] direction. Yellow and blue balls represent pore space. Color scheme: Zn polyhedra, light blue; C, grey; O, red. Guest molecules and hydrogen atoms are omitted for clarity

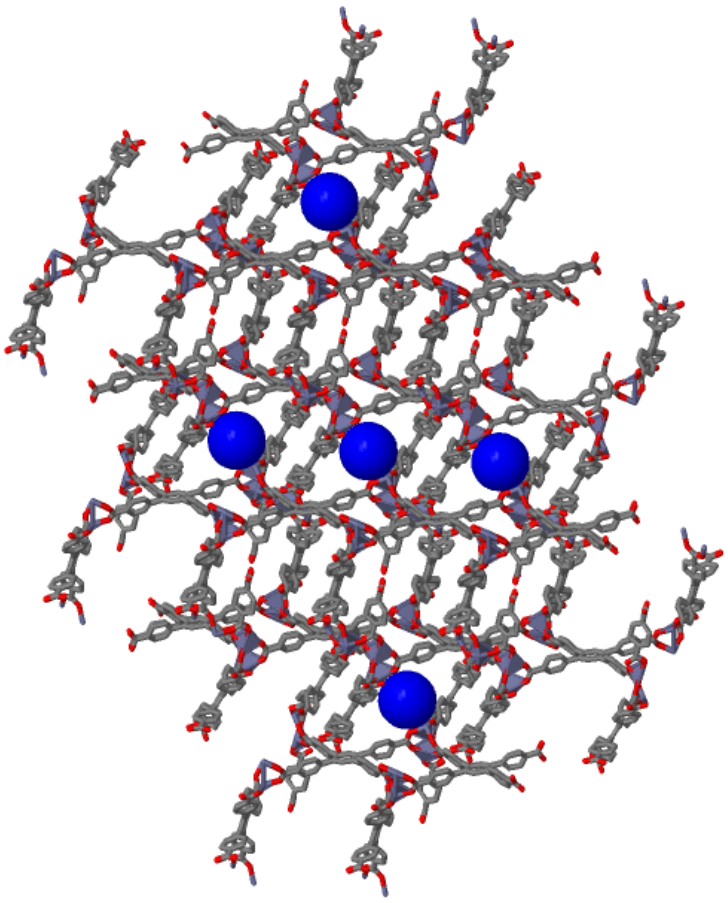

Figure 6.21 Continued

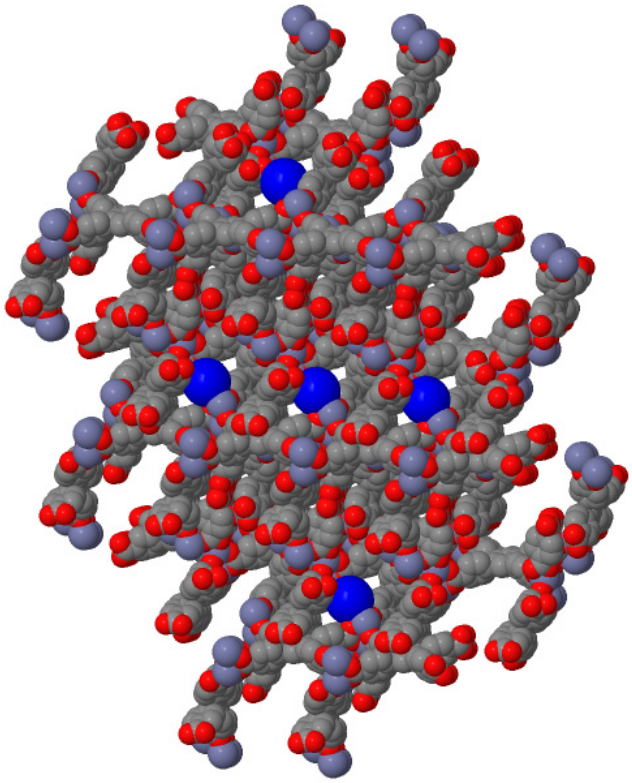

Figure 6.21 Continued

Table 6.1 Crystallographic data for CdBTTB

Compound	CdBTTB
Formula	$C_{68}H_{40}Cd_3O_{18}$
Fw	1482.20
Crystal size(mm)	0.10 × 0.10 × 0.07
Space group	*P2221*
a(Å)	28.677(2)
b(Å)	15.8555(11)
c(Å)	21.4018(15)
$\alpha(^o)$	90
$\beta(^o)$	90
$\gamma(^o)$	90
$V(Å^3)$	9731.1(12)
Z	4
$\lambda(Cu\ K\alpha)$(Å)	1.5406
$D_c(g/cm^3)$	1.012
$\mu(mm^{-1})$	0.696
T(K)	296(2)
Total reflections	208073
Unique data collected	33626
Observed reflections	26750
*R*int	0.0797
parameters	803
R_1, *w*R(I > 2σ(I))[a]	0.0453, 0.1092
R_1, *w*R(all data)[b]	0.0587, 0.1138
$w=1/〔\sigma^2(F_0^2)+(aP)^2+bP〕$	a= 0.0664,b= 0.0000
Goodness-of-fit-on F^2	0.969
$\Delta\rho_{min}$ and $\Delta\rho_{max}(e\ Å^{-3})$	-1.791, 4.042

[a] $R = \sum||F_0|-|F_c||)/\sum|F_0|$ [b] $wR = |\sum w(F_0-F_c)^2/\sum w(F_0^2)^2|^{1/2}$

Table 6.2 Crystallographic data for MgBTTB

Compound	MgBTTB
Formula	$C_{18}H_{12}Mg_{0.5}O_5$
Fw	320.43
Crystal size(mm)	0.12 × 0.12 × 0.10
Space group	*C2/c*
a(Å)	17.823(3)
b(Å)	30.112(4)
c(Å)	10.7574(12)
α(°)	90
β(°)	118.559(11)
γ(°)	90
V(Å^3)	5070.9(12)
Z	8
λ(*Cu K*α)(Å)	1.5406
D_c(g/cm^3)	0.839
μ(mm^{-1})	0.623
T(K)	173(2)
Total reflections	18512
Unique data collected	4164
Observed reflections	2175
*R*int	0.1015
parameters	211
R_1, *w*R(I > 2σ(I))[a]	0.0885, 0.2417
R_1, *w*R(all data)[b]	0.1274, 0.2709
$w=1/〔\sigma^2(F_0^2)+(aP)^2+bP〕$	a= 0.1632,b= 0.0000
Goodness-of-fit-on F^2	0.969
$\Delta\rho_{min}$ and $\Delta\rho_{max}$(e Å^{-3})	-0.497, 0.365

Table 6.3 Crystallographic data for NiBTTB

Compound	NiBTTB
Formula	$C_{17}H_{23}$ $Ni_{0.5}O_{11}$
Fw	432.71
Crystal size(mm)	0.12 × 0.12 × 0.06
Space group	*P-1*
a(Å)	6.2836(16)
b(Å)	10.732(3)
c(Å)	14.356(4)
$\alpha(^{o})$	95.441(4)
$\beta(^{o})$	98.941(4)
$\gamma(^{o})$	103.448(4)
$V(Å^3)$	921.4(4)
Z	2
$\lambda(Cu\ K\alpha)$(Å)	1.5406
$D_c(g/cm^3)$	1.560
$\mu(mm^{-1})$	0.619
T(K)	173(2)
Total reflections	18553
Unique data collected	5623
Observed reflections	3345
*R*int	0.0849
parameters	259
R_1, *w*R(I > 2σ(I))[a]	0.0861, 0.2371
R_1, *w*R(all data)[b]	0.1400, 0.2785
$w=1/[\sigma^2(F_0^2)+(aP)^2+bP]$	a= 0.1583,b= 0.6508
Goodness-of-fit-on F^2	1.035
$\Delta\rho_{min}$ and $\Delta\rho_{max}$(e $Å^{-3}$)	-1.242, 0.150

Table 6.4 Crystallographic data for ZnBTTB

Compound	ZnBTTB
Formula	$C_{34}H_{18}O_8Zn$
Fw	619.85
Crystal size(mm)	0.14 × 0.14 × 0.08
Space group	*P-1*
a(Å)	12.0239(15)
b(Å)	13.4820(17)
c(Å)	14.0414(18)
$\alpha(^o)$	70.491(2
$\beta(^o)$	77.141(2)
$\gamma(^o)$	89.312(2)
$V(Å^3)$	2086.9(5)
Z	2
λ(*Mo K*α)(Å)	1.5406
$D_c(g/cm^3)$	0.986
$\mu(mm^{-1})$	0.625
T(K)	173(2)
Total reflections	41163
Unique data collected	12616
Observed reflections	7101
*R*int	0.0722
parameters	388
R_1, *w*R(I > 2σ(I))[a]	0.0826 , 0.2258
R_1, *w*R(all data)[b]	0.1239 , 0.2444
$w=1/〔\sigma^2(F_0^2)+(aP)^2+bP〕$	a= 0.1349 ,b= 0.0000
Goodness-of-fit-on F^2	1.036
$\Delta\rho_{min}$ and $\Delta\rho_{max}$(e $Å^{-3}$)	-0.735 , 0.098 2

Table 6.5 Crystallographic data for ZnBTTBBDC

Compound	ZnBTTBBDC
Formula	$C_{110}H_{64}O_{32}Zn_6$
Fw	2289.83
Crystal size(mm)	0.12 × 0.12 × 0.06
Space group	*P-1*
a(Å)	15.8225(5)
b(Å)	16.8196(5)
c(Å)	28.4760(11)
$\alpha(^o)$	96.700(2)
$\beta(^o)$	100.221(3)
$\gamma(^o)$	109.597(2)
$V(Å^3)$	6898.0(4)
Z	2
$\lambda(Cu\ K\alpha)$(Å)	1.5406
$D_c(g/cm^3)$	1.095
$\mu(mm^{-1})$	1.655
T(K)	173(2)
Total reflections	63257
Unique data collected	21990
Observed reflections	14161
*R*int	0.0446
Parameters	1314
R_1, *w*R(I > 2σ(I))[a]	0.1090 , 0.3324
R_1, *w*R(all data)[b]	0.1317 , 0.3571
$w=1/〔\sigma^2(F_0^2)+(aP)^2+bP〕$	a= 0.2000,b= 0.0000
Goodness-of-fit-on F^2	1.326
$\Delta\rho_{min}$ and $\Delta\rho_{max}$(e $Å^{-3}$)	-1.583 , 1.577

6.3.5 Surface area, Bulk Phase Purity and Thermal properties

After synthesis, samples CdBTTB, MgBTTB, NiBTTB, ZnBTTB and ZnBTTBBDC were solvent exchanged with either chloroform, or dichloromethane, or methanol and activated at 150 ˚C for overnight under vacuum. However, solvent exchange always gave poor surface areas except in the case of NiBTTB. For the case of NiBTTB, solvent exchange with chloroform and activation at 120 ˚C gave larger surface area. Therefore, activation temperatures and activation times of samples of CdBTTB, MgBTTB, ZnBTTB and ZnBTTBBDC were varied systematically. The activation temperatures were varied from 100 to 350 ˚C within interval range of 50 ˚C and their activation times were varied from an hour to overnight under vacuum. BET surface areas were measured after each activation process. For CdBTTB, the largest surface area was obtained when the sample was activated under vacuum at 300 ˚C for an hour. In case of ZnBTTBBDC and ZnBTTB, the largest surface areas were obtained when the samples were activated under vacuum at 250 ˚C for short period of time (1 hour for ZnBTTBBDC and 2 hours for ZnBTTB). Although activation temperatures of MgBTTB were varied systematically, it still showed poor surface areas. However, we activated at 120 ˚C for overnight for gas sorption measurements at room temperature.

Table 6.6 shows the summary of activation procedure for these MOFs along with their predicted accessible surface areas.[10] The experimental BET surface areas for CdBTTB, ZnBTTBBDC, and ZnBTTB are much smaller than that of surface areas calculated geometrically from the perfect crystal structure with nitrogen molecule as a probe.[10] As activation for these samples was done at near to their decomposition temperatures for a

short period of time, it is quite possible that the some of the pores of these samples could have been collapsed or there may be defects or trapped residual solvent molecules present in the samples. This point will be revisited in the later discussion. Note that TGA measurements alone cannot be used to determine the stability of an open structure since it may collapse without a notable change in weight.

Although the calculated accessible surface area is high for MgBTTB, it always showed negligible uptake of nitrogen at 77 K. However, the same sample does adsorb CO_2, CH_4 and N_2 at 298 K. Solvent molecules were not completely removed for this material at 120 ˚C (shown in TGA measurements, Figure 6.32), although it was activated for 12 hrs under vacuum. We believe that the solvent molecules might have clogged some of the pores or might have partially blocked the larger pores, rendering this MOF very small pores, closer to the kinetic diameter of nitrogen (~ 3.64 Å). For tightly constricted pores, it is possible that nitrogen molecules cannot overcome the diffusional resistances to fill the pores at 77 K, whereas at 298 K, diffusion occurs readily due to the additional thermal energy. Similar behavior has observed in other studies.[11-15]

Table 6.6 Properties of MOFs synthesized in this work

MOF	Pore size (Å)	Pore volume (cm^3/g)	BET surface area (m^2/g)	Activation process (under vacuum)	Thermal stability	Features	Predicted accessible surface area (m^2/g)
MgBTTB	8.555	0	0	120 ˚C (12 h)	120 ˚C	1-D pore system, open Mg sites	2437
ZnBTTBBDC	4.243	0.209	441	250 ˚ C (1h)	350 ˚C	2-D pore system, open Zn sites	1114
NiBTTB	4.291	0.2	391	Chloroform Exchange and 120 ˚ C (12h)	350 ˚C	1-D pore system, open Ni sites	442
CdBTTB	5.413	0.190	415	300 ˚ C (1h)	350 ˚C	3-D pore system, open Cd sites	2180
ZnBTTB	4.468	0.251	447	250 ˚ C (2h)	300 ˚C	3-D pore system, interpenetrated	1372

The N_2 adsorption/desorption isotherms measured at 77 K for compounds CdBTTB, NiBTTB, ZnBTTB and ZnBTTBBDC reveal typical type-I behavior, as expected for microporous materials. Fitting the Brunauer-Emmett-Teller (BET) equation to their respective N_2 adsorption isotherms within the range $0.007<P/P_0<0.03$ gives an estimated surface area of 415 m^2/g for CdBTTB, 391 m^2/g for NiBTTB, 447 m^2/g for ZnBTTB and 441 m^2/g for ZnBTTBBDC. The Dubinin-Astakhov (DA) equation gives an estimated pore volume of 0.190 cm^3/g for CdBTTB, 0.2 cm^3/g for NiBTTB, 0.251 cm^3/g for ZnBTTB and 0.209 cm^3/g for ZnBTTBBDC. All compounds are stable in air and insoluble in water and most of the common organic solvents such as chloroform, methanol, acetone, toluene, and dimethyl formamide.

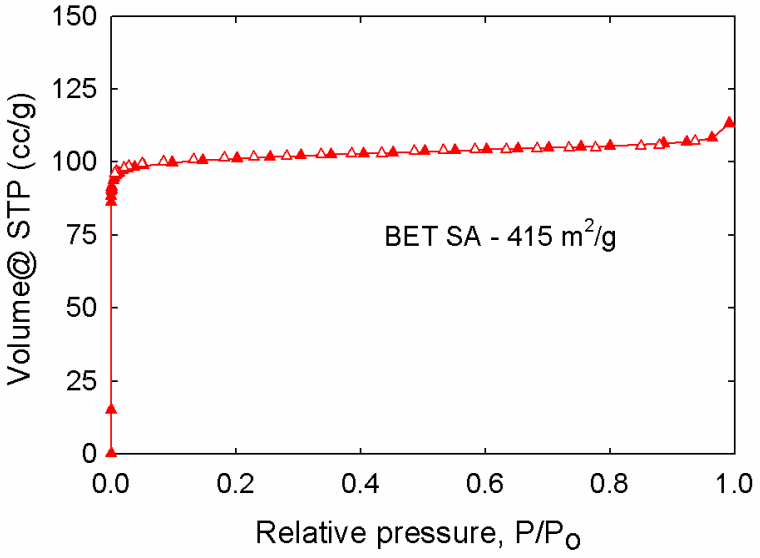

Figure 6.22 Nitrogen isotherm of activated CdBTTB at 77 K (closed symbols – adsorption, open symbols – desorption)

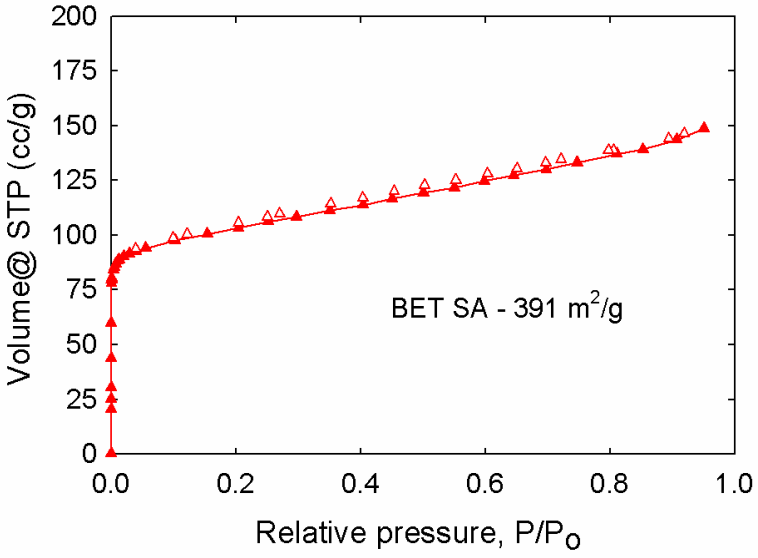

Figure 6.23 Nitrogen isotherm of activated NiBTTB at 77 K (closed symbols – adsorption, open symbols – desorption)

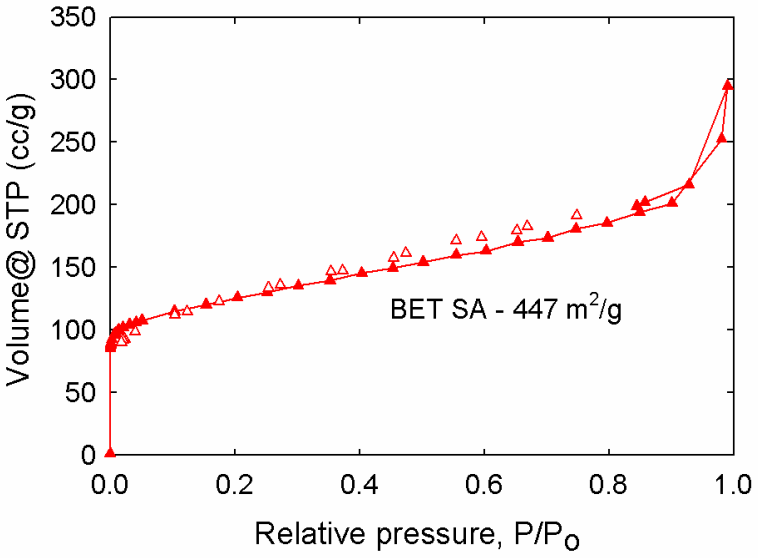

Figure 6.24 Nitrogen isotherm of activated ZnBTTB at 77 K (closed symbols – adsorption, open symbols – desorption)

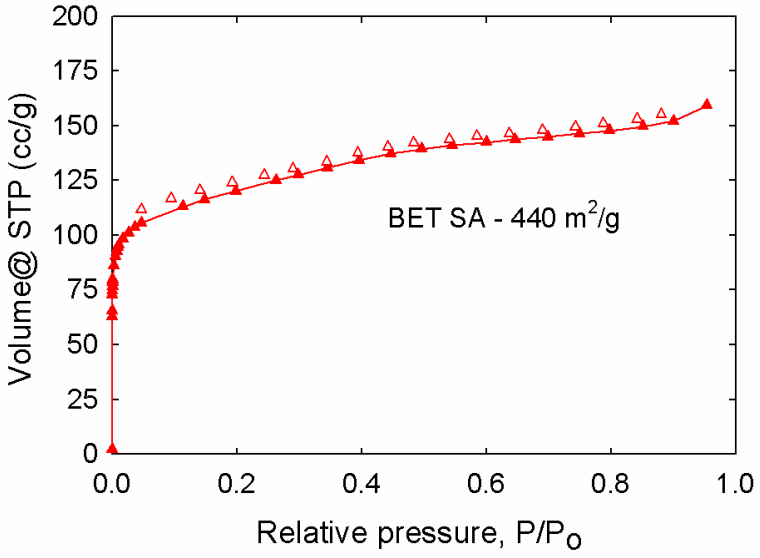

Figure 6.25 Nitrogen isotherm of activated ZnBTTBBDC at 77 K (closed symbols – adsorption, open symbols – desorption)

In order to confirm the phase purity of the bulk materials CdBTTB, MgBTTB, NiBTTB, ZnBTTB and ZnBTTBBDC, PXRD experiments were carried out. The PXRD experimental and simulated patterns for each MOF are shown in Figures 6.26-6.30. As shown in the figures, all major peaks of as-synthesized powder X-ray patterns (PXRDs) agree reasonably well with that of simulated PXRD patterns. In CdBTTB, ZnBTTB, and ZnBTTBBDC there are some missing or extra minor peaks that could be attributed to the impurities present in these samples. For ZnBTTB, the simulated patterns have too many peaks that are very close to each other. Note that molybdenum X-ray system was used for measurement of single crystal data for ZnBTTB as the diffraction intensity was too weak for this crystal, while for other MOFs, copper X-ray system was used.

In all the activated samples, there was a loss of transparency and single crystallinity. The PXRD pattern of activated NiBTTB is coincident with the corresponding patterns simulated from single-crystal XRD structure. However, for activated samples of CdBTTB, ZnBTTB and ZnBTTBBDC, some peaks were lost after activation with the major framework structure maintained. This suggests that some of the pores could have been partially collapsed in these MOFs, which could be the reason for their lower surface areas. Upon resolvation in DEF and water, the PXRD patterns of ZnBTTB and ZnBTTBBDC were regenerated. For the case of CdBTTB, the structure did not change upon resolvation and was the same as its activated sample. In case of MgBTTB, upon activation some peaks were slightly shifted from the simulated peak position. However, when MgBTTB was immersed in DEF for one day, the PXRD pattern of MgBTTB is regenerated, thus indicating this structure is flexible, and the original structure is restored

on reintroduction of the guest molecules. It is probable that the less rigid linker BTTB added a degree of flexibility that allowed for any small perturbations in these structures without decomposing the structure.

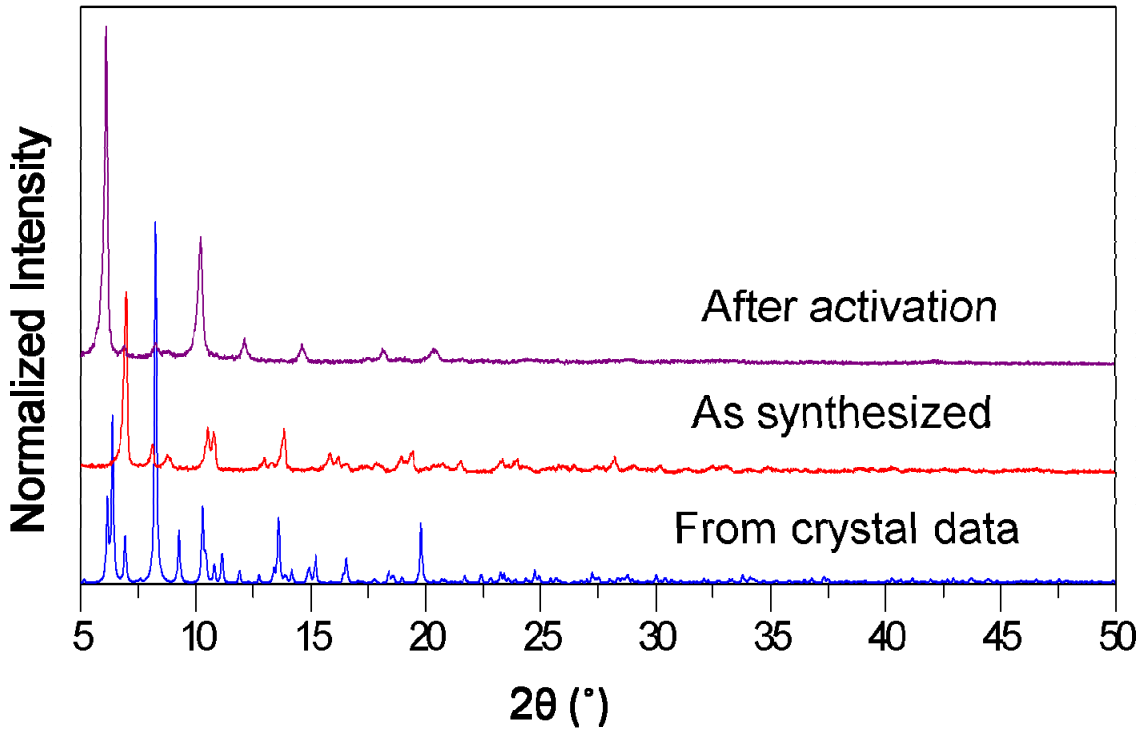

Figure 6.26 Simulated, as synthesized and activated powder X-ray diffraction patterns of CdBTTB

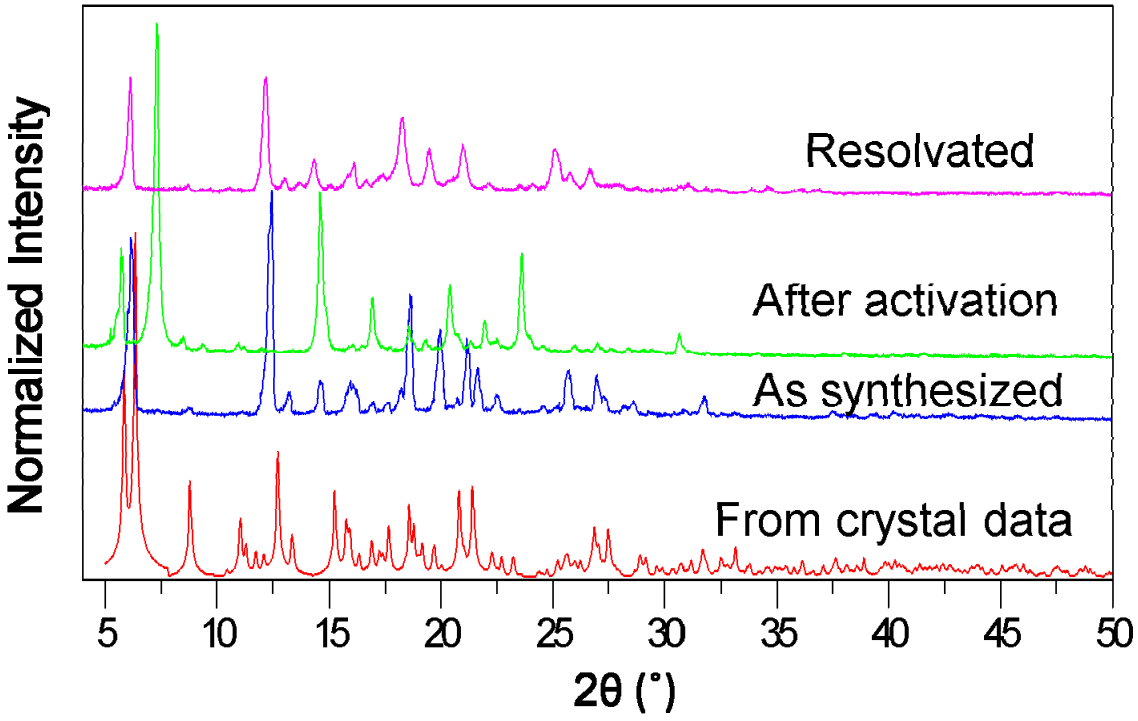

Figure 6.27 Simulated, as synthesized, activated and resolvated powder X-ray diffraction patterns of MgBTTB

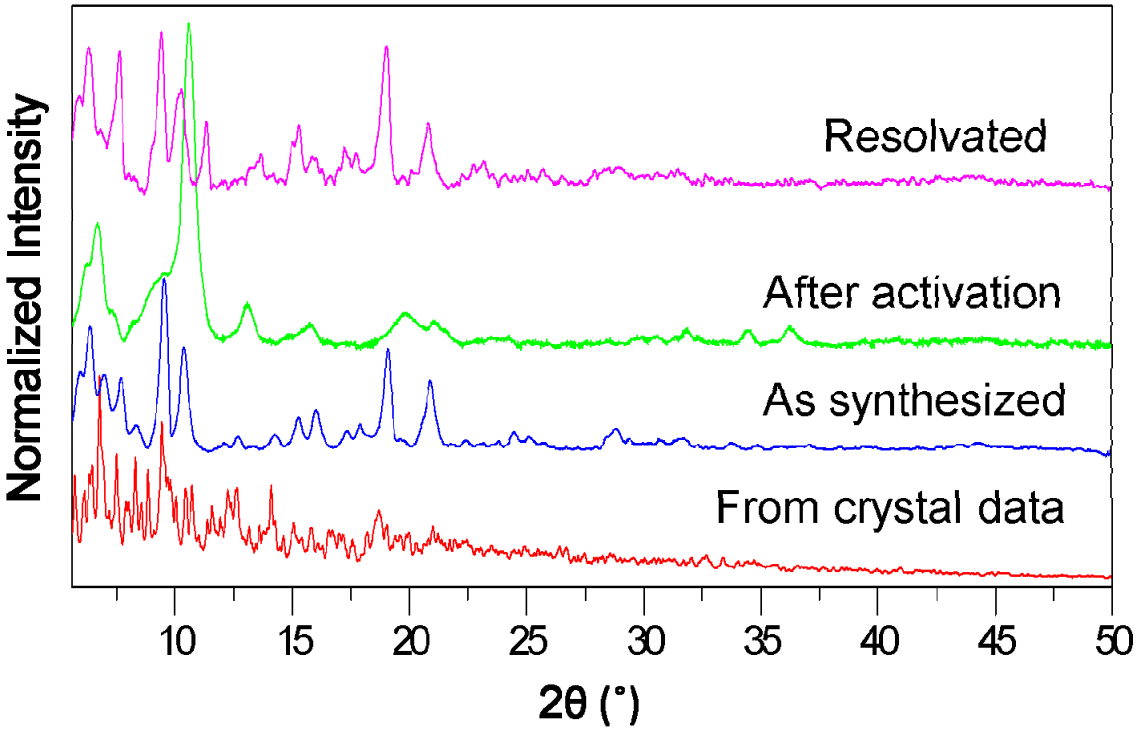

Figure 6.28 Simulated, as synthesized, chloroform exchanged and activated powder X-ray diffraction patterns of ZnBTTB

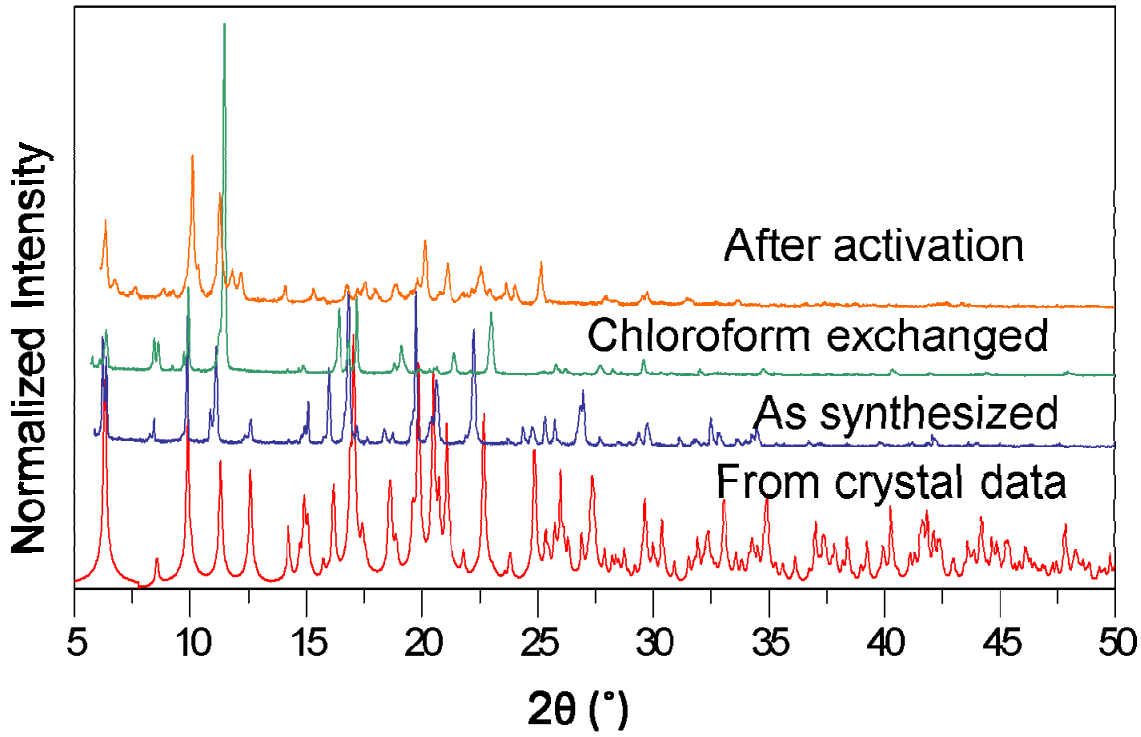

Figure 6.29 Simulated, as synthesized, activated and resolvated powder X-ray diffraction patterns of NiBTTB

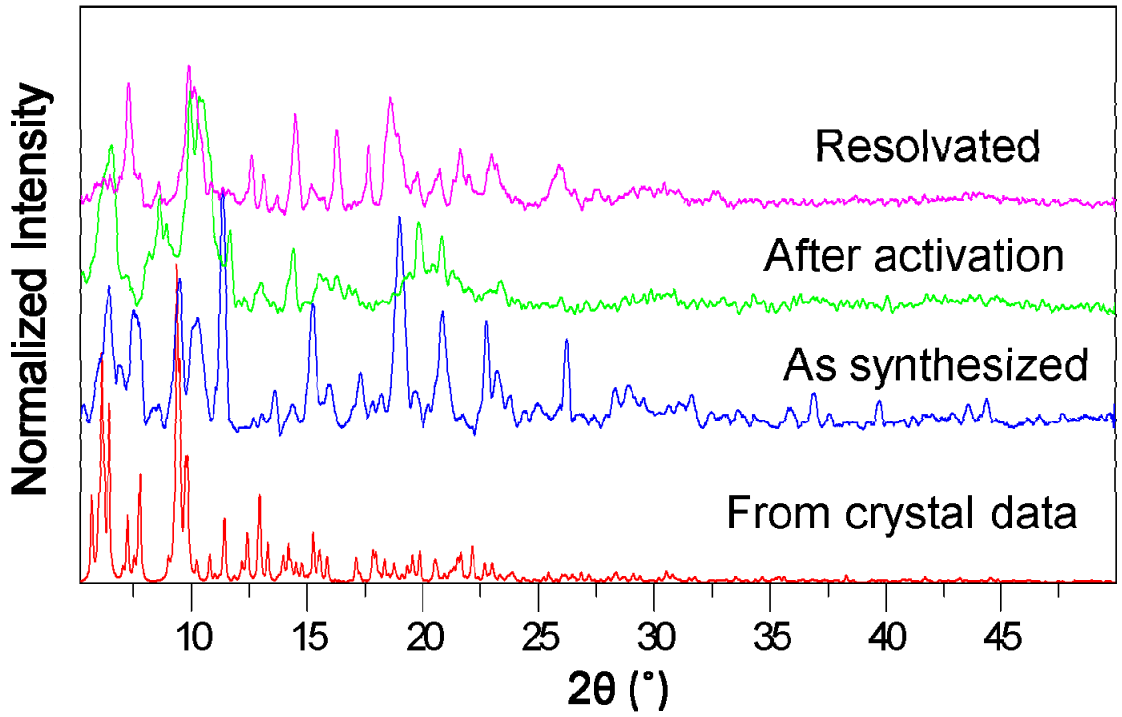

Figure 6.30 Simulated, as synthesized, activated and resolvated powder X-ray diffraction patterns of ZnBTTBBDC

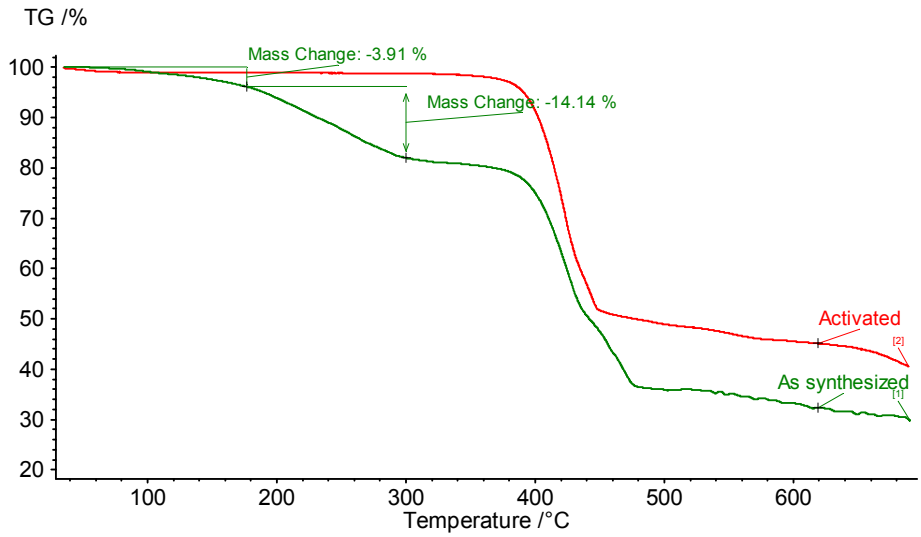

Figure 6.31 TGA trace of CdBTTB

Thermogravimetric data of all MOFs synthesized in this work are shown in Figures 6.31-6.36. CdBTTB displays a thermal stability of ~ 350 ˚C. A steady weight loss of ~ 18%, corresponding to removal of coordinated water molecules and uncoordinated solvent molecules is seen between room temperature and 300 ˚C, and a rapid weight loss beyond 400 ˚C suggests the framework breaks down due to the decomposition of BTTB ligand. Removal of guest molecules from CdBTTB was done at 300 ˚C for 1 hr, and this was confirmed from the thermogravimetric data and PXRD data of activated sample of CdBTTB.

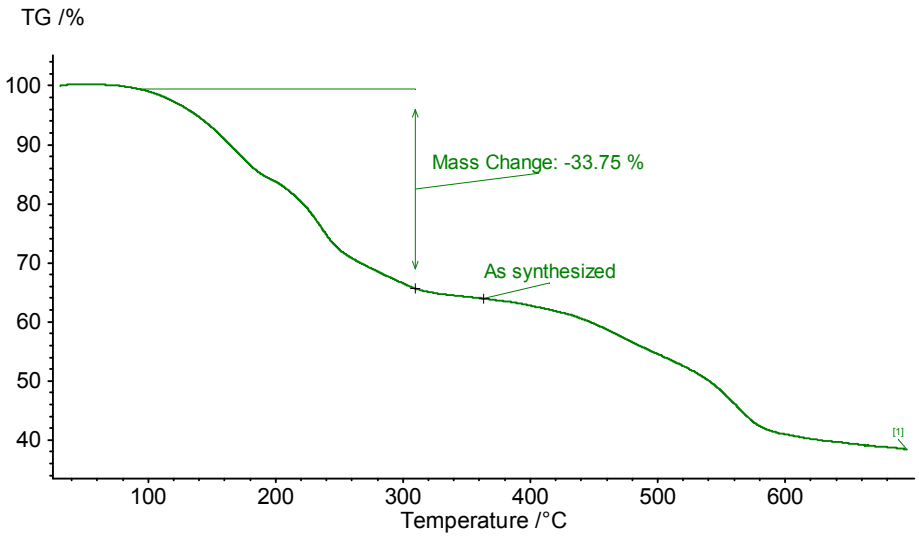

Figure 6.32 TGA trace of MgBTTB

MgBTTB undergoes steady weight loss between 100 ˚C to 300 ˚C, corresponding to the loss of ethanol and uncoordinated DEF molecules. Beyond 350 ˚C, it undergoes a rapid weight loss that can be attributed to the framework decomposition. There is no well-defined plateau seen for this MOF, which suggests that the thermal stability of MOF is very low (~ 100 – 120 ˚C).

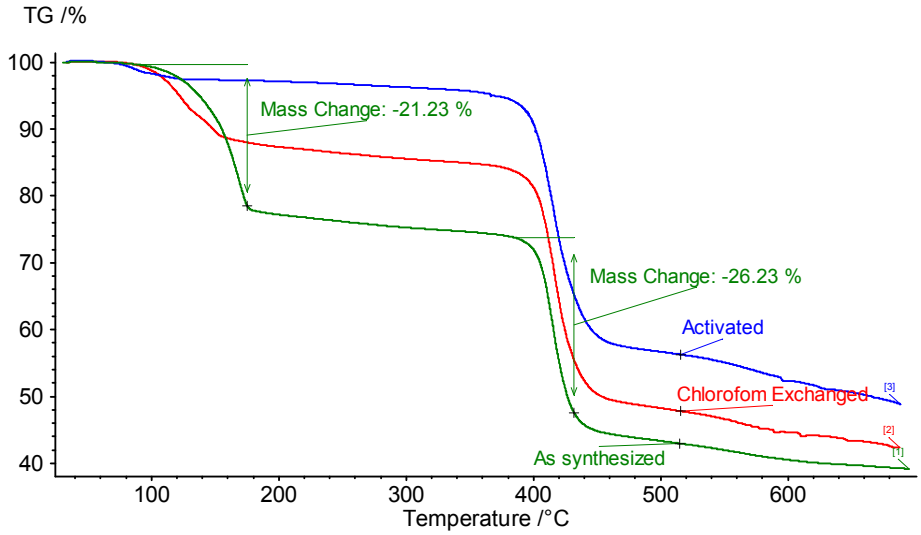

Figure 6.33 TGA trace of NiBTTB

The TGA curve of NiBTTB shows that initial weight loss begins at 100 ˚C and continues till 150 ˚C and then reaches a plateau. The total weight loss over this range is ~21 % ,which corresponds to loss of most of the coordinated and uncoordinated solvent molecules. This compound has a thermal stability of 350 ˚C. Beyond this temperature, it undergoes a rapid weight loss that can be attributed to the decomposition of organic linkers. Removal of guest molecules from NiBTTB was done with chloroform exchange and activation at 150 ˚C for 12 hrs and this was confirmed from the thermogravimetric data and PXRD data of activated sample of NiBTTB.

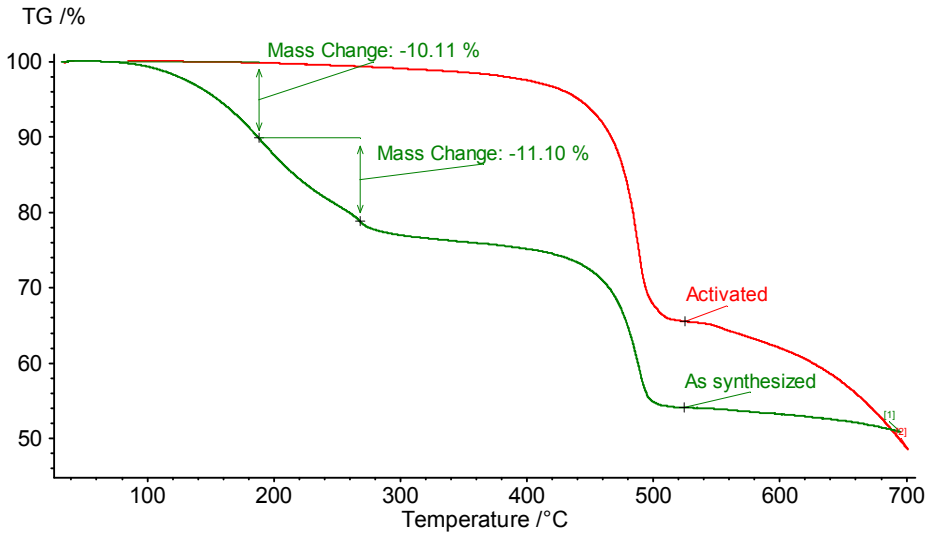

Figure 6.34 TGA trace of ZnBTTB

ZnBTTB undergoes a steady weight loss of ~ 21 % of uncoordinated solvent molecules from 80 ˚C to 250 ˚C and reaches a small region of plateau from 250 to 300 ˚C. Removal of guest molecules from ZnBTTB was done at 250 ˚C for 1 hr and this was confirmed from the thermogravimetric data and PXRD data of activated sample of ZnBTTB.

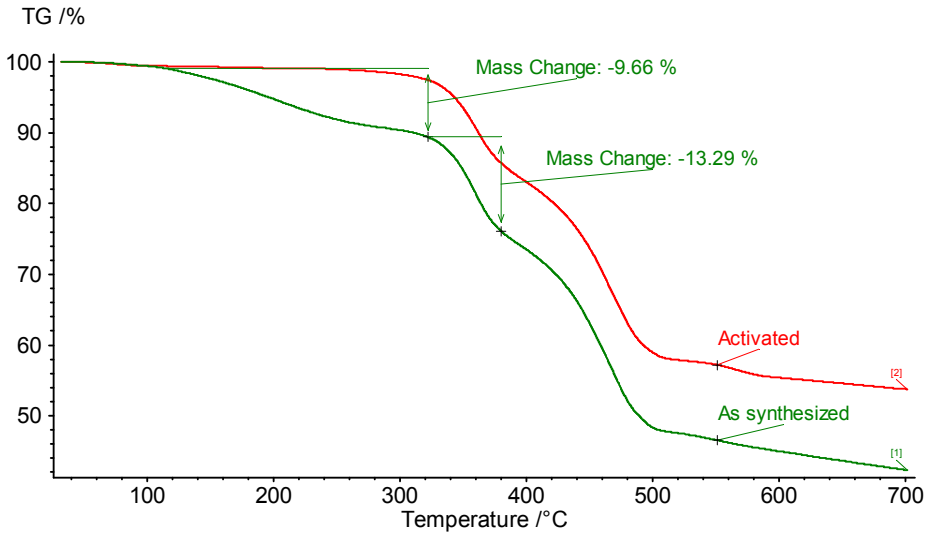

Figure 6.35 TGA trace of ZnBTTBBDC

ZnBTTBBDC undergoes a steady weight loss of ~ 10 %, from 100 to 300 ˚C and then reaches a small plateau region, and beyond 350 ˚C, a rapid weight loss occurs. The weight loss of ~ 10 % corresponds to removal of coordinated and uncoordinated solvent molecules. Removal of guest molecules from ZnBTTBBDC was done at 250 ˚C for 1 hr and this was confirmed from the thermogravimetric data and PXRD data of activated sample of ZnBTTBBDC.

6.4 CONCLUSIONS

Five new MOFs, CdBTTB, MgBTTB, NiBTTB, ZnBTTB and ZnBTTBBDC were synthesized by solvothermal technique using a tetracarboxylate building block 4,4′,4″,4‴-benzene-1,2,4,5-tetrayltetrabenzoic acid (BTTB) in combination with different metal salts and/or co-ligand terepthalic acid (BDC). All the MOFs exhibited different network topologies. Metal centers played an important role in governing the coordination motifs. In all these complexes, the BTTB ligand displayed different degrees of deprotonation and bridging fashions. All the MOFs synthesized in this work except MgBTTB demonstrated good surface areas, thermal stability, and permanent porosity.

6.5 REFERENCES

(1) Ferey, G. *Chem. Soc. Rev.* **2008**, *37*, 191.

(2) Lee, J.; Farha, O. K.; Roberts, J.; Scheidt, K. A.; Nguyen, S. T.; Hupp, J. T. *Chem. Soc. Rev.* **2009**, *38*, 1450.

(3) Li, J. R.; Kuppler, R. J.; Zhou, H. C. *Chem. Soc. Rev.* **2009**, *38*, 1477.

(4) Ma, L. F.; Li, C. P.; Wang, L. Y.; Du, M. *Crystal Growth & Design* **2010**, *10*, 2641.

(5) Bae, Y. S.; Spokoyny, A. M.; Farha, O. K.; Snurr, R. Q.; Hupp, J. T.; Mirkin, C. A. *chem. commun* **2010**, *46*, 3478.

(6) Farha, O. K.; Malliakas, C. D.; Kanatzidis, M. G.; Hupp, J. T. *J. Am. Chem. Soc.* **2010**, *132*, 950.

(7) Mulfort, K. L.; Farha, O. K.; Malliakas, C. D.; Kanatzidis, M. G.; Hupp, J. T. *Chem. Eur. J.* **2010**, *16*, 276.

(8) Farha, O. K.; Mulfort, K. L.; Hupp, J. T. *Inorg. Chem* **2008**, *47*, 10223.

(9) Spek, A.L. **2005**, PLATON, A Multipurpose Crystallographic Tool, Utrecht University, Utrecht, The Netherlands.

(10) Duren, T.; Millange, F.; Frey, G.; Walton, K. S.; Snurr, R. Q. *J. Phys. Chem. C* **2007**, *111*, 15350.

(11) Garrido, J.; Linnaressolano, A.; Martinmartinez, J. M.; Molinasabio, M.; Rogriguezreinoso, F.; Torregrosa, R. *Langmuir* **1987**, *3*, 76.

(12) Lozano-Castello, D.; Cazorla-Amoros, D.; Linares-Solano, A. *Carbon* **2004**, *42*, 1233.

(13) Bae, Y. S.; Farha, O. K.; Hupp, J. T.; Snurr, R. Q. *J. Mater. Chem* **2009**, *19*, 2131.

(14) Bae, Y. S.; Mulfort, K. L.; Frost, H.; Ryan, P.; Punnathanam, S.; Broadbelt, L. J.; Hupp, J. T.; Snurr, R. Q. *Langmuir* **2008**, *24*, 8592.

(15) Nguyen, T. X.; Bhatia, S. K. *J. Phys. Chem. C* **2007**, *111*, 2212.

CHAPTER 7

SYNTHESIS, X-RAY CRYSTAL STRUCTURES OF COBALT (II) AND ZINC (II) METAL ORGANIC FRAMEWORKS ASSEMBLED FROM BTTB LIGAND AND DIPYRIDAL STRUTS

7.1 INTRODUCTION

Metal-organic coordination polymers have gained significant attention in recent years as materials for applications in areas such as gas storage, separations,[1] catalysis,[2,3] drug delivery,[4,5] sensing, luminescent and magnetic applications.[6] Compared with conventional porous materials, such as zeolites or activated carbons, these coordination polymers have greater potential because of their fine tunable pore structures and adjustable chemical functionality.[7, 8] Separation of gas molecules by size exclusion effect can be achieved by deliberate control and tuning of small pores within porous MOFs. In this regard, the "pillaring" strategy is of particular interest and importance. Over the past several years, many groups[9-13] have focused on development, design, and synthesis of pillared frameworks for their functional properties and dynamic features. The designing of a pillared three-dimensional (3-D) MOF involves using an appropriate bridging linker to act as a pillar to connect with well-defined two-dimensional (2D) grid sheets formed from paddle wheel clusters $M_2(COO)_4$ (M = Cu^{2+}, Zn^{2+}, and Co^{2+}) as nodes and bicarboxylates or tetracarboxylate ligands (as shown in Figure 7.1). The pores within pillared 3D MOFs are predetermined by the different combinations of carboxylate ligands and pillar linkers. The pillared layer approach in combination with interpenetration strategy (as shown in Figure 7.1), can guide the realization of small micropores and help in tuning for use in highly selective separation and purification of

small molecules.[14] Furthermore, this approach enhances the stability of the ultimate framework and makes it easier to obtain the targeted product.[15]

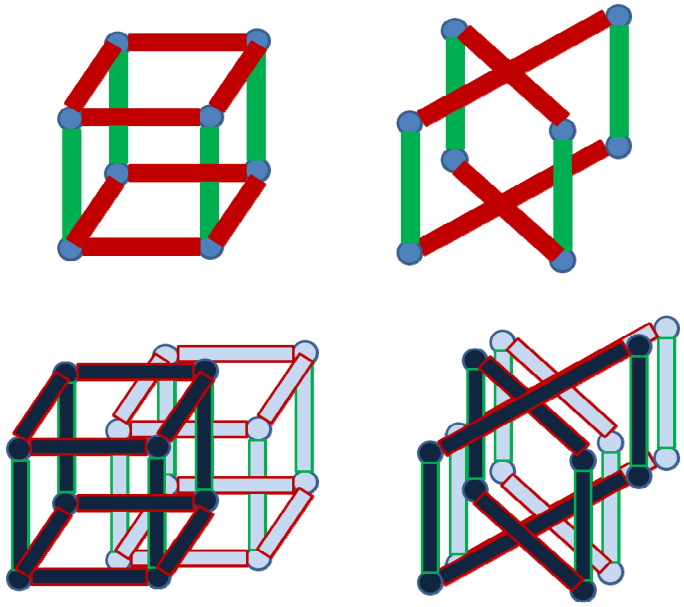

Figure 7.1 Cartoon representation of formation of pillared layer frameworks from bicarboxylate ligand (top left) and tetracarboxylate ligand (top right) pillared by dipyridyl strut (green). The blue corners are the cobalt or copper or zinc paddlewheel nodes. b) Interpenetrated pillared layer frameworks from bicarboxylate ligand (bottom left) and tetracarboxylate ligand (bottom right). Light blue and dark blue represents different frameworks.

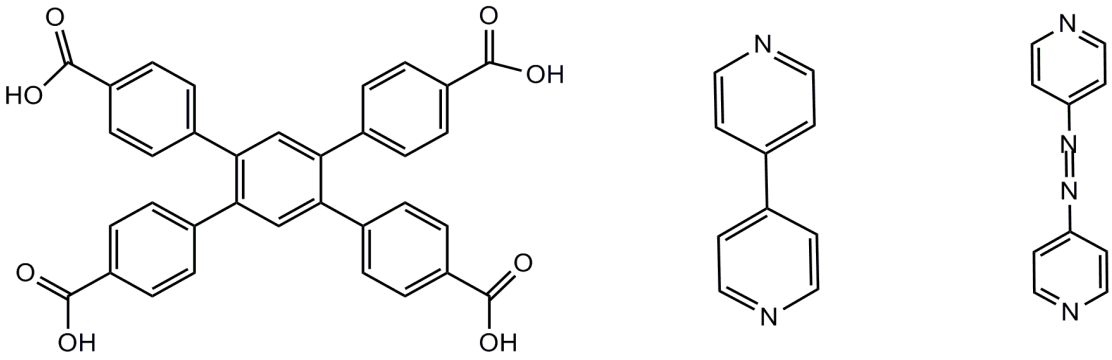

BTTB BPY AZPY

Figure 7.2 Organic struts employed in this work

In this work, we have chosen BTTB as carboxylate linker (4, 4', 4'', 4'''-benzene-1, 2, 4, 5-tetrayltetrabenzoic acid (BTTB)) and bipyridine (BPY) and azopyridine (AZPY) (shown in Figure 7.2) as pillars for the construction of paddle wheel type MOFs. We have chosen BTTB as the carboxylate linker due to the following reasons: a) they contain four potential metal binding sites, which can yield the formation of a MOF through multiple bonding interactions. b) its rigidness can enable the preparation of permanently porous materials and c) its long molecular structure can give rise to the formation of microporous coordination frameworks through framework interpenetration (d) there are only a few reports of MOFs[13, 16-18] containing this carboxylic acid. BPY and AZPY were chosen as pillars as they are widely used for the construction of pillared type of MOFs. They can act as a rigid pillared building block to form robust MOFs with metal ions and the axial nitrogen atoms can participate in coordination bonding and can play an important role in the assembly of MOFs. Furthermore, in the case of AZPY ligand, the free basic nitrogen centers might potentially serve as the primary adsorption sites.[19]

In this chapter, we report the synthesis, crystal structures and gas sorption properties of four pillared 3D MOFs (cobalt and zinc) constructed from BTTB as carboxylate linker and BPY and AZPY ligands as pillars. These MOFs are formulated as $\{[Co_2(BTTB).(BPY)].(H_2O)(DEF)_2\}_n$(**CoBTTBBPY**), $\{[Zn_2(BTTB).(BPY)].(DEF)_2\}_n$ (**ZnBTTBBPY**), $\{[Co_2(BTTB).(AZPY))].(DEF)_2\}_n$ (**CoBTTBAZPY**) and $\{[Zn_2(BTTB).(AZPY))].(DEF)_2\}_n$ (**ZnBTTBAZPY**). These MOFs have been determined by single crystal X-ray diffraction analyses and further characterized by PXRD, thermogravimetric analyses, and nitrogen adsorption at 77 K.

7.2 EXPERIMENTAL SECTION

7.2.1 Materials and methods

All commercially available chemicals and solvents are of reagent grade and were used as received without further purification. Thermogravimetric analyses (TGA) were carried out in the temperature range of 25-700 ˚C on a NETSZCH TG/Mass spectrometry analyzer under helium with a heating rate of 5 ˚C/min. Powder X-ray diffraction patterns (PXRD) were recorded on a X'Pert X-ray PANalytical diffractometer with an X'accelerator module using Cu Kα (λ = 1.5418 Å) radiation at room temperature, with a step size of 0.02˚ in 2θ. Nitrogen adsorption isotherms were measured at 77 K with an Autosorb 1-MP from Quantachrome Instruments. Carbon dioxide (CO_2), nitrogen (N_2), and methane (CH_4) sorption experiments at 298 K were carried out using a Intelligent Gravimetric Analyzer (IGA-1 series, Hiden Analytical Ltd). The as-synthesized samples (~ 50 mg) were placed in a sample pan and dried under high vacuum at 150 ˚C for 12 h to remove the solvated molecules prior to measurements.

Synthesis of complex CoBTTBBPY. A mixture of $Co(NO_3)_2.6H_2O$ (58.2 mg, 0.2 mmol), BTTB (55.8 mg, 0.1 mmol), and BPY (15.6 mg, 0.1 mmol) was dissolved in 5 mL of DEF/ethanol/water (2:2:1,v/v). Two drops of 1N HCl was added to the mixture, and the final mixture was placed in a Parr Teflon-lined stainless steel container under autogenous pressure and heated at 100 ˚C for 4 days. Large quantities of purple-block crystals were obtained. The crystals were filtered off, washed with mother liquid, and dried at ambient conditions. Elemental analysis (%) calcd : C 61.6 H 5.16 N 5.32 Found: C 61.99 H 5.07 N 5.19. Yield: 79 mg (75%, based on Co).

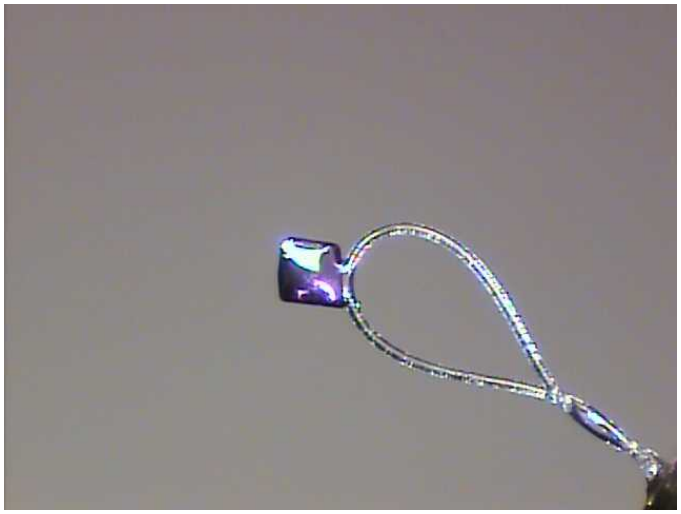

Figure 7.3 Photograph of single crystal of CoBTTBBPY (size (mm) – 0.1 x 0.12 x 0.08)

Synthesis of complex ZnBTTBBPY. A mixture of $Zn(NO_3)_2.6H_2O$ (59.4 mg, 0.2 mmol), BTTB (55.8 mg, 0.1 mmol), and BPY (15.6 mg, 0.1 mmol) was dissolved in 5 mL of DEF/ethanol/water (2:2:1,v/v). Two drops of 1N HCl was added to the mixture, and the final mixture was placed in a Parr Teflon-lined stainless steel container under autogenous pressure and heated at 100 ˚C for 4 days. Large quantities of colorless-block

crystals were obtained. The crystals were filtered off, washed with mother liquid, and dried at ambient conditions. Elemental analysis (%) calcd : C 61.42 H 5.72 N 5.31 Found: C 61.77 H 5.51 N 5.26. Yield: 79 mg (74.8%, based on Zn).

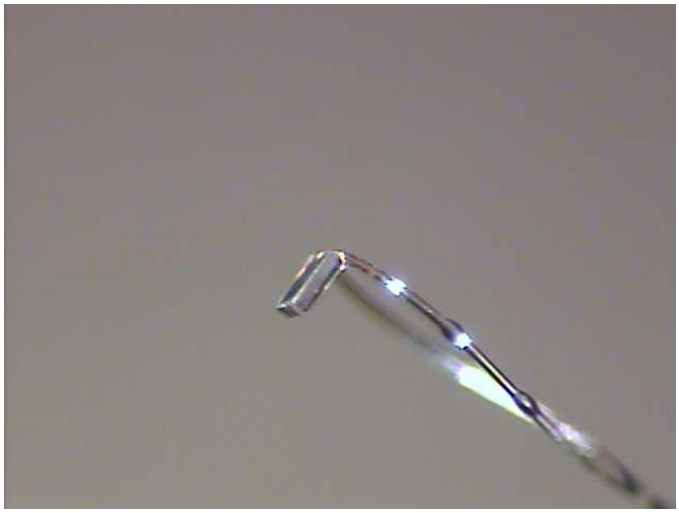

Figure 7.4 Photograph of single crystal of ZnBTTBBPY (size (mm) – 0.12 x 0.1 x 0.1)

Synthesis of complex CoBTTBAZPY. A mixture of $Co(NO_3)_2.6H_2O$ (43.6 mg, 0.2 mmol), BTTB (55.8 mg, 0.1 mmol), and AZPY (18.4 mg, 0.1 mmol) was dissolved in 5 mL of DEF/ethanol/water (2:2:1,v/v). Two drops of 1N HCl was added to the mixture, and the final mixture was placed in a Parr Teflon-lined stainless steel container under autogenous pressure and heated at 100 ˚C for 4 days. Large quantities of red plate crystals were obtained. The crystals were filtered off, washed with mother liquid, and dried at ambient conditions. Elemental analysis (%) calcd : C 61.34 H 5.04 N 7.80 Found: C 59.11 H 4.93 N 7.08. Yield: 82.7 mg (76.79 % based on Co)

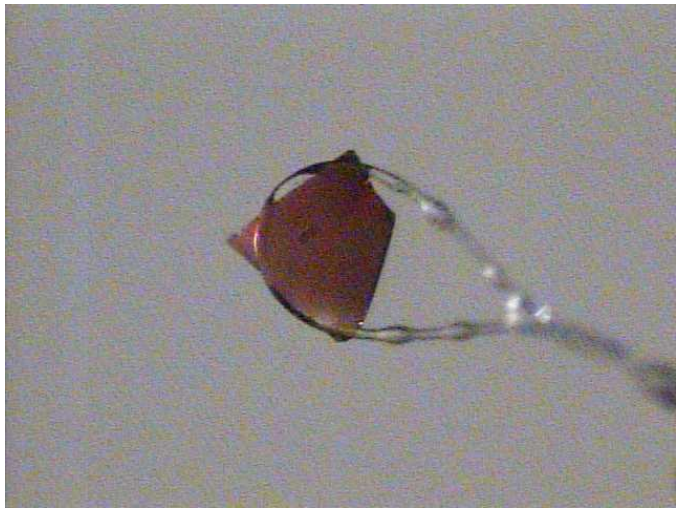

Figure 7.5 Photograph of single crystal of CoBTTBAZPY (size (mm) – 0.1 x 0.1 x 0.08)

Synthesis of complex ZnBTTBAZPY. A mixture of $Zn(NO_3)2.6H_2O$ (59.4 mg, 0.2 mmol), BTTB (55.8 mg, 0.1 mmol), and AZPY (18.4 mg, 0.1 mmol) was dissolved in 5 mL of DEF/ethanol/water (2:2:1,v/v). Two drops of 1N HCl was added to the mixture, and the final mixture was placed in a Parr Teflon-lined stainless steel container under autogenous pressure and heated at 100 ˚C for 4 days. Large quantities of orange plate crystals were obtained. The crystals were filtered off, washed with mother liquid, and dried at ambient conditions. Elemental analysis (%) calcd : C 60.61 H 4.99 N 7.71 Found: C 59.48 H 5.38 N 7.87. Yield: 83.4 mg (76.5 % based on Zn).

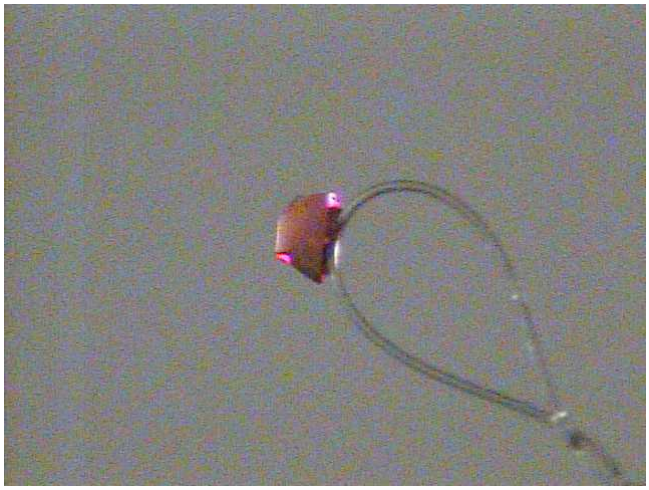

Figure 7.6 Photograph of single crystal of ZnBTTBAZPY (size (mm) – 0.05 x 0.32 x 0.36)

7.2.2 X-ray crystallography

All single crystal data were collected on a Bruker SMART APEX CCD sealed tube diffractometer by using Cu-*K*α radiation with a graphite monochromator. Crystals of the MOFs were mounted on nylon CryoLoops with Paratone-N. The structure was solved by direct methods and refined using the SHELXTL-97 software suite. Anisotropic thermal parameters were refined for all nonhydrogen atoms; hydrogen atoms were refined isotropically as riding atoms. Some of the hydrogen atoms could not be resolved, and thus were not included in the analysis. The guest molecules inside the pores could not be refined owing to severe disorder, as common to microporous MOFs. The final structural model was refined without the guest molecules by using the SQUEEZE option of PLATON.[20]

7.3 RESULTS AND DISCUSSION

7.3.1 Crystal structure description of ZnBTTBBPY and CoBTTBBPY

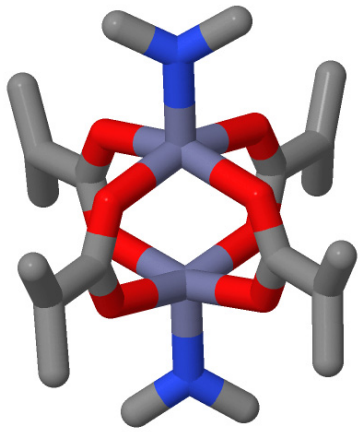

Figure 7.7 Paddlewheel cluster of ZnBTTBBPY, color scheme: Zn light blue; O red; C gray; N dark blue

The structures of both materials CoBTTBBPY and ZnBTTBBPY are identical, thus only ZnBTTBBPY structure will be described. Single-crystal X-ray structural analysis showed that compound ZnBTTBBPY crystallizes in the space group *Imma*. The asymmetric unit of ZnBTTBBPY contains a half of Zn(II) ion, a one-fourth of BTTB and a one-fourth of BPY. The Zn1 center is coordinated by four oxygen atoms from four different BTTB ligands and one nitrogen atom (N1) from one BPY ligand (Figure 7.7). Zn2 center coordination environment is similar to Zn1 center. The Zn(II) – Zn(II) distance is 2.727 Å and the average Zn-O_{BTTB} and Zn-N_{BPY} distances are 2.026 Å and 2.05 Å. The framework of ZnBTTBBPY reveals that the framework is composed of paddle-wheel binuclear Zn_2 units which are bridged by four BTTB ligands to form a 2D square grid $\{Zn_2(BTTB)_4\}$. The dihedral angles between the neighboring square units formed by the carboxylate carbon atoms of paddle-wheel SBUs are 93.32˚, 85.64˚, 86.92˚

and 93.32˚. The 2D square grids are further pillared by bipyridine occupying the axial sites of the Zn_2 paddle wheels to form 3D MOF. The overall structure consists of a pair of identical nets that are mutually interpenetrated with each other to form a 2-fold interpenetrated 3D framework (Figure 7.8)

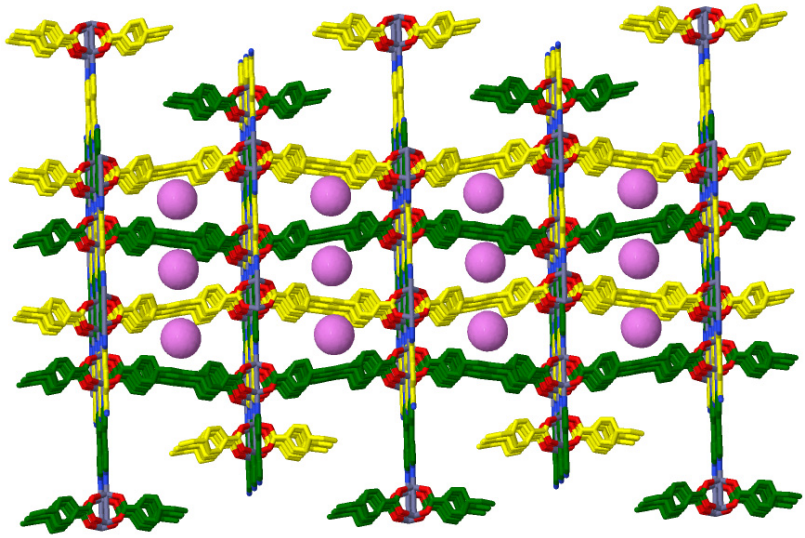

Figure 7.8 Two types of cavities in ZnBTTBBPY: (a) viewed down [0 1 0] direction, wireframe model view; (b) viewed down [0 1 0] direction, space filling model view; (c) viewed down [0 $\bar{1}$ 1] direction, wireframe model view; (d) viewed down [0 $\bar{1}$ 1] direction, space filling model view; Color scheme: Yellow and green colors represent different frameworks; Zn, light blue; C, grey; O, red; N dark blue. Guest molecules and hydrogen atoms are omitted for clarity

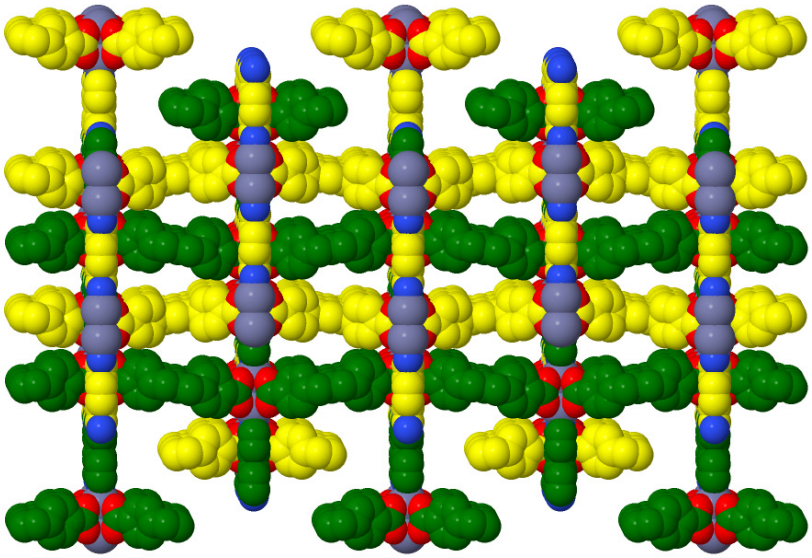

Figure 7.8 Continued

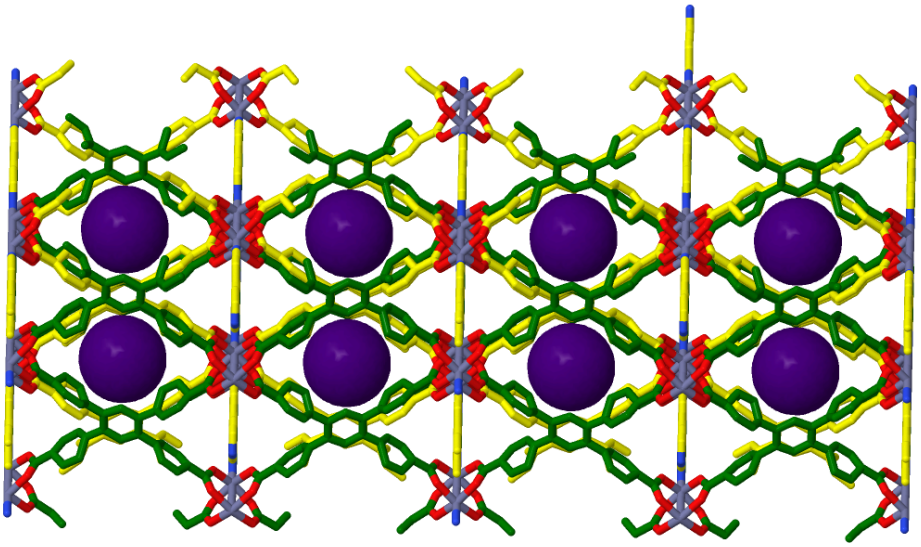

Figure 7.8 Continued

.

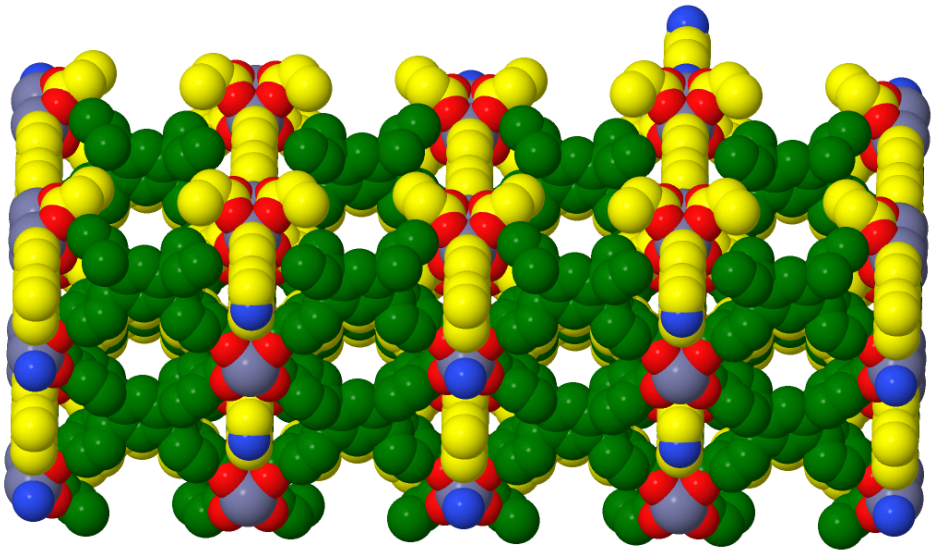

Figure 7.8 Continued

Framework ZnBTTBBPY is involved in face-to-face π-π interactions with those of adjacent interpenetrated net. The structure has open channels of 4.064 Å in [0 1 0] direction and 6.044 Å in [0 $\bar{1}$ 1] direction (Figure 7.8). The calculations using PLATON[20] suggest that 39.2 % void space of the total crystal volume after removal of guest molecules.

Previously, Hupp and co-workers reported porous MOF from zinc and organic building blocks BTTB and BPY but with a different solvent (DMF) and reaction temperature (80 ˚C). Despite the same reactants, the framework structure of the present compound 2 is completely different from this previous structure, indicating that the change of solvent

and temperature greatly affects the framework structure.[13] The compound described by Hupp and co-workers crystallizes in the *P21* phase and has cell parameters of 14.008 Å, 11.5210 Å, 15.701 Å, cell angles of 90˚, 90.679˚, 90˚ and cell volume of 2516.73 $Å^3$, while our compound ZnBTTBBPY crystallizes in *Imma* phase and has cell parameters of 30.9468 Å, 11.6254 Å, 13.9673 Å, cell angles of 90˚, 90˚, 90˚ and cell volume of 5025 $Å^3$.

7.3.2 Synthesis of complex CoBTTBAZPY and ZnBTTBAZPY

Single-crystal X-ray diffraction reveals that complexes CoBTTBAZPY and ZnBTTBAZPY are isostructural and both crystallize in the space group *P-1*. The following discussions on the structural aspects will mainly be focused on complex CoBTTBAZPY. The asymmetric unit of CoBTTBAZPY contains a two Co(II) ions, a one BTTB and one AZPY. In CoBTTBAZPY, a pair of Co(II) centers forms a $\{Co_2(O_2CR)_4\}$ paddlewheel SBU unit and nitrogen atoms of AZPY ligand are coordinated at the axial sites of the Co(II) ions (similar to Figure 7.7). The Co(II) – Co(II) distance is 2.739 Å and the average Co-O_{BTTB} and Co-N_{AZPY} distances are 2.017 Å and 2.046 Å. The dihedral angles between the neighboring square units formed by the carboxylate carbon atoms of paddle-wheel SBUs are 93.32˚, 85.64˚, 86.92˚ and 93.32˚ and thus paddle-wheel SBUs linked by AZPY construct a 3D framework. Because of the existence of large channels in CoBTTBAZPY, the final structure is a 2-fold interpenetrating framework. Two such porous nets interpenetrate each other, providing a 3D porous framework (Figure 7.9). Framework CoBTTBAZPY is involved in face-to-face π-π interactions with the adjacent interpenetrated net. The structure has open channels of 1 Å and 4.942 Å in [1 0 0] direction, 4.942 Å in [$\bar{1}$ 1 1] direction and 6.617 Å

in [1 0 1] direction (Figure 7.10). The calculations using PLATON[20] suggest that 39.4 % void space of the total crystal volume after removal of guest molecules.

Previously, Hupp and co-workers reported porous MOF from zinc and organic building blocks BTTB and AZPY but with a different solvent (DMF) and reaction temperature (80 ˚C). Despite the same reactants, the framework structure of the present compound ZnBTTBBAZPY is completely different from that of previously reported, indicating that the change of solvent and temperature greatly affects the framework structure.[13] The compound described by Hupp and co-workers crystallizes in the *Pmc21* phase and has cell parameters of 15.6540 Å, 15.9467 Å, 11.6268 Å, cell angles of 90˚, 90˚, 90˚ and cell volume of 2902.39 $Å^3$ while our compound ZnBTTBAZPY crystallizes in *P-1* phase and has cell parameters of 11.3501 Å, 15.5941 Å, 15.8560 Å, cell angles of 102.41˚, 105.03˚, 90.13˚ and cell volume of 2688.34 $Å^3$.

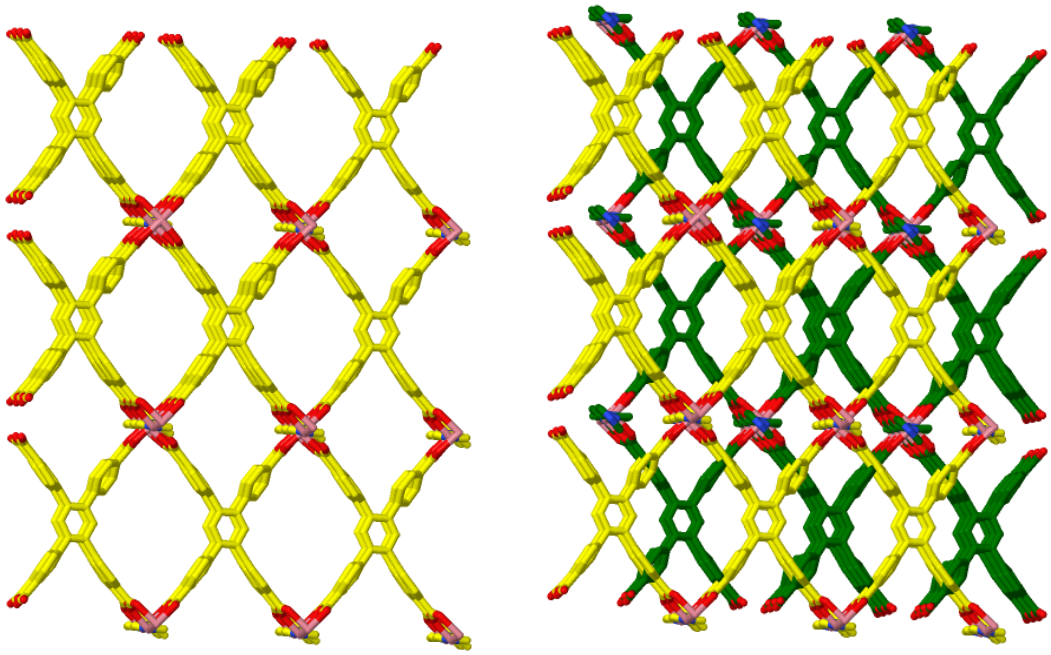

Figure 7.9 Perspective view of CoBTTBAZBPY displaying single 2D layer (left) and two fold interpenetration (right). Yellow and green colors represent different frameworks. Color scheme: Co, pink; O, red. Guest molecules and hydrogen atoms are omitted for clarity

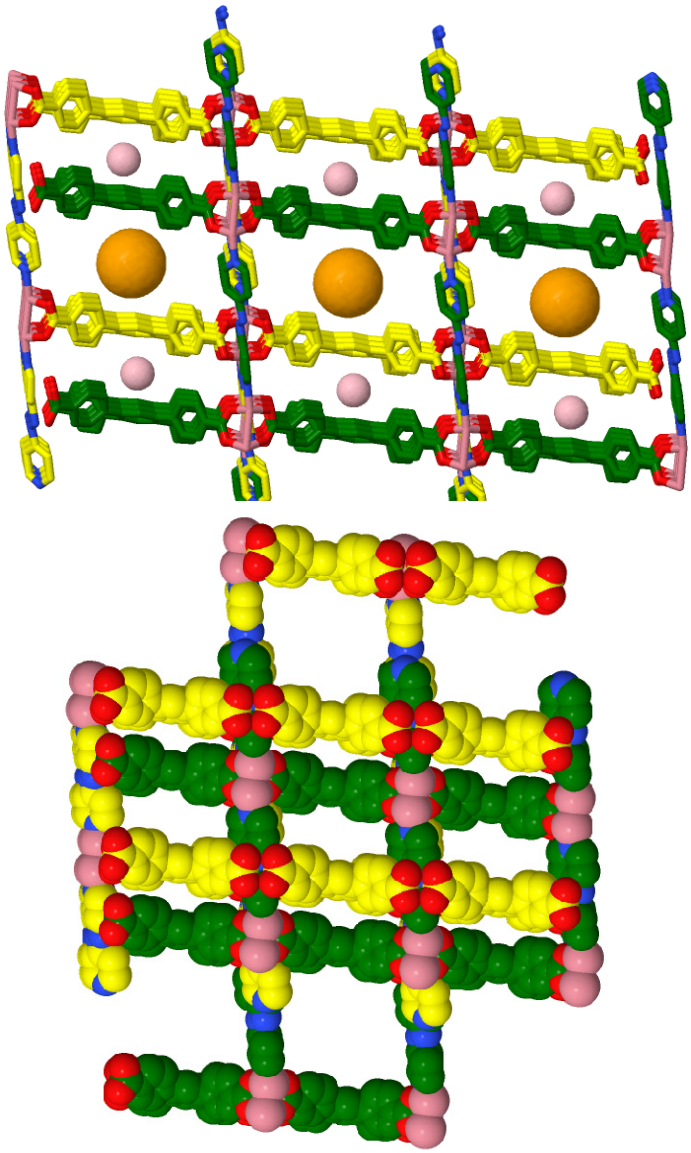

Figure 7.10 a) Perspective view of the 3D network of CoBTTBAZPY along the [1 0 0] direction b) along the [$\bar{1}$ 1 1] direction c) Space filling model view along [1 0 1] direction. Yellow and green colors represent different frameworks. Light pink, Orange and blue balls represent pore space. Color scheme: Co pink; C, grey; O, red; N, blue. Guest molecules and hydrogen atoms are omitted for clarity

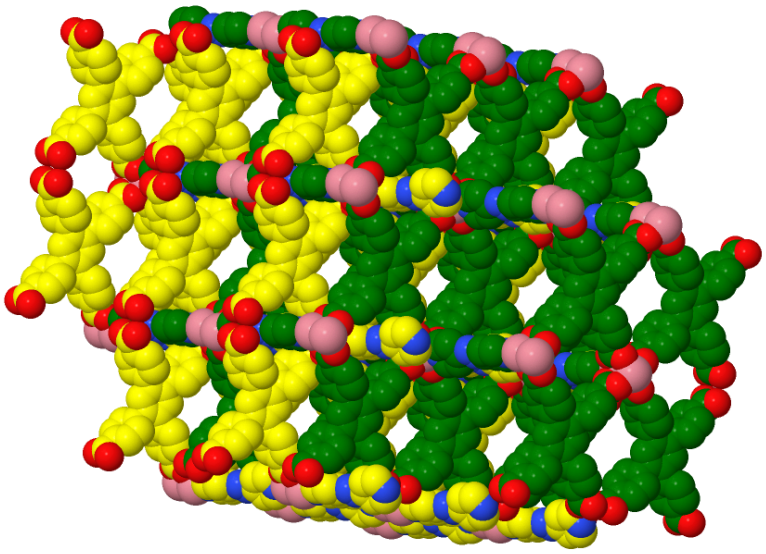

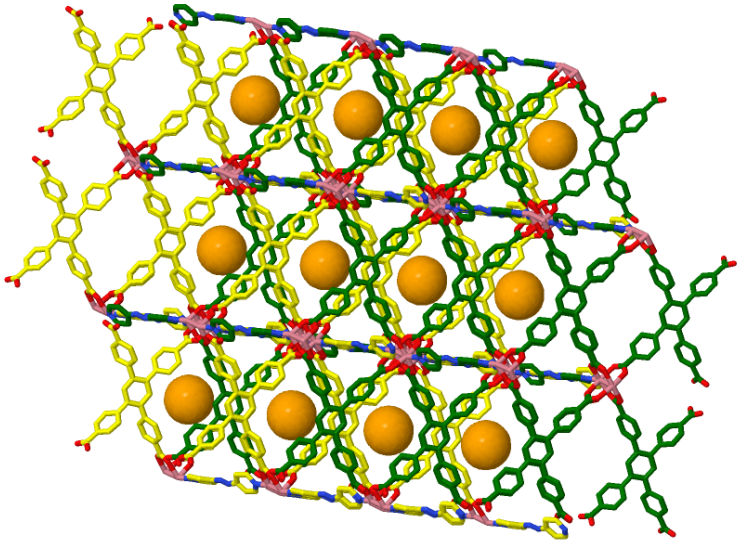

Figure 7.10 Continued

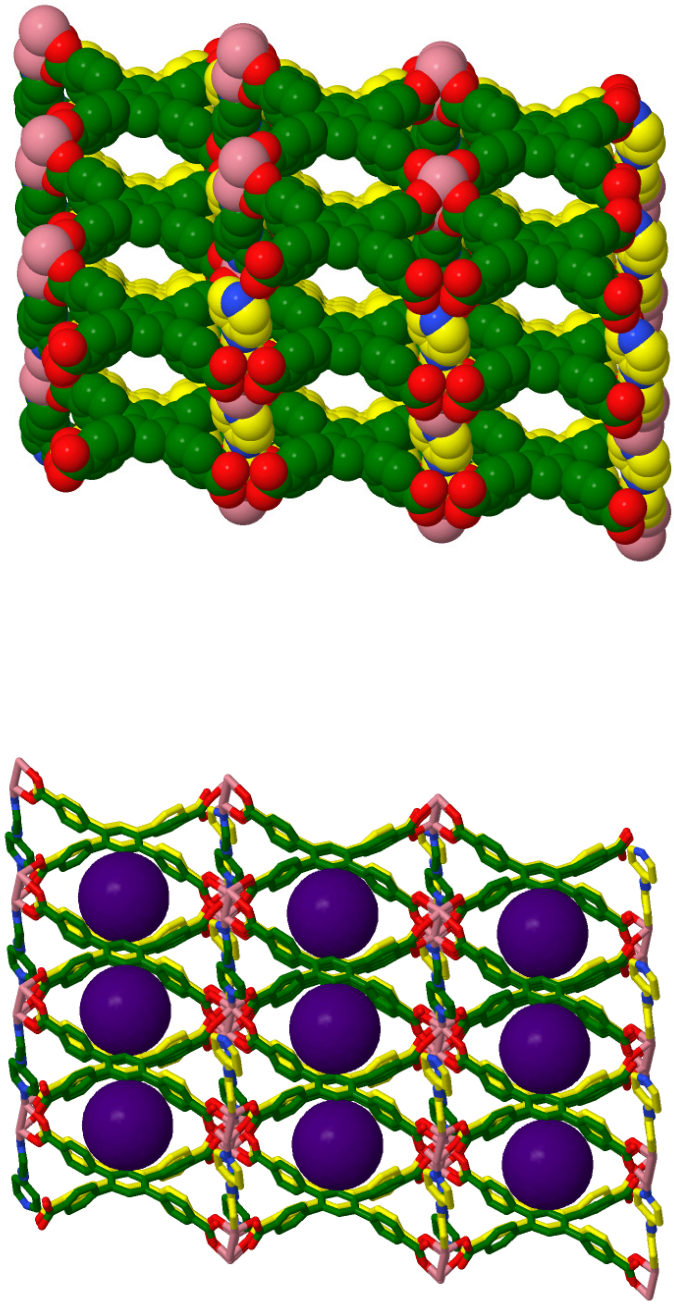

Figure 7.10 Continued

Table 7.1 Crystallographic data for CoBTTBBPY

Compound	CoBTTBBPY
Formula	$C_{22}H_{12}CoNO_4$
Fw	411.24
Crystal size(mm)	0.10 × 0.12 × 0.08
Space group	*Imma*
a(Å)	31.02(5)
b(Å)	11.74(2)
c(Å)	13.91(3)
$\alpha(^o)$	90
$\beta(^o)$	90
$\gamma(^o)$	90
$V(Å^3)$	5066(16)
Z	8
$\lambda(Cu\ K\alpha)$(Å)	1.5406
$D_c(g/cm^3)$	1.078
$\mu(mm^{-1})$	0.698
T(K)	173(2)
Total reflections	208073
Unique data collected	2494
Observed reflections	2159
*R*int	0.0639
parameters	150
R_1, *w*R(I > 2σ(I))[a]	0.1378 , 0.4237
R_1, *w*R(all data)[b]	0.1519, 0.4377
$w=1/\ [\sigma^2(F_0^2)+(aP)^2+bP]$	a= 0.2000,b= 0.0000
Goodness-of-fit-on F^2	2.122
$\Delta\rho_{min}$ and $\Delta\rho_{max}(e\ Å^{-3})$	-2.059, 6.463

[a] $R = \sum||F_0|-|F_c||)/\sum|F_0|$ [b] $wR = |\sum w(F_0-F_c)^2/\sum w(F_0^2)^2|^{1/2}$

Table 7.2 Crystallographic data for ZnBTTBBPY

Compound	ZnBTTBBPY
Formula	$C_{22}H_{12}NO_4Zn$
Fw	419.70
Crystal size(mm)	0.12 × 0.10 × 0.10
Space group	*Imma*
a(Å)	30.947(8)
b(Å)	11.625(3)
c(Å)	13.967(4)
α(°)	90
β(°)	90
γ(°)	90
V(Å^3)	5025(2)
Z	8
λ(*Cu K*α)(Å)	1.5406
D_c(g/cm^3)	1.110
μ(mm^{-1})	0.998
T(K)	296(2)
Total reflections	46289
Unique data collected	3691
Observed reflections	3135
*R*int	0.0726
parameters	139
R_1, *w*R(I > 2σ(I))[a]	0.1467 , 0.4539
R_1, *w*R(all data)[b]	0.1618 , 0.4681
w=1/〔$\sigma^2(F_0^2)$+$(aP)^2$+bP〕	a= 0.2000,b= 0.0000
Goodness-of-fit-on F^2	2.198
$\Delta\rho_{min}$ and $\Delta\rho_{max}$(e Å^{-3})	-2.142, 4.794

[a] $R = \sum||F_0|-|F_c||/\sum|F_0|$ [b] $wR = |\sum w(F_0-F_c)^2/\sum w(F_0^2)^2|^{1/2}$

Table 7.3 Crystallographic data for CoBTTBAZPY

Compound	CoBTTBAZPY
Formula	$C_{44}H_{26}Co_2N_4O_8$
Fw	856.55
Crystal size(mm)	0.10 × 0.10 × 0.08
Space group	*P-1*
a(Å)	11.3737(15)
b(Å)	15.705(2)
c(Å)	15.742(2)
α(°)	103.207(2)
β(°)	105.386(2)
γ(°)	90.300(2)
V(Å^3)	2632.9(6)
Z	2
λ(*Cu K*α)(Å)	1.5406
D_c(g/cm^3)	1.080
μ(mm^{-1})	0.675
T(K)	173(2)
Total reflections	53396
Unique data collected	15909
Observed reflections	9350
*R*int	0.0637
parameters	523
R_1, *w*R(I > 2σ(I))[a]	0.0691, 0.1921
R_1, *w*R(all data)[b]	0.1016, 0.2059
$w=1/〔\sigma^2(F_0^2)+(aP)^2+bP〕$	a= 0.1583,b= 0.6508
Goodness-of-fit-on F^2	1.103
$\Delta\rho_{min}$ and $\Delta\rho_{max}$(e Å^{-3})	-2.296, 2.433

[a] $R = \sum||F_0|-|F_c||)/\sum|F_0|$ [b] $wR = |\sum w(F_0-F_c)^2/\sum w(F_0^2)^2|^{1/2}$

7.3.3 Surface area, Bulk Phase Purity and Thermal properties

Table 7.4 Properties of pillared type MOFs synthesized in this work

MOF	Pore size (Å)	Pore volume (cm^3/g)	BET surface area (m^2/g)	Activation process (under vacuum)	Thermal stability	Features	Predicted accessible surface area (m^2/g)
ZnBTTBBPY	4.064	0.38	841	Chloroform Exchange and 120 ° C (12h)	350 °C	2-D pore system, interpenetrated	1660
CoBTTBAZPY	4.942	0.389	805	Chloroform Exchange and 120 ° C (12h)	300 °C	3-D pore system, interpenetrated	2038
ZnBTTBAZPY	4.942	0.357	647	Chloroform Exchange and 120 ° C (12h)	300 °C	3-D pore system, interpenetrated	-
CoBTTBBPY	4.064	0.396	843	Chloroform Exchange and 120 ° C (12h)	400 °C	2-D pore system, interpenetrated	-

After the synthesis, all MOFs synthesized in this work were solvent exchanged with chloroform and activated at 120 °C overnight under vacuum. BET surface areas were measured after each activation process. The properties of MOFs synthesized in this work along with the BET surface areas and predicted accessible surface areas[21] are shown in Table 7.4. The experimental BET surface areas are only half of that calculated geometrically from the perfect crystal structure with nitrogen molecule as a probe[21]. This discrepancy can be attributed to the crystal defects present in the experimental samples. The presence of trapped solvent molecules in the crystals can be ruled out here as theromogravimetric measurements showed complete removal of solvent molecules.

The N_2 adsorption/desorption isotherms measured at 77 K for compounds CoBTTBBPY, ZnBTTBBPY, CoBTTBAZPY and ZnBTTBAZPY reveals typical type-I behavior, as

expected for microporous materials. Fitting the Brunauer-Emmett-Teller (BET) equation to their respective N_2 adsorption isotherms within the range $0.007<P/P_0<0.03$ gives an estimated surface area of 843 m^2/g for CoBTTBBPY, 841 m^2/g for ZnBTTBBPY, 805 m^2/g for CoBTTBAZPY and 647 m^2/g for ZnBTTBAZPY. The Dubinin-Astakhov (DA) equation gives an estimated pore volume of 0.396 cm^3/g for CoBTTBBPY, 0.38 cm^3/g for ZnBTTBBPY, 0.389 cm^3/g for CoBTTBAZPY and 0.357 cm^3/g for ZnBTTBAZPY.

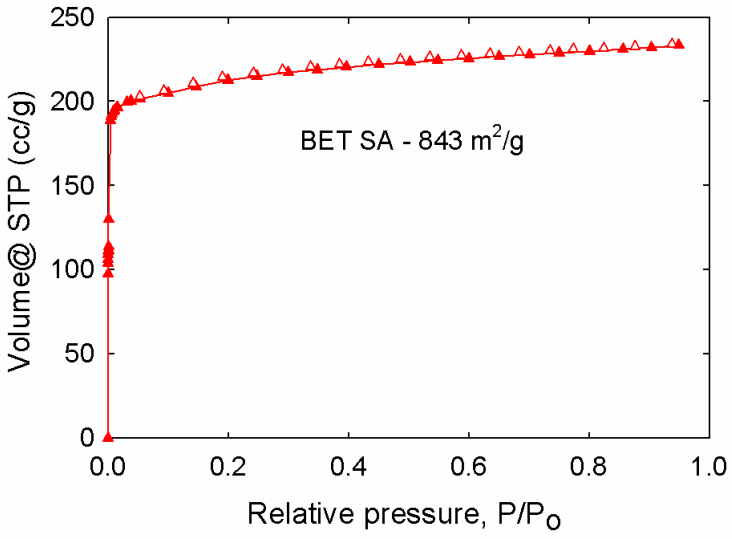

Figure 7.11 Nitrogen isotherm of activated CoBTTBBPY at 77 K (closed symbols – adsorption, open symbols – desorption)

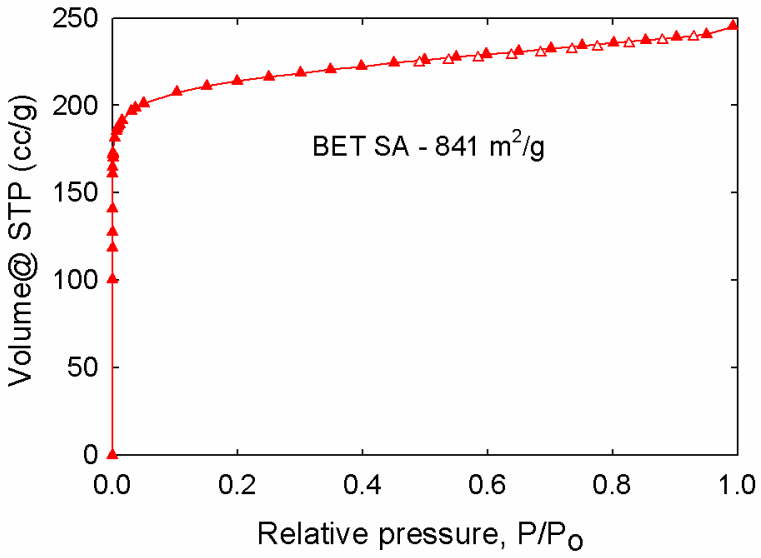

Figure 7.12 Nitrogen isotherm of activated ZnBTTBBPY at 77 K (closed symbols – adsorption, open symbols – desorption)

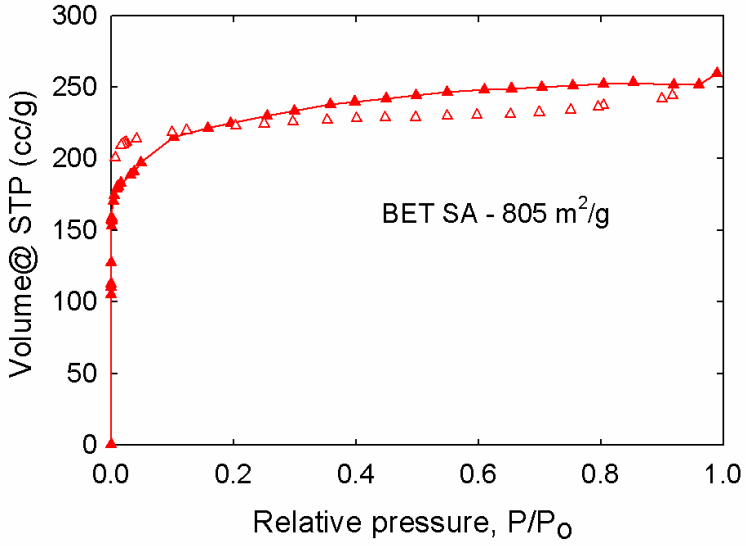

Figure 7.13 Nitrogen isotherm of activated CoBTTBAZPY at 77 K (closed symbols – adsorption, open symbols – desorption)

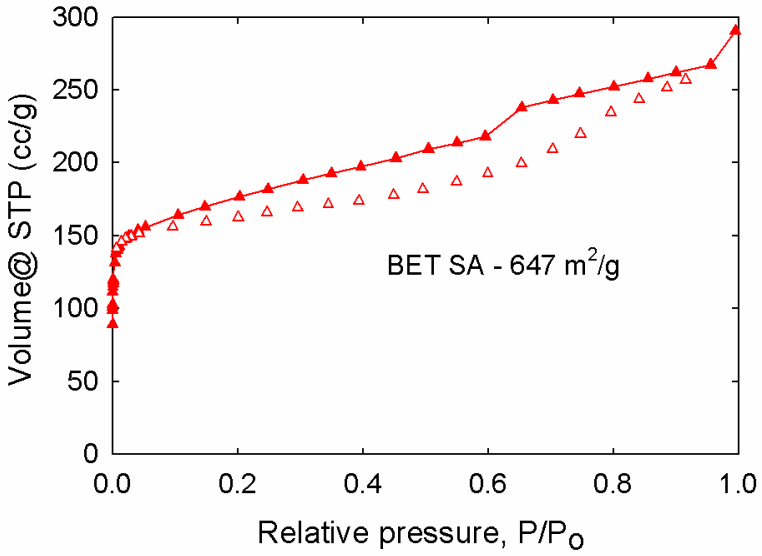

Figure 7.14 Nitrogen isotherm of activated ZnBTTBAZPY at 77 K (closed symbols – adsorption, open symbols – desorption)

In order to confirm the phase purity of the bulk materials ZnBTTBBPY, CoBTTBBPY, ZnBTTBAZPY, and CoBTTBAZPY, PXRD experiments were carried out. The PXRD experimental and simulated patterns for each MOF are shown in Figures 7.15 - 7.20. Note that, single-crystal X-ray data for ZnBTTBAZPY was not obtained. Therefore, their experimental PXRD patterns were compared to the simulated patterns of CoBTTBAZPY. Figure 7.15 shows that CoBTTBBPY and ZnBTTBBPY are isostructural while Figure 7.18 shows that CoBTTBAZPY and ZnBTTBAZPY are isostructural. Figures 7.16 and 7.17 show that the as-synthesized and activated frameworks of ZnBTTBBPY and CoBTTBBPY have PXRD patterns that are coincident with the corresponding patterns simulated from single-crystal XRD structures. Figure

7.19 shows that all the peaks of activated ZnBTTBAZPY matches well with the corresponding patterns simulated from single-crystal XRD structure of CoBTTBAZPY, while for the as-synthesized sample of ZnBTTBAZPY and the activated, chloroform exchanged and the as-synthesized samples of CoBTTBAZPY (as seen in Figure 7.20), only the major peaks of their PXRD patterns match well with that of simulated pattern. The minor peaks at 10˚, 11˚, however do not appear in their PXRD patterns. All compounds CoBTTBBPY, ZnBTTBBPY, CoBTTBAZPY and ZnBTTBAZPY are stable in air and insoluble in water, and most of the common organic solvents such as chloroform, methanol, acetone, toluene, and dimethyl formamide.

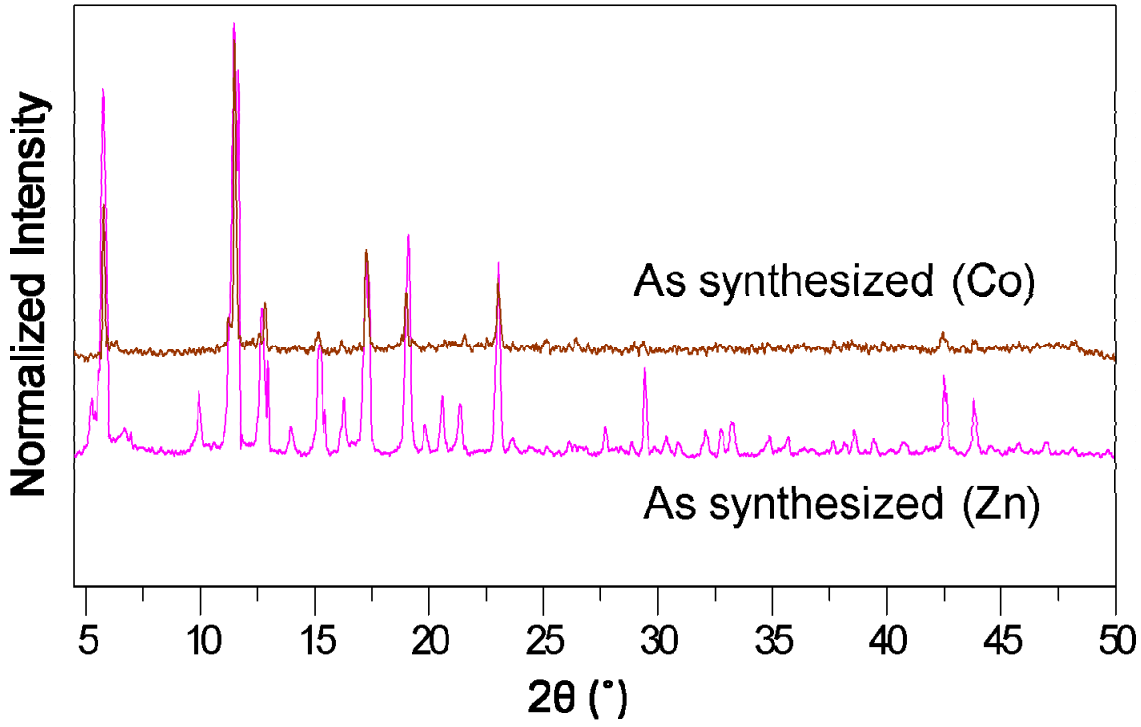

Figure 7.15 As synthesized powder X-ray diffraction patterns of CoBTTBBPY and ZnBTTBBPY

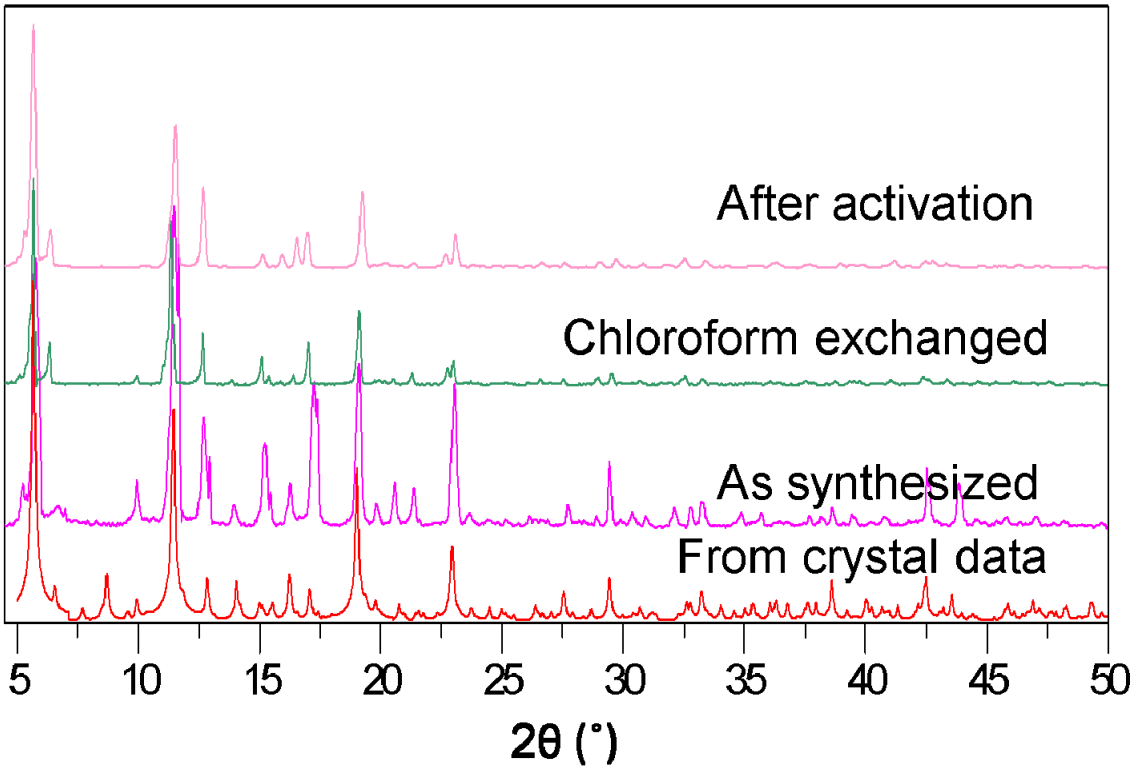

Figure 7.16 Simulated, as synthesized, chloroform exchange and activated powder X-ray diffraction patterns of ZnBTTBBPY

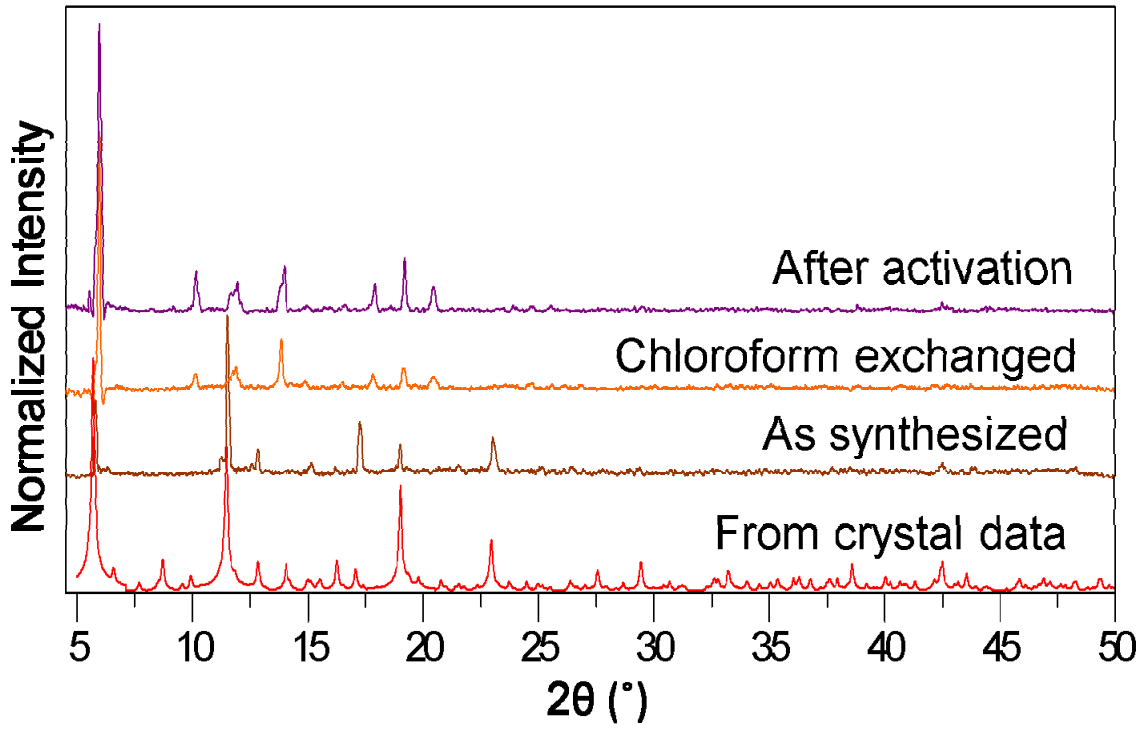

Figure 7.17 Simulated, as synthesized, chloroform exchange and activated powder X-ray diffraction patterns of CoBTTBBPY

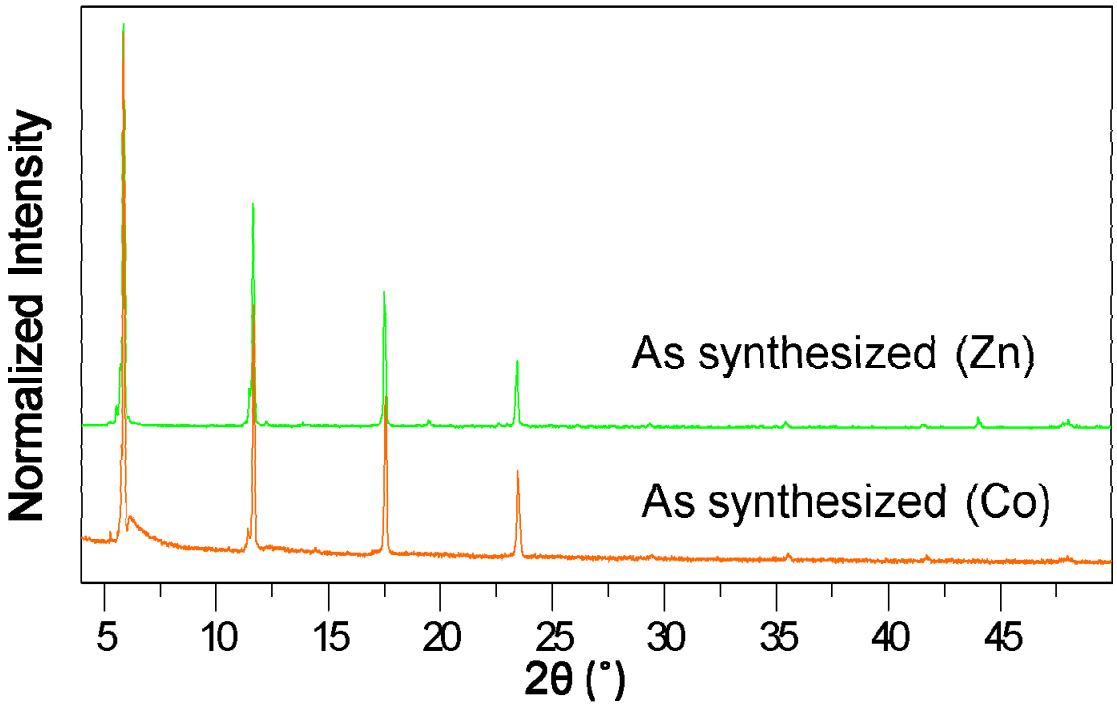

Figure 7.18 As synthesized powder X-ray diffraction patterns of CoBTTBAZPY and ZnBTTBAZPY

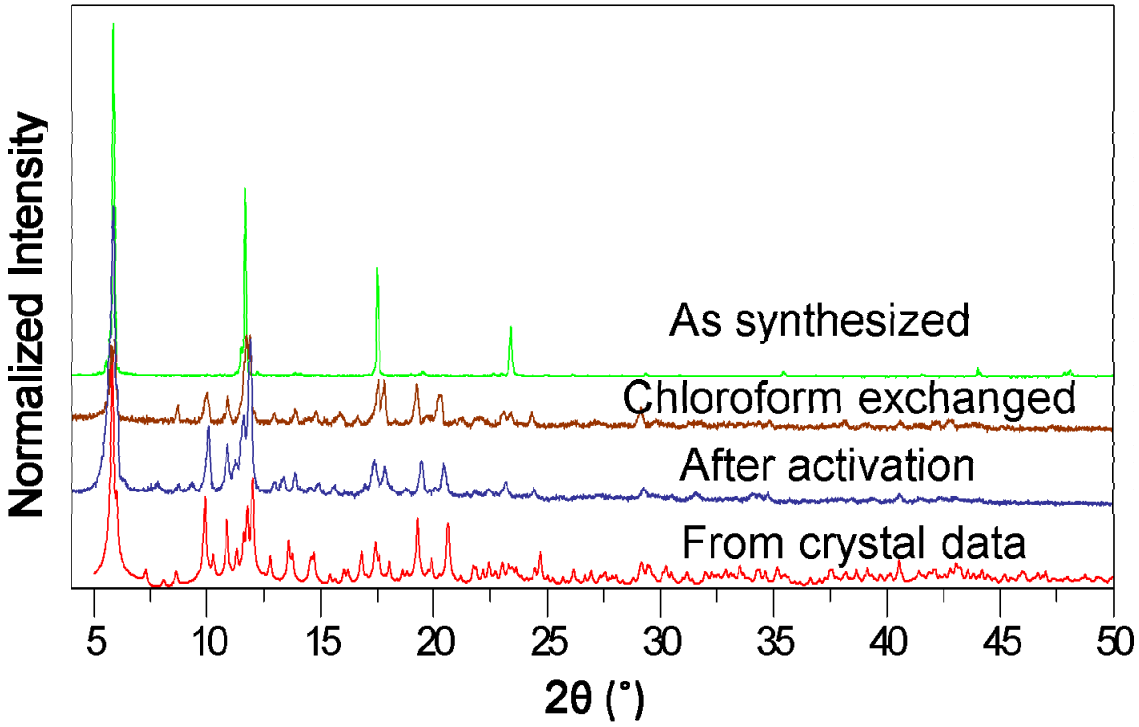

Figure 7.19 Simulated, as synthesized, chloroform exchange, and activated powder X-ray diffraction patterns of ZnBTTBAZPY

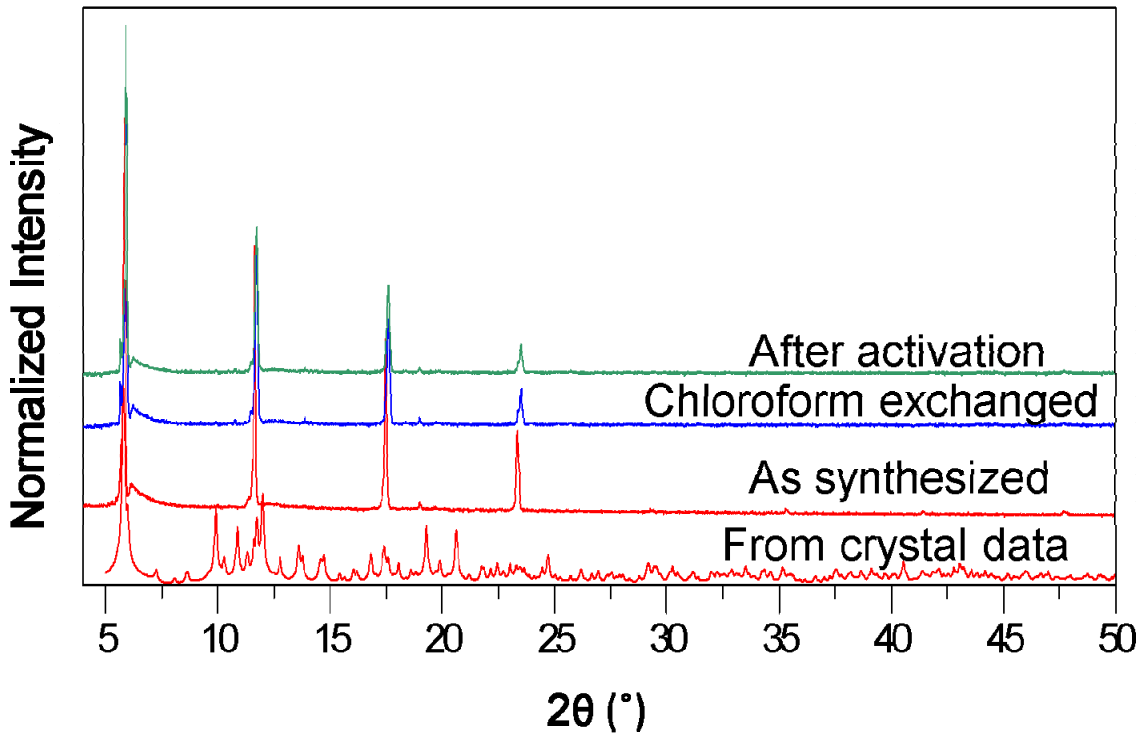

Figure 7.20 Simulated, as-synthesized, chloroform exchanged and activated powder X-ray diffraction patterns of CoBTTBAZPY

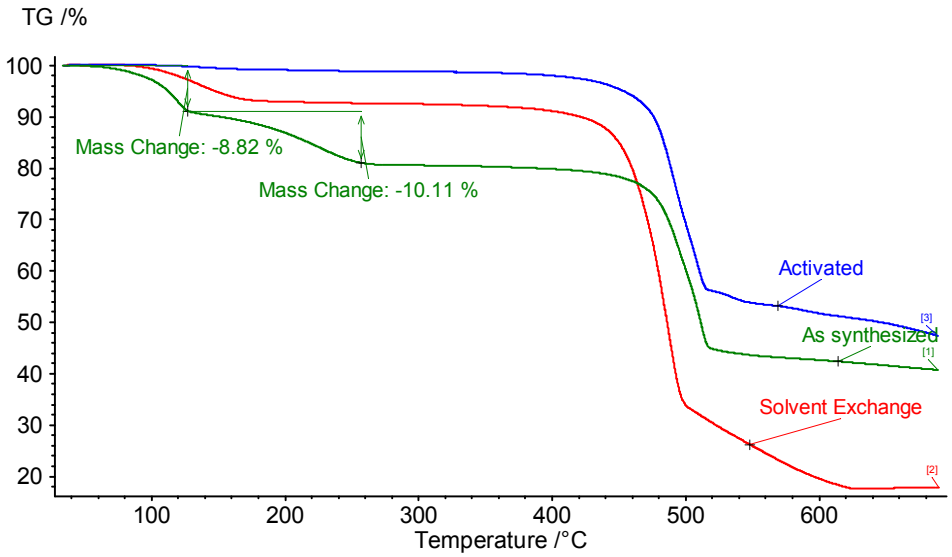

Figure 7.21 TGA trace of CoBTTBBPY

Thermogravimetric data of all MOFs synthesized in this work are shown in Figures 7.21 – 7.24. CoBTTBBPY displays a thermal stability of ~ 450 ˚C (shown in Figure 7.21). A two step steady weight loss of ~ 18%, corresponding to removal of uncoordinated solvent molecules is seen between room temperature and 250 ˚C and a rapid weight loss beyond 500 ˚C suggests the framework breakdown due to the decomposition of BTTB ligand. Guest molecules were solvent exchanged with chloroform and removal of guest molecules in CoBTTBBPY was done at 120 ˚C for 12 hr under vacuum and this was confirmed from the thermogravimetric data and PXRD data of activated sample of CoBTTBBPY.

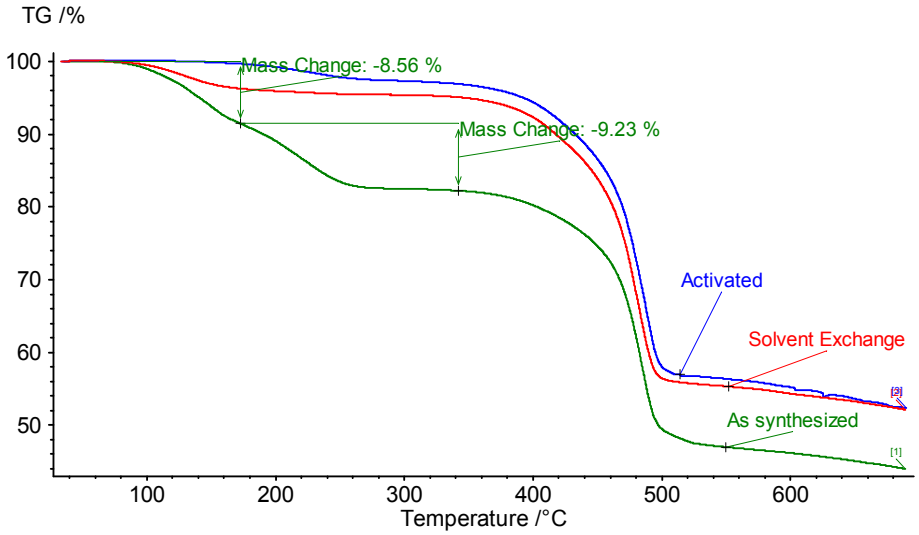

Figure 7.22 TGA trace of ZnBTTBBPY

The TGA curve of ZnBTTBBPY (Figure 7.22) shows that initial weight loss begins at 100 ˚C and continues till 250 ˚C and then reaches a plateau. The total weight loss over this range is ~18 % which corresponds to loss of most of the coordinated and uncoordinated solvent molecules. This compound has a thermal stability of 350 ˚C. Beyond this temperature, it undergoes a rapid weight loss that can be attributed to the decomposition of organic linkers. Removal of guest molecules from ZnBTTBBPY was done with chloroform exchange and activation at 120 ˚C for 12 hrs under vacuum and this was confirmed from the thermogravimetric data and PXRD data of activated sample of ZnBTTBBPY.

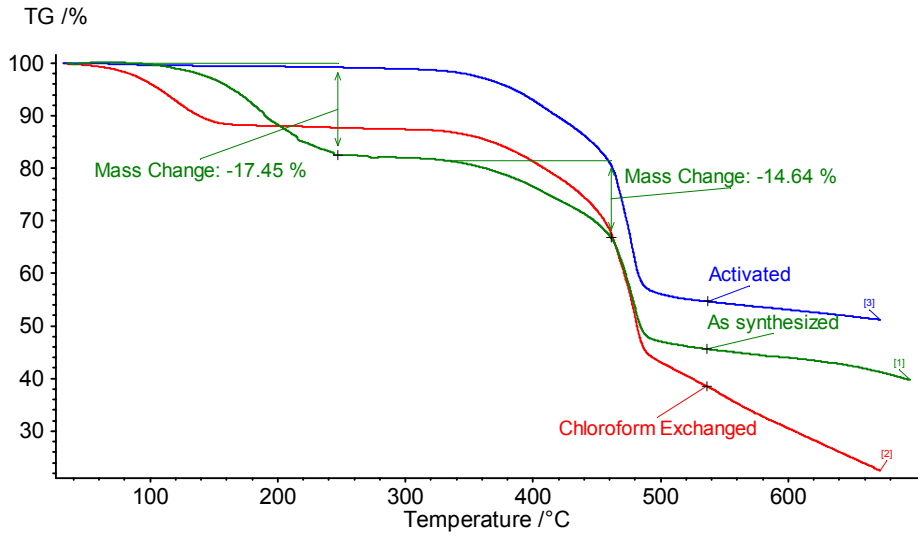

Figure 7.23 TGA trace of CoBTTBAZPY

CoBTTBAZPY undergoes a steady weight loss of ~ 18 % of uncoordinated solvent molecules from 120 ˚C to 250 ˚C and reaches a small region of plateau from 250 to 300 ˚C (as shown in Figure 7.23). Removal of guest molecules from CoBTTBAZPY was done with chloroform exchange and activation at 120 ˚C for 12 hr under vacuum and this was confirmed from the thermogravimetric data and PXRD data of activated sample of CoBTTBAZPY.

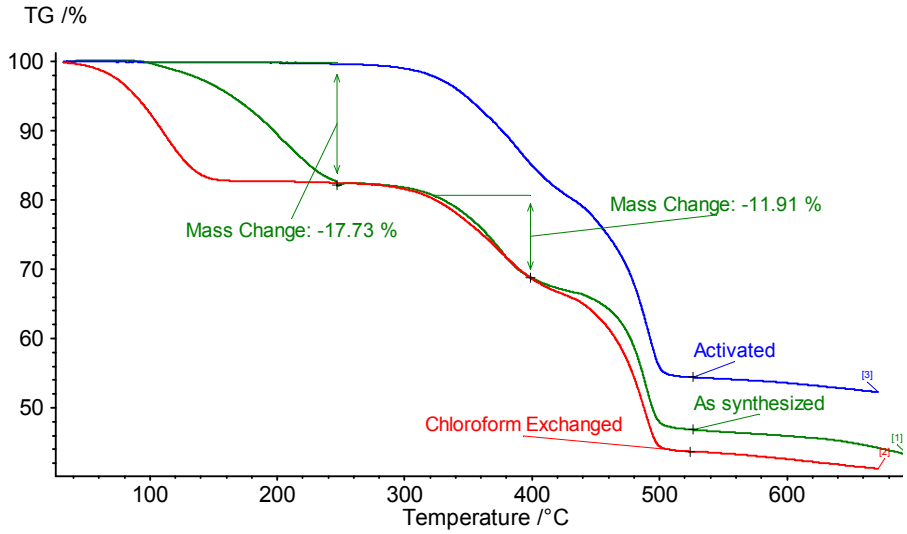

Figure 7.24 TGA trace of ZnBTTBAZPY

ZnBTTBAZPY undergoes a steady weight loss of ~ 18 %, from 120 to 250 ˚C and then reaches a small region of plateau and beyond 325 ˚C, a rapid weight loss occurs (as shown in Figure 7.24). The weight loss of ~ 18 % corresponds to removal of uncoordinated solvent molecules. Removal of guest molecules from ZnBTTBAZPY was done with chloroform exchange and activation at 120 ˚C for 12 hr under vacuum and this was confirmed from the thermogravimetric data and PXRD data of activated sample of ZnBTTBAZPY.

7.4 CONCLUSIONS

Four new pillared layer MOFs, CoBTTBBPY, ZnBTTBBPY, CoBTTBAZPY and ZnBTTBAZPY were synthesized by solvothermal technique using a tetracarboxylate building block 4,4′,4″,4‴-benzene-1,2,4,5-tetrayltetrabenzoic acid (BTTB) in combination with different metal salts and co-ligands bipyridine (BPY) and azopyridine (AZPY). CoBTTBBPY and ZnBTTBBPY were found to be isostructural with each other and CoBTTBAZPY and ZnBTTBAZPY were found to be isostructural with each other. All pillared layer MOFs demonstrated high surface areas, good thermal stability and permanent porosity.

7.5 REFERENCES

(1) Li, J. R.; Kuppler, R. J.; Zhou, H. C. *Chem. Soc. Rev.* **2009**, *38*, 1477.

(2) Lee, J.; Farha, O. K.; Roberts, J.; Scheidt, K. A.; Nguyen, S. T.; Hupp, J. T. *Chem. Soc. Rev.* **2009**, *38*, 1450.

(3) Corma, A.; Garcia, H.; Xamena, F. X. L. *Chem. Rev* **2010**, *110*, 4606.

(4) Hinks, N. J.; McKinlay, A. C.; Xiao, B.; Wheatley, P. S.; Morris, R. E. *Microporous Mesoporous Mater.* **2010**, *129*, 330.

(5) Keskin, S.; Kizilel, S. *Ind. Eng. Chem. Res* **2011**, *50*, 1799.

(6) Kuppler, R. J.; Timmons, D. J.; Fang , Q. R.; Li, J. R.; Makal, T. A.; Young, M. D.; Yuan, D. Q.; Zhao, D.; Zhuang, W. J.; Zhou, H. C. *Coordination Chemistry Reviews* **2009**, *253*, 3042.

(7) Eddaoudi, M.; Kim, J.; Rosi, N.; Vodak, D.; Wachter, J.; O'Keeffe, M.; Yaghi, O. M. *Science* **2002**, *295*, 469.

(8) Banerjee, R.; Furukawa, H.; Britt, D.; Knobler, C.; O'Keeffe, M.; Yaghi, O. M. *J. Am. Chem. Soc.* **2009**, *131*, 3875.

(9) Chen, B.; Ma, S.; Zapata, F.; Fronczek, F. R.; Lobkovsky, E. B.; Zhou, H. *Inorg. Chem.* **2007**, *46*, 1233-1236.

(10) Kitagawa, S.; Kitaura, R.; Noro, S. *Angew. Chem. Int. Ed.* **2004**, *43*, 2334.

(11) Xue, M.; Zhu, G. S.; Zhang, Y. J.; Fang, Q. R.; Hewitt, I. J.; Qiu, S. L. *Crystal Growth & Design* **2008**, *8*, 427.

(12) Dybtsev, D. N.; Chun, H.; Kim, K. *Angew. Chem. , Int. Ed.* **2004**, *43*, 5033.

(13) Farha, O. K.; Malliakas, C. D.; Kanatzidis, M. G.; Hupp, J. T. *J. Am. Chem. Soc.* **2010**, *132*, 950.

(14) Chen, B. L.; Ma, S. Q.; Zapata, F.; Fronczek, F. R.; Lobkovsky, E. B.; Zhou, H. C. *Inorg. Chem.* **2007**, *46*, 1233.

(15) Du, X. D.; Xiao, H. P.; Zhou, X. H.; Wu, T.; You, X. Z. *Journal of Solid State Chemistry* **2010**, *183*, 1464.

(16) Mulfort, K. L.; Farha, O. K.; Malliakas, C. D.; Kanatzidis, M. G.; Hupp, J. T. *Chem. Eur. J.* **2010**, *16*, 276.

(17) Bae, Y. S.; Farha, O. K.; Hupp, J. T.; Snurr, R. Q. *J. Mater. Chem* **2009**, *19*, 2131.

(18) Gadzikwa, T.; Farha, O. K.; Mulfort, K. L.; Hupp, J. T.; Nguyen, S. T. *chem. commun* **2009**, *25*, 3720.

(19) Zelenak, V.; Vargova, Z.; Almasi, M.; Zelenakova, A.; Kuchar, J. *Microporous Mesoporous Mater.* **2010**, *129*, 354.

(20) Spek, A.L. **2005**, PLATON, A Multipurpose Crystallographic Tool, Utrecht University, Utrecht, The Netherlands.

(21) Duren, T.; Millange, F.; Frey, G.; Walton, K. S.; Snurr, R. Q. *J. Phys. Chem. C* **2007**, *111*, 15350.

CHAPTER 8

SEPARATION OF CARBON DIOXIDE MIXTURES USING BTTB BASED FRAMEWORKS

In Chapter 6 and 7, we described the synthesis and crystal structures of BTTB based MOFs: CdBTTB, MgBTTB, NiBTTB, ZnBTTB, ZnBTTBBDC, CoBTTBBPY, ZnBTTBBPY, CoBTTBAZPY and ZnBTTBAZPY. In this chapter, we describe the adsorption of CO_2, CH_4, and N_2 as single components and as binary mixture, in these BTTB based MOFs. A systematic study of adsorption for these MOFs should provide insight into the importance of their structural properties (pore size, surface area, pore volume, open metal sites) on adsorption separations of CO_2/CH_4 and CO_2/N_2. The activation procedure for the MOFs considered in this chapter is presented in Table 8.1. Adsorption data for MOFs CdBTTB, MgBTTB, ZnBTTB and ZnBTTBBDC should be interpreted cautiously as their experimental BET surface areas are much smaller than that of predicted accessible surface areas[1]. Activation was done near their decomposition temperatures for a short period of time for these samples to get larger surface areas. However, it is quite possible that the some of the pores of these samples could have partially collapsed or may have defects or trapped residual solvent molecules present in the samples. Note that MgBTTB showed negligible uptake of nitrogen at 77 K but the same sample does adsorb CO_2, CH_4 and N_2 at room temperature. Solvent molecules were not completely removed for this material at 120 ˚C, although it was activated for 12 hrs under vacuum and therefore, these solvent molecules might have clogged some of the pores or might have partially blocked the larger pores, rendering this MOF very small

pores, closer to the kinetic diameter of nitrogen (~ 3.64 Å). For tightly constricted pores, it is possible that nitrogen molecules cannot overcome the diffusional resistances to fill the pores at 77 K, whereas at 298 K, diffusion occurs readily due to the additional thermal energy. Similar behavior has observed in other studies.[2-6]

Table 8.1 Activation procedure, BET surface areas and predicted accessible surface areas of BTTB MOFs

MOF	BET surface area (m^2/g)	Predicted accessible surface area (m^2/g)	Activation process (under vacuum)
CdBTTB	415	2180	300 ˚ C (1h)
MgBTTB	0	2437	120 ˚ C (12h)
ZnBTTB	447	1371	250 ˚ C (2h)
ZnBTTBBDC	441	1114	250 ˚ C (1h)
NiBTTB	391	442	Chloroform Exchange and 120 ˚ C (12h)
ZnBTTBBPY	841	1660	Chloroform Exchange and 120 ˚ C (12h)
CoBTTBBPY	843	-	Chloroform Exchange and 120 ˚ C (12h)
ZnBTTBAZPY	647	-	Chloroform Exchange and 120 ˚ C (12h)
CoBTTBAZPY	805	2038	Chloroform Exchange and 120 ˚ C (12h)

8.1 PURE GAS ADSORPTION ISOTHERMS

Adsorption isotherms of all BTTB based MOFs are shown in Figures 8.1-8.6 for low pressures as well as up to a pressure of 2 MPa. All the isotherms for CO_2 and CH_4 show type I behavior with the exception of CO_2 isotherm for MgBTTB. As expected, all MOFs studied here have a higher adsorption preference for CO_2 over the other two sorbates at all pressures. All the isotherms are reversible. CO_2 is more strongly adsorbed than CH_4 and N_2 for two reasons. First, CO_2 has a significant quadrupole moment, and nitrogen has a weaker quadrupole moment, whereas CH_4 is nonpolar. Second, the temperature of 298 K considered here is subcritical for CO_2 (T_C = 304.4 K), that is, CO_2 is more condensable than CH_4 and N_2 at 298 K.[7]

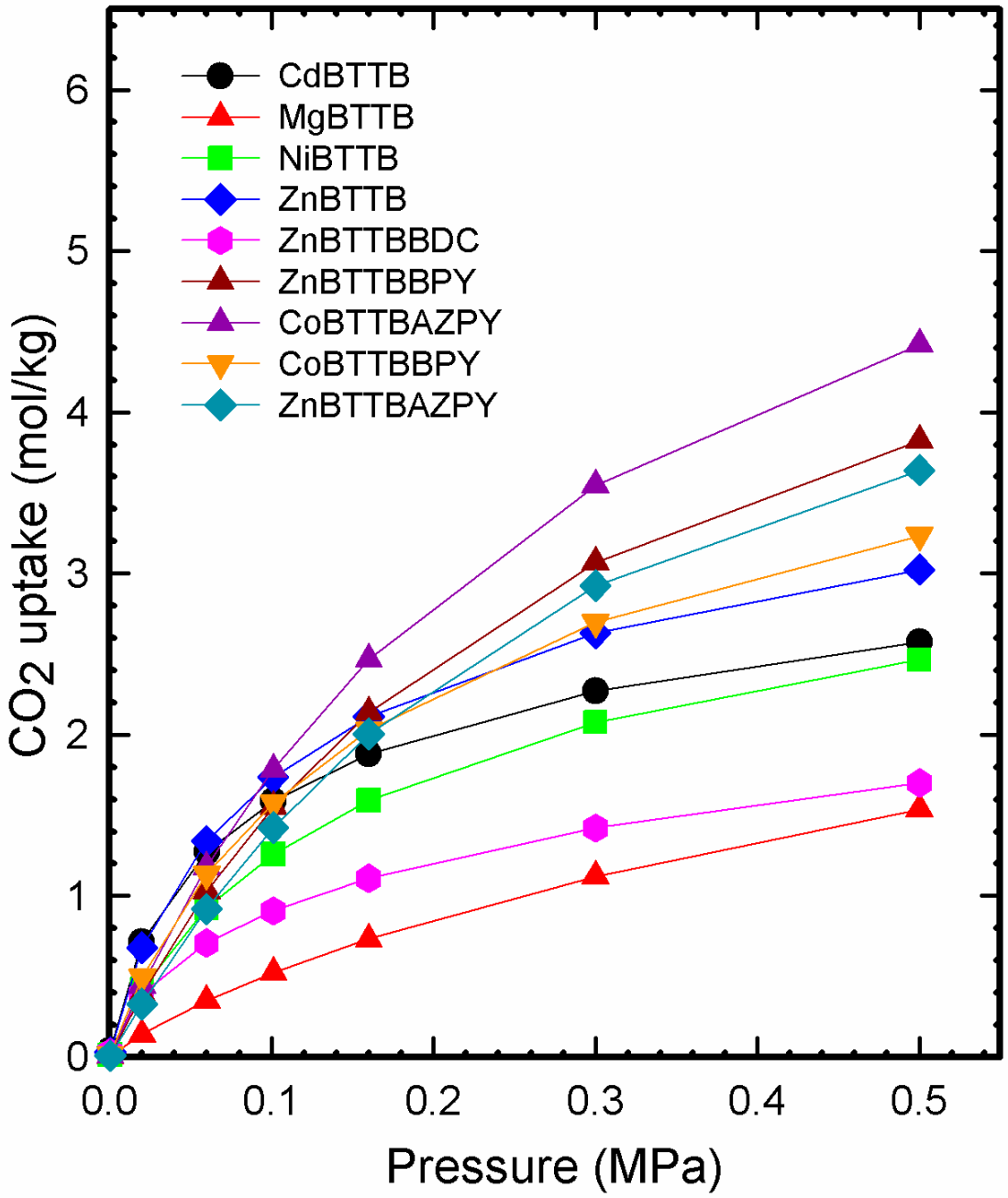

Figure 8.1 CO_2 sorption isotherms for desolvated compounds at 298K in the lower pressure region

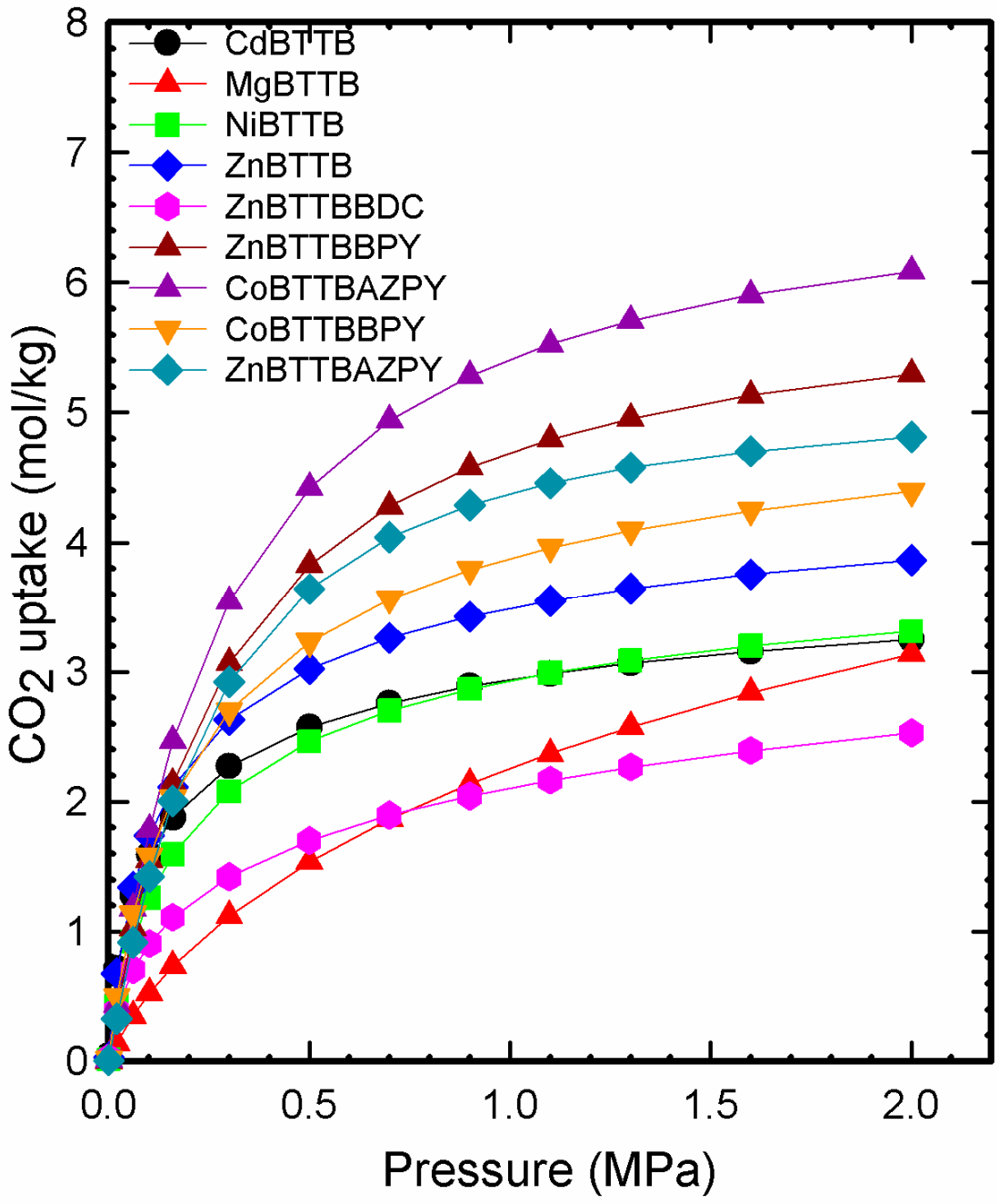

Figure 8.2 CO_2 sorption isotherms for desolvated compounds at 298K

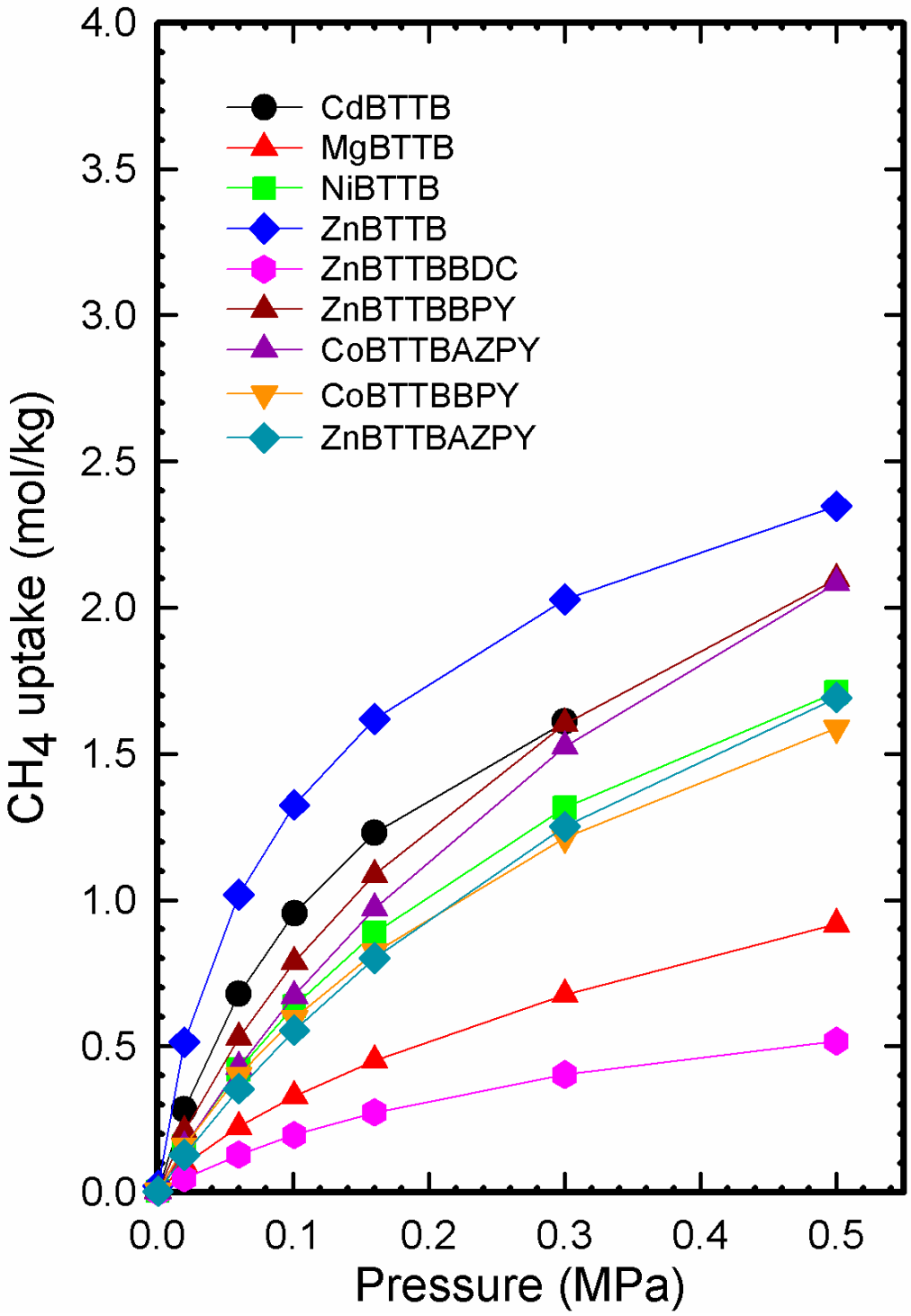

Figure 8.3 CH_4 sorption isotherms for desolvated compounds at 298K in the lower pressure region

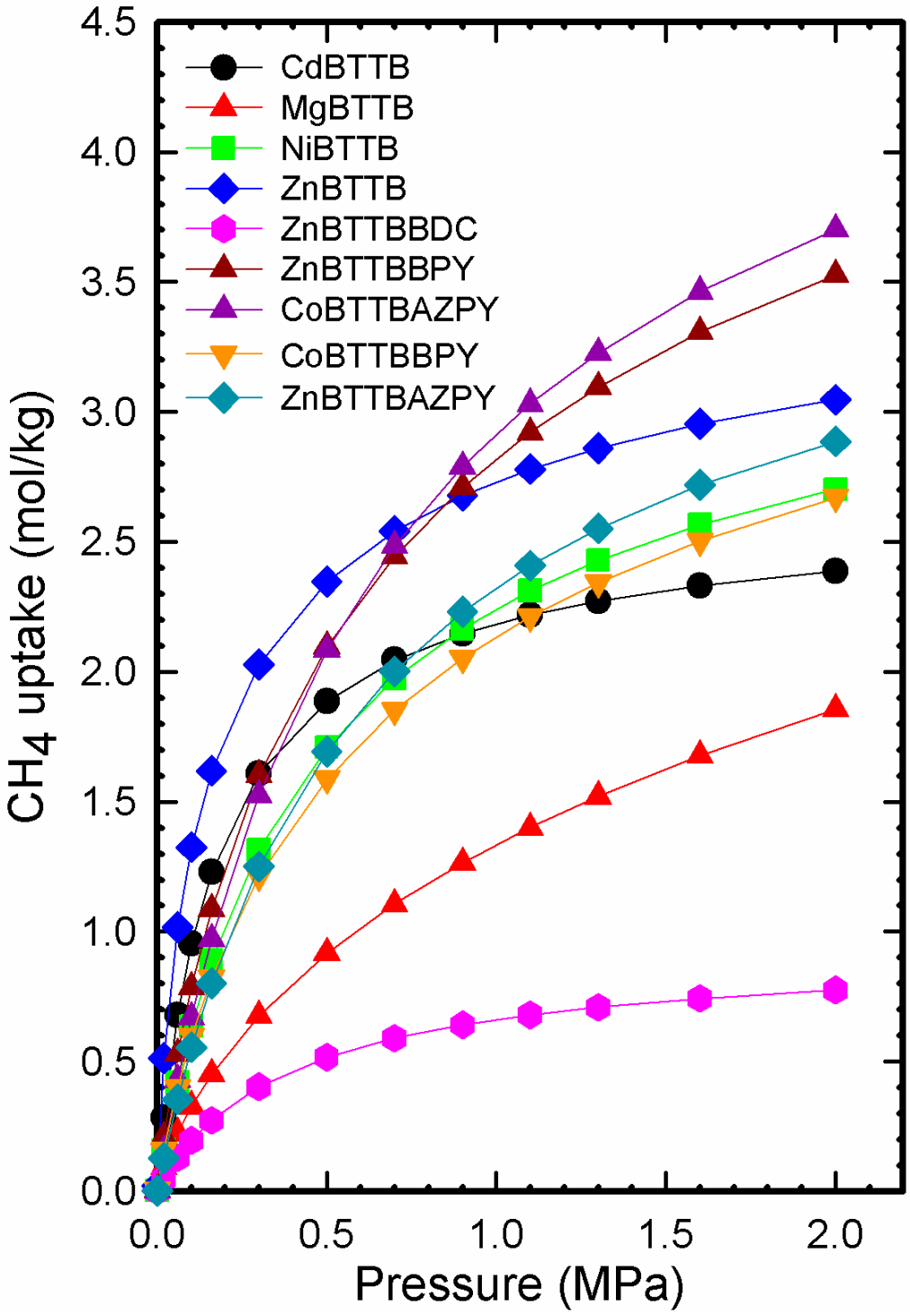

Figure 8.4 CH_4 sorption isotherms for desolvated compounds at 298K

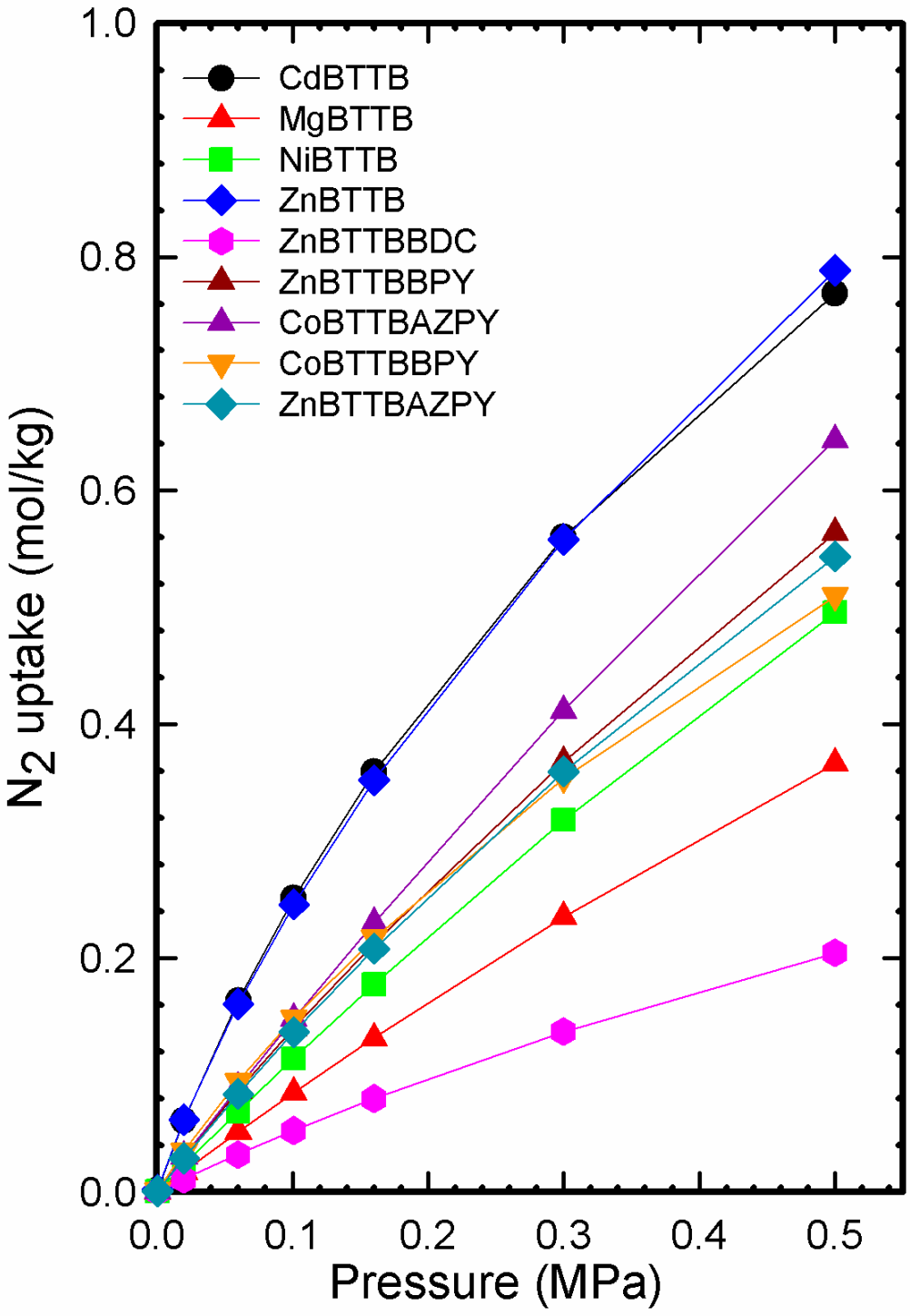

Figure 8.5 N_2 sorption isotherms for desolvated compounds at 298K in the lower pressure region

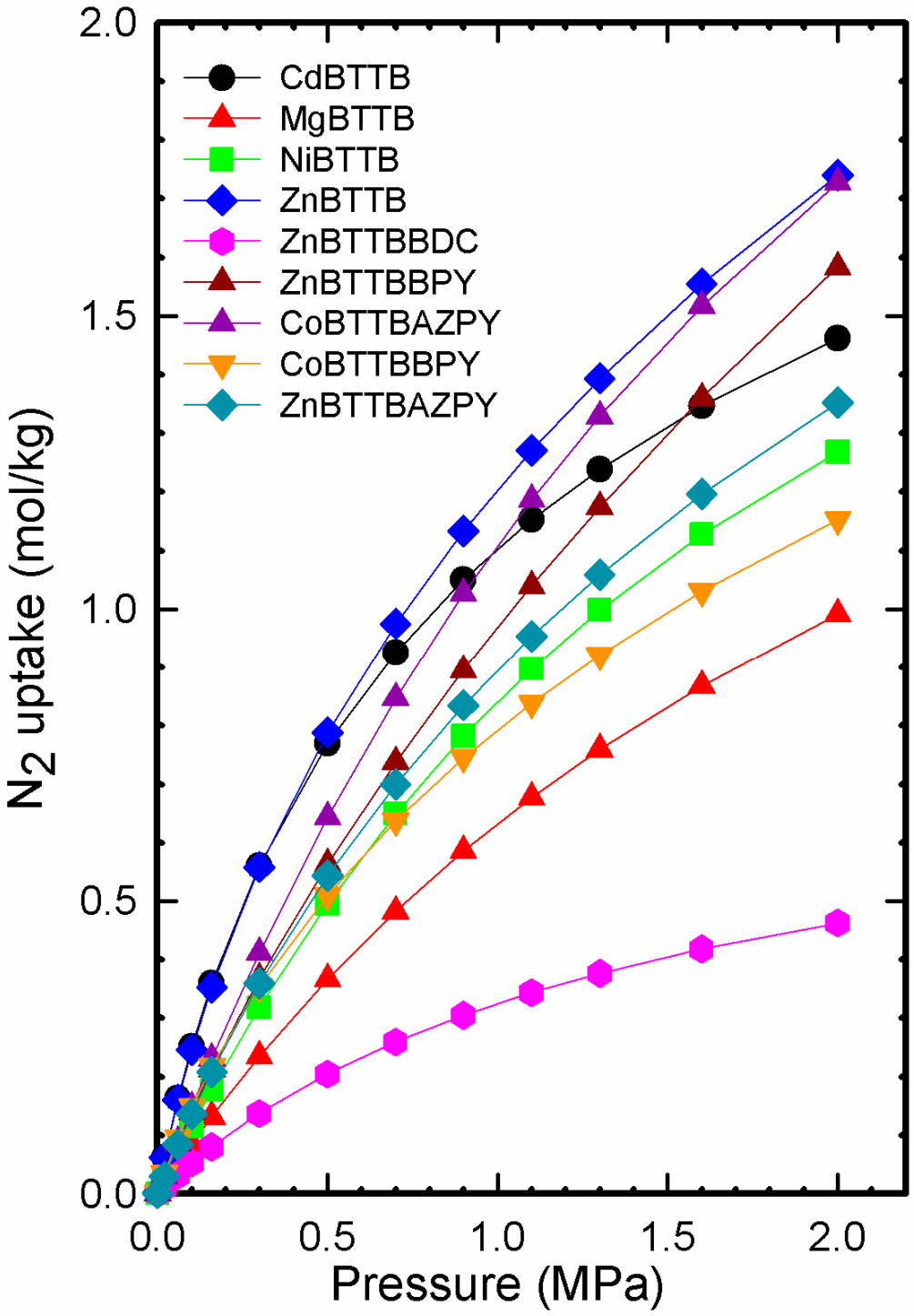

Figure 8.6 N_2 sorption isotherms for desolvated compounds at 298K

The Toth equation was used to model the adsorption isotherms as it provided the best fit for the experimental gas adsorption data for all the MOFs studied here. The Toth equation is given by[8]

$$N = N_s \frac{bP}{[1 + (bP)^t]^{1/t}}$$

where N is the adsorption loading, N_s is the saturation or maximum loading, t is a parameter that is usually less than 1. The more the parameter t deviates from unity, the more the heterogeneous is the system. The parameters b and t are specific for adsorbate-adsorbent pairs. The optimal parameters from the fitting of the Toth equation with the experimental data are tabulated in Table 8.2.

Table 8.2 Optimal parameters for the Toth equation in fitting experimental data on all MOFs

	CO_2			CH_4			N_2		
Adsorbents	N_s (mol/kg)	b (kPa^{-1})	t	N_s (mol/kg)	b (kPa^{-1})	t	N_s (mol/kg)	b (kPa^{-1})	t
CdBTTB	4.186	0.0234	0.5133	2.672	0.0063	0.8876	2.7581	0.0012	0.6773
MgBTTB	11.204	0.0009	0.4509	8.8909	0.0009	0.3745	2.2946	0.0004	1
NiBTTB	4.1762	0.0073	0.6665	3.6322	0.0024	0.8194	2.2532	0.0005	1.1755
ZnBTTB	4.7821	0.0129	0.6087	3.8696	0.0122	0.59	7.1994	0.0005	0.4741
ZnBTTBBDC	5.9918	0.0172	0.322	0.959	0.0027	0.9105	0.8254	0.0007	0.9618
CoBTTBBPY	5.4668	0.006	0.7168	4.3193	0.022	0.6629	3.6377	0.0005	0.5847
ZnBTTBBPY	6.0717	0.0034	1.003	5.7204	0.0022	0.6608	11.18	0.0001	0.5625
CoBTTBAZPY	6.9198	0.0034	1.0269	5.441	0.0015	0.0083	3.7236	0.0004	1.0504
ZnBTTBAZPY	5.2015	0.0033	1.2276	3.9517	0.0017	0.9055	3.348	0.0004	0.0132

Henry's constants were computed for each sorbate for all MOFs and are shown in Table 8.3. These values provide information on the strength of interaction between the molecule and the surface. At lower pressures up to 25 kpa, adsorption capacities of CO_2 follows the order of decreasing Henry's constant with ZnBTTBBDC~CdBTTB>ZnBTTB> CoBTTBBPY~NiBTTB>ZnBTTBBPY> CoBTTBAZPY> ZnBTTBAZPY>MgBTTB.

Table 8.3 Henrys constants for CO_2, CH_4 and N_2 and selectivity for CO_2 at low coverage

MOF	Pore size (Å)	Pore Volume (cm^3/g)	Features	Henry's constants (mol/kg.kPa)			Selectivity at low coverage	
				CO_2	CH_4	N_2	CO_2/CH_4	CO_2/N_2
CoBTTBBPY	4.064	0.396	2-D pore system, interpenetrated	0.0326	0.0095	0.0020	1.64	12.65
CoBTTBAZPY	4.942	0.389	3-D pore system, interpenetrated	0.0234	0.0083	0.0015	2.83	15.41
ZnBTTBBPY	4.064	0.38	2-D pore system, interpenetrated	0.0206	0.0125	0.0016	1.3	15.71
ZnBTTBAZPY	4.942	0.357	3-D pore system, interpenetrated	0.0169	0.0067	0.0015	5.82	28.37
ZnBTTB	4.468	0.251	3-D pore system, interpenetrated	0.0616	0.0474	0.0039	2.51	11.42
ZnBTTBBDC	4.243	0.209	2-D pore system, open Zn sites	0.1032	0.0026	0.0006	39.53	184.18
NiBTTB	4.291	0.2	1-D pore system, open Ni sites	0.0305	0.0088	0.0012	3.47	26.32
CdBTTB	5.413	0.190	3-D pore system, open Cd sites	0.0978	0.0168	0.0034	3.45	16.65
MgBTTB	8.555	0	1-D pore system, open Mg sites	0.0099	0.0081	0.0009	1.21	11.29

CdBTTB and ZnBTTBBDC show larger Henry constant owing to the presence of open cadmium and zinc sites that enhance the electrostatic interactions with the quadrupole moment of carbon dioxide. Although the pore size of ZnBTTB is less than CdBTTB, higher adsorption capacities are seen in CdBTTB because the strong electrostatic

interactions of open cadmium sites dominate the small pore size differences. Although NiBTTB has open nickel sites, its uptake is lower compared to CdBTTB due to its one dimensional pore system that restrict the diffusion of CO_2 molecules. BPY- based MOFs showed slightly higher Henry's constants compared to AZPY -based MOFs due to their lower pore sizes. However, in the region 0.15 – 0.5 MPa, CoBTTBAZPY showed higher adsorption uptake compared to BPY-based MOFs. This is due to the electrostatic interactions between free nitrogen atoms and quadrupole moment of carbon dioxide molecules. MgBTTB has the lowest Henry's constant suggesting incomplete activation, pore blockage or partial collapse of the structure upon evacuation.

At higher pressures, adsorption capacities for CO_2 do not correlate well with their pore volume and they follow the order of CoBTTBAZPY>ZnBTTBBPY>ZnBTTBAZPY CoBTTBBPY>ZnBTTB>CdBTTB~NiBTTB>MgBTTB>ZnBTTBBDC. CoBTTBAZPY showed higher adsorption capacities compared to other MOFs due to its larger pore volumes and higher surface area. One would expect that ZnBTTBAZPY should have similar adsorption capacities as CoBTTBAZPY due to isostructural framework. However, this trend was not seen in ZnBTTBAZPY due to its lower surface area and lower pore volume compared to CoBTBAZPY. The CO_2 uptake in ZnBTTBBPY is greater than CoBTTBBPY, although they both have similar surface areas and pore volumes. This could be due to the metal effect on CO_2 uptake. It is probable that the greater charge density of ZnBTTBBPY has attributed to attraction of more CO_2 molecules compared to CoBTTBBPY. ZnBTTB has greater adsorption capacities compared to CdBTTB due to its larger pore volumes and higher surface area. Identical adsorption capacities are seen in NiBTTB and CdBTTB due to similar pore volumes.

Surprisingly, ZnBTTBBDC exhibited the lowest adsorption capacities after 1 MPa, although it has pore volumes are similar to CdBTTB and NiBTTB. It could be that its pores are relatively inaccessible as compared to other MOFs.

At lower pressures, for CH_4, the order follows ZnBTTB>CdBTTB>ZnBTTBBPY~CoBTTBBPY>NiBTTB~CoBTTBAZPY>MgBTTB > ZnBTTBAZPY>ZnBTTBBDC. Due to its nonpolar nature, the interaction of CH_4 molecules with open cadmium sites is not enhanced significantly compared to the interaction of CO_2 molecules with open cadmium sites. Therefore, ZnBTTB exhibits higher adsorption capacity for CH_4 than CdBTTB at lower pressures due to smaller pores. NiBTTB and CoBTTBAZPY almost show similar adsorption capacities for methane due to their nearly similar pore sizes.

The same order as seen for CH_4 is observed for N_2 at lower pressures with the exception of MgBTTB having greater adsorption capacities than ZnBTTBBDC and BPY- and AZPY- based MOFs having similar adsorption capacities. Stronger confinement effects in BPY based MOFs offset the slightly weaker electrostatic effects arising from free nitrogen atoms in AZPY based MOFs. Therefore, similar nitrogen uptakes were seen in BPY and AZPY based MOFs at lower pressures. CdBTTB has greater adsorption capacities than NiBTTB due to its three dimensional pore system and slightly stronger interactions with weaker quadrupole moment of nitrogen.

8.2 BINARY MIXTURE ADSORPTION

To explore mixture adsorption, adsorption equilibrium data and adsorption selectivities were estimated using IAST for binary mixtures of CO_2/CH_4 and CO_2/N_2 at 50% CO_2 composition. IAST has been successfully applied to zeolites and MOFs for prediction of binary gas adsorption.[9] In this study, the Toth equation was used to fit the pure isotherms of CO_2, CH_4, and N_2, and the fitted isotherm parameters were used to predict the selectivity of CO_2 over CH_4 and N_2 in all the MOFs by IAST. The separation of the CO_2/CH_4 and CO_2/N_2 mixtures is quantified by the selectivity $S_{ij} = \left({}^{x_i}/_{x_j}\right)\left({}^{y_j}/_{y_i}\right)$, where x_i and y_i are the mole fractions of component i in the adsorbed and bulk phases, respectively. The selectivities for CO_2 over CH_4 and N_2 are shown in Figures 9.6 and 9.7. For the application of a MOF in flue gas and natural gas applications, the selectivity for adsorption of CO_2 over N_2 and CH_4, respectively, is highly important.

ZnBTTBBDC shows the highest selectivity for CO_2 over CH_4 and N_2 among all the MOFs studied here. The selectivity for the CO_2/CH_4 and CO_2/N_2 mixture in ZnBTTBBDC showed a slight decrease and then increased with pressure. The initial decrease is attributed to the heterogeneous distribution of adsorption sites, and the later increase is due to the cooperative interactions of adsorbed CO_2 molecules. Very high selectivities in ZnBTTBBDC implies that the effect of framework polarity is significant. In addition, there may be some donor-acceptor affinity between the CO_2 molecules and Lewis acidic Zn^{+2} ions. As the kinetic diameters of CO_2 (3.3 Å), CH_4(3.8 Å) and N_2(3.54 Å) are comparable to the pore size (4.468 Å) of interpenetrating MOF ZnBTTB, they

compete with each other for the constricted pores yielding lower selectivity for CO_2. As expected, MgBTTB resulted in lower selectivities due to the presence of residual solvent in the pores. The selectivity for CO_2 over CH_4 and N_2 decreases with increase in pressure for both CdBTTB and NiBTTB. This is because the adsorption sites in CdBTTB and NiBTTB are heterogeneous. First, the CO_2 molecules occupy the favorable exposed metal sites and then with increasing pressure, the CO_2 molecules occupy less favorable adsorption sites competing with methane or nitrogen molecules. Among the BPY and AZPY based MOFs, the selectivities for CO_2 over methane and nitrogen followed the order of CoBTTBBPY>CoBTTBAZPY>ZnBTTBAZPY>ZnBTTBBPY. The selectivities for CO_2 over nitrogen and methane for these MOFs increase with increase in pressure as a result of preferential interaction of CO_2 with the framework and cooperative attraction between adsorbed CO_2 molecules.

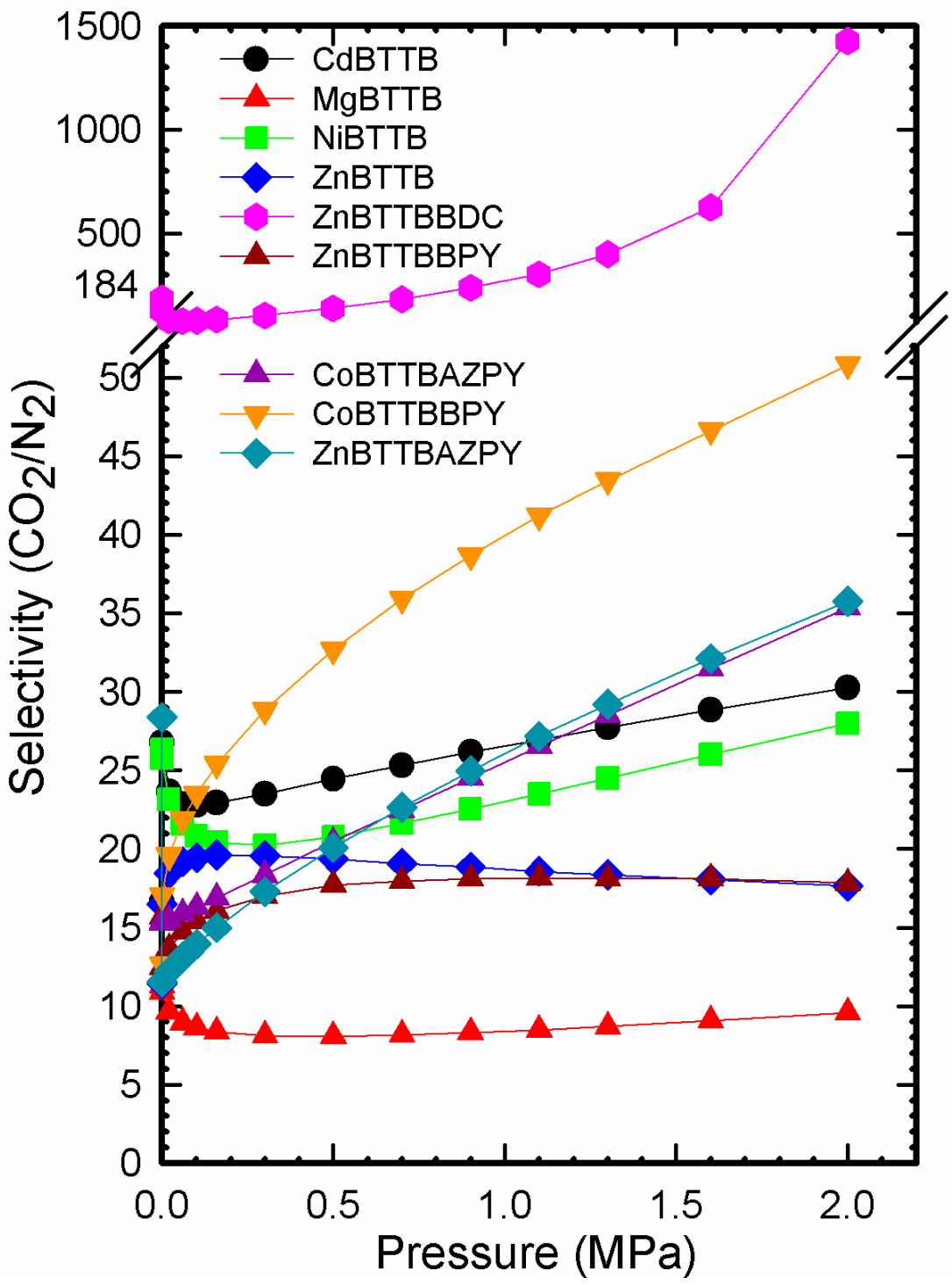

Figure 8.7 Estimated IAST selectivities for CO_2 for equimolar binary mixture CO_2 and N_2 at 298K

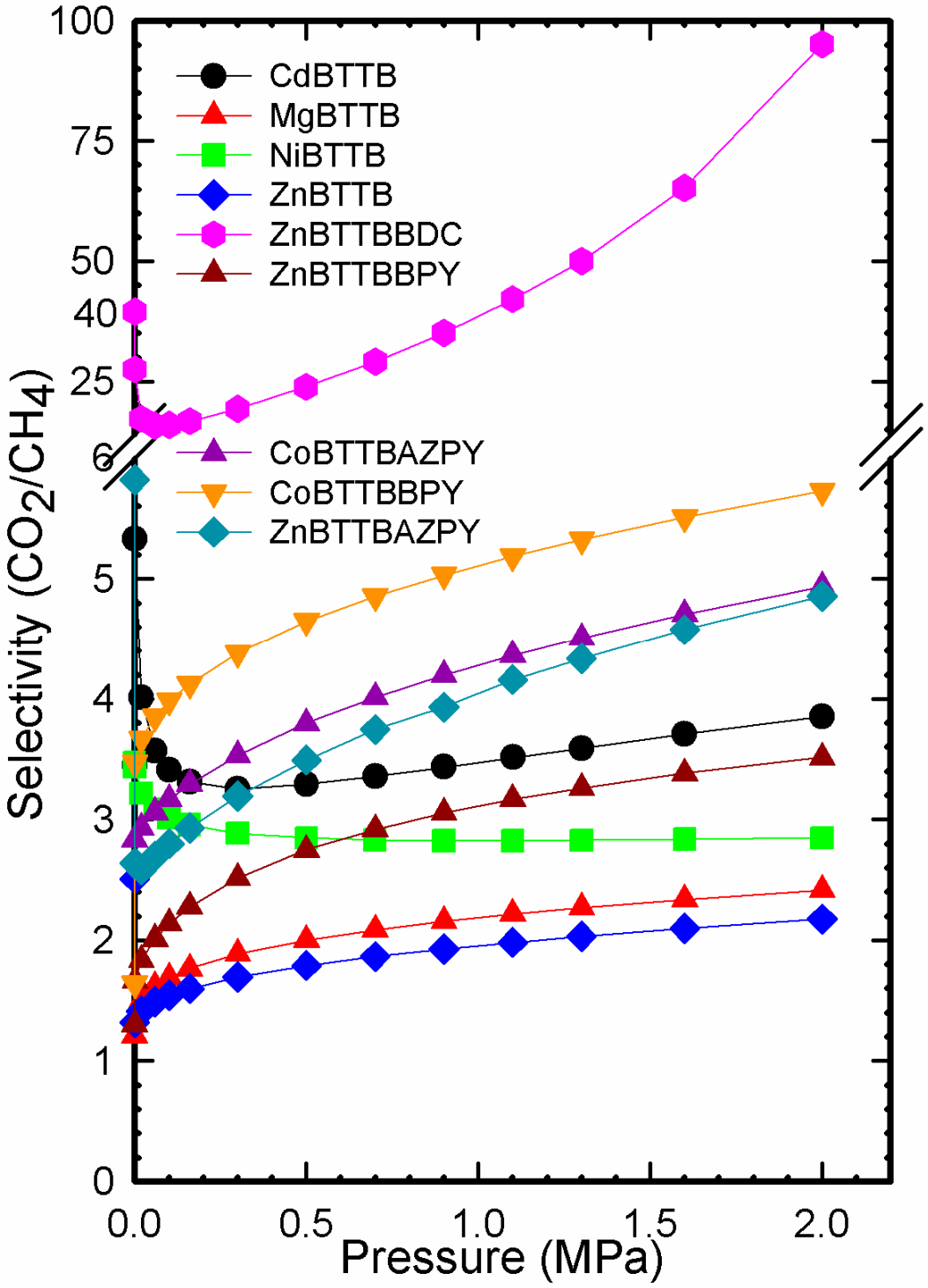

Figure 8.8 Estimated IAST Selectivities for CO_2 for equimolar binary mixture CO_2 and CH_4 at 298K

8.3 COMPARISON OF BTTB MOFS CO_2 SEPARATION PERFORMANCE WITH MOFS AND ZEOLITES REPORTED IN THE LITERATURE

Ideal adsorbent materials for CO_2 capture applications should have a high adsorption capacity and high selectivity for CO_2 at lower pressures and a moderate heat of adsorption. However, achieving high adsorption capacities might negatively affect heats of adsorption or selectivities. Therefore, one needs to look at the trade-off between adsorption capacities, heats of adsorption, and adsorption selectivities. For example, zeolite 13X has shown very high adsorption capacities for CO_2 at 1 bar (~ 4.7 mmol/g)[10], but this material has very high heats of adsorption (~50 kJ/mol) (see Appendix C) and requires considerable heating and associated costs to regenerate. No attempt was made to measure the adsorption data at different temperatures to calculate the heats of adsorption for the BTTB based MOFs. Hence no comparison of heats of adsorption was made here with the literature. A comparison of the adsorption capacities for CO_2 and estimated IAST selectivities of CO_2 over N_2 and CH_4 at 1 bar and 298 K for BTTB based MOFs and MOFs reported in the literature are shown in Figures 8.9 and 8.10. Desolvated compounds CdBTTB, MgBTTB, NiBTTB, ZnBTTB, ZnBTTBDC, CoBTTBBPY, ZnBTTBBPY, CoBTTBAZPY and ZnBTTBAZPY adsorb CO_2 up to ~ 1.63, 0.5, 1.3, 1.77, 0.92, 1.6, 1.54, 1.8 and 1.4 mol/kg , respectively, at 1 bar and 298 K. The adsorption capacities are comparable to IRMOF-1 (~ 1.1 mmol/g),[11] IRMOF-3 (~ 1.3 mmol/g),[11, 12] Cu-BTB (2 mmol/g)[12] and ZnBDCDABCO (~ 2.2 mmol/g)[13] under the same conditions. However, their uptakes are substantially smaller than the best MOFs Mg-DOBDC (~ 5.5 mol/g),[10] Cu-BTC (~4.28 mmol/g)[13], bio-MOF(~4.1 mmol/g),[14] $H_3[Cu_4Cl_3)$-$(BTTri)_8]$ (~ 3.25 mmol/g)[15] and zeolites 13X (~ 4.7 mmol/g).[10] Note that Cu-BTC, Mg-DOBDC and $H_3[Cu_4Cl_3)$-$(BTTri)_8]$ have open metal sites, bio-MOF-11

has Lewis basic amine and pyrimidine functionalities decorating the pores while 13X has exposed sodium cations.

The selectivities for CO_2/N_2 separation at 1 bar and 298 K are ~ 77 in ZnBTTBBDC, 23 in CdBTTB, 21 in NiBTTB, 20 in ZnBTTB, 9 in MgBTTB, ~ 24 in CoBTTBBPY, 15 in ZnBTTBBPY, 16 in CoBTTBAZPY, and 14 in ZnBTTBAZPY (Figure 9.5). The selectivity in ZnBTTBBDC is substantially higher than those in some well-known materials, such as zeolite Na-4A (18.8)[16], activated carbon Norit R1(15.3),[17] IRMOF-1 (6)[13], IRMOF-3 (8),[13] Cu-BTC (20),[13] MOF-508b(3-6).[18] This is because of the high polarity of the framework, presence of open metal sites, and smaller pores that should enhance the selectivity of the more strongly adsorbed CO_2 over N_2 due to the increased potential.

The selectivities for CO_2/CH_4 separation at 1 bar and 298 K are ~ 16 in ZnBTTBBDC, 4 in CdBTTB, 3 in NiBTTB, 2 in ZnBTTB, 2 in MgBTTB, ~ 4 in CoBTTBBPY, 2 in ZnBTTBBPY, 3 in CoBTTBAZPY and ZnBTTBAZPY (Figure 8.6). The selectivity in ZnBTTBBDC is higher than those in some well-known materials, such as IRMOF-1 (2-3),[19] Cu-BTC (6-9),[19] [19]MOF-508b (3-6)[20] and comparable to that of carborane-based MOFs (17).[21] The results of ZnBTTBBDC look promising for both CO_2/N_2 and CO_2/CH_4 separations; however very low adsorption capacities at lower pressures limit the application of this MOF for CO_2 capture.

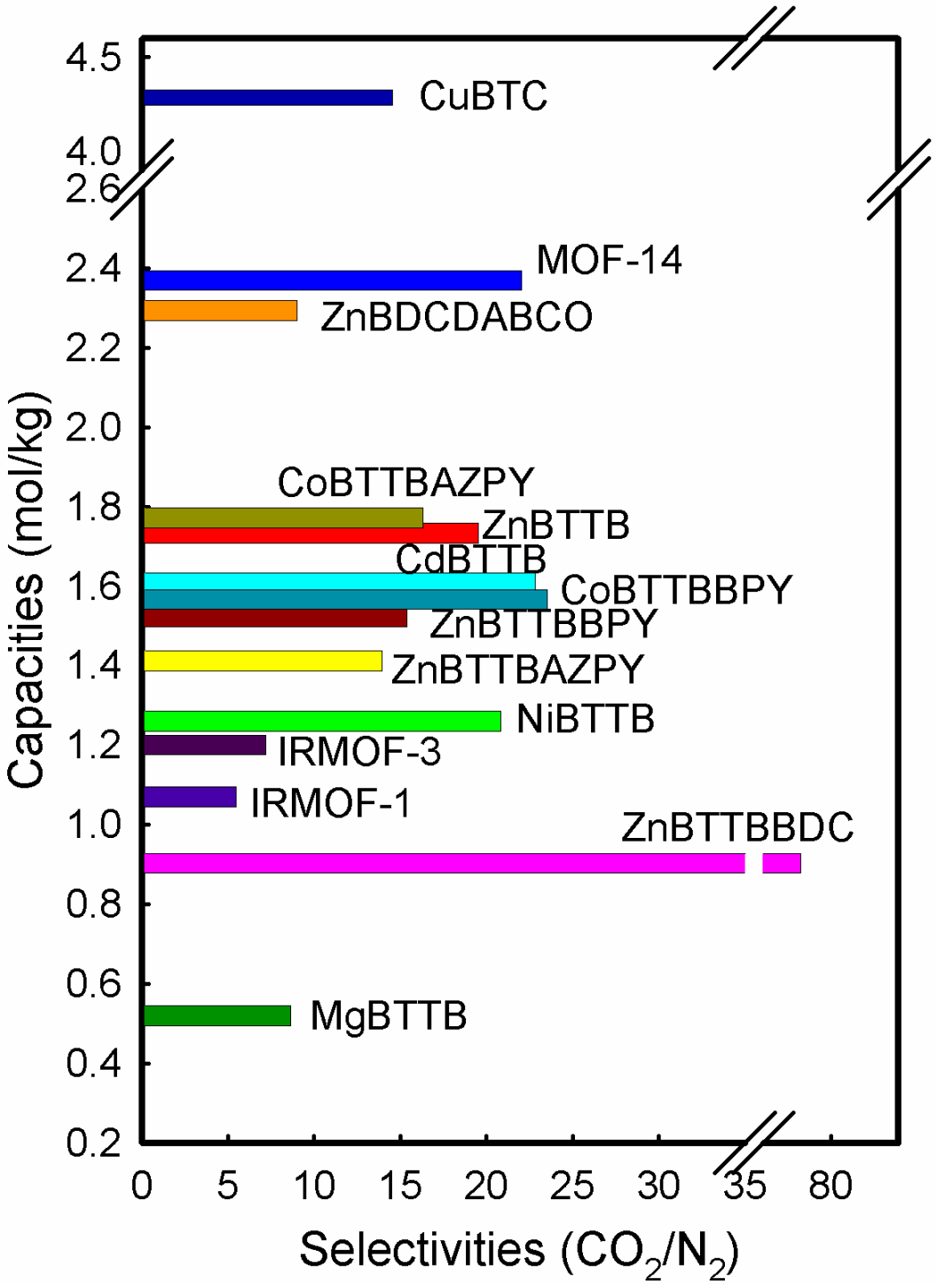

Figure 8.9 Bar graphs showing capacities of CO_2 and IAST selectivities for equimolar binary mixture CO_2 and N_2 at 1 bar and 298K

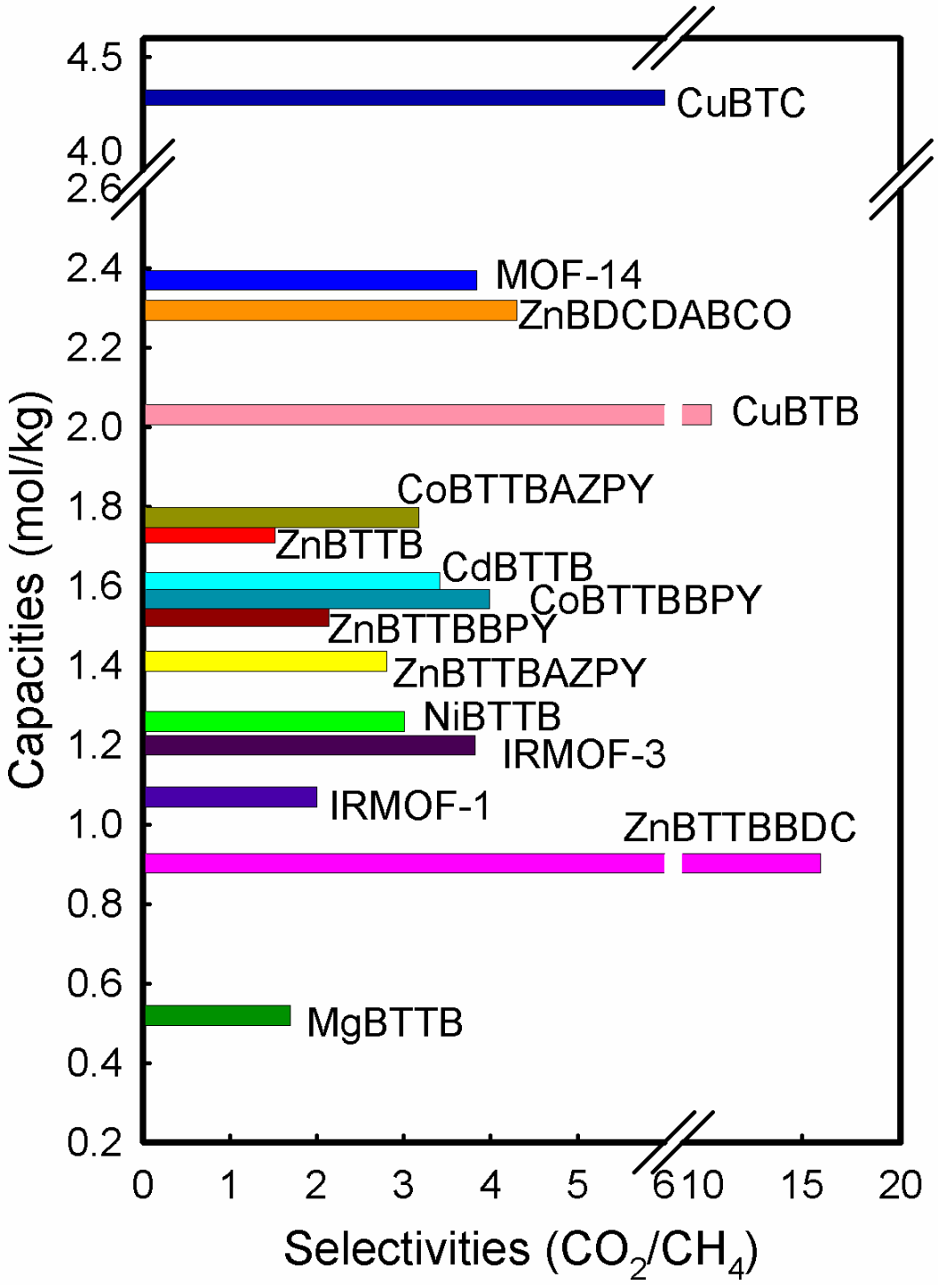

Figure 8.10 Bar graphs showing capacities of CO_2 and IAST selectivities for equimolar binary mixture CO_2 and CH_4 at 1 bar and 298K

8.4 CONCLUSIONS

The role of open metal sites and pore sizes has been found to be crucial in deciding the capacity and selectivity for CO_2 from mixtures of natural gas and flue gas. The coordinate strength for the unsaturated metal centers toward CO_2 molecules varies from one MOF type to another. The mixture adsorption results show that ZnBTTBBDC is a good candidate for CO_2 capture from flue gases and natural gas streams due to high selectivity. However, the limitation of this MOF is the low adsorption capacities of CO_2 at ambient conditions. CdBTTB also showed good capacities and good selectivities for CO_2. Our results suggest that further, rational development of new MOF compounds for CO_2 capture applications should focus on enriching open metal sites, increasing the pore volume, and minimizing the size of large pores.

8.5 REFERENCES

(1) Duren, T.; Millange, F.; Frey, G.; Walton, K. S.; Snurr, R. Q. *J. Phys. Chem. C* **2007**, *111*, 15350.

(2) Garrido, J.; Linnaressolano, A.; Martinmartinez, J. M.; Molinasabio, M.; Rogriguezreinoso, F.; Torregrosa, R. *Langmuir* **1987**, *3*, 76.

(3) Lozano-Castello, D.; Cazorla-Amoros, D.; Linares-Solano, A. *Carbon* **2004**, *42*, 1233.

(4) Bae, Y. S.; Farha, O. K.; Hupp, J. T.; Snurr, R. Q. *J. Mater. Chem* **2009**, *19*, 2131.

(5) Bae, Y. S.; Mulfort, K. L.; Frost, H.; Ryan, P.; Punnathanam, S.; Broadbelt, L. J.; Hupp, J. T.; Snurr, R. Q. *Langmuir* **2008**, *24*, 8592.

(6) Nguyen, T. X.; Bhatia, S. K. *J. Phys. Chem. C* **2007**, *111*, 2212.

(7) Babarao, R.; Jiang, J. W. *J. Am. Chem. Soc.* **2009**, *131*, 11417.

(8) Duong, D. D. In *Adsorption Analysis: Equilibria and Kinetics;* Imperial College Press: London, 1998.

(9) Keskin, S.; Liu, J.; Rankin, R. B.; Johnson, J. K.; Sholl, D. S. *Ind. Eng. Chem. Res.* **2009**, *48*, 2355.

(10) Caskey, S. R.; Wong-Foy, A. G.; Matzger, A. J. *J. Am. Chem. Soc.* **2008**, *130*, 10870.

(11) Millward, A. R.; Yaghi, O. M. *Journal of the American Chemical Society* **2005**, *127*, 17998.

(12) Mu, B.; Li, F.; Walton, K. S. *chem. commun* **2009**, 18, 2493.

(13) Karra, J. R.; Walton, K. S. *J. Phys. Chem. C* **2010**, *114*, 15735.

(14) An, J.; Geib, S. J.; Rosi, N. L. *J. Am. Chem. Soc.* **2010**, *132*, 39.

(15) Demessence, A.; D'Alessandro, D. M.; Foo, M. L.; Long, J. R. *J. Am. Chem. Soc.* **2009**, *131*, 8784.

(16) Jiang, J. W.; Sandler, S. I. *Langmuir* **2006**, *22*, 5702.

(17) Dreisbach, F.; Staudt, R.; Keller, J. U. *Adsorption* **1999**, *5*, 215.

(18) Bárcia, P. S.; Zapata, F.; Silva, J. A. C.; Rodrigues, A. E.; Chen, B. L. *J. Phys. Chem. B* **2007**, *111*, 6101.

(19) Yang, Q. Y.; Zhong, C. L. *J. Phys. Chem. B.* **2006**, *110*, 17776.

(20) Bastin, L.; Barcia, P. S.; Hurtado, E. J.; Silva, J. A. C.; Rodrigues, A. E.; Chen, B. *J. Phys. Chem. C* **2008**, *112*, 1575.

(21) Bae, Y. S.; Farha, O. K.; Sponkoyny, A. M.; Mirkin, C. A.; Hupp, J. T.; Snurr, R. Q. *Chemical Communications* **2008**, , 4135.

CHAPTER 9

STRUCTURAL STABILITY OF BTTB BASED FRAMEWORKS UNDER HUMID CONDITIONS

9.1 INTRODUCTION

Many separation applications are complicated by the presence of small quantities of water, and its removal is extremely important in the case of porous materials that are sensitive to moisture. Removal of moisture could help in facilitating the materials handling and reduce costs. Despite the importance of water stability of MOFs for technological applications, only a few water sorption studies have been reported. Many MOFs are unstable in the presence of moisture and often require inert conditions to handle them.

Greathouse and Allendorf reported that MOF-5 dissociates upon contact with water due to ligand displacement at metal sites.[1] Li and Yang found that MOF-177 adsorbs ~ 10 wt% H_2O and is unstable upon exposure to ambient air in 3 days.[2] Liang et al. reported water vapor adsorption studies on $Zn_2(BDC)_2(DABCO)$ and $Ni_2(BDC)_2(DABCO)$ and found that the structures of the two MOFs are stable up to 30 % relative humidity water vapor sorption, but collapsed after 60% relative humidity water vapor sorption.[3] Kondo et al. investigated water adsorption isotherms on three-dimensional (3-D) pillared-layer MOFs $Cu_2(pzdc)_2(pyz)$ and $Cu_2(pzdc)_2(bpe)$ and $Cu_2(pzdc)_2(bpy)$ and found that as the pillared ligand becomes longer, the water adorption amount is larger.[4] Kusgens et al. measured water adsorption isotherms for CuBTC, ZIF-8, MIL-100 (Fe) and DUT-4 and found that ZIF-8, MIL-100 (Fe) and MIL-101 were water stable.[5] Low et al. investigated the steam stability of several well-known MOFs at various saturations and temperatures

and found that strength of the bond between metal oxide cluster and the bridging linker is important in determining the hydrothermal stability of the MOF.[6] Liu et al. studied the adsorption equilibrium of CO_2, H_2O, and CO_2/H_2O for two MOFs, HKUST-1 and Ni/DOBDC, and found that adsorbed water vapor impacts CO_2 adsorption in the MOFs.[7] They reported that small amount of water vapor helped to increase slightly the CO_2 capacity in HKUST-1 whereas the opposite effect was seen in case of Ni/DOBDC. Recently, Schoenecker et al. have investigated the water vapor adsorption properties of several well-known MOFs, Cu-BTC, UIO-66, UMCM-1, DMOF, DMOF-NH_2, UMCM-1-NH_2, UIO-66-NH_2 and found that DMOF and UIO-66 were the most stable. This stability was attributed to higher basicity of organic ligands (DABCO) relative to carboxylic acid groups (BDC) and higher coordination number of Zr.[8]

To further address the issue of water stability of MOFs, a systematic study of the effect of water vapor on the BTTB based MOFs, CdBTTB, NiBTTB, ZnBTTB, ZnBTTBBDC, ZnBTTBBPY, CoBTTBBPY, ZnBTTBAZPY, CoBTTBAZPY was undertaken. Metal atoms in CdBTTB and ZnBTTBBDC are unsaturated after complete desolvation. These unsaturated metal centers can coordinate with polar water molecules and can lead to greater water adsorption capacities. NiBTTB has a 2D layered structure and also it has open nickel sites upon desolvation. The coordination environment in ZnBTTB is different from that of CdBTTB and NiBTTB. It has a 3D structure with pores in two directions. The zinc atoms in ZnBTTB are surrounded by oxygen atoms from BTTB ligand and have no open zinc sites. CoBTTBBPY and ZnBTTBBPY are isostructural and can be described as two-fold interpenetrating 3D MOFs with open channels of 4.064 in [0 1 0] direction and 6.044 Å in [0 $\bar{1}$ 1] direction. The MOF frameworks are made from 2D

$M_2(BTTB)_4$ sheets and are further pillared by the BPY linker. We hypothesized that these two MOFs constructed with pyridyl based ligands are more water stable because of their metal-ligand bond strengths. The greater basicity of the pyridyl linker, as compared to typical carboxylate linkers, results in stronger metal-ligand bonds, and therefore, a purported resistance to hydrolysis.[9]

CoBTTBAZPY and ZnBTTBAZPY are identical in structure and can be described as two-fold interpenetrating 3D MOFs with open channels of open channels of 1 Å and 4.942 Å in [1 0 0] direction, 4.942 Å in [$\bar{1}$ 1 1] direction and 6.617 Å in [1 0 1] direction. In these MOFs, the BTTB ligands connect the M(II) ions (M = Co, Zn) into a 2D layer along the xy plane, and the azpy pillars extend these layers into a 3D coordination framework. AZPY spacers have free nitrogen coordination sites and can interact preferentially with polar water molecules.

This diverse set of structures with differing coordination environments should offer insight into the factors that make MOFs water stable. Water vapor adsorption equilibria was studied using a gravimetric system. Powder X-ray diffraction (PXRD) was used to determine if the structure remains untransformed with exposure to different humid conditions.

9.2 EXPERIMENTAL SECTION

9.2.1 Methods

Thermogravimetric analyses (TGA) were carried out in the temperature range of 25-700 ˚C on a NETSZCH TG/Mass spectrometry analyzer under helium with a heating rate of 5 ˚C/min. Powder X-ray diffraction patterns (PXRD) were recorded on a X'Pert X-ray PANalytical diffractometer with an X'accelerator module using Cu Kα (λ = 1.5418 Å) radiation at room temperature, with a a step size of 0.02˚ in 2θ. Water vapor sorption isotherms were measured using an Intelligent Gravimetric Analyzer (IGA-3 series, Hiden Analytical Ltd.). Dry air was used as the carrier gas, with a portion of the carrier gas being bubbled through a vessel of deionized water. The relative humidity (RH) was controlled by varying the ratio of saturated air and dry air via two mass flow controllers. Experiments were conducted up to 90% RH due to water condensation in the apparatus at higher humidities. The total gas flow rate was 100 cc/min for the entire experiment. Prior to the adsorption measurement in order to remove adsorbed molecules, the sample was treated under the vacuum at different activation temperatures for the samples (shown in Table 9.1), until no further weight loss was observed. Each adsorption/desorption step was allowed to approach equilibrium over a period of 2 – 24 hrs for each relative humidity point. Nitrogen adsorption isotherms at 77 K were run and PXRD patterns were measured after exposure to water vapor and thermal activation in order to know whether the structures of MOFs are retained.

9.3 RESULTS AND DISCUSSION

9.3.1 Water vapor adsorption isotherms

The properties of BTTB MOFs along with the BET surface areas before and after water adsorption experiments are tabulated in Table 9.1. As can be seen from Table 9.1 only MOFs NiBTTB, ZnBTTBBPY and CoBTTBBPY are stable after water exposure. This point will be revisited in later discussion. Figure 9.1 shows the water vapor adsorption isotherms at 25 ˚C for CdBTTB, ZnBTTB and ZnBTTBBDC. The amount of water vapor adsorbed increased with increase in relative humidity in all the MOFs. The water vapor isotherm for CdBTTB is steeper than that for the ZnBTTB, especially in the lower humidity region. Water vapor is strongly adsorbed in CdBTTB because of its high affinity with the open cadmium sites. Furthermore, its interconnected 3D pore system with relatively large pore size allows easy diffusion of water molecules into the framework and facilitates it to adsorb more water vapor compared to ZnBTTB and ZnBTTBBDC. The water vapor capacities at 90% relative humidity are 14.5 mol/kg (26.5 wt %) for CdBTTB, 12 mol/kg (21.6 wt %) for ZnBTTB and 5.2 mol/kg (9.3 wt %) for ZnBTTBBDC.

In the higher humidity region, the water uptake increased sharply in the case of CdBTTB and ZnBTTB due to the condensation of water in the pores. The desorption branch did not follow the adsorption branch for the samples, showing large hysteresis. The hysteresis is larger in ZnBTTB compared to CdBTTB. Furthermore, it can be seen that a significant amount of water is retained in the pores of the MOFs, even when the stream was

switched to dry air. These findings suggest that most of adsorbed water molecules are strongly bound in the ZnBTTB and CdBTTB crystals.

Table 9.1 BET surface areas before and after water runs for all the MOFs synthesized in this work

MOF	Pore size (Å)	Pore volume (cm^3/g)	BET surface area (m^2/g)	Activation process (under vacuum)	Thermal stability	Features	BET surface area (after water runs)	Change in surface area (%)
CdBTTB	5.413	0.190	415	300 ˚ C (1h)	350 ˚C	3-D pore system, open Cd sites	0	100
ZnBTTB	4.468	0.251	447	250 ˚ C (2h)	300 ˚C	3-D pore system, interpenetrated	0	100
ZnBTTBBDC	4.243	0.209	441	250 ˚ C (1h)	350 ˚C	2-D pore system, open Zn sites	220	50
NiBTTB	4.291	0.2	391	Chloroform Exchange and 120 ˚ C (12h)	350 ˚C	1-D pore system, open Ni sites	391	0
ZnBTTBBPY	4.064	0.38	841	Chloroform Exchange and 120 ˚ C (12h)	350 ˚C	2-D pore system, interpenetrated	841	0
CoBTTBBPY	4.064	0.396	843	Chloroform Exchange and 120 ˚ C (12h)	400 ˚C	2-D pore system, interpenetrated	843	0
ZnBTTBAZPY	4.942	0.357	647	Chloroform Exchange and 120 ˚ C (12h)	300 ˚C	3-D pore system, interpenetrated	370	43
CoBTTBAZPY	4.942	0.389	805	Chloroform Exchange and 120 ˚ C (12h)	300 ˚C	3-D pore system, interpenetrated	356	56

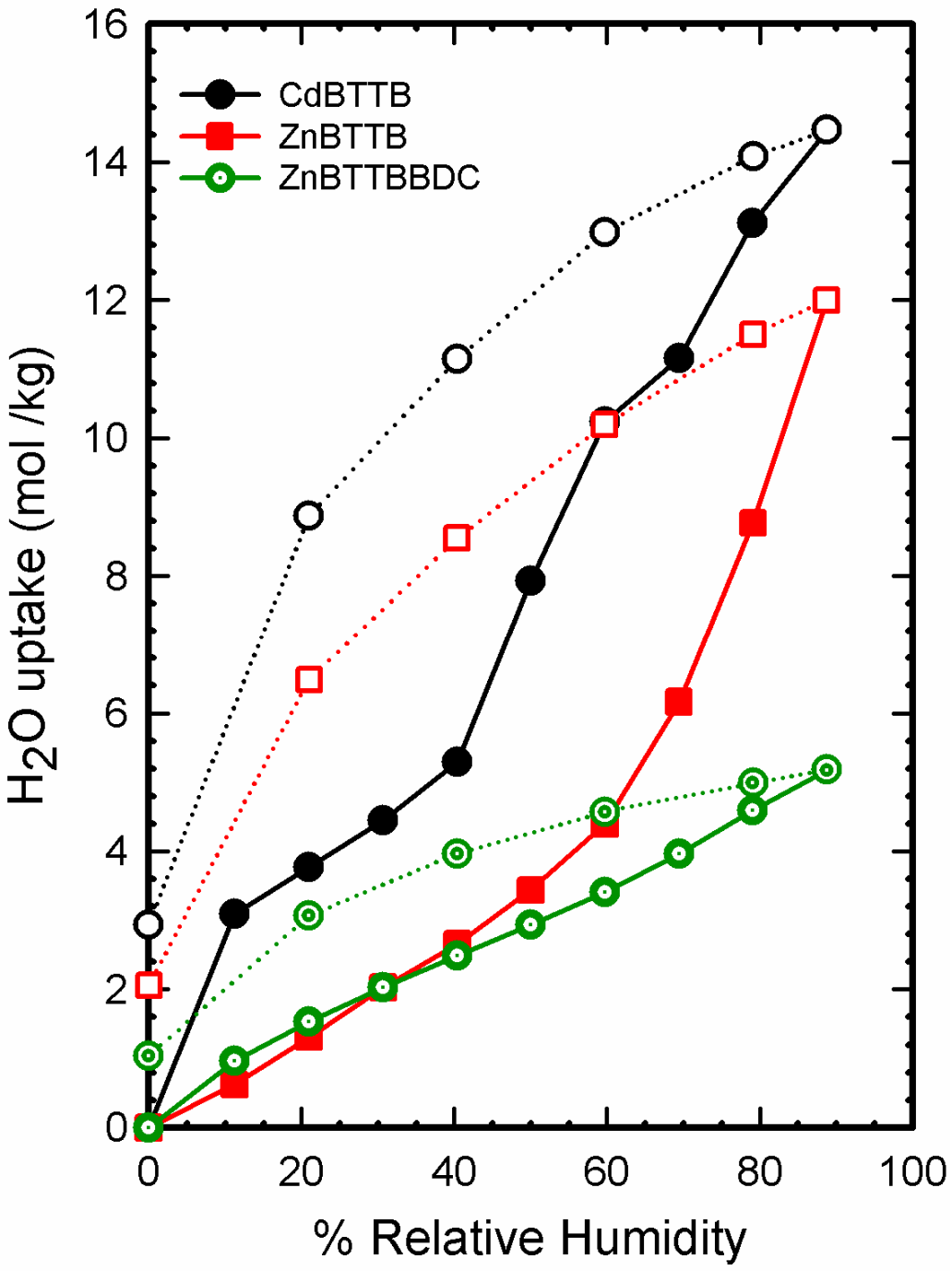

Figure 9.1 Water vapor sorption/desorption isotherms for desolvated compounds of CdBTTB, ZnBTTB and ZnBTTBBDC (solid curves – adsorption, dashed curves – desorption)

The XRD patterns of the samples after the water sorption experiments were compared with that of the activated samples (Figures 9.2 -9.4). The XRD powder patterns of ZnBTTB and CdBTTB confirmed the partial decomposition of MOF. Most of the peaks disappeared and the amorphous background increased. The reflections are partly shifted in case of CdBTTB. After thermal treatment of water vapor exposed samples, the structures of CdBTTB and ZnBTTB completely collapsed as evidenced from XRD patterns and surface area measurements (as shown in Table 9.1). Surface area loss was 100% in both the MOFs. It was recently reported in the literature that MOF-5 is less stable due to its 4-coordinate Zn ions[6] and therefore the zinc-oxygen bonds of the linkers are highly susceptible to displacement by the incoming water molecules.[1] Therefore, the degradation of ZnBTTB is not surprising, considering that the coordination environment of Zn ions in ZnBTTB is identical to MOF-5.[1] However, it is surprising to see that CdBTTB is not stable considering its higher coordination number (6) of Cd ions when solvated. Two of the Cd ions are surrounded by chelating oxygen atoms that have very weak interactions with the Cd ions. Therefore, cadmium-oxygen bonds of the chelated linkers are perhaps more susceptible to displacement by the incoming water molecules.

Unlike CdBTTB and ZnBTTB, ZnBTTBBDC was not significantly degraded structurally. This could be due to the different coordination environment of ZnBTTBBDC compared to ZnBTTB to CdBTTB. When solvated, all zinc ions in all the three different metal-carboxylate clusters of ZnBTTBBDC are 4- and 6-coordinate, and the three different metal-carboxylate clusters are connected to each other with different BTTB ligands. This leads to greater stability in the presence of water compared to CdBTTB and ZnBTTB. These results show that how the metal clusters are connected to

each other are also important in addition to the coordination number when considering the stability of a MOF structure with respect to reaction with water vapor. The XRD pattern of ZnBTTBBDC after water sorption experiments and thermal activation still showed some of the initial XRD peaks, but other peaks disappeared, indicating a loss of crystallinity and partial collapse of the structure (Figure 9.4). The N_2 sorption isotherms of the samples were measured again after water sorption and thermal activation. The surface area loss of 50% is consistent with the partial collapse of the structure as indicated by PXRD (Table 9.1).

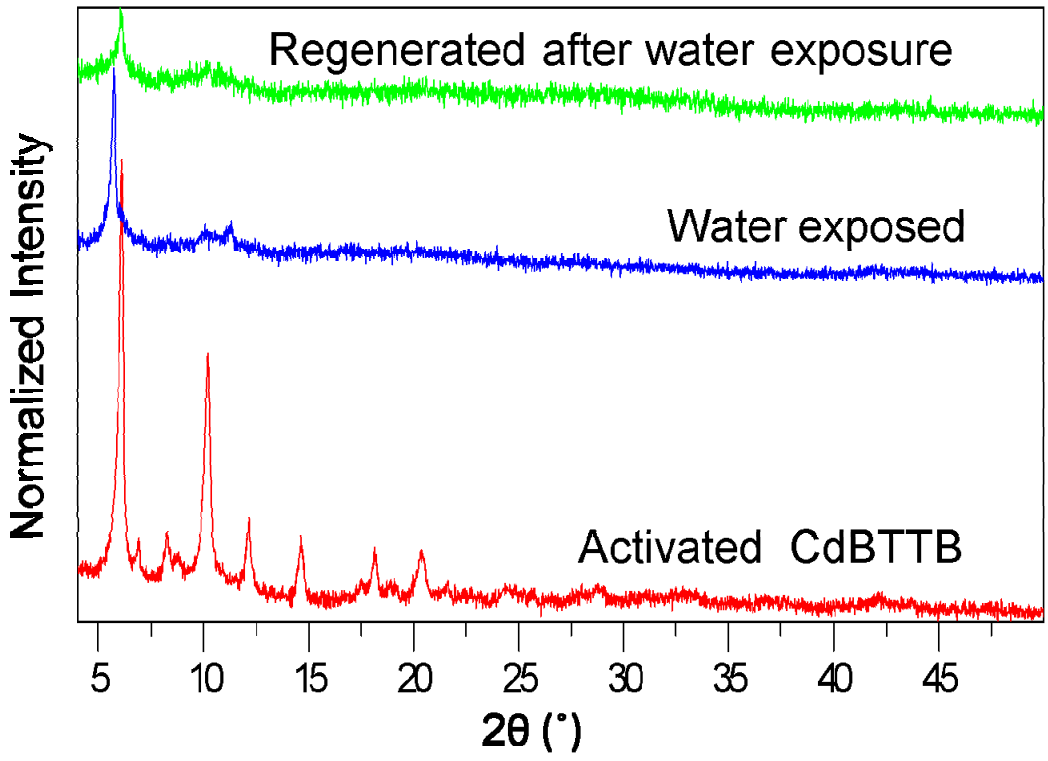

Figure 9.2 Activated, water exposed and regenerated after water exposure powder X-ray diffraction patterns of CdBTTB

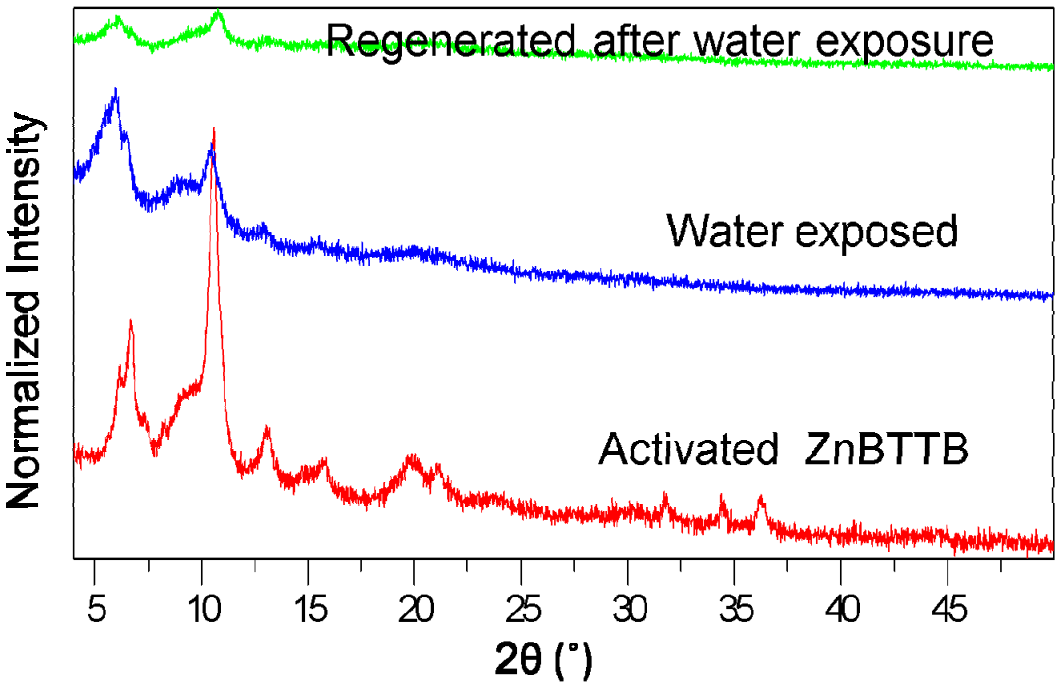

Figure 9.3 Activated, water exposed and regenerated after water exposure powder X-ray diffraction patterns of ZnBTTB

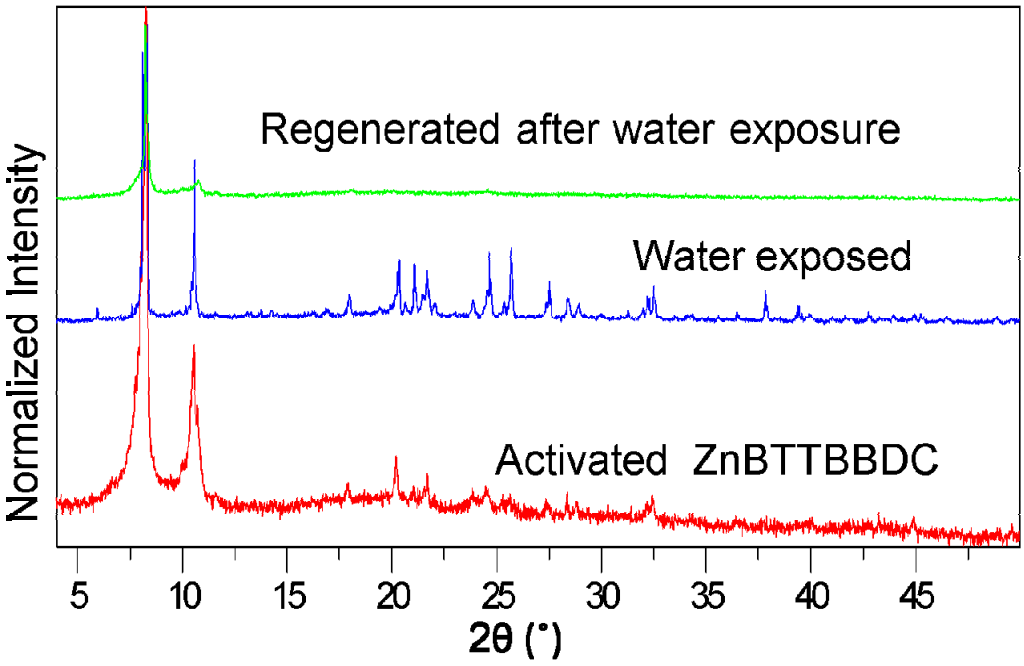

Figure 9.4 Activated, water exposed and regenerated after water exposure powder X-ray diffraction patterns of ZnBTTBBDC

Figure 9.5 shows the water vapor adsorption isotherms at 25 ˚C for NiBTTB, ZnBTTBBPY and CoBTTBBPY. NiBTTB showed slightly higher water vapor uptake compared to ZnBTTBBPY and CoBTTBPY at lower humidity region due to the electrostatic interactions between open nickel sites and water vapor. This behavior was also seen with CO_2 adsorption for this MOF. However the water uptake is very small in this MOF compared to other open metal site MOFs, CdBTTB and ZnBTTBBDC. One explanation for this observation is that the two-dimensional net structure and one-dimensional pore channels restrict the diffusion of water molecules. The non-polar

interactions between BTTB linkers are dominant in the case of NiBTTB that ensured minimal wetting of the pores.

The water adsorption and desorption isotherms showed complete reversibility for NiBTTB, while hysteresis was seen in the case of CoBTTBBPY and ZnBTTBBPY. The adsorption loadings are very small in these MOFs, implying that the structure of all these MOFs is resistive against water. The isotherms for these compounds can be classified as type VII according to IUPAC[10], indicating that these materials are very hydrophobic. Both these MOFs showed similar adsorption uptakes till 70% relative humidity due to their isostructural nature and similar pore sizes. Very high adsorption loadings (9.59 mol/kg at 80% RH, 14.1 mol/kg at 90% RH) were observed for the case of ZnBTTBBPY (not shown in Figure). However, the same trend was not seen with CoBTTBPY. It still remains unclear what could have caused this unexpected behavior at those higher humidity region for ZnBTTBBPY. Further studies are ongoing in our lab to reconfirm this observation. It was reported in the literature that ZnBDCDABCO showed hydrophobic character due to the Zn-N coordination from the DABCO linker.[8] Therefore, the hydrophobicity of BPY based MOFs is not surprising, considering that the coordination environment of Zn ions or Co ions in these MOFs is identical to ZnBDCDABCO. In these BPY-based MOFs, Zn-N or Co-N coordination from the bipyridyl linker renders these MOFs more hydrophobic character. Additionally, all zinc or cobalt ions are coordinated to oxygen atoms and nitrogen, and there are no free coordination sites available for water to readily interact with.

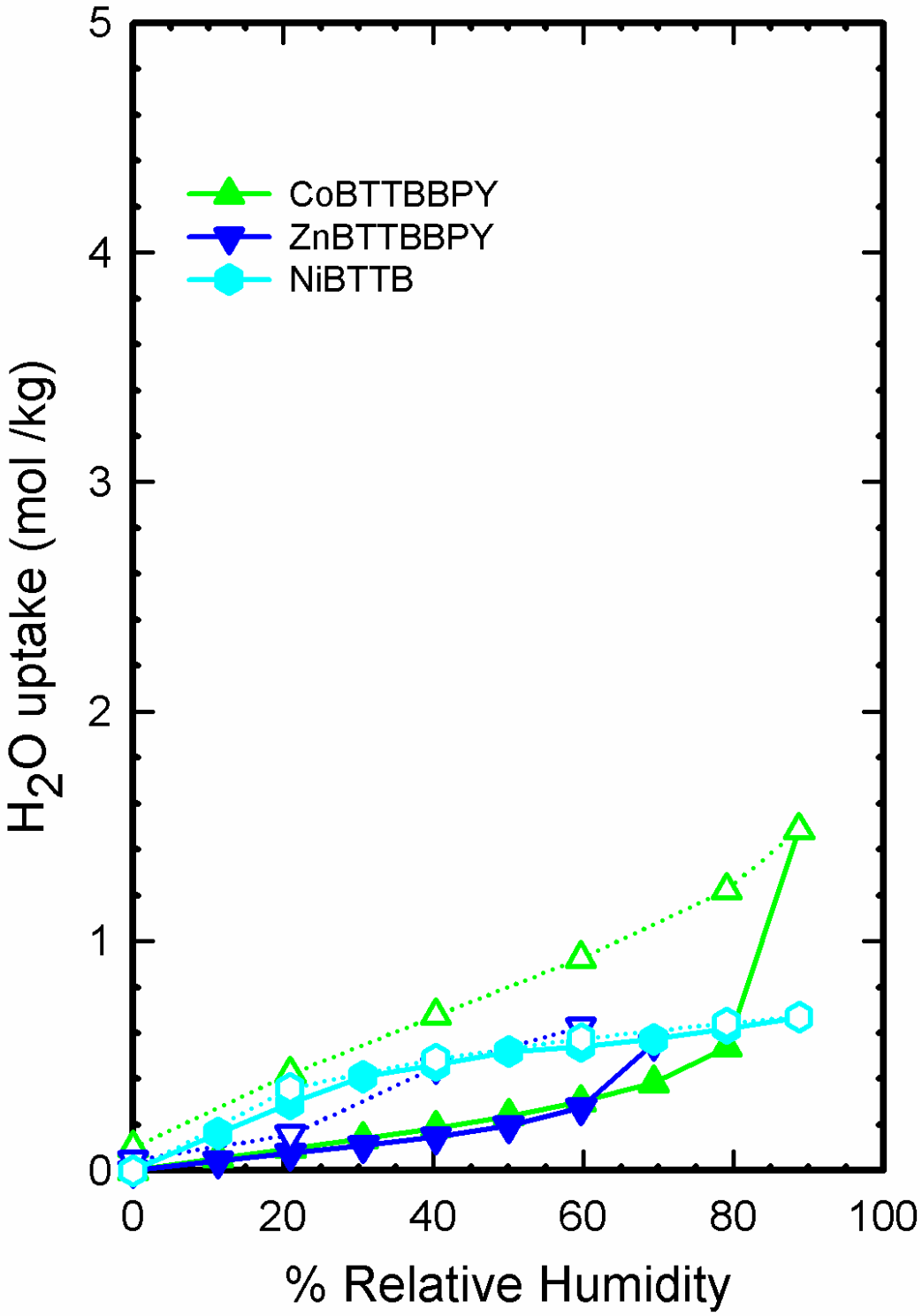

Figure 9.5 Water vapor sorption/desorption isotherms for desolvated compounds of CoBTTBPY, ZnBTTBBPY and NiBTTB. (solid curve – adsorption, dashed curves – desorption)

Figures 9.6 – 9.8 show the PXRD patterns of activated MOF, water vapor exposed MOF and regenerated MOF after exposure to water vapor. Minimal changes in the PXRD patterns were observed indicating that these three materials were stable even after exposure to high levels of humidity (Figures 9.6 and 9.7). Surface areas remain unchanged for all the three samples after water vapor exposure (Table 9.1) and thermal activation, indicating that these MOFs maintained their structural integrity even after activation. These results suggest that mixed ligand MOFs made from BTTB and pyridyl based ligands are more stable than single ligand MOFs made from BTTB. The hydrophobicity of these materials can ensure minimal wetting of the pores and therefore the capacities and selectivities for adsorptive separations can remain high.

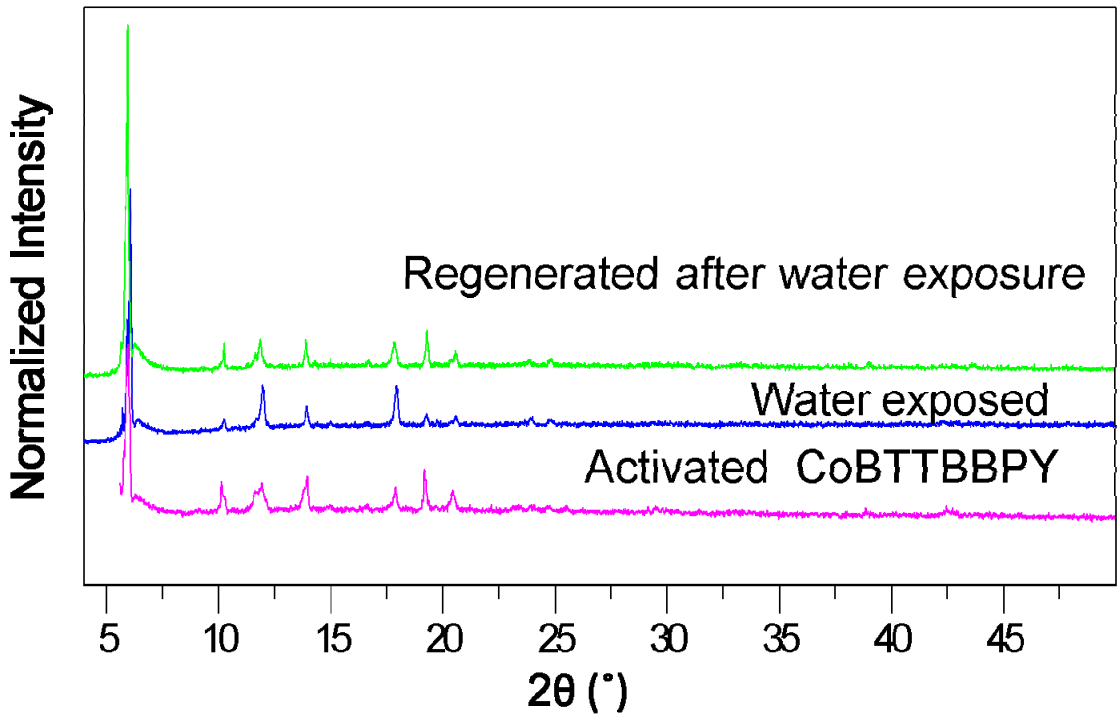

Figure 9.6 Activated, water exposed and regenerated after water exposure powder X-ray diffraction patterns of CoBTTBBPY

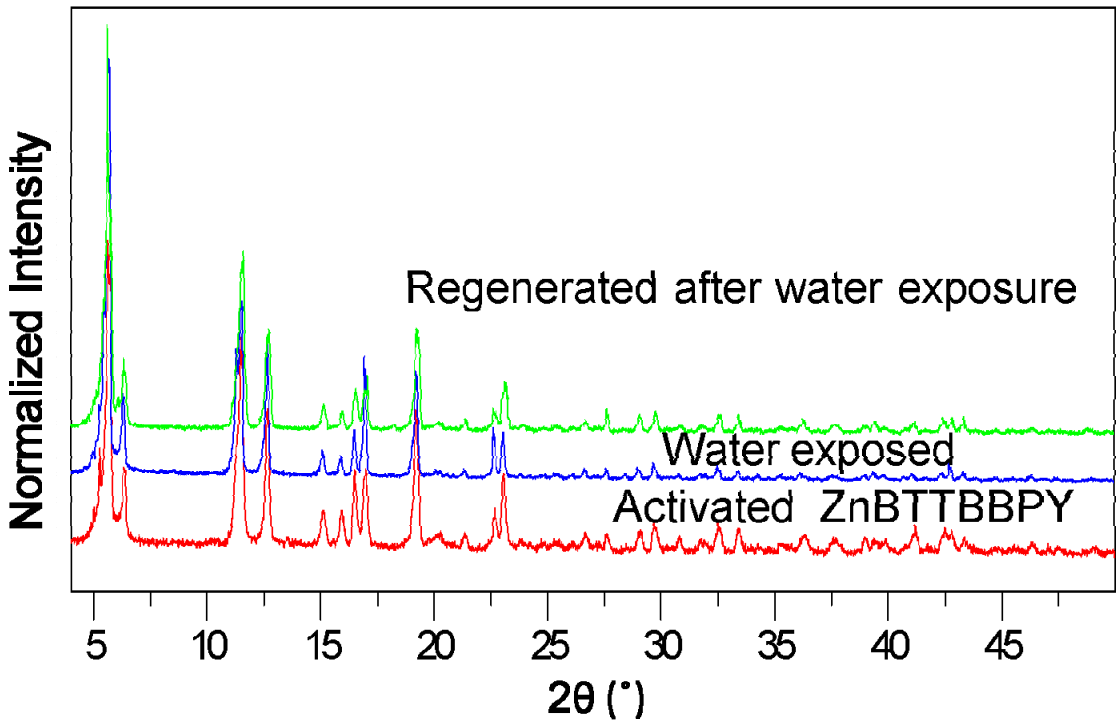

Figure 9.7 Activated, water exposed and regenerated after water exposure powder X-ray diffraction patterns of ZnBTTBBPY

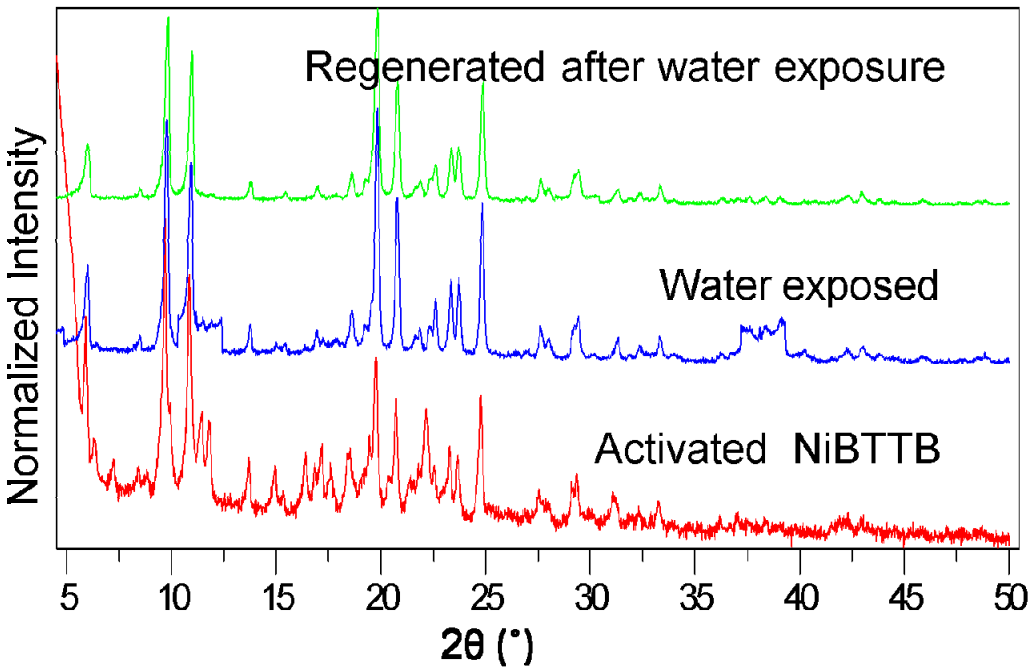

Figure 9.8 Activated, water exposed and regenerated after water exposure powder X-ray diffraction patterns of NiBTTB

Figure 9.9 shows the water vapor adsorption isotherms at 25 ˚C for CoBTTBAZPY and ZnBTTBAZPY. The amount of water vapor adsorbed increases gradually with increase in relative humidity up to 40% relative humidity. As both the MOFs are isostructural and have similar pore sizes, the water uptake was almost the same in both the MOFs up to 40% relative humidity. In the higher humidity region, the water uptake increased sharply in both the MOFs. This is probably the result of condensation of water in the pores. Their uptakes varied at higher humidity regions due to the difference in BET surface areas and

pore volumes. The water vapor capacities at 90% relative humidity are 12.3 mol/kg (22.1 wt %) for CoBTTBAZPY and 10.8 mol/kg (19.3 wt %) for ZnBTTBAZPY. The water vapor isotherms in both the MOFs were irreversible and exhibited large hysteresis. The hysteresis is larger in CoBTTBAZPY compared to ZnBTTBAZPY. Furthermore, it can be seen that there are small portions of water retained in the pores of the MOFs even when the stream was switched to dry air. This suggests that some adsorbed molecules are strongly bound in both the MOFs. It is probable that free nitrogen sites could have played a role in enhancing the affinity of both the MOFs with the polar water molecules.

The XRD patterns after water sorption experiments and thermal activation (Figure 9.10 and Figure 9.11) still showed some of the initial XRD peaks, but other peaks disappeared, indicating a loss of crystallinity and partial collapse of the structure. The N_2 sorption isotherms of the samples were measured again after water sorption and thermal activation. Surface area loss was significant. The BET surface areas loss was 56 % for CoBTTBAZPY and 43 % for ZnBTTBAZPY (as shown in Table 9.1).

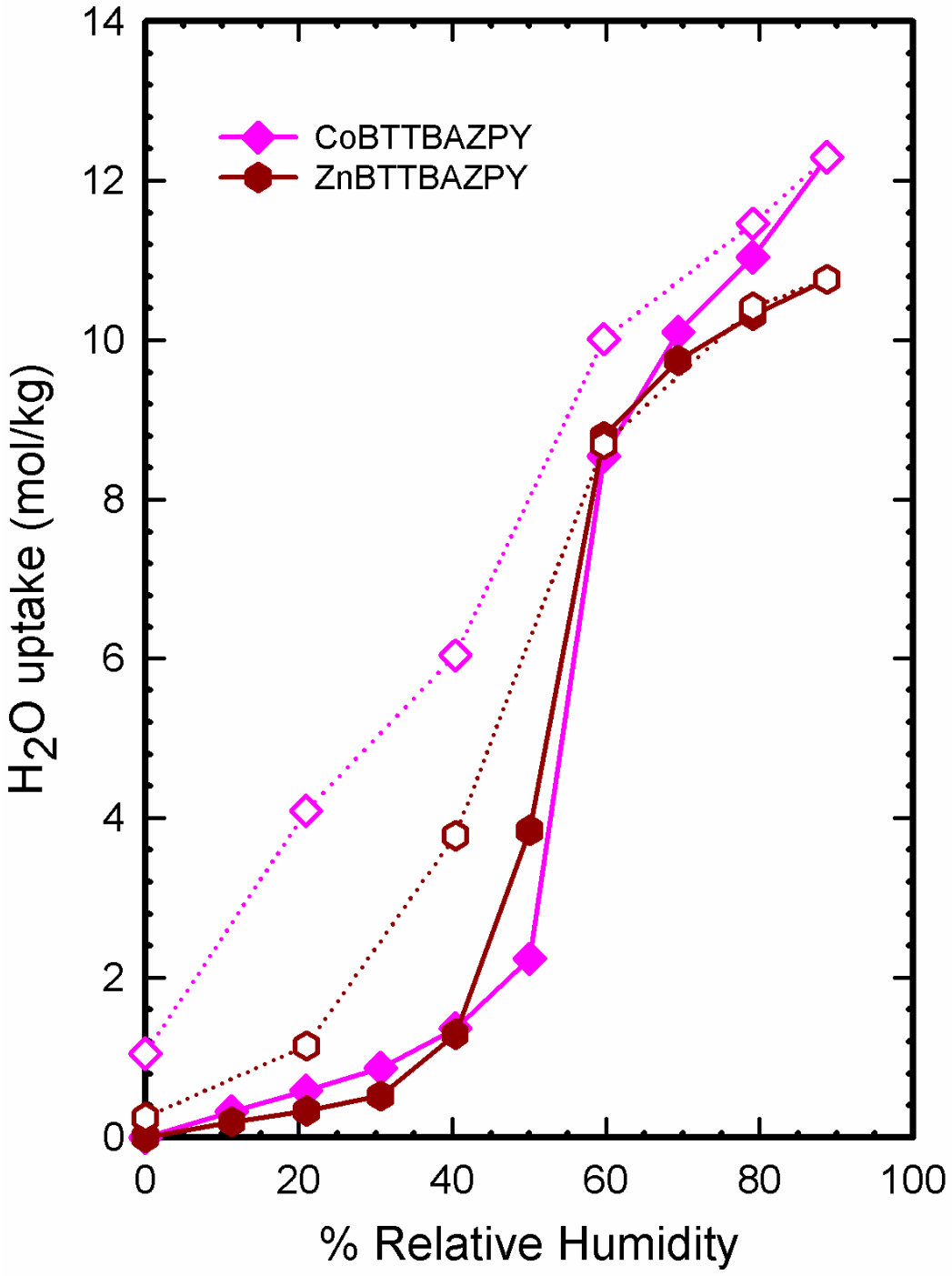

Figure 9.9 Water vapor sorption/desorption isotherms for desolvated compounds of CoBTTBAZPY and ZnBTTBAZPY. (solid curves – adsorption, dashed curves – desorption)

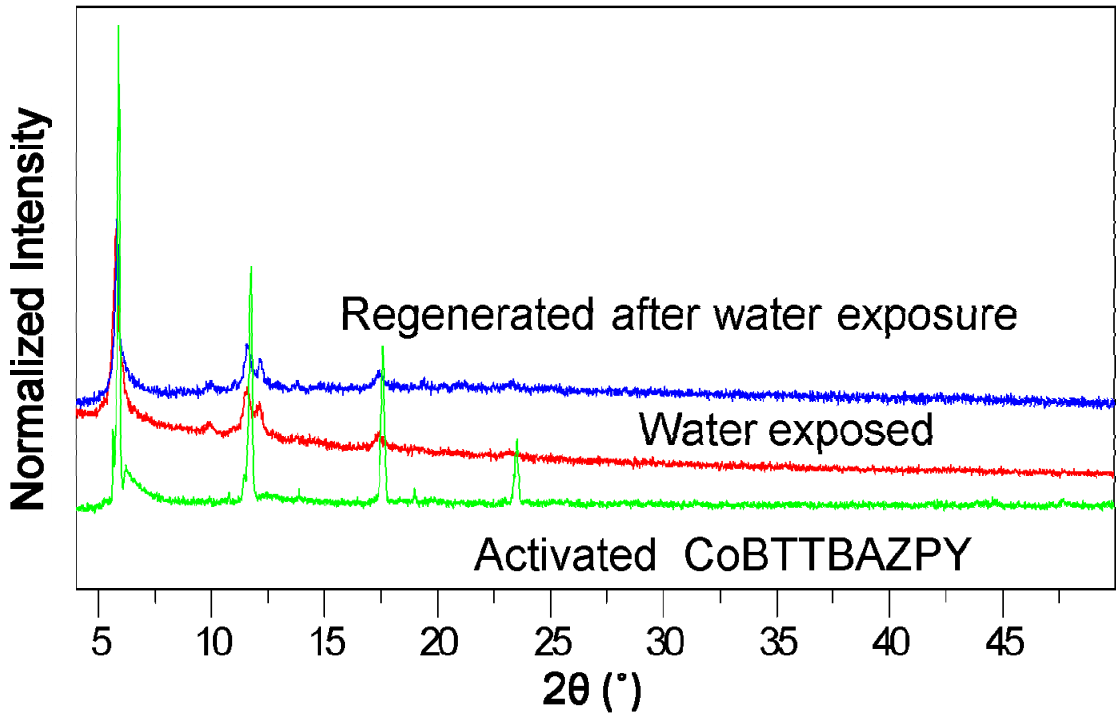

Figure 9.10 Activated, water exposed and regenerated after water exposure powder X-ray diffraction patterns of CoBTTBAZPY

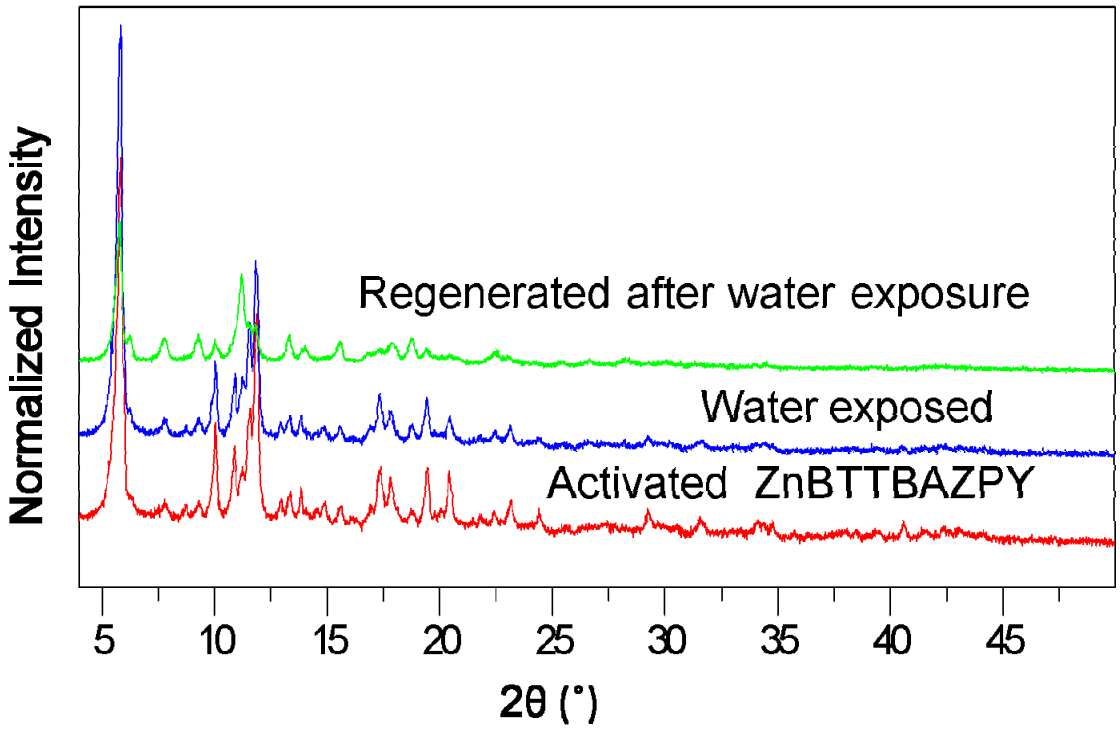

Figure 9.11 Activated, water exposed and regenerated after water exposure powder X-ray diffraction patterns of ZnBTTBAZPY

The water vapor adsorption in AZPY based MOFs (pore size of 4.942 Å) are compared with BPL activated carbon[11, 12] (pore size of 6-18 Å) and traditional mesoporous materials,[13] MCM-41 (mean pore size of 30 Å) and SBA-15 (mean pore size of 50 Å). As can be seen from the Figure 9.12 that all the materials display type V behavior[10], indicative of their low sorption at lower relative humidity and suddenly high water sorption at higher levels of relative humidity. Capillary condensation for CoBTTBAZPY and ZnBTTBAZPY is observed at 40% relative humidity, while that of BPL activated carbon, MCM-41 and SBA-15 is observed at 50%, 65% and 80% relative humidity

respectively. This indicates that capillary condensation occurs first at lower levels of relative humidity for the material with the smaller pores, followed by the material with the next larger pore size and so on. All these materials have heterogeneity in their system. For example, silanol groups, carbonyl groups, etc provide heterogeneity in mesoporous silica and activated carbons while free nitrogen sites provide heterogeneity in AZPY-based MOFs. For these type of materials, surface adsorption is dominant at lower relative humidities due to heterogenous nature of the material while condensed water fills pores at higher relative humidities.[13, 14]

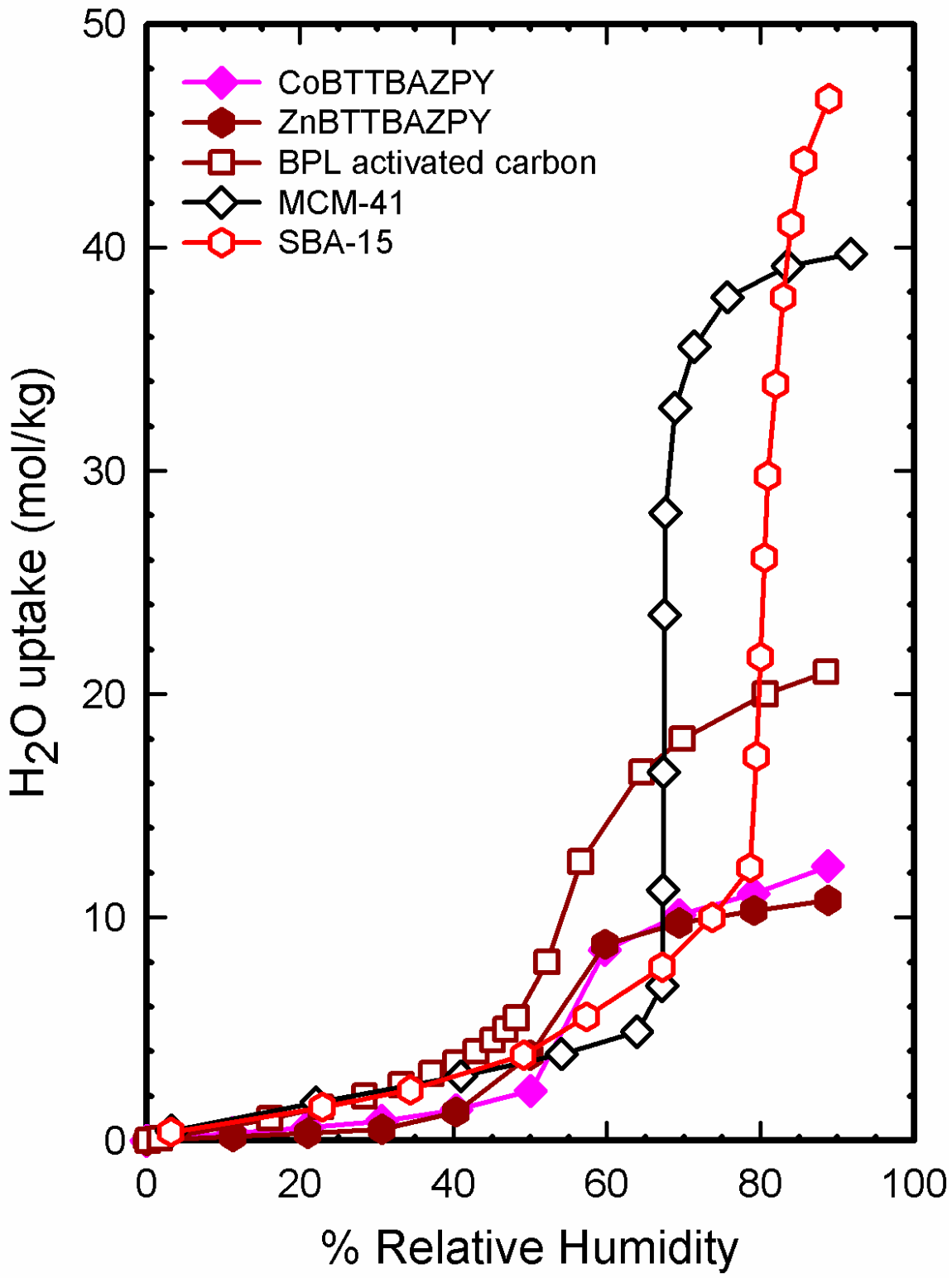

Figure 9.12 Water vapor sorption/desorption isotherms for desolvated compounds of CoBTTBAZPY, ZnBTTBAZPY, BPL activated carbon, SBA-15 and MCM-41.

The results of the BTTB based MOFs were compared with zeolites 5A[1] (calcium form of zeolite A) and 13X[1] (sodium form of zeolite X), hydrophilic MOFs[8] (CuBTC and UIO-66) and hydrophobic MOF (Znbdcdabco)[8] (as shown in Figure 9.13). Zeolites and Cu-BTC MOF exhibit type I behavior due to the electrostatic interactions of polar water molecules and the metal cations or open copper sites. Although CdBTTB, NiBTTB, and ZnBTTBBDC have open metal sites, none of the BTTB MOFs exhibit type I behavior. This indicates that the water-surface interactions in BTTB MOFs are not as strong as compared to zeolites and Cu-BTC. This could be due to the presence of large number of non-polar aromatic rings of BTTB ligands in their frameworks. Water vapor capacities at 90% relative humidity are 27.6 mol/kg (49.6 wt %) for CuBTC and 22.4 mol/kg (41.3 wt %) for UIO-66 significantly higher than all the BTTB based MOFs. Compared to hydrophobic MOF ZnBDCDABCO, water uptake is less in ZnBTTBBPY and CoBTTBBPY. However, all the pillared type MOFs have a very low uptake compared to zeolites and other MOFs. These findings suggest that MOFs made from nitrogen bearing ligands are more stable compared to other metal-carboxylate MOFs.

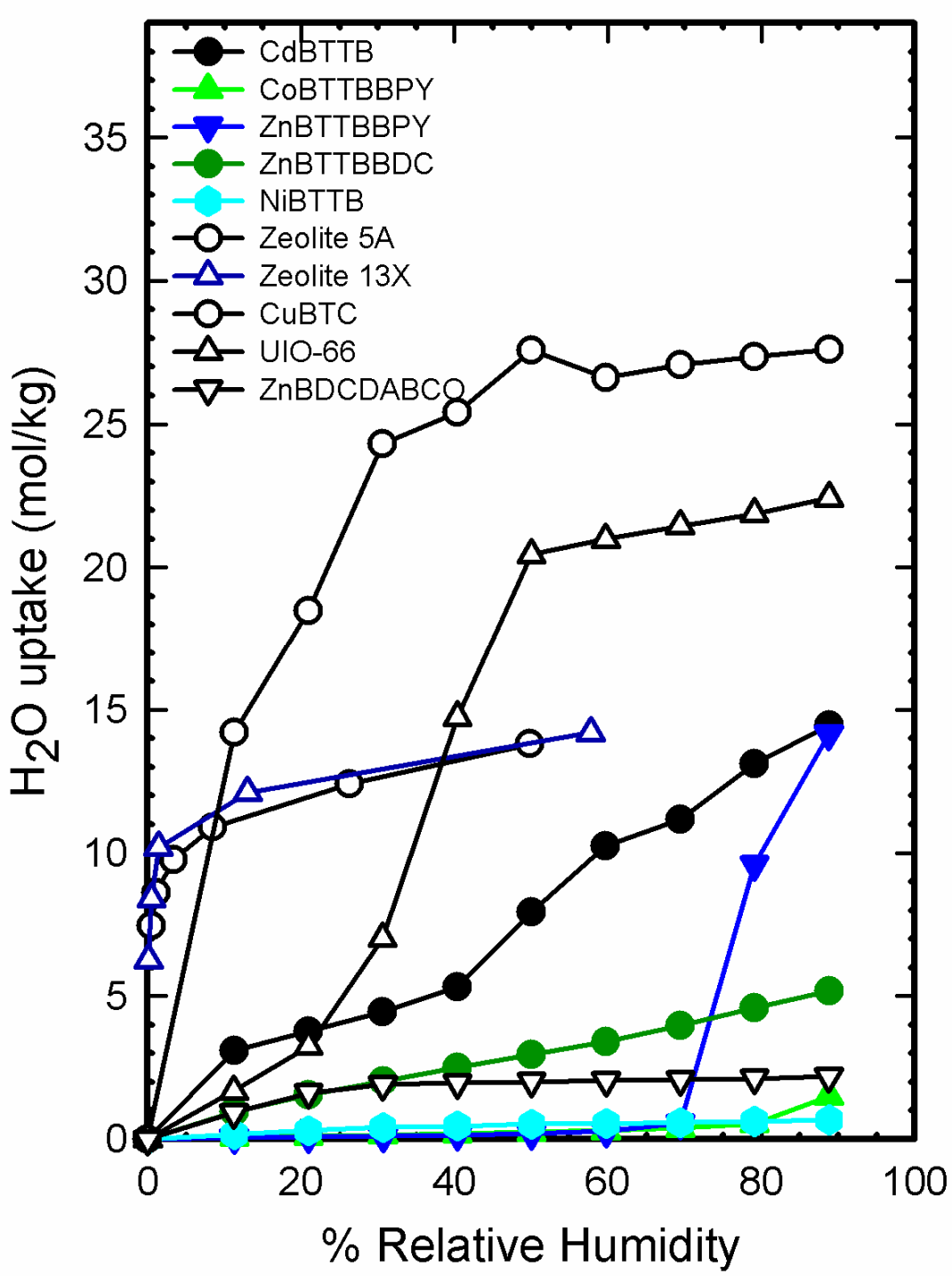

Figure 9.13 Water vapor sorption/desorption isotherms for desolvated compounds of BTTB based MOFs, CuBTC, ZnBDCDABCO, UIO-66 and zeolites, 5A and 13X.

9.4 CONCLUSIONS

The water vapor stability of the BTTB based MOFs was investigated by conducting water vapor adsorption experiments and subsequent structural analysis on these MOFs. The crystal structures of ZnBTTB and CdBTTB were completely degraded after water exposure and regeneration. The instability of ZnBTTB was attributed to the four-coordinate zinc carboxylate system while that of CdBTTB was attributed to weak cadmium-carboxylate system. The crystal structure of ZnBTTBBDC showed structure retention after water exposure, although loss of crystallinity was observed after thermal activation. This was attributed to 6-coordinate zinc-carboxylate system and the metal-oxide clusters arrangement. CoBTTBAZPY and ZnBTTBAZPY showed analogous behavior as mesoporous silicas and BPL activated carbon. The crystal structure of AZPY-based MOFs showed loss of crystallinity after water exposure. This was attributed to the strong interactions between water molecules and free nitrogen sites. ZnBTTBBPY, CoBTTBBPY and NiBTTB showed hydrophobic nature compared to other BTTB based MOFs, Cu-BTC, UIO-66, zeolites and mesoporous silicas. BPY-based MOFs showed analogous behavior as hydrophobic MOF ZnBDCDABCO. The results of this study suggest that MOFs connected through nitrogen-bearing ligands show greater water stability than materials constructed solely through carboxylic acid groups.

9.5 REFERENCES

(1) Wang, Y.; Levan, M. D. *J. Chem. Eng. Data* **2009**, , 2839.

(2) Li, Y.; Yang, R. T. *Langmuir* **2007**, *23*, 12937.

(3) Liang, Z. J.; Marshall, M.; Chaffee, A. L. *Microporous Mesoporous Mater.* **2010**, *132*, 305.

(4) Kondo, A.; Daimaru, T.; Noguchi, H.; Ohba, T.; Kaneko, K.; Kanob, H. *Journal of Colloid and Interface Science* **2007**, *314*, 422.

(5) Kusgens , P.; Rose, M.; Senkovska, I.; Frode, H.; Hensche, l. A.; Siegle, S.; Kaskel, S. *Microporous Mesoporous Mater.* **2009**, *120*, 325.

(6) Low, J. J.; Benin, A. I.; Jakubczak, P.; Abrahamian, J. F.; Faheem, S. A.; Willis, R. R. *J. Am. Chem. Soc.* **2009**, *131*, 15834.

(7) Liu, J.; Wang, Y.; Benin, A. I.; Jakubczak, P.; Willis, R. R.; LeVan , M. D. *Langmuir* **2010**, *26*, 14301.

(8) Schoenecker, P.; Carson, C.; Walton, K. S. *Microporous Mesoporous Mater.* , under review

(9) Choi, H. J.; Dinca, M.; Dailly, A.; Long, J. R. *Energy Environ. Sci.* **2010**, *3*, 117.

(10) Ng, E. P.; Mintova, S. *Microporous Mesoporous Mater.* **2008**, *114*, 1.

(11) Rudisill, E. N.; Hacskaylo, J. J.; Levan, M. D. *Ind. Eng. Chem. Res* **1992**, *31*, 1122.

(12) Qi, N.; Levan, M. D. *Carbon* **2005**, *43*, 2258.

(13) Oh, J. S.; Shim, W. G.; Lee, J. W.; Kim, J. H.; Moon, H.; Seo, G. *J. Chem. Eng. Data* **2003**, *48*, 1458.

(14) Liu, J. C.; Monson, P. A. *Langmuir* **2005**, *21*, 10219.

CHAPTER 10

CONCLUSIONS AND RECOMMENDATIONS

10.1 CONCLUSIONS

The research presented in this work is primarily concerned with developing an understanding of the relationship between MOF structural features (pore size, pore volume, surface area, unsaturated metal sites, electrostatics) and adsorption properties of smaller gas molecules (CO, CO_2, N_2) and finding a porous metal organic framework material with large capacity, high selectivity and high hydrothermal stability for CO_2 capture applications. To summarize, this research has contributed to the following:

10.1.1 Molecular Modeling

GCMC simulations were found to predict adsorption equilibria of CO_2, CO, and N_2 in Cu-BTC, IRMOF-1, and Zn MOF in good agreement with the measured experimental data. Detailed studies of CO adsorption on Cu-BTC reveal that the electrostatic interactions between CO and Cu-BTC framework atoms dominate adsorption while CO-CO interactions are insignificant. The simulation studies of CO_2 adsorption suggest that MOFs with smaller pores can have a similar impact on CO_2 adsorption as larger-pore MOFs with open metal sites. CO isotherms suggest that relative pore size has a much smaller impact on adsorption compared to MOFs possessing open metal sites. The binary mixture (CO_2/CO, CO_2/N_2) results show that these MOFs are actually more selective in the mixtures than the pure isotherms would suggest. Cu-BTC is more selective for CO_2

over N_2 at all concentrations of CO_2, while IRMOF-3 is surprisingly selective for CO_2 over CO at higher concentrations of CO_2. The mixture results also show that the effect of gas mixture composition on selectivity is more pronounced at higher pressures. This work shows that open metal sites and small pore diameters are important for high CO_2 selectivity at low pressure (< 5 bar). At high pressure, MOFs that maintain high pore volume while incorporating functional groups into the structure provide the greatest CO_2 selectivities.

10.1.2 Synthesis

Four new single ligand MOFs, CdBTTB, MgBTTB, NiBTTB, ZnBTTB and five new mixed ligand MOFs, ZnBTTBBDC, ZnBTTBBPY, CoBTTBBPY, ZnBTTBAZPY, and CoBTTBAZPY, were synthesized by solvothermal technique using a tetracarboxylate building block 4,4′,4″,4‴-benzene-1,2,4,5-tetrayltetrabenzoic acid (BTTB) in combination with different metal salts and/or co-ligands terepthalic acid (BDC), bipyridine (BPY) and azopyridine (AZPY). All the single ligand MOFs exhibit different network topologies. CoBTTBBPY and ZnBTTBBPY were found to be isostructural with each other. Similarly, CoBTTBAZPY and ZnBTTBAZPY were found to be isostructural with each other. However, all the mixed ligands, ZnBTTBBDC, BPY based MOFs, AZPY based MOFs all exhibit different topologies. In all these complexes, the BTTB ligand displays different degrees of deprotonation and bridging fashions. Metal centers play an important role in governing the coordination motifs. Although, compounds CdBTTB, MgBTTB, NiBTTB, and ZnBTTB were prepared by using $Cd(NO_3)_2.6H_2O$,

$Mg(NO_3)_2.6H_2O$, $Ni(NO_3)_2.6H_2O$, $Zn(NO_3)_2.4H_2O$ with the same ligands under similar solvothermal conditions, they show completely different structures.

10.1.3 Adsorption Experiments

The role of open metal sites and pore sizes has been found to be crucial in deciding the capacity and selectivity for CO_2 from mixtures of natural gas and flue gas. The coordinate strength for the unsaturated metal centers toward CO_2 molecules varies from one MOF type to another. The mixture adsorption results show that ZnBTTBBDC is a good candidate for the CO_2 capture from flue gases and natural gas streams. However, the limitation of this MOF is the low adsorption capacities of CO_2 at ambient conditions. CdBTTB also showed good capacities and good selectivities for CO_2. Our results suggest that further, rational development of new MOF compounds for CO_2 capture applications should focus on enriching open metal sites, increasing the pore volume, and minimizing the size of large pores.

The water vapor stability of the BTTB based MOFs was investigated by conducting water vapor adsorption runs on these MOFs. ZnBTTBBPY, CoBTTBBPY and NiBTTB showed hydrophobic nature compared to other BTTB based MOFs. The results of this study suggest that MOFs connected through nitrogen-bearing ligands show greater water stability than materials constructed solely through carboxylic acid groups.

10.2 FUTURE PERSPECTIVES

There are opportunities for portions of this work to be extended. My recommendations for future research are as follows:

Flexibility of MOFs: In the simulations, $Zn_2(bdc)_2(dabco)$ structure was constructed by using the atomic coordinates reported and this MOF lattices were assumed to be rigid in the simulations. This MOF has been reported as a flexible and dynamic MOF[1] and has shown unusual guest-induced structural changes – the framework expands upon guest release and shrinks upon guest uptake. Therefore, it would be appropriate to consider the flexibility of the MOF structure while computing the single component and mixture isotherms to see if the flexibility of the framework has a significant influence on the adsorption properties of the gases studied here.

Identifying reaction trends: In this study, BTTB based MOFs crystals were grown using mixed solvent system (DEF/ethanol/water) and temperature 100 ˚C. It is important to understand how subtle changes, such as temperature, solvent system, reaction time, metal salt to ligand molar ratio, can influence framework crystallization. This would give us a better understanding of the effect of different reaction parameters on the crystallization process and help us in optimizing the reaction conditions and identifying the reaction trends. These studies can make significant contributions to the state of art of this growing field.

Exploration of new MOFs: This study has explored only the reaction of metals Cd, Ni, Co, Zn, and Mg with the BTTB ligand sytem. Other metal centers such as lanthanides

could be chosen to try with BTTB ligand system. This could yield luminescent materials that could have potential applications in sensors and other areas.

Supercritical CO_2 drying: The removal of solvent for some of the MOFs, CdBTTB, ZnBTTB, ZnBTTBBDC and MgBTTB, was done near the decomposition temperatures for a short period of time. Although these MOFs gave reasonable BET surface areas, we still believe that some of the pores could have been collapsed at those high temperatures. This could be prevented by exchanging the solvent with ethanol and performing the supercritical CO_2 drying. Such type of drying treatment has been performed on some MOFs in the literature and has shown remarkable improvements in surface areas.[2] Hence, we believe that performing supercritical CO_2 drying could enhance the BET surface areas and increase the stability of activated MOFs.

Multicomponent mixture studies: This work has performed only the individual water vapor and CO_2 adsorption equilibrium studies on BTTB based MOFs, but not the mixture studies. In practice, a gas or gas mixture usually contains a small amount of moisture. The presence of water in the MOFs may be beneficial or adverse to CO_2 capture performance.[3] Hence, future studies should focus on studying the effects of water vapor on CO_2 capture performance. This would give us a better idea of the role that water vapor plays in the interaction and possible blocking of the open metal sites and active adsorption sites. Furthermore, the presence of contaminants, such as NO_x, SO_x, etc in the flue gas and natural gas streams could lead to a reduction in CO_2 performance in MOFs. So, there is a need to study and understand the impact of contaminants on MOF structure and CO_2 adsorption properties.

Investigation of structural effects at the molecular level: Although we have performed experimental investigations on the adsorption properties of BTTB based MOFs, our understanding of the effects of structural features on the adsorption properties at the molecular level is as yet incomplete. Molecular simulations might be a suitable tool to complement experimental efforts.

In-situ Infrared spectroscopy studies: CdBTTB, NiBTTB data have shown higher adsorption capacities and selectivities for CO_2 at lower pressures. We attributed this behavior to the presence of open metal sites in these MOFs. However, this needs to be further examined. In-situ infrared spectroscopy studies on these MOFs could be helpful in providing insight into molecular-level details of the influences of the location of open cadmium sites and nickel sites on the adsorption of carbon dioxide in such type of topologies.

Validation of IAST Theory: Ideal adsorbed solution theory (IAST) was applied to predict the adsorption isotherms of CO_2/N_2 and CO_2/CH_4 gas mixture in BTTB based MOFs. However, the validity of IAST theory for prediction of adsorption isotherms is debatable. So, multi-component adsorption equilibrium studies and molecular modeling studies should be performed on these MOFs in order to verify the prediction of adsorption isotherms from IAST theory.

Long term stability of MOFs: Despite the utmost importance of the long term stability of MOFs, no studies addressed this issue through extensive recycling. The lifetime of adsorbents, which determines the frequency of their replacement, is a critical property of equal importance as adsorption capacity, selectivity, and kinetics, with direct impact on

the economics of commercial scale operations. So cycle tests or reusability tests could be carried to test the stability after sufficiently long operation time.

Proposal of New ligands: Most of the BTTB based MOFs were unstable in the presence of humid air streams. This was because of the weak basicity of the BTTB ligand. Utilization of higher basic organic ligands can lead to more robust MOFs and can be stable in the presence of moisture. We propose here two ligands 6,6′,6″,6‴-(pyrazine-2,3,5,6-tetrayl)tetrakis(1,2,4,5-tetrazine-3-carboxylic acid) (PTTTCA) and 6,6′,6″-(1,3,5-triazine-2,4,6-triyl)tris(1,2,4,5-tetrazine-3-carboxylic acid) (TTTCA) (Figure 10.1) with higher basicity in this work. There are no MOFs reported on these ligands so far. We envision that MOFs constructed from these two ligands (shown in Fig) and different metal clusters, could lead to more robust and thermally stable MOFs and could be highly selective for CO_2 adsorption separations. Therefore, future studies could focus on designing and synthesizing these types of ligands.

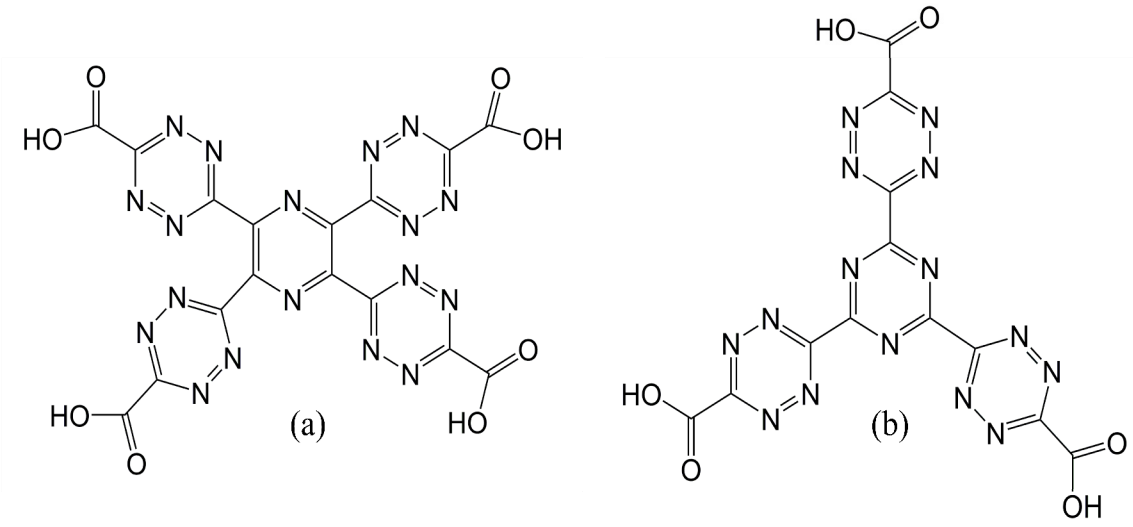

Figure 10.1 Structure of Ligands a) PTTTCA) and b) TTTCA

This work has investigated only the application of the synthesized MOFs for CO_2 capture applications. However, the BTTB based MOFs could be explored for a number of other applications.

Separation of alkane mixtures: Their selective adsorption and high thermal stability could make these BTTB based MOFs potentially useful for alkane separations. In the petroleum industry, the separation of linear from branched alkanes is an important process to boost octane ratings in gasoline.[4] Therefore, these MOFs could be explored for adsorptive separation of adsorptive separation of alkanes, such as mixtures of 2-methylbutane, n-pentane, 2,2-dimethylbutane, 2-methylpentane, and n-hexane.

Air purification: Filtration adsorbents are critical in removal of chemical warfare agents and other toxic chemicals in both military and non-military applications. The impregnated activated carbon has proven to be effective in containing a range of toxic gases, but they are not completely effective against filtering high vapor pressure gases, such as CO, NO_x, and ethylene oxide.[5] So, the MOFs synthesized in this work could be explored for these applications.

Separation of alkylaromatic isomers: The separation of C8 alkylaromatic compounds such as p-xylene, m-xylene, and ethylbenzene has been a challenging problem due to the similarities of their boiling points.[6] Zeolites are currently being used for the recovery of para-xylene and ethylbenzene.[6] The MOFs discovered in this study could be explored for these applications.

Separation of rare gases: Separation of rare gases, such as krypton and xenon, is expensive and is currently being done by cryogenic distillation in the chemical industry.[7]

BTTB MOFs synthesized in this work have the potential to make an impact here due to their selective adsorption, uniformly arranged pores and absence of blocked bulk volume. Therefore, further studies could address the separation of these rare gases by adsorption on these MOFs.

Other separations: BTTB based MOFs could be of interest in other applications such as CO_2/H_2, CH_4/N_2, O_2/N_2, solvent removal from air, odors from air, and separations of alcohols from water.[5]

Thin films and Membrane applications: There are only a few thin film studies on MOFs.[8] So, future studies should focus on synthesizing thin films to understand its potential application in separation of mixture of various gases and vapors, including linear, branched, and cyclic hydrocarbons, H_2, O_2, N_2, and H_2O. In this study, ZnBTTBBDC has shown high adsorption selectivities but low adsorption capacities. This material could be of interest in membrane separations. Therefore, experimental and molecular modeling studies should be conducted on this MOF to understand its diffusion properties of single component and mixtures. Another application of the MOFs that can be of interest could be in mixed matrix membrane applications to enhance the selectivity and throughput.

Drug delivery and Catalysis applications: Outside the scope of this research, the BTTB based MOFs could be explored for medical applications, such as the storage of nitric oxide for drug delivery to prevent platelet aggregation and aid in wound repair.[9] Their applications in catalysis could be of interest as some of the MOFs had open metal

sites and their Lewis acidity and catalytic activity could be probed for different catalytic reactions.[10]

10.3 REFERENCES

(1) Dybtsev, D. N.; Chun, H.; Kim, K. *Angew. Chem. , Int. Ed.* **2004**, *43*, 5033.

(2) Farha, O. K.; Hupp, J. T. *Acc. Chem. Res.* **2010**, *43*, 1166.

(3) Liu, J.; Wang, Y.; Benin, A. I.; Jakubczak, P.; Willis, R. R.; LeVan , M. D. *Langmuir* **2010**, *26*, 14301.

(4) Dubbeldam, D.; Galvin, C. J.; Walton, K. S.; Ellis, D. E.; Snurr, R. Q. *J. Am. Chem. Soc.* **2008**, *130*, 10884.

(5) Britt, D.; Tranchemontagne, D.; Yaghi, O. M. *Proc. Natl. Acad. Sci. U. S. A.* **2008**, *105*, 11623-11627.

(6) Alaerts, L.; Maes, M.; Giebeler, L.; Jacobs, P. A.; Martens, J. A.; Denayer, J. F. M.; Kirschhock, C. E. A.; De Vos, D. E. *J. Am. Chem. Soc.* **2008**, *130*, 14170-14178.

(7) Czaja, A. U.; Trukhan, N.; Müller , U. *Chem. Soc. Rev.* **2009**, *38*, 1284.

(8) Shekhah, O.; Liu, J.; Fischer, R. A.; Wöll, C. *Chem. Soc. Rev.* **2009**, *40*, 1081.

(9) Keskin, S.; Kizilel, S. *Ind. Eng. Chem. Res* **2011**, *50*, 1799.

(10) Corma, A.; Garcia, H.; Xamena, F. X. L. *Chem. Rev* **2010**, *110*, 4606.

APPENDIX A

EXPERIMENTAL AND MOLECULAR SIMULATION STUDIES OF CO_2, CO, AND N_2 ADSORPTION IN METAL ORGANIC FRAMEWORKS

Experimental Section

Zinc nitrate tetrahydrate ($Zn(NO_3)_2.4H_2O$), p-benzenedicarboxylic acid (H_2BDC,), N,N'-dimethylformamide(DMF), 1,4-diazabicyclo[2.2.2]octane(dabco), Copper nitrate trihydrate ($Cu(NO_3)_2.3H_2O$) , 1,3,5-benzenetricarboxylic acid (H_3BTC), Ethanol, were all purchased from fisher and used as received. Powder X-day diffraction (XRD) patterns were recorded with a Bruker AXS D8 Advance diffractometer using nickel-filtered Cu Kα radiation ($\lambda = 1.5418$ Å) operated at 40 kV and 40 mA. SEM photographs were taken using a Hitachi SEM-3500N equipped with a model S-6542 absorbed electron detector. Nitrogen adsorption/desorption isotherms at 77 K were measured with an Autosorb 1-MP from Quantachrome Instruments. Prior to nitrogen physisorption measurements, the activated samples of Cu-BTC and Zn MOF were degassed at 150 °C for overnight using the degasser of the gas sorption apparatus.

Synthesis of Cu-BTC

The synthesis procedure reported by Schlichte et al[1] was followed for this MOF. Cu-BTC was synthesized under mild hydrothermal conditions using Teflon-lined 45-mL Parr autoclaves. For the synthesis of Cu-BTC, 0.875 g of $Cu(NO_3)_2\ 3H_2O$ were dissolved in 12 ml de-ionized water and mixed with 0.42 g of trimesic acid dissolved in 12 ml ethanol.

The reaction mixture was stirred for 1 h to ensure homogeneity prior to heating. The reactants were heated at 130°C for 24 hours. After reaction, products were filtered,

washed with ethanol, and dried in air. Then the sample was kept in a Petri dish and evacuated for overnight in a vacuum oven at 150° C to remove the solvent molecules.

Synthesis of $Zn_2(bdc)_2(dabco)$:

The synthesis procedure reported by Lee et al[2] was followed for this MOF. A mixture of $Zn(NO_3)_2.4H_2O$ (0.935 g), H_2BDC (0.616 g), dabco (0.219 g) and 90 ml of DMF were stirred for 30 minutes and then transferred to a Teflon-lined autoclave and heated in an oven at 120 ^oC for 3 days. After reaction, the white crystals were filtered and washed with DMF (10 mL x 3). The crystals were then evacuated at 200 ^oC for 16 hours to give a 1685 m^2/g sample.

Gravimetric measurements:

Gases CO_2 (99.8%), CO (99.5%), N_2 were obtained from Linweld, Inc. (Manhattan, KS) and the adsorption isotherms of CO_2 and CO on Cu-BTC were measured gravimetrically using GHP-100 VTI equipment. This equipment employs a magnetic suspension balance to measure the change in mass of samples deposited in a stainless steel sample holder, suspended within the high pressure adsorption chamber. Prior to the measurements, the sample was outgassed by heating in vaccum at 150 ^oC until the weight was constant (overnight). Successive amounts of adsorbate are then dosed in the adsorption chamber at room temperature 298 K. After each admission, the pressure, the temperature, and the adsorbed mass are measured at regular intervals. Once equilibrium is reached, the temperature, pressure, and mass signals are stored and a new amount of gas is admitted.

The procedure is fully automated. An average time of 30 minutes was set to obtain one adsorbed mass. After the completion of the asdorbate run, helium was dosed into the adsorption cell. The helium run was made to account for the buoyancy correction arising from the variation of the gas density change and and adsorbed phase volume change with the variation in pressure.

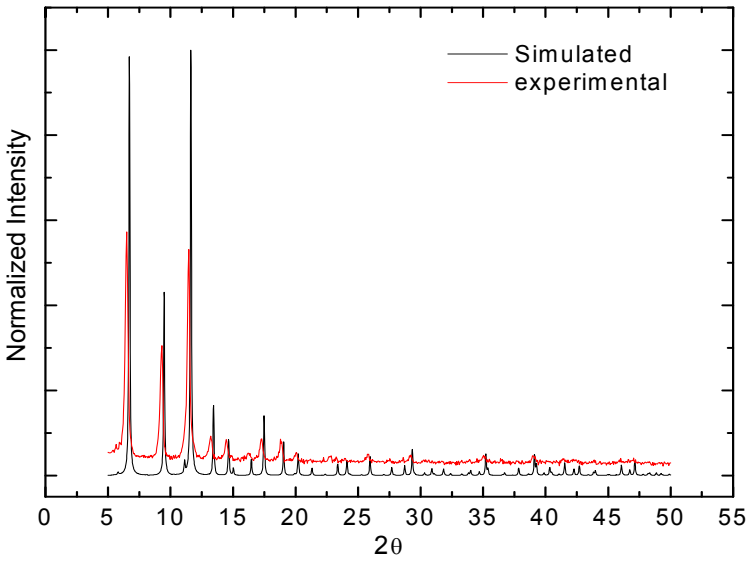

Figure A.1 PXRD patterns for simulated and synthesized Cu-BTC sample.

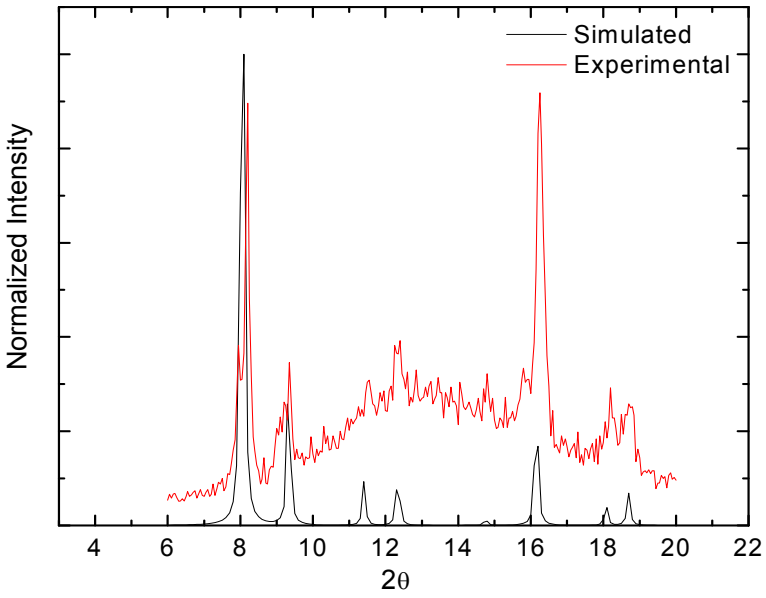

Figure A.2 PXRD patterns for simulated and synthesized Zn MOF sample.

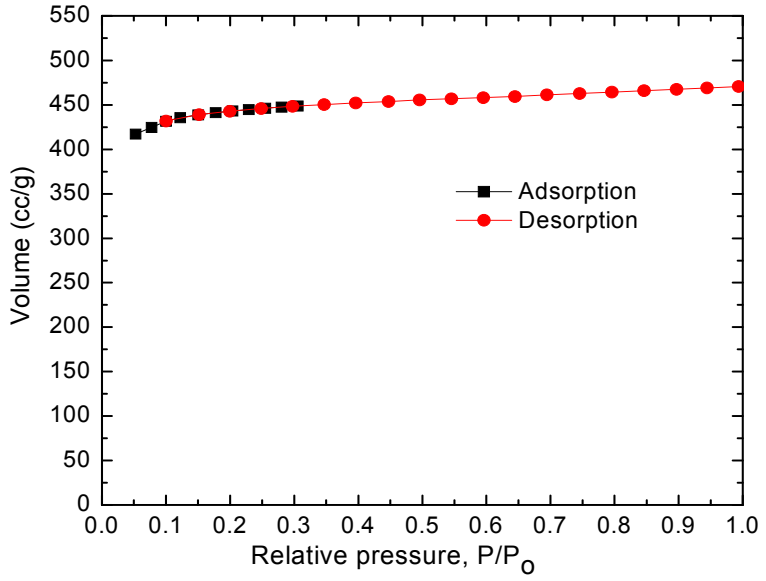

Figure A.3 N_2 adsorption/desorption measurements for Cu-BTC at 77 K. (BET surface area of 1339 m^2/g was obtained for the range $0.05<P/P_o<0.3$)

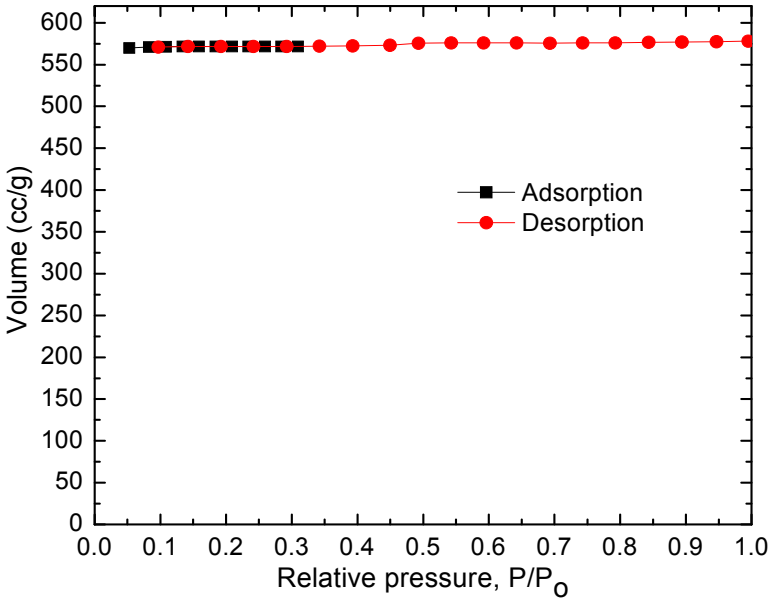

Figure A.4 N_2 adsorption/desorption measurements for Zn MOF at 77 K. (BET surface area of 1685 m^2/g was obtained for the range $0.05<P/P_o<0.3$)

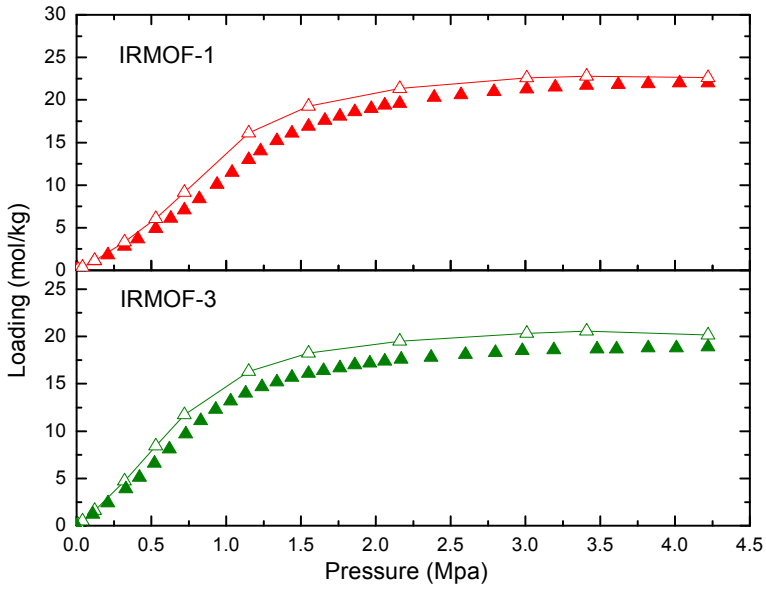

Figure A.5 CO_2 Adsorption isotherms calculated from GCMC simulations vs available experimental isotherms

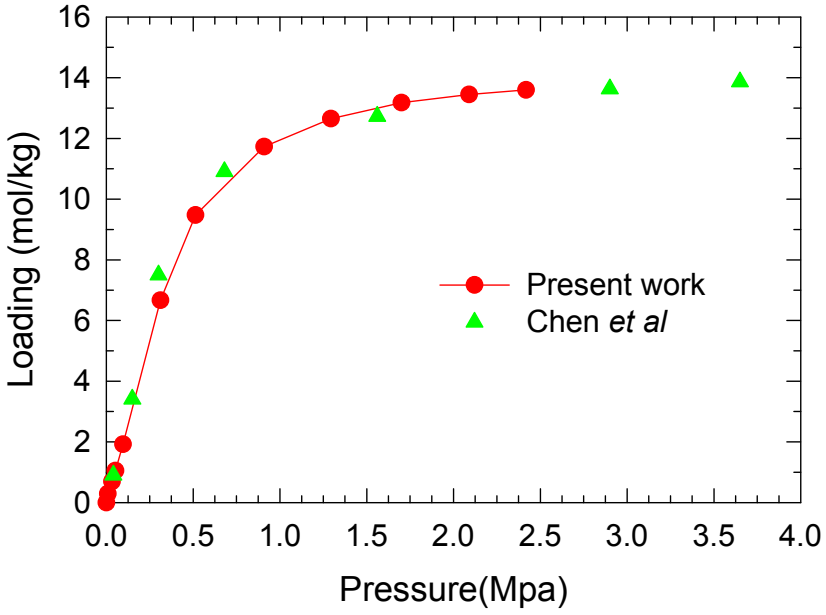

Figure A.6 Comparison of experimental CO_2 Adsorption isotherms of Zn MOF in present work vs literature

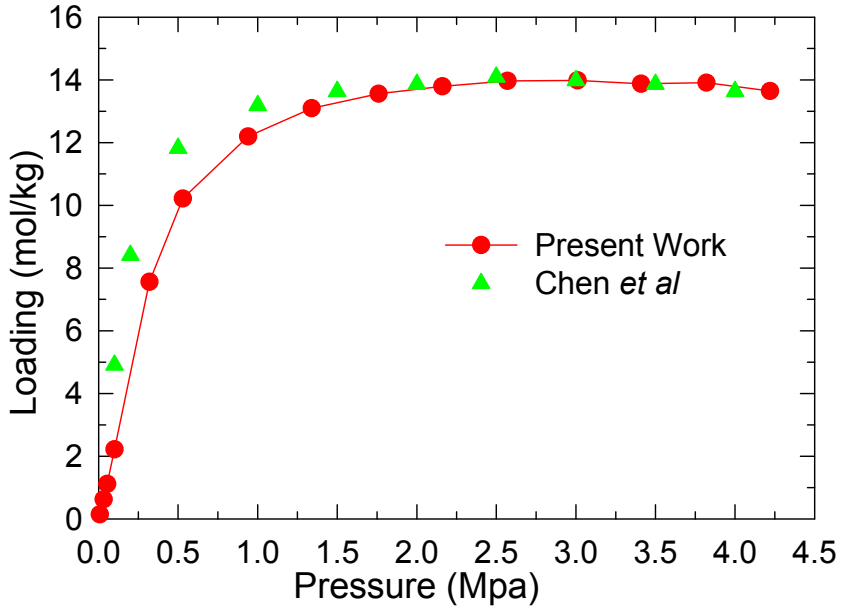

Figure A.7 Comparison of simulated CO_2 Adsorption isotherms of Zn MOF in present work vs literature

Figure A.7 shows the simulated adsorption isotherms of CO_2 in Zn MOF of present work and Chen *et al* work. Chen *et al* work has considered the partial charges on the framework while the present work has ignored the partial charges on the Zn MOF framework. The simulated data of CO_2 of Zn MOF in present work matches well with the reported simulated data at higher pressures. This suggests that electrostatic interactions between the CO_2 molecules and the framework are negligible in Zn MOF.

The discrepancies between the simulated data of Chen *et al* and our simulated data at lower pressures could be due to the following reasons: 1) It could be that partial charges computed by DFT in Chen *et al* work may not be accurate enough to account for this discrepancy at lower pressures. 2) CO_2 models used in the present work and Chen *et al* are slightly different in their bond lengths and charges. 3) The numbers of trial moves used in GCMC simulation are also different in both the works. Present work has carried out only three types of moves - translation, insertion and deletion whereas Chen *et al* have carried out five types of moves - displacement, rotation, partial regrowth at a neighboring position; entire regrowth at a new position; and swap with reservoir including creation and deletion at equal probability.

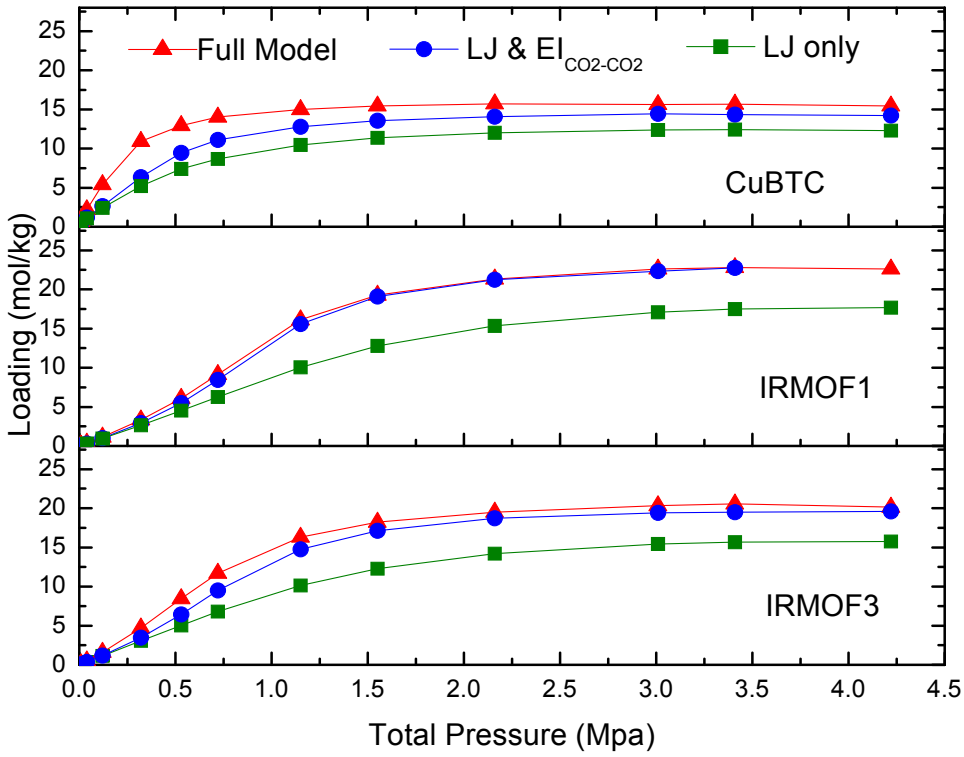

Figure A.8 Effect of electrostatic interactions on CO_2 adsorption in Cu-BTC, IRMOF-1 and IRMOF-3. (Full model considers Lennard-Jones interactions (LJ), sorbate-sorbate and sorbate-MOF electrostatic interactions. LJ and $EI_{CO2\text{-}CO2}$ considers LJ interactions and neglects electrostatic interactions with the framework)

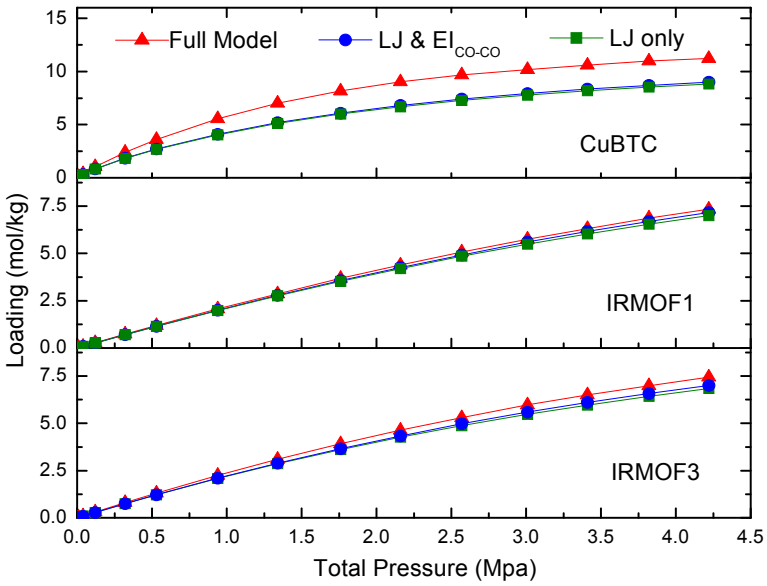

Figure A.9 Effect of electrostatic interactions on CO adsorption in Cu-BTC, IRMOF-1 and IRMOF-3.

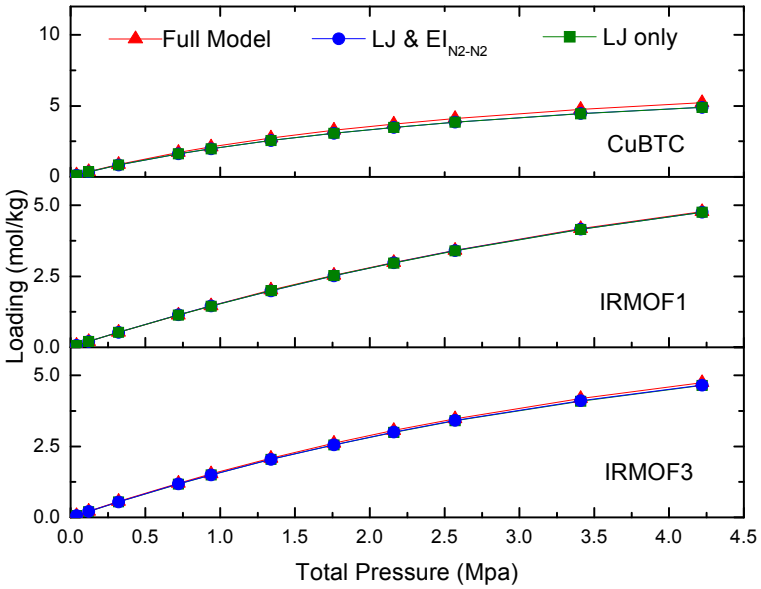

Figure A.10 Effect of electrostatic interactions on N_2 adsorption in Cu-BTC, IRMOF-1 and IRMOF-3

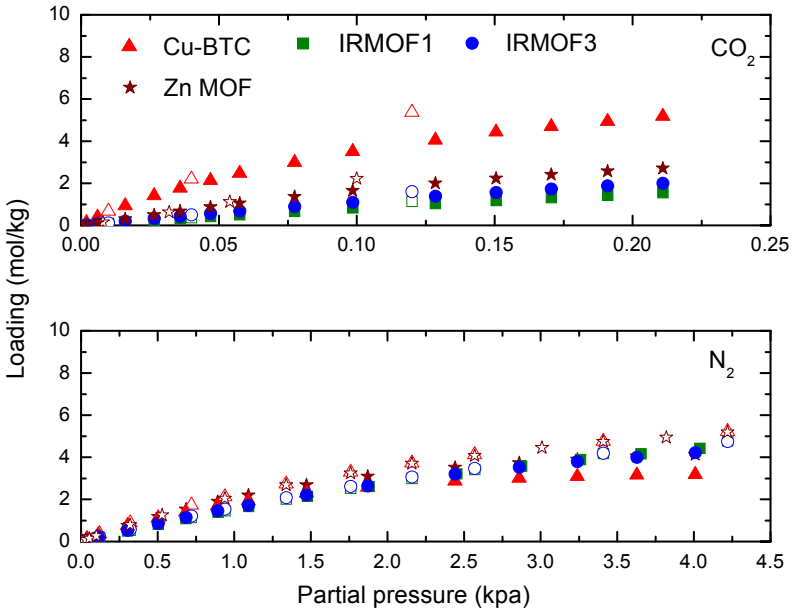

Figure A.11 Comparison of single-component (unfilled symbols) and 5:95 CO_2/N_2 binary mixture (filled symbols) adsorption isotherms for Cu-BTC, Zn MOF, IRMOF-1 and IRMOF-3 at 298 K.

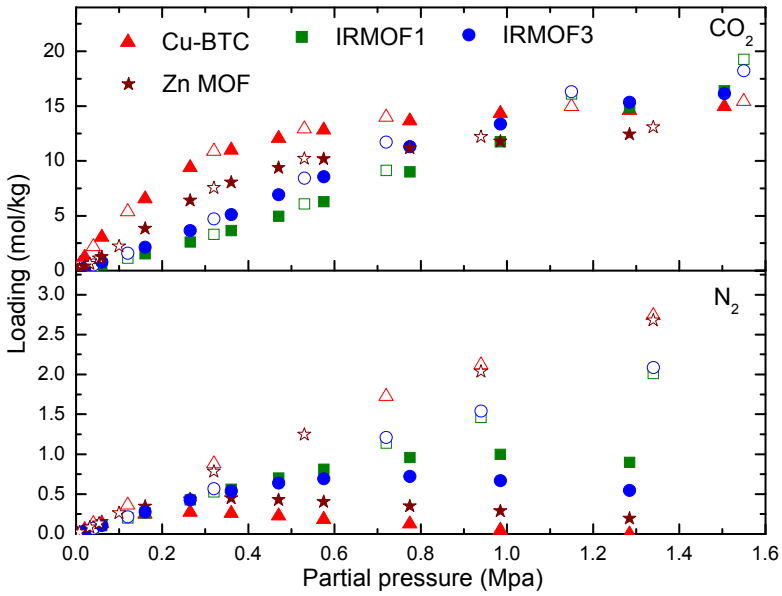

Figure A.12 Comparison of single-component (unfilled symbols) and 50:50 CO_2/N_2 binary mixture (filled symbols) adsorption isotherms for Cu-BTC, Zn MOF, IRMOF-1 and IRMOF-3 at 298 K.

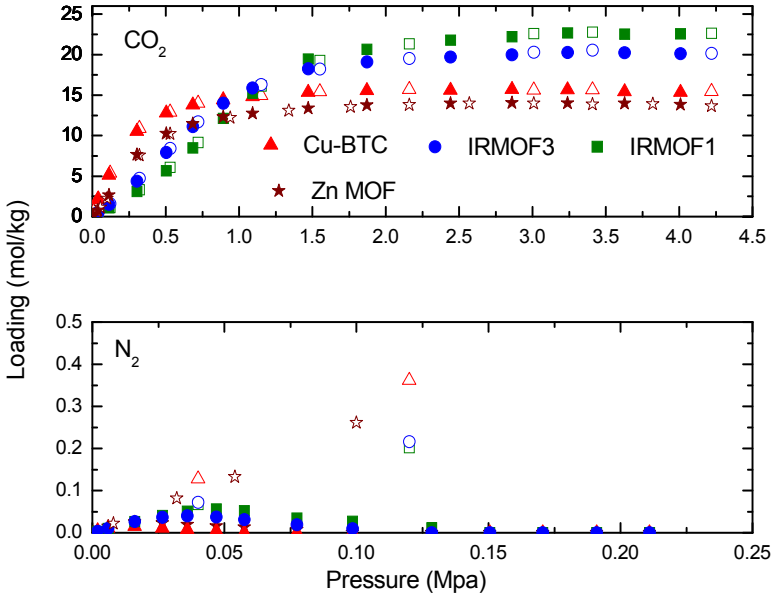

Figure A.13 Comparison of single-component (unfilled symbols) and 95:5 CO_2/N_2 binary mixture (filled symbols) adsorption isotherms for Cu-BTC, Zn MOF, IRMOF-1 and IRMOF-3 at 298 K.

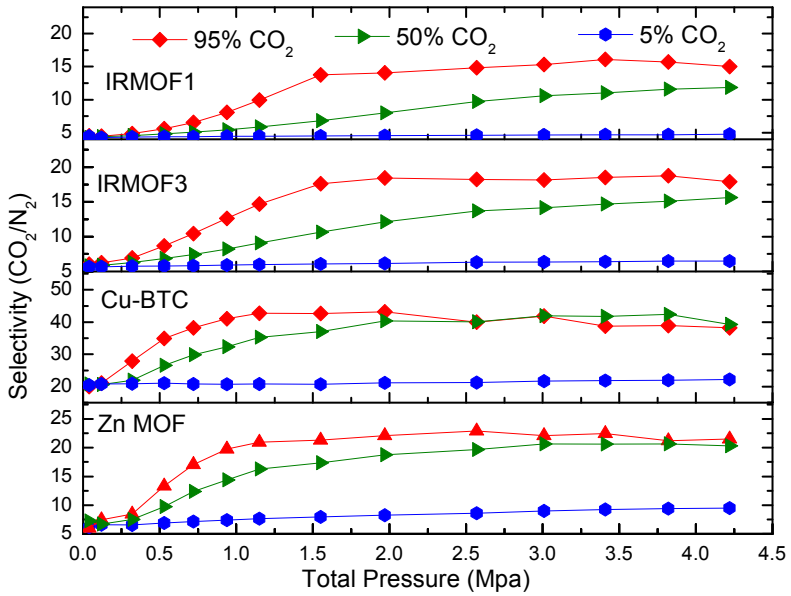

Figure A.14 Adsorption selectivities for CO_2 over N_2 as a function of composition in Cu-BTC, IRMOF-1, IRMOF-3, and Zn MOF at 298 K

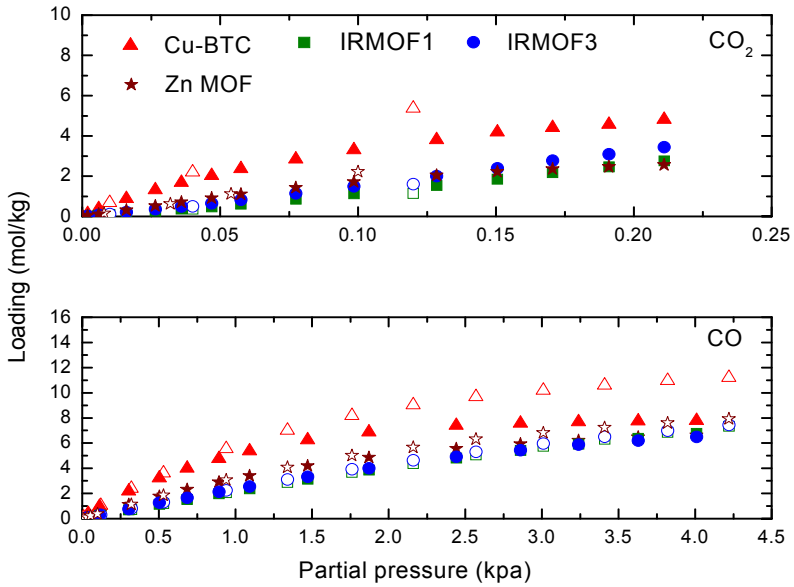

Figure A.15 Comparison of single-component (unfilled symbols) and 5:95 CO_2/CO binary mixture (filled symbols) adsorption isotherms for Cu-BTC, IRMOF-1, IRMOF-3, and Zn MOF at 298 K.

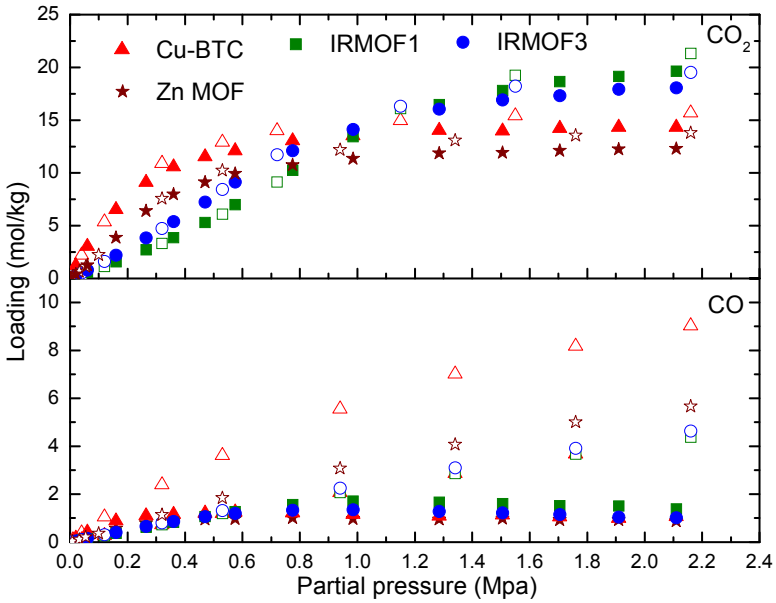

Figure A.16 Comparison of single-component (unfilled symbols) and 50:50 CO_2/CO binary mixture (filled symbols) adsorption isotherms for Cu-BTC, IRMOF-1, IRMOF-3, and Zn MOF at 298 K.

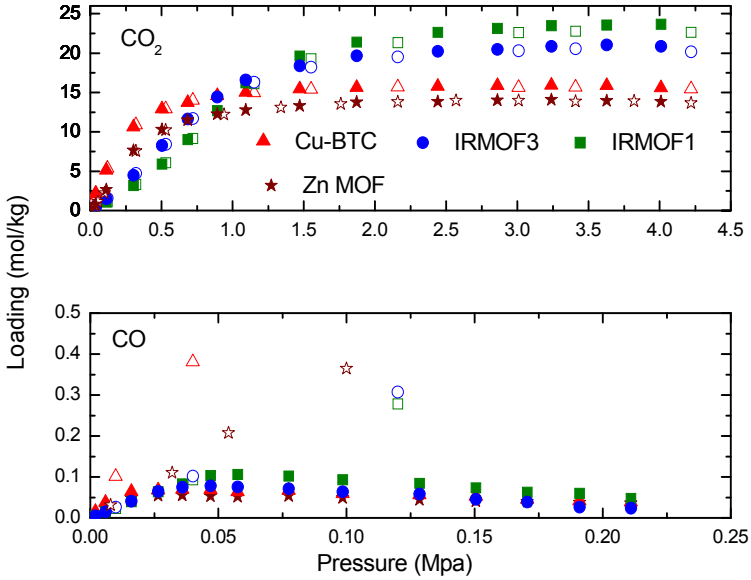

Figure A.17 Comparison of single-component (unfilled symbols) and 95:5 CO_2/CO binary mixture (filled symbols) adsorption isotherms for Cu-BTC, IRMOF-1, IRMOF-3, and Zn MOF at 298 K.

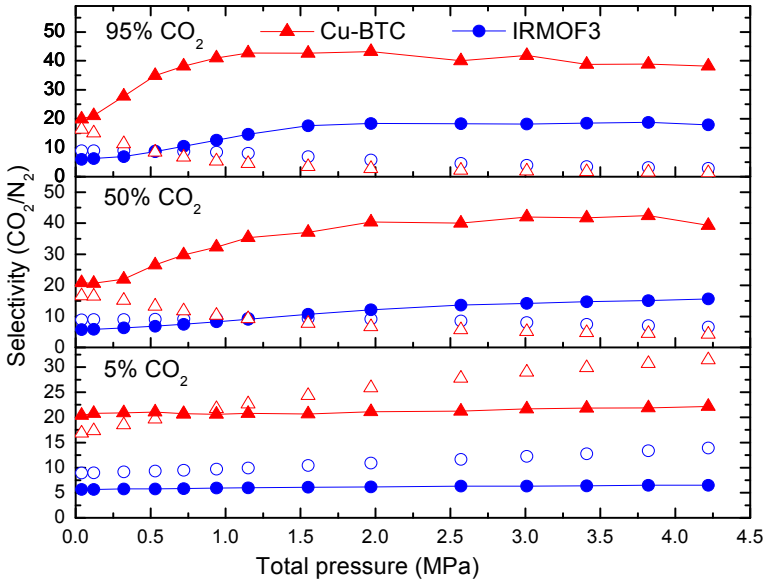

Figure A.18 Adsorption selectivities calculated using gcmc (filled symbol) and pure component data (unfilled symbol) for CO_2 over N_2 in mixtures of 5%, 50%, and 95% CO_2 in Cu-BTC, and IRMOF-3 at 298 K

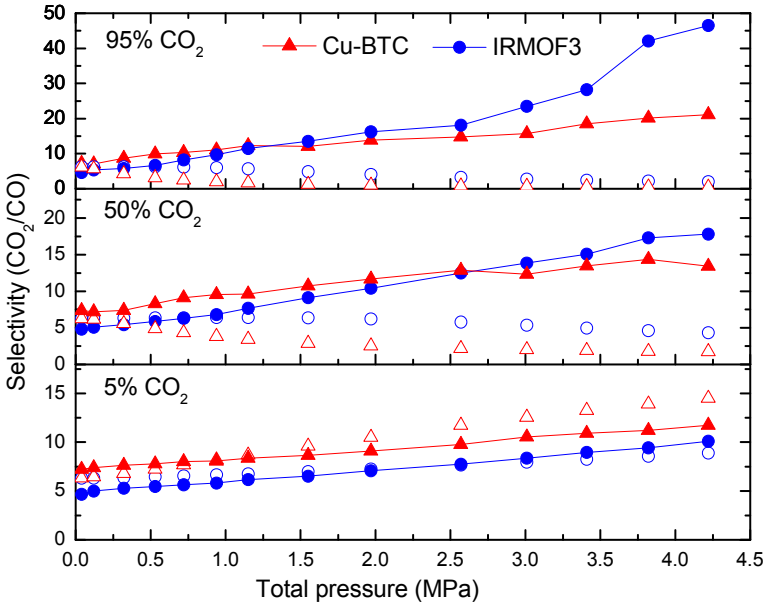

Figure A.19 Adsorption selectivities calculated using gcmc (filled symbol) and pure component data (unfilled symbol) for CO_2 over CO in mixtures of 5%, 50%, and 95% CO_2 in Cu-BTC, and IRMOF-3 at 298 K

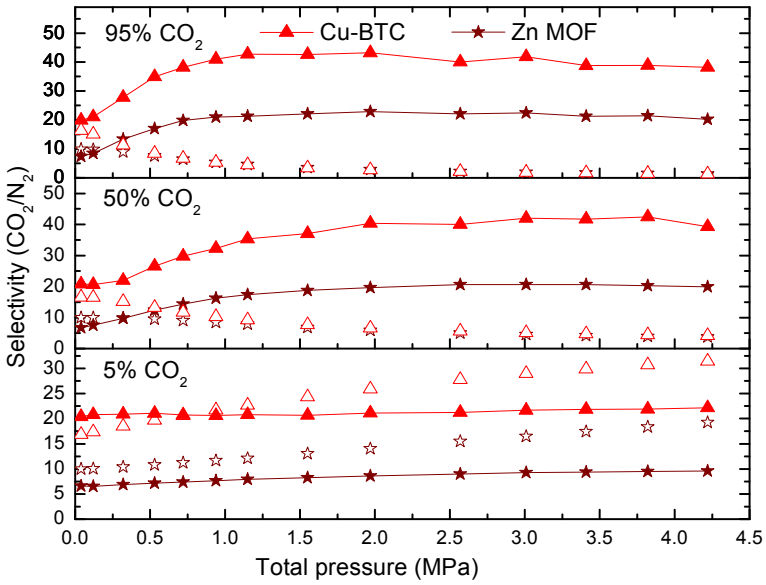

Figure A.20 Adsorption selectivities calculated using GCMC (filled symbol) and pure component data (unfilled symbol) for CO_2 over N_2 in mixtures of 5%, 50%, and 95% CO_2 in Cu-BTC, and Zn MOF at 298 K

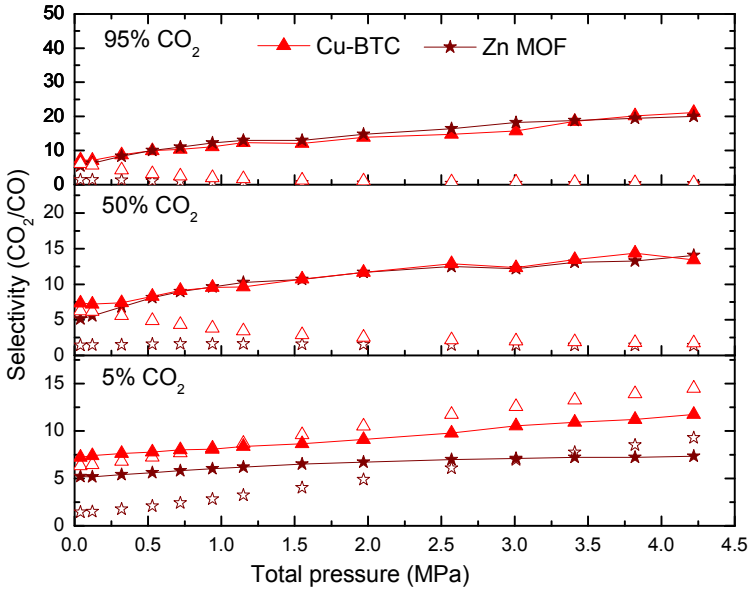

Figure A.21 Adsorption selectivities calculated using GCMC (filled symbol) and pure component data (unfilled symbol) for CO_2 over CO in mixtures of 5%, 50%, and 95% CO_2 in Cu-BTC, and Zn MOF at 298 K.

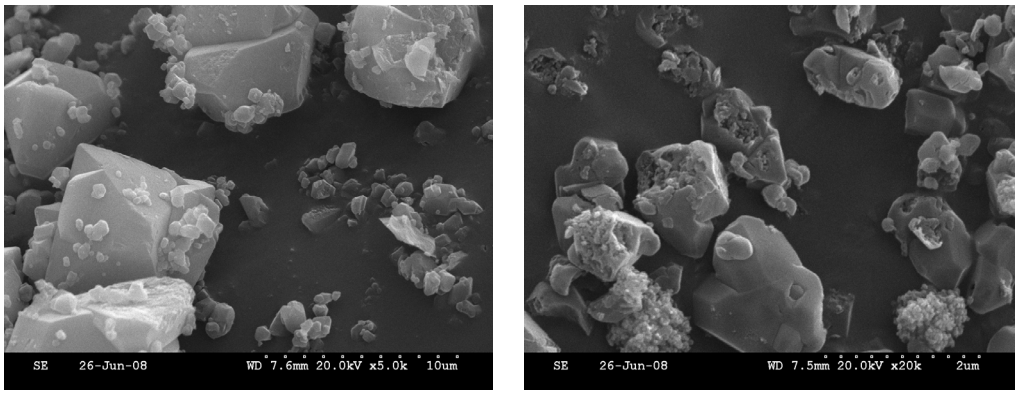

Figure A.22 SEM Photographs of Cu-BTC

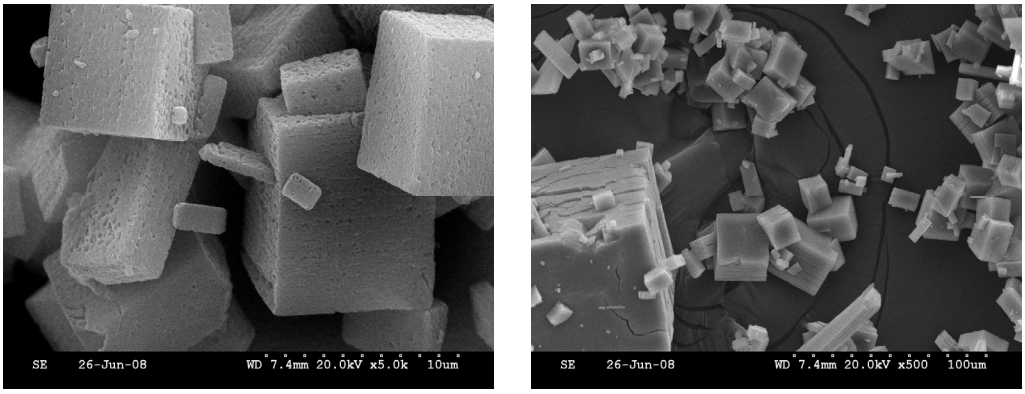

Figure A.23 SEM photographs of Zn MOF

References

(1) Schlichte, K.; Kratzke, T.; Kaskel, S. *Microporous Mesoporous Mater.* **2004***, 73*, 81.

(2) Lee, J. Y.; Olson, D. H.; Pan, L.; Emge, T. J.; Li, J. *Adv. Funct. Mater.* **2007***, 17*, 1255.

APPENDIX B

EXPERIMENTAL STUDIES OF CO AND CO_2 ADSORPTION IN CU-BTC AND DABCO BASED METAL ORGANIC FRAMEWORKS

INTRODUCTION

A fundamental understanding of the role of pore size and open metal sites is crucial in the design of new nanoporous materials for the adsorption and storage of different gases like CO_2 and CO. These gases have been given significant attention during the recent years. CO_2 is a major greenhouse gas contributing to global warming and CO is a major industrial pollutant gas. Various adsorbents such as activated carbon, molecular sieves and zeolites have been examined for their storage and adsorptive separation from different mixtures.[1] Metal organic frameworks, MOFs, built from a metal group and an organic linker, are a recent addition to this class of porous materials. They have some special attributes like the ordered structures; extra high porosity; high surface areas and their pore size can be controlled by modifying the metal group or organic linker.[2] These properties of MOF can improve the gas storage and separation from their mixtures.

Metal sites in porous materials (activated carbon, zeolites, MOFs) are known to have a strong influence on the resulting adsorption properties.[1] We have shown in our molecular modeling studies that the partial charges on the metal sites in CuBTC play a significant role in enhancing the resulting adsorption properties. [3]Adsorbent pore size is also one of the key factors in affecting the gas adsorption. We hypothesize that the open

metal sites and adsorbent pore size could play a significant role in CO and CO_2 adsorption. CO with its dipole and quadruple moment and CO_2 with its quadruple moment could enhance the interaction with the positive charges on the metal sites. In order to understand the effect of open metal sites and adsorbent pore size in the adsorption of CO and CO_2 in metal organic frameworks, we have conducted experimental studies on CO and CO_2 adsorption on one well known MOF, Cu-BTC that has open metal sites and three other relatively new MOFs, M[BDC][DABCO] (M denotes Zn, Co or Cu) that are isostructural in nature and do not have open metal sites. Zeolite 4A was taken as standard material for reference. For CO_2 adsorption, sodium form of zeolite X (13X) and calcium form of zeolite A (5A) were chosen and for CO adsorption, sodium form of zeolite A (4A) and 5A were chosen as reference materials. The data for the adsorption isotherms of 5A and 13X were taken from the literature.[4, 5]

SYNTHESIS AND CHARACTERIZATION

Zinc nitrate tetrahydrate ($Zn(NO_3)_2.4H_2O$), p-benzenedicarboxylic acid (H_2BDC,), N,N'-dimethylformamide(DMF), 1,4-diazabicyclo[2.2.2]octane(DABCO), Cobalt (II) acetate tetrahydrate , Copper nitrate trihydrate ($Cu(NO_3)_2.3H_2O$) , 1,3,5-benzenetricarboxylic acid (H_3BTC), Ethanol, Methanol, Pyridine were all purchased from fisher and used as received. PXRD measurements were collected on a Bruker AXS D8 Advance diffractometer operated at 40 kV and 40 mA with monochromated Cu K_α radiation (λ = 1.5406 Å) with a scan speed of 2.5 sec/step and a step size of 0.1 ^{o} .

Synthesis of Zn[bdc][dabco]. The procedure reported by Lee et al [6] was followed for the preparation of this MOF. A mixture of $Zn(NO_3)_2.4H_2O$ (0.935 g), H_2BDC (0.616 g), TED (0.219 g) and 90 ml of DMF were stirred for 30 minutes and then transferred to a Teflon-lined autoclave and heated in an oven at 120 ^oC for 2 days. The white crystals were filtered and washed with DMF (10 mL x 3). The crystals were then evacuated at 200 ^oC for 16 hours to give a 2024 m^2/g sample

Synthesis of Cu[bdc][dabco]. The procedure reported by Lee et al [6] was followed for the preparation of this MOF. A mixture of $Cu(NO_3)_2.3H_2O$ (0.432 g), H_2BDC (0.410 g), TED (0.291 g) and 90 ml of DMF were stirred for 30 minutes and then transferred to a Teflon-lined autoclave and heated in an oven at 120 ^oC for 2 days. The light green crystals were filtered and washed with DMF (10 mL x 3). The crystals were then evacuated at 200 ^oC for 16 hours to give a 1010 m^2/g sample

Synthesis of Co[bdc][dabco]. The procedure reported by Takei et al [7] was followed for the preparation of this MOF. A mixture of $Co(CH_3COO)_2.4H_2O$ (0.25 g), H_2BDC (0.2 g), distilled water (400 mL) and 100 mL of pyridine solution were stirred for 1 hour and the mixture was allowed to stand for one week at room temperature leaving a pink, plate-like crystal precipitate. The pink precipitate (0.3 g) along with TED (0.3 g) were added to the methanol solution (300 mL) and stirred for 24 hours at 65 ^oC to form a purplish-red powder. This precipitate was washed with methanol and dried at 200 ^oC under vacuum for overnight to give a 898 m^2/g sample.

Synthesis of Cu-BTC. The procedure reported by Schlichte et al [8] was followed for the preparation of this MOF. A mixture of $Cu(NO_3)_2.3H_2O$ (5.25 g), BTC(2.52g),

deionized water (72 mL) and 72 ml of ethanol were stirred for 30 minutes and then transferred to a Teflon-lined autoclaves and heated in an oven at 130 ^{o}C for 19 hours. The light blue crystals were filtered and washed with ethanol (10 mL x 3). The crystals were then evacuated at 200 ^{o}C for 16 hours to give a 1339 m^2/g sample.

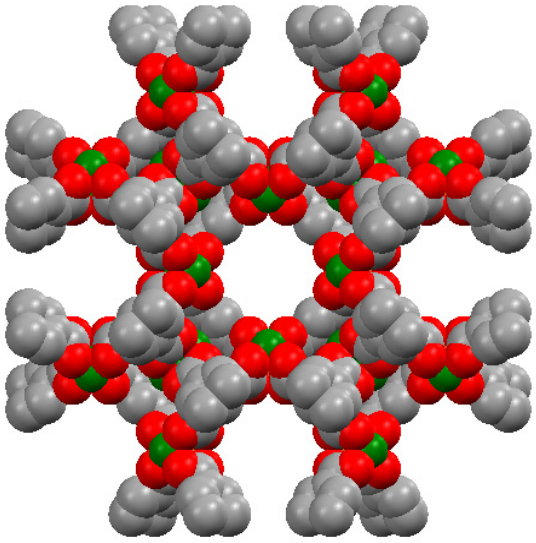

Figure B.1 Perspective view of the 3D network of Cu-BTC along [1 0 0] direction Color scheme: Cu, green; C, grey; O, red

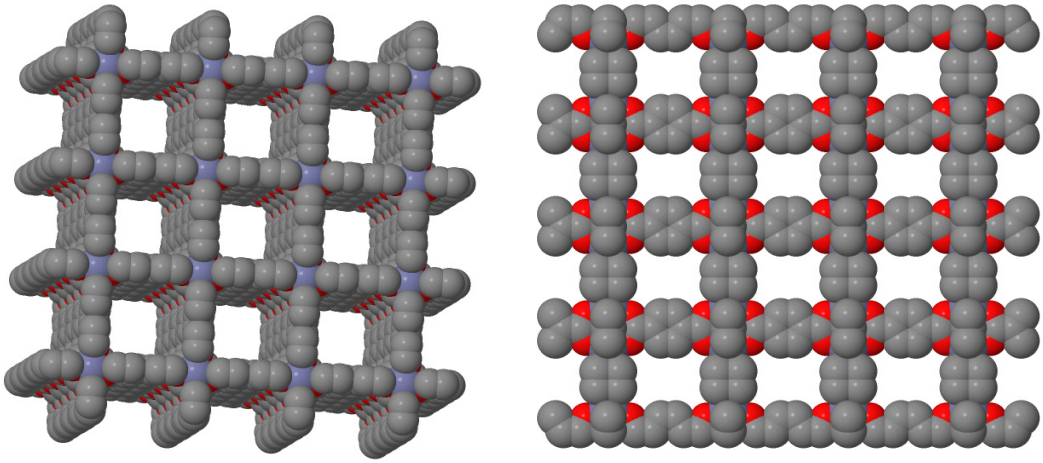

Figure B.2 Perspective view of the 3D network of M[bdc][dabco] along [1 0 0] and [0 1 0] direction Color scheme: Zn, light blue; C, grey; O, red

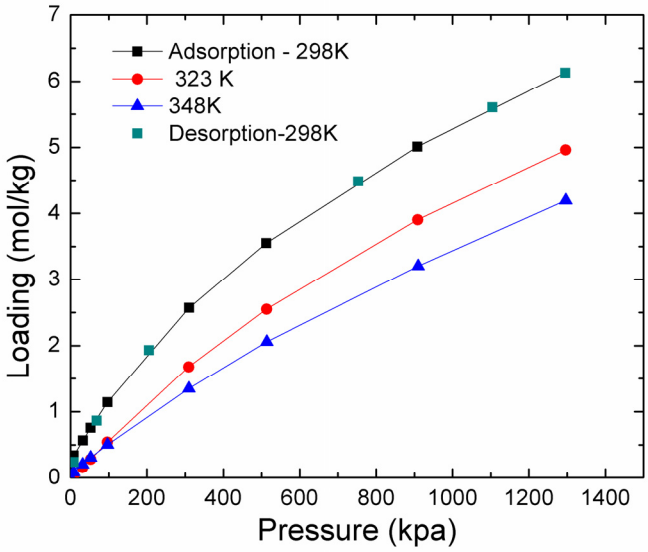

Figure B.3 CO adsorption isotherms of Cu-BTC at 298K, 323K and 348K

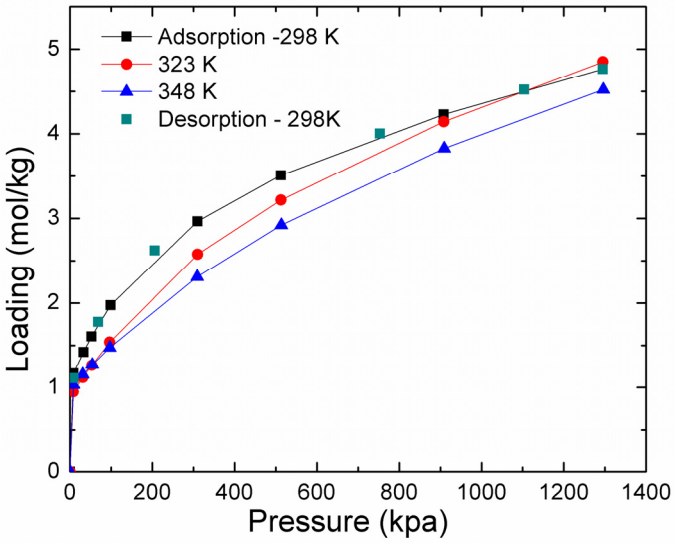

Figure B.4 CO adsorption isotherms of zeolite 4A at 298K, 323K and 348K

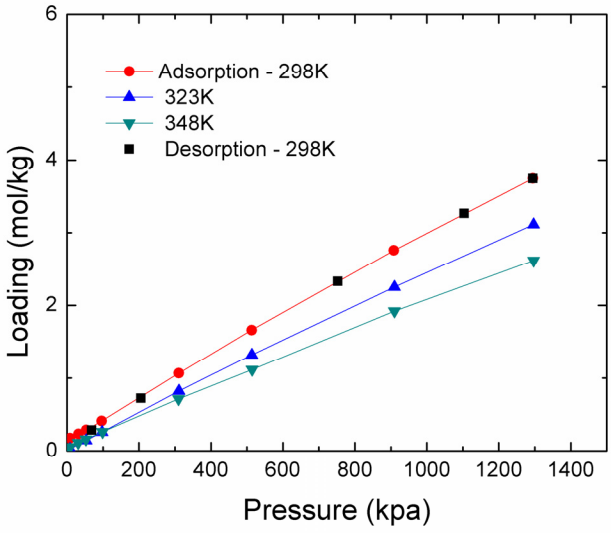

Figure B.5 CO adsorption isotherms of Zn[bdc][dabco] at 298K, 323K and 348K

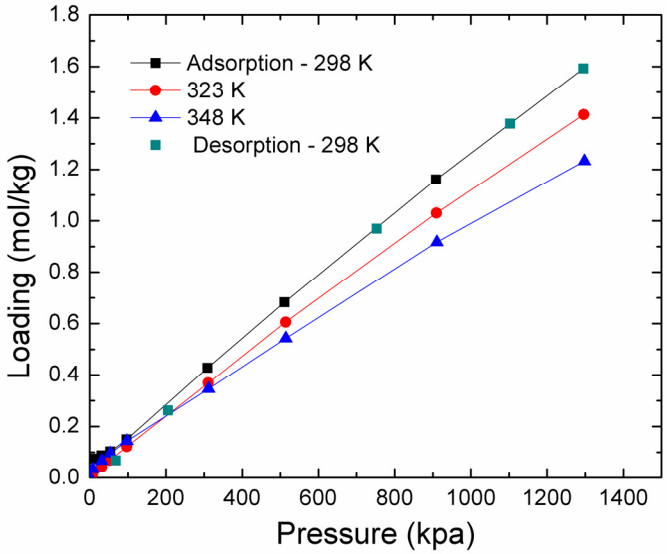

Figure B.6 CO adsorption isotherms of Cu[bdc][dabco] at 298K, 323K and 348K

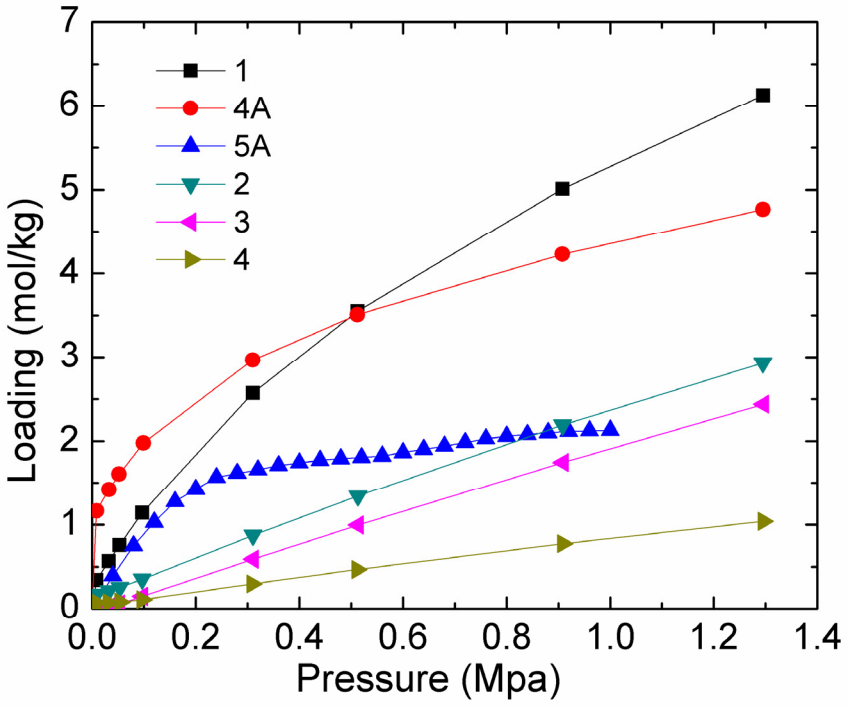

Figure B.7 Isotherms of CO uptake for Cu-BTC, 4A, 5A, and M[bdc][dabco] at 298 K.

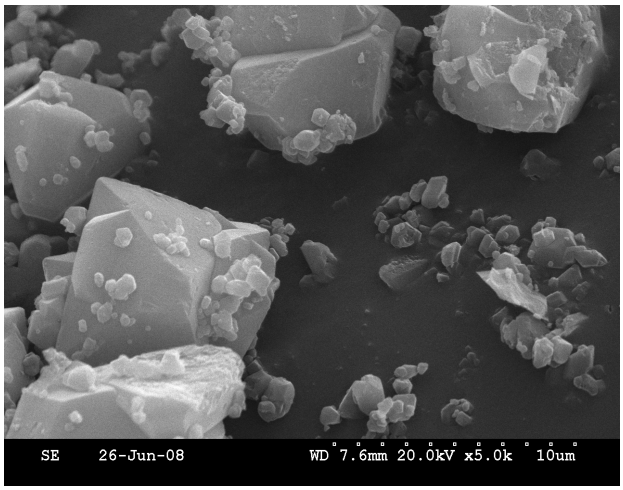

Figure B.8 SEM photograph of Cu-BTC

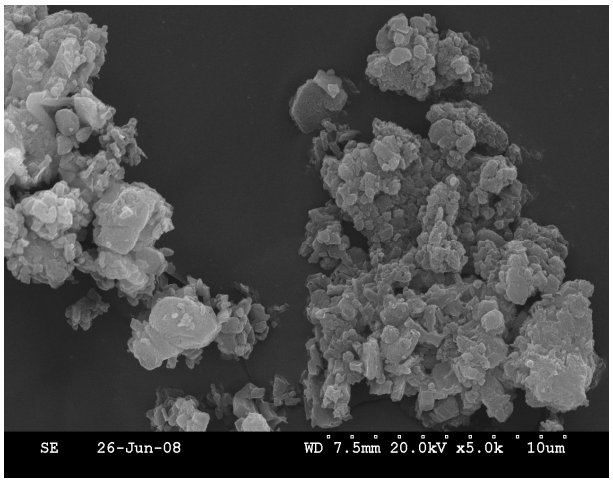

Figure B.9 SEM photographs of Co[bdc][dabco]

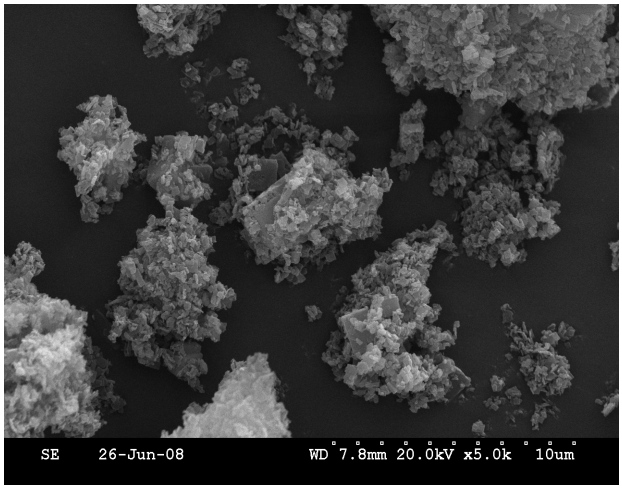

Figure B.10 SEM photograph of Cu[bdc][dabco]

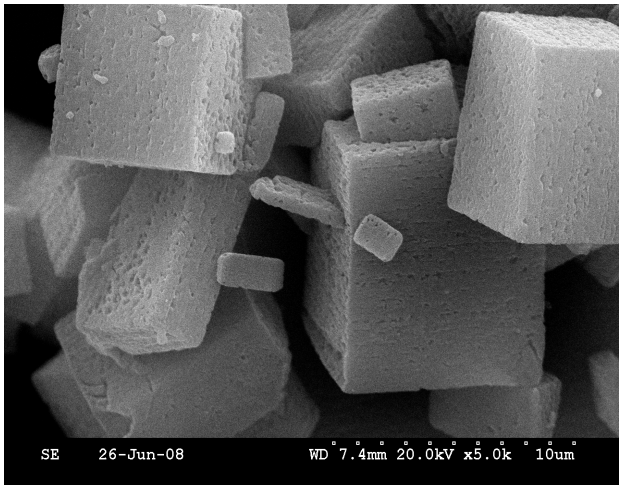

Figure B.11 SEM micrographs of Zn[bdc][dabco]

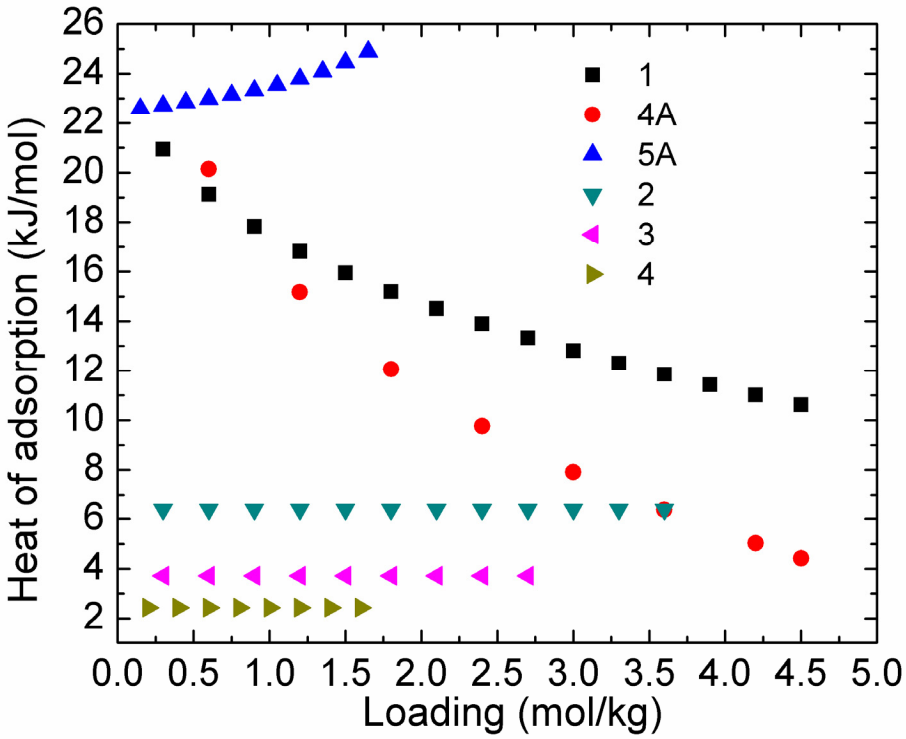

Figure B.12 Isosteric heat of adsorption of CO for Cu-BTC, 4A, 5A, and M[bdc][dabco]

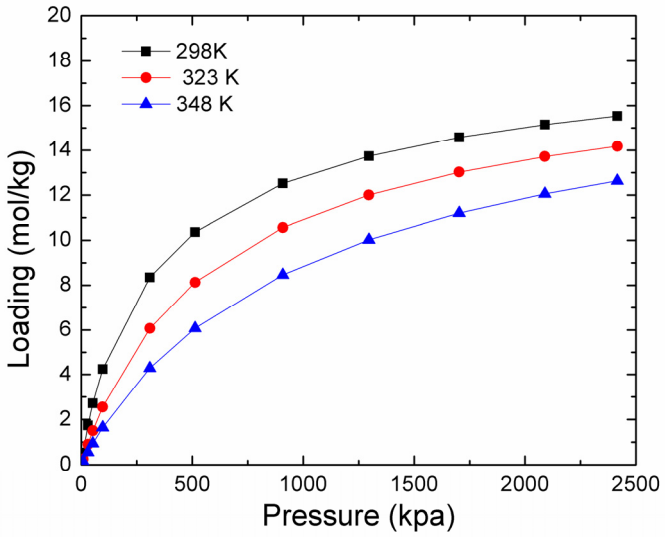

Figure B.13 CO_2 adsorption isotherms of CuBTC at 298K, 325K and 348K

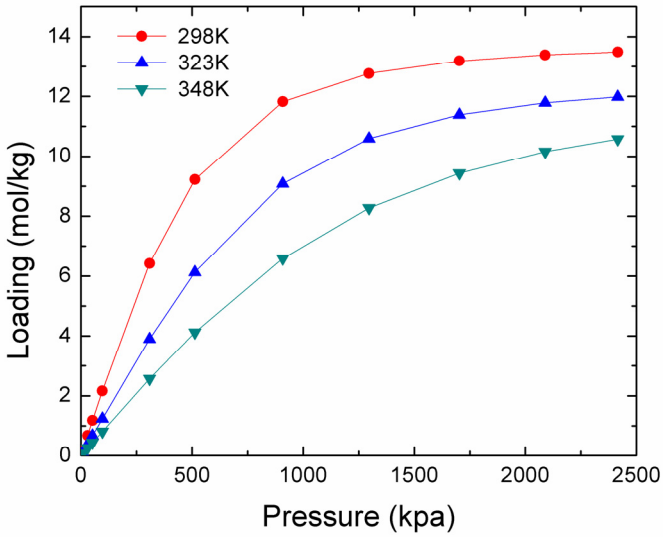

Figure B.14 CO_2 adsorption isotherms of Zn[bdc][dabco] at 298K, 325K and 348K

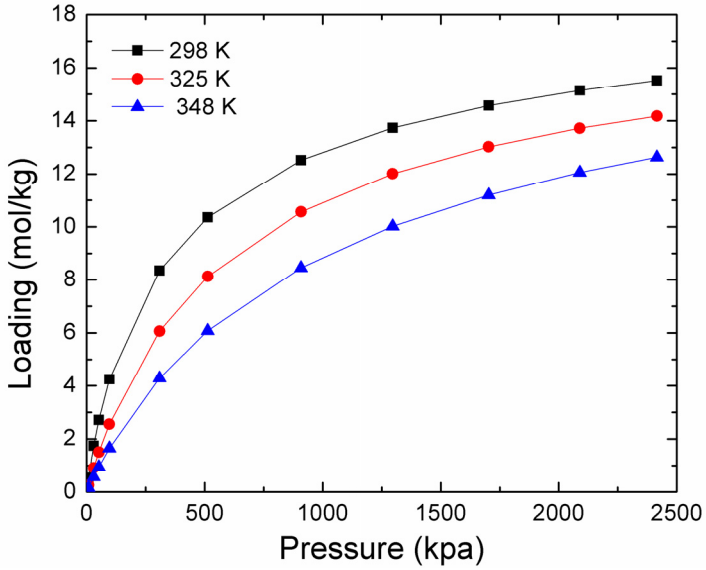

Figure B.15 CO_2 adsorption isotherms of Co[bdc][dabco] at 298K, 325K and 348K

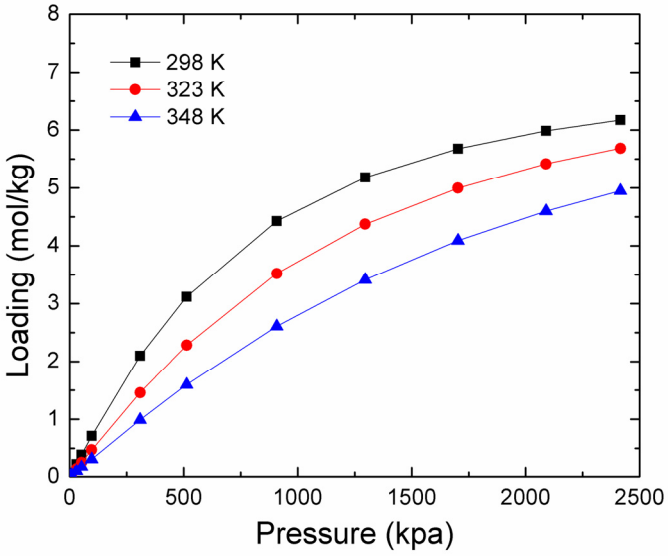

Figure B.16 CO_2 adsorption isotherms of Cu[bdc][dabco] at 298K, 325K and 348K

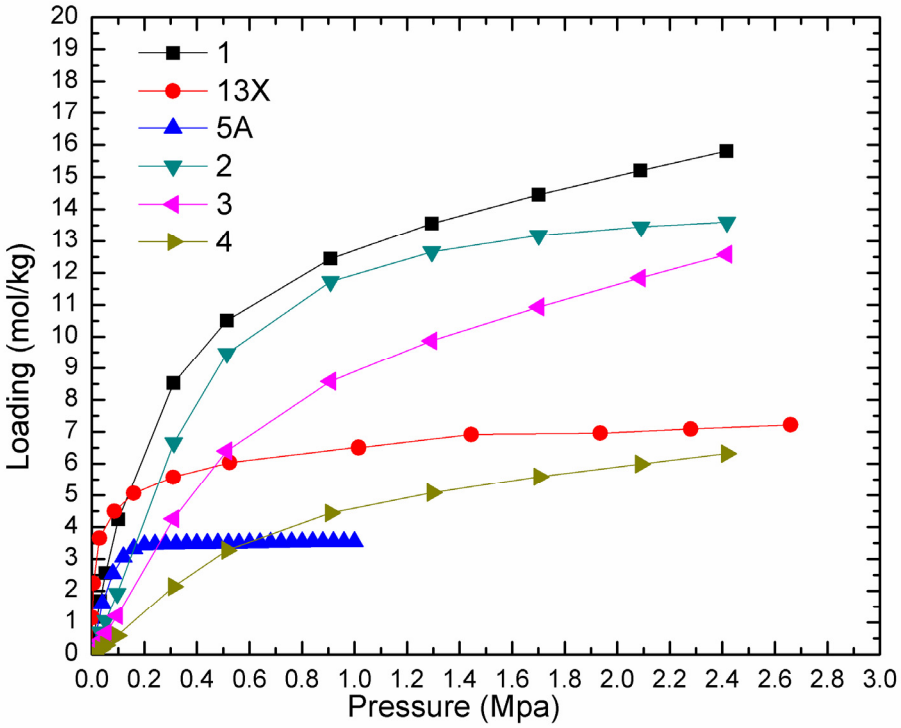

Figure B.17 Isotherms of CO_2 uptake for Cu-BTC, 4A, 5A, and M[bdc][dabco]

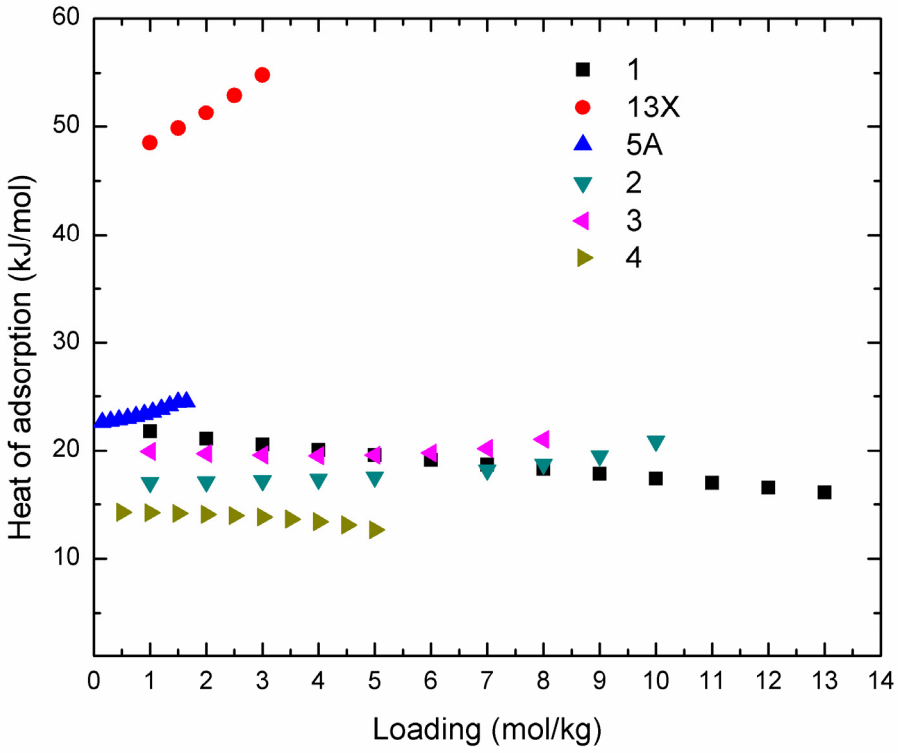

Figure B.18 Isosteric heat of adsorption of CO_2 for Cu-BTC, 4A, 5A, and M[bdc][dabco]

REFERENCES

(1) Yang, R. T. In *Gas Separation by Adsorption Processes;* Imperial College Press: London, **1997**.

(2) Li, J. R.; Kuppler, R. J.; Zhou, H. C. *Chem. Soc. Rev.* **2009**, *38*, 1477.

(3) Karra, J. R.; Walton, K. S. *Langmuir* **2008**, *24*, 8620-862.

(4) Pakseresht, S.; Kazemeini, M.; Akbarnejad, M. M. *Separation and purification technology* **2002**, *28*, 53.

(5) Cavenati, S.; Grande, C. A.; Rodrigues, A. E. *J. Chem. Eng. Data.* **2004**, *49*, 1095-1101.

(6) Lee, J. Y.; Olson, D. H.; Pan, L.; Emge, T. J.; Li, J. *Adv. Funct. Mater.* **2007**, *17*, 1255-1262.

(7) Takei, T.; Ii, T.; Kawashima, J.; Ohmura, T.; Ichikawa, M.; Hosoe, M.; Shinya, Y.; Kanoya, I.; Mori, W. *Chemistry letters* **2007**, *36*, 1136.

(8) Schlichte, K.; Kratzke, T.; Kaskel, S. *Microporous Mesoporous Mater.* **2004**, *73*, 81.

APPENDIX C

RAW DATA

Table C.1 Sorption data for Cu-BTC CO_2 isotherm at 298 K, 323 K, and 348 K

298 K		323 K		348 K	
Pressure (kPa)	Loading (mol/kg)	Pressure (kPa)	Loading (mol/kg)	Pressure (kPa)	Loading (mol/kg)
0.045	0.000	0.123	0.000	0.117	0.000
7.694	0.637	9.224	0.325	7.788	0.186
31.342	1.683	31.712	0.890	31.374	0.583
52.385	2.551	52.775	1.417	52.667	0.923
100.710	4.241	96.799	2.447	97.170	1.608
311.321	8.527	312.685	6.254	312.954	4.326
513.663	10.503	515.121	8.299	515.858	6.156
908.869	12.437	909.139	10.551	911.649	8.516
1294.319	13.550	1296.180	11.833	1297.632	9.978
1701.517	14.452	1701.893	12.853	1703.287	11.150
2088.003	15.201	2089.250	13.735	2089.834	12.020
2416.595	15.800	2418.109	14.375	2418.807	12.710
2088.850	15.204	8.168	0.291	8.477	0.237
1711.302	14.476				
1105.137	13.062				
753.014	11.861				
205.944	7.001				

Table C.2 Sorption data for Cu-BTC CO isotherm at 298 K, 323 K, and 348 K

298 K		323 K		348 K	
Pressure (kPa)	Loading (mol/kg)	Pressure (kPa)	Loading (mol/kg)	Pressure (kPa)	Loading (mol/kg)
0.104	0.000	0.127	0.000	0.162	0.000
8.324	0.339	8.009	0.014	8.009	0.086
31.995	0.568	30.994	0.153	31.407	0.204
52.596	0.757	52.524	0.281	52.729	0.306
96.572	1.141	96.582	0.541	96.965	0.501
310.051	2.571	309.067	1.679	309.770	1.351
512.620	3.551	513.283	2.550	513.975	2.059
908.168	5.011	908.827	3.905	910.100	3.205
1294.985	6.131	1296.083	4.960	1296.384	4.194
1103.955	5.605	1104.309	4.474	1103.024	3.732
752.673	4.487	752.692	3.438	752.634	2.812
205.427	1.932	205.535	1.193	205.606	1.015
68.156	0.863	68.052	0.404	67.994	0.452
8.120	0.239	8.094	0.017	8.094	0.184

Table C.3 Sorption data for Cu-BTC CH_4 isotherm at 298 K, 323 K, and 348 K

298 K		323 K		348 K	
Pressure (kPa)	Loading (mol/kg)	Pressure (kPa)	Loading (mol/kg)	Pressure (kPa)	Loading (mol/kg)
0.120	0.000	0.127	0.000	0.104	0.000
7.814	0.128	8.876	0.074	7.730	0.122
31.244	0.463	32.485	0.238	31.745	0.265
53.850	0.664	53.018	0.375	53.349	0.387
99.722	1.077	97.254	0.651	97.764	0.605
308.092	2.437	313.331	1.841	310.109	1.509
513.766	3.498	515.225	2.787	516.027	2.260
908.947	5.185	910.477	4.366	912.286	3.587
1295.543	6.567	1296.453	5.702	1298.441	4.679
1700.799	7.780	1702.864	6.874	1704.362	5.721
2088.512	8.769	2089.149	7.859	2091.406	6.590
2417.164	9.527	2418.239	8.662	2419.642	7.323
2086.846	8.847	8.087	0.093	8.025	0.277
1711.816	7.880				
1101.484	5.849				
753.056	4.344				
205.606	1.256				

Table C.4 Sorption data for Cu-BTC N_2 isotherm at 298 K, 323 K, and 348 K

298 K		323 K		348 K	
Pressure (kPa)	Loading (mol/kg)	Pressure (kPa)	Loading (mol/kg)	Pressure (kPa)	Loading (mol/kg)
0.062	0.000	0.127	0.000	0.120	0.000
8.081	0.249	8.077	0.024	8.857	0.065
31.020	0.314	31.322	0.093	31.751	0.131
52.382	0.374	54.512	0.160	52.576	0.189
96.449	0.519	96.738	0.282	97.027	0.300
310.788	1.231	311.665	0.891	311.999	0.782
513.260	1.846	514.263	1.426	515.413	1.230
908.343	2.941	909.272	2.395	910.662	2.080
1294.806	3.906	1296.089	3.236	1297.128	2.806
1701.611	4.835	1702.322	4.102	1703.618	3.564
1700.266	4.830	8.110	0.030	7.935	0.133
1104.654	3.428				
752.715	2.499				
205.232	0.829				
68.134	0.343				
7.863	0.116				

Table C.5 Sorption data Zn[bdc][dabco] CO_2 isotherm at 298 K, 323 K, and 348 K

298 K		323 K		348 K	
Pressure kPa	Loading mol/kg	Pressure kpa	Loading mol/kg	Pressure kpa	Loading mol/kg
0.068	0.000	0.107	0.000	0.107	0.000
8.129	0.289	8.032	0.088	8.032	0.298
32.349	0.692	31.735	0.321	31.735	0.455
52.524	1.054	52.817	0.540	52.817	0.597
96.757	1.920	97.134	1.039	97.134	0.911
311.590	6.665	312.464	3.873	312.464	2.551
513.770	9.475	515.537	6.304	515.537	4.078
908.885	11.727	910.837	9.166	910.837	6.614
1293.926	12.653	1296.359	10.485	1296.359	8.317
1700.432	13.178	1702.432	11.291	1702.432	9.413
2090.257	13.449	2089.227	11.790	2089.227	10.141
2417.635	13.596	2418.291	12.054	2418.291	10.587
2092.439	13.449	2084.839	11.820		
1715.625	13.173				
1106.670	12.264				
754.472	11.091				
206.834	4.422				
68.452	1.376				

Table C.6 Sorption data for Zn[bdc][dabco] CO isotherm at 298 K, 323 K, and 348 K

Pressure (kPa)	Loading (mol/kg)	Pressure (kPa)	Loading (mol/kg)	Pressure (kPa)	Loading (mol/kg)
0.169	0.000	0.114	0.000	0.130	0.000
8.493	0.176	7.902	0.029	7.928	0.056
32.268	0.234	53.340	0.145	31.264	0.113
53.606	0.287	97.092	0.259	52.391	0.162
96.520	0.412	310.782	0.824	98.417	0.264
310.447	1.067	513.653	1.322	309.651	0.713
513.071	1.662	909.665	2.253	514.302	1.116
908.284	2.758	1296.563	3.111	909.856	1.922
1294.751	3.743	1.293	0.023	1296.531	2.618
1103.906	3.265			1.393	0.080
751.965	2.330				
205.330	0.723				
68.039	0.287				

Table C.7 Sorption data for Zn[bdc][dabco] CH_4 isotherm at 298 K, 323 K, and 348 K

Pressure (kPa)	Loading (mol/kg)	Pressure (kPa)	Loading (mol/kg)	Pressure (kPa)	Loading (mol/kg)
0.127	0.000	0.162	0.000	0.120	0.000
31.793	0.084	7.905	0.298	7.931	0.336
52.924	0.191	31.290	0.367	52.930	0.481
97.004	0.432	52.388	0.434	97.368	0.624
309.145	1.606	96.809	0.606	309.609	1.333
514.185	2.676	311.671	1.540	515.215	1.951
909.061	4.502	513.802	2.369	910.857	3.151
1295.891	5.983	909.252	3.879	1296.583	4.204
1701.637	7.276	1295.433	5.179	1702.673	5.200
2088.587	8.325	1701.802	6.345	2089.779	6.083
2357.348	8.971	2088.652	7.383	2370.875	6.663
2086.830	8.318	2409.908	8.095	67.958	0.537
1711.085	7.300	67.309	0.444		
1105.391	5.284				
752.686	3.811				
205.541	1.011				
68.059	0.230				

Table C.8 Sorption data for Zn[bdc][dabco] N_2 isotherm at 298 K, 323 K, and 348 K

Pressure (kPa)	Loading (mol/kg)	Pressure (kPa)	Loading (mol/kg)	Pressure (kPa)	Loading (mol/kg)
0.075	0.000	0.110	0.000	0.084	0.000
311.321	0.813	311.402	0.716	311.652	0.688
513.698	1.324	513.640	1.148	514.263	1.048
908.574	2.273	909.668	1.973	910.035	1.711
1295.751	3.141	1294.637	2.732	1296.859	2.372
1702.504	3.993	1702.137	3.496	1702.838	3.036
1702.069	3.992	8.103	0.029		
1103.273	2.707				
753.439	1.894				
205.612	0.517				
68.065	0.149				

Table C.9 Sorption data for Cu[bdc][dabco] CO_2 isotherm at 298 K, 323 K, and 348 K

Pressure (kPa)	Loading (mol/kg)	Pressure (kPa)	Loading (mol/kg)	Pressure (kPa)	Loading (mol/kg)
0.127	0.000	0.123	0.000	0.127	0.000
7.795	0.014	8.116	0.045	8.139	0.054
32.229	0.164	31.179	0.144	31.426	0.130
52.196	0.289	52.599	0.238	55.132	0.205
96.718	0.584	97.101	0.435	97.079	0.336
311.516	2.140	312.750	1.450	312.889	0.983
513.851	3.277	514.848	2.346	515.930	1.593
908.538	4.440	910.279	3.592	911.068	2.635
1296.170	5.085	1296.037	4.341	1296.797	3.427
1701.679	5.588	1701.926	4.933	1702.218	4.072
2087.720	5.995	2089.961	5.398	2089.419	4.583
2416.154	6.317	2418.372	5.742	2418.843	4.968
2087.931	5.997	205.577	0.954	205.622	0.656
1713.884	5.603	68.254	0.311	68.173	0.258
1104.374	4.802				
754.047	4.099				
205.785	1.413				
68.348	0.410				

Table C.10 Sorption data for Cu[bdc][dabco] CO isotherm at 298 K, 323 K, and 348 K

Pressure (kPa)	Loading (mol/kg)	Pressure (kPa)	Loading (mol/kg)	Pressure (kPa)	Loading (mol/kg)
0.107	0.000	0.130	0.000	0.130	0.000
8.159	0.075	8.084	0.015	7.782	0.034
30.926	0.087	31.163	0.043	31.283	0.067
54.012	0.103	52.534	0.068	54.093	0.096
96.598	0.150	96.877	0.121	97.111	0.143
308.625	0.428	310.859	0.369	311.434	0.346
511.236	0.683	513.744	0.606	514.095	0.543
908.359	1.161	909.509	1.030	910.815	0.917
1295.433	1.592	1296.274	1.413	1297.911	1.232
1102.981	1.378	1104.637	1.221	1103.403	1.087
753.186	0.969	753.183	0.876	753.202	0.794
205.548	0.262	205.515	0.275	205.509	0.297
68.085	0.068	67.737	0.112	68.056	0.165
				7.915	0.107

Table C.11 Sorption data for Cu[bdc][dabco] CH_4 isotherm at 298 K, 323 K, and 348 K

Pressure (kPa)	Loading (mol/kg)	Pressure (kPa)	Loading (mol/kg)	Pressure (kPa)	Loading (mol/kg)
0.101	0.000	0.114	0.000	0.130	0.000
10.487	0.130	7.938	0.076	12.059	0.093
31.732	0.149	52.229	0.164	53.304	0.177
52.921	0.178	97.335	0.243	97.826	0.255
97.147	0.254	309.648	0.663	313.948	0.594
311.727	0.761	515.995	1.027	516.608	0.874
513.887	1.204	910.379	1.707	911.779	1.434
910.301	1.976	1297.083	2.242	1297.892	1.882
1296.011	2.601	1703.056	2.786	1703.475	2.388
1702.124	3.155	2089.396	3.214	2090.075	2.740
2088.753	3.613	2418.739	3.580	2418.973	3.072
2418.076	3.962	68.166	0.206	68.043	0.264
2086.658	3.609				
1711.624	3.166				
1104.644	2.302				
753.810	1.684				
205.645	0.486				
68.033	0.136				

Table C.12 Sorption data for Cu[bdc][dabco] N_2 isotherm at 298 K, 323 K, and 348 K

Pressure (kPa)	Loading (mol/kg)	Pressure (kPa)	Loading (mol/kg)	Pressure (kPa)	Loading (mol/kg)
0.058	0.000	0.130	0.000	0.127	0.000
8.074	0.123	7.902	0.022	7.876	0.053
31.261	0.127	31.313	0.047	31.615	0.084
52.154	0.132	52.401	0.069	52.765	0.111
96.176	0.165	97.072	0.114	97.173	0.155
308.670	0.378	311.499	0.332	312.009	0.330
513.127	0.578	514.098	0.527	514.682	0.503
908.291	0.952	910.171	0.901	909.054	0.840
1294.787	1.296	1296.359	1.243	1296.752	1.126
1701.845	1.637	1702.722	1.578	1703.076	1.419
1700.156	1.633	1702.605	1.578	1703.719	1.429
1104.855	1.119	1103.806	1.071	1103.361	0.988
753.894	0.791	753.115	0.758	753.244	0.713
205.366	0.234	205.466	0.226	205.395	0.274
68.104	0.084	68.111	0.088	68.091	0.161
8.123	0.017				

Table C.13 Sorption data for Co[bdc][dabco] CO_2 isotherm at 298 K, 323 K, and 348 K

298 K		323 K		348 K	
Pressure (kPa)	Loading (mol/kg)	Pressure (kPa)	Loading (mol/kg)	Pressure (kPa)	Loading (mol/kg)
0.081	0.000	0.032	0.000	0.107	0.000
7.779	0.164	8.152	0.252	8.496	0.066
31.731	0.426	32.121	0.391	31.832	0.174
53.865	0.665	54.759	0.528	52.645	0.271
96.672	1.212	96.868	0.802	97.345	0.479
311.420	4.260	312.022	2.336	309.677	1.457
513.211	6.405	513.925	3.744	515.598	2.415
908.069	8.585	909.223	5.654	910.925	4.021
1293.283	9.864	1294.631	6.821	1297.187	5.264
1701.069	10.932	1701.815	7.759	1702.618	6.270
2086.834	11.836	2087.726	8.485	2089.152	7.074
2416.150	12.579	2416.638	9.129	2418.430	7.677
1924.034	11.457	2088.246	8.532	2089.240	7.094
1711.910	10.980	1710.179	7.801	1711.234	6.307
1104.485	9.328	1104.988	6.344	1103.669	4.696
755.334	7.980	753.505	5.066	753.511	3.457
206.191	2.870	8.185	0.230	205.548	0.967
68.156	0.879			67.971	0.357
8.023	0.118			8.155	0.091

Table C.14 Sorption data for Co[bdc][dabco] CO isotherm at 298 K, 323 K, and 348 K

298 K		323 K		348 K	
Pressure (kPa)	Loading (mol/kg)	Pressure (kPa)	Loading (mol/kg)	Pressure (kPa)	Loading (mol/kg)
0.117	0.000	0.130	0.000	0.097	0.000
32.365	0.021	7.951	0.018	9.039	0.002
52.495	0.058	31.248	0.061	31.335	0.043
96.692	0.148	53.460	0.101	53.109	0.082
310.694	0.589	96.881	0.176	99.063	0.159
513.432	0.994	311.191	0.536	309.762	0.484
908.941	1.746	513.520	0.870	514.143	0.803
1295.761	2.437	910.084	1.506	910.223	1.415
1103.919	2.101	1295.959	2.086	1296.810	1.964
753.540	1.460	1103.919	1.806	1102.958	1.701
205.434	0.375	753.345	1.278	752.923	1.199
68.173	0.085	205.323	0.398	205.401	0.381
		68.020	0.168	68.075	0.162
		7.918	0.066	8.061	0.068

Table C.15 Sorption data for Co[bdc][dabco] CH_4 isotherm at 298 K, 323 K, and 348 K

298 K		323 K		348 K	
Pressure (kPa)	Loading (mol/kg)	Pressure (kPa)	Loading (mol/kg)	Pressure (kPa)	Loading (mol/kg)
0.123	0.000	0.114	0.000	0.052	0.000
31.634	0.067	9.019	0.047	7.779	0.087
52.742	0.130	31.784	0.116	31.335	0.157
97.098	0.290	53.346	0.181	53.401	0.219
309.002	1.022	97.248	0.307	97.322	0.327
515.014	1.672	312.724	0.915	310.051	0.809
909.688	2.787	515.985	1.454	516.098	1.228
1295.300	3.748	910.493	2.416	911.243	2.054
1701.471	4.639	1296.713	3.293	1297.934	2.802
2088.207	5.399	1703.004	4.095	1703.358	3.521
2417.235	5.998	2089.438	4.841	2089.782	4.139
2084.268	5.429	2418.359	5.404	2418.486	4.685
1713.414	4.694	2090.659	4.834	2088.051	4.131
1104.410	3.285	8.116	0.079	1712.452	3.549
753.121	2.313			1103.179	2.439
204.745	0.535			752.777	1.749
66.331	0.033			205.405	0.606
				67.322	0.296
				7.990	0.164

Table C.16 Sorption data for Co[bdc][dabco] N_2 isotherm at 298 K, 323 K, and 348 K

298 K		323 K		348 K	
Pressure (kPa)	Loading (mol/kg)	Pressure (kPa)	Loading (mol/kg)	Pressure (kPa)	Loading (mol/kg)
0.107	0.000	0.091	0.000	0.120	0.000
8.019	0.006	7.928	0.027	7.844	0.063
32.391	0.050	31.420	0.066	31.556	0.108
52.447	0.087	52.443	0.100	52.937	0.146
96.871	0.172	96.971	0.175	97.335	0.214
311.441	0.579	311.668	0.532	311.019	0.508
514.121	0.952	514.182	0.856	513.000	0.764
909.629	1.656	910.035	1.471	910.071	1.307
1296.657	2.312	1296.381	2.056	1296.537	1.806
1702.465	2.970	1702.381	2.644	1653.218	2.251
1702.293	2.970	1702.270	2.648	1653.679	2.238
1105.017	1.989	7.902	0.027	7.824	0.128
753.131	1.378				
205.483	0.372				
68.059	0.107				

Table C.17 Sorption data for zeolite 4A CO isotherm at 298 K, 323 K, and 348 K

298 K		323 K		348 K	
Pressure (kPa)	Loading (mol/kg)	Pressure (kPa)	Loading (mol/kg)	Pressure (kPa)	Loading (mol/kg)
0.049	0.000	0.052	0.000	0.039	0.000
8.315	1.166	8.084	0.950	8.090	1.032
32.443	1.421	31.215	1.119	31.092	1.155
52.063	1.605	52.966	1.263	53.869	1.271
98.764	1.975	96.478	1.537	96.751	1.475
309.921	2.966	310.288	2.577	309.197	2.308
512.133	3.510	512.610	3.216	513.607	2.921
907.814	4.229	908.544	4.143	909.584	3.829
1294.874	4.766	1295.212	4.850	1296.102	4.523
1103.523	4.524	1103.712	4.500	1103.728	4.189
752.874	4.003	751.530	3.815	754.641	3.519
205.499	2.621	205.112	2.139	205.457	1.981
68.312	1.778	68.039	1.350	68.104	1.372
8.818	1.110	7.788	0.874	7.788	1.040

Table C.18 Sorption data for MOF-14 CO_2 isotherm at 278 K, 298 K, and 318 K

278 K		298 K				318 K	
Pressure	Loading	Pressure	Loading	Pressure	Loading	Pressure	Loading
(kPa)	(mol/kg)	(kPa)	(mol/kg)	(kPa)	(mol/kg)	(kPa)	(mol/kg)
0.406	0.059	0.000	0.000	1660.904	10.186	0.000	0.000
1.155	0.155	1.275	0.052	1780.656	10.392	1.342	0.042
50.212	2.480	21.347	0.853	1900.594	10.574	50.453	1.074
100.273	3.501	41.192	1.395	2000.714	10.708	100.339	1.697
201.088	4.962	61.304	1.811	1919.610	10.594	201.355	2.611
401.195	7.233	81.189	2.147	1799.912	10.417	401.008	3.871
601.021	8.933	100.219	2.427	1600.193	10.072	601.035	4.851
801.021	10.007	219.717	3.721	1399.886	9.656	800.954	5.693
1000.834	10.671	340.003	4.710	1199.992	9.129	1000.874	6.450
1200.754	11.129	459.781	5.560	999.819	8.435	1200.821	7.108
1401.636	11.497	579.506	6.323	800.166	7.561	1400.955	7.670
1600.634	11.767	699.551	7.015	600.072	6.476	1600.794	8.204
1802.011	11.991	819.490	7.624	399.899	5.195	1800.741	8.679
2000.688	12.176	939.495	8.167	199.885	3.580	1999.525	9.018
1899.953	12.080	1059.434	8.635	99.685	2.467	1899.926	8.878
1500.180	11.625	1179.800	9.042	50.065	1.648	1499.164	7.955
1000.099	10.682	1299.712	9.398	29.606	1.163	999.124	6.467
500.059	8.155	1420.719	9.704	9.881	0.498	499.939	4.393
0.460	0.045	1540.711	9.966	0.246	0.003	0.366	0.009

Table C.19 Sorption data for MOF-14 CH_4 and N_2 isotherms at 298 K

298 K			
CH_4		N_2	
Pressure	Loading	Pressure	Loading
(kPa)	(mol/kg)	(kPa)	(mol/kg)
2.825	0.000	0.406	0.000
50.841	0.542	19.904	0.038
75.590	0.740	39.909	0.077
100.767	0.925	59.888	0.114
150.506	1.233	80.000	0.152
200.714	1.510	99.858	0.187
300.460	1.954	200.032	0.362
500.326	2.603	399.899	0.684
888.794	3.436	599.952	0.976
1099.845	3.729	800.006	1.241
1299.779	4.010	999.992	1.490
1699.632	4.466	1199.966	1.722
2000.019	4.755	1400.046	1.922
		1599.939	2.130
		1799.806	2.325
		1901.035	2.414

Table C.20 Sorption data for CdBTTB CO_2, CH_4 and N_2 isotherms at 298 K

298 K					
CO_2		CH_4		N_2	
Pressure	Loading	Pressure	Loading	Pressure	Loading
(kPa)	(mol/kg)	(kPa)	(mol/kg)	(kPa)	(mol/kg)
0.553	0.000	0.620	0.000	0.580	0.000
51.495	1.119	10.549	0.157	10.215	0.050
71.581	1.385	20.211	0.281	20.438	0.077
100.968	1.633	40.190	0.501	35.806	0.115
150.573	1.888	59.888	0.676	50.600	0.147
300.647	2.287	80.134	0.828	70.686	0.189
500.366	2.556	99.979	0.952	100.714	0.249
700.219	2.733	150.239	1.197	150.079	0.337
899.538	2.863	300.032	1.611	200.192	0.415
1100.139	2.969	500.032	1.884	300.393	0.554
1399.765	3.096	699.939	2.039	500.300	0.771
1699.244	3.196	899.872	2.143	700.179	0.920
2000.100	3.282	1099.899	2.216	900.032	1.054
1200.139	3.023	1399.805	2.295	1099.939	1.161
599.952	2.678	1699.485	2.351	1399.685	1.284
100.233	1.712	2000.567	2.389	1699.725	1.378
20.051	0.756			1999.445	1.451

Table C.21 Sorption data for MgBTTB CO_2, CH_4 and N_2 isotherms at 298 K

298 K					
CO_2		CH_4		N_2	
Pressure	Loading	Pressure	Loading	Pressure	Loading
(kPa)	(mol/kg)	(kPa)	(mol/kg)	(kPa)	(mol/kg)
0.633	0.022	0.486	0.076	0.460	0.049
1.676	0.029	2.224	0.085	1.729	0.051
20.265	0.119	20.492	0.136	20.385	0.065
40.257	0.217	40.524	0.184	40.537	0.079
60.329	0.315	60.676	0.229	60.315	0.093
80.428	0.409	80.802	0.272	79.840	0.106
100.380	0.500	100.660	0.314	100.192	0.120
150.600	0.709	150.279	0.413	150.106	0.151
200.086	0.890	200.339	0.504	200.380	0.183
300.166	1.186	300.126	0.665	300.019	0.243
499.992	1.595	500.340	0.924	500.019	0.359
699.859	1.881	700.099	1.118	699.899	0.466
899.738	2.110	900.006	1.276	899.872	0.564
1099.832	2.312	1100.073	1.409	1100.073	0.657
1399.578	2.595	1399.872	1.580	1399.805	0.786
1699.311	2.889	1699.832	1.721	1699.672	0.906
2000.153	3.233	1999.538	1.843	1999.378	1.015

Table C.22 Sorption data for MgBTTB CO_2, CH_4 and N_2 isotherms at 278 K

278 K									
CO_2				CH4				N_2	
Pressure	Loading	Pressure	Loading	Pressure	Loading	Pressure	Loading	Pressure	Loading
(kPa)	(mol/kg)	(kPa)	(mol/kg)	(kPa)	(mol/kg)	(kPa)	(mol/kg)	(kPa)	(mol/kg)
0.366	0.000	1999.739	4.477	0.433	0.042	1999.659	2.051	0.460	0.046
2.090	0.014	1699.993	4.168	2.184	0.062	1699.966	1.928	1.890	0.049
20.211	0.178	1499.926	3.910	20.759	0.155	1500.113	1.842	20.492	0.070
40.551	0.358	1349.732	3.642	40.738	0.245	1349.919	1.771	40.644	0.089
60.596	0.525	1199.979	3.229	60.289	0.317	1199.992	1.695	60.369	0.107
80.615	0.681	1000.380	2.820	80.388	0.384	1000.126	1.579	80.120	0.125
100.794	0.823	700.046	2.386	100.593	0.446	700.006	1.356	100.179	0.143
150.386	1.114	500.126	2.081	150.266	0.591	500.219	1.153	150.279	0.186
200.446	1.340	349.878	1.789	200.246	0.715	350.119	0.944	200.326	0.228
300.233	1.664	200.099	1.343	300.500	0.920	200.099	0.656	300.019	0.307
500.019	2.080	99.872	0.824	500.126	1.201	100.246	0.395	500.072	0.452
699.939	2.386	50.386	0.448	700.006	1.390	50.199	0.237	699.966	0.581
899.899	2.667	19.837	0.185	899.925	1.536	20.064	0.132	900.032	0.698
1099.739	2.994			1099.805	1.655			1100.059	0.804
1399.952	3.747			1400.099	1.805			1399.765	0.947
1699.097	4.175			1699.578	1.933			1699.485	1.079
1999.739	4.477			1999.659	2.051			1999.472	1.198

Table C.23 Sorption data for ZnBTTB CO_2, CH_4 and N_2 isotherms at 298 K

CO_2		CH_4		N_2	
Pressure	Loading	Pressure	Loading	Pressure	Loading
(kPa)	(mol/kg)	(kPa)	(mol/kg)	(kPa)	(mol/kg)
1.902	0.080	1.835	0.110	1.715	0.026
10.013	0.356	11.256	0.404	10.748	0.058
20.557	0.642	20.905	0.560	20.183	0.081
39.935	1.051	41.084	0.808	40.068	0.125
60.261	1.356	59.793	0.968	60.261	0.166
80.132	1.586	80.547	1.164	80.039	0.202
100.485	1.769	100.472	1.294	99.750	0.239
149.984	2.094	150.078	1.570	149.917	0.328
200.138	2.321	200.605	1.766	199.911	0.410
300.205	2.627	300.485	2.056	300.004	0.549
499.977	2.987	499.964	2.391	499.991	0.783
699.964	3.218	700.004	2.579	699.911	0.975
899.911	3.386	899.857	2.693	899.844	1.139
1099.964	3.523	1099.951	2.725	1099.577	1.280
1399.938	3.685	1399.884	2.865	1399.924	1.456

Table C.23 Continued

1699.403	3.813	1699.270	2.973	1699.831	1.606
1999.083	3.917	1999.831	3.063	1999.430	1.729
1499.898	3.734	1499.911	2.884	1499.804	1.499
1099.964	3.533	1099.951	2.679	1099.911	1.273
700.258	3.251	700.125	2.366	699.991	0.952
399.977	2.878	399.964	1.948	399.911	0.652
199.870	2.377	200.418	1.429	199.924	0.388
99.790	1.837	100.392	0.958	99.777	0.226
49.837	1.303	49.784	0.603	49.944	0.133
9.826	0.438	10.454	0.225	9.706	0.053

Table C.24 Sorption data for NiBTTB CO_2, CH_4 and N_2 isotherms at 298 K

298 K							
CO_2				CH_4		N_2	
Pressure (kPa)	Loading (mol/kg)	Pressure (kPa)	Loading (mol/kg)	Pressure (kPa)	Loading (mol/kg)	Pressure (kPa)	Loading (mol/kg)
0.379	0.000	1700.434	3.248	0.526	0.000	0.526	0.003
21.200	0.178	2000.460	3.358	20.906	0.161	20.759	0.008
41.259	0.625	1999.672	3.356	50.734	0.367	50.573	0.037
60.943	0.911	1600.100	3.221	70.418	0.481	70.151	0.061
79.893	1.117	1199.805	3.046	100.339	0.635	100.500	0.099
100.821	1.296	800.166	2.806	150.346	0.852	150.159	0.161
149.878	1.594	599.925	2.634	300.152	1.312	300.193	0.325
200.486	1.807	400.219	2.389	500.099	1.706	500.152	0.503
299.711	2.095	250.106	2.089	700.032	1.975	800.019	0.719
399.965	2.297	100.045	1.462	899.979	2.168	1099.819	0.895
499.832	2.450	50.119	0.993	1100.006	2.314	1399.952	1.041
599.805	2.568			1399.832	2.480	1699.592	1.163
699.792	2.673			1699.512	2.604	1999.485	1.272
899.899	2.834			2000.554	2.700		
1099.471	2.966						
1399.578	3.125						

Table C.25 Sorption data for CoBTTBBPY CO_2, CH_4 and N_2 isotherms at 298 K

298 K					
CO_2		CH_4		N_2	
Pressure	Loading	Pressure	Loading	Pressure	Loading
(kPa)	(mol/kg)	(kPa)	(mol/kg)	(kPa)	(mol/kg)
0.540	0.003	0.553	0.000	20.425	0.000
2.090	0.040	1.836	0.010	40.524	0.055
21.387	0.469	20.946	0.150	60.155	0.087
51.442	1.001	51.415	0.342	80.388	0.106
75.456	1.326	75.871	0.475	100.246	0.127
102.250	1.616	102.184	0.601	200.099	0.274
200.740	2.307	200.299	0.966	299.899	0.375
400.299	3.010	400.513	1.436	399.939	0.452
600.179	3.398	600.326	1.733	499.899	0.520
800.019	3.659	800.219	1.950	599.925	0.580
1100.059	3.935	1100.099	2.197	699.698	0.628
1399.939	4.137	1399.832	2.389	799.778	0.671
1700.153	4.298	1699.498	2.549	899.885	0.710
1999.685	4.433	1999.565	2.688	999.578	0.746
1199.939	4.001	1999.565	2.688	1199.752	0.811
800.206	3.651	1200.220	2.269	1599.418	0.908
200.286	2.299	800.246	1.954	1999.725	0.973
100.259	1.592				

Table C.26 Sorption data for ZnBTTBBPY CO_2, CH_4 and N_2 isotherms at 298 K

CO_2				CH_4		N_2	
Pressure	Loading	Pressure	Loading	Pressure	Loading	Pressure	Loading
(kPa)	(mol/kg)	(kPa)	(mol/kg)	(kPa)	(mol/kg)	(kPa)	(mol/kg)
0.379	0.000	1649.973	5.156	0.874	0.063	0.460	0.000
20.037	0.364	1250.213	4.908	50.720	0.510	19.890	0.009
39.882	0.697	1100.527	4.784	70.873	0.614	40.363	0.036
60.128	1.006	849.892	4.512	100.219	0.768	60.235	0.065
79.880	1.286	750.173	4.370	149.892	1.014	80.294	0.093
99.912	1.545	549.905	3.985	299.083	1.581	100.259	0.120
149.825	2.076	349.892	3.342	499.177	2.092	149.959	0.184
199.738	2.488	200.099	2.474	699.712	2.454	200.086	0.245
299.751	3.081	149.892	2.052	899.391	2.720	300.072	0.342
399.591	3.484	100.032	1.521	1101.890	2.932	399.899	0.457
599.899	4.055			1412.167	3.190	599.738	0.662
799.551	4.437			1691.614	3.364	799.805	0.840
999.538	4.690			2000.086	3.508	999.631	0.995
1199.712	4.877					1199.551	1.132
1299.765	4.953					1399.618	1.253
1400.233	5.020					1599.685	1.362
1600.447	5.136					1799.966	1.459
1800.059	5.231					1999.431	1.549
1999.873	5.309						

Table C.27 Sorption data for ZnBTTBBDC CO_2, CH_4 and N_2 isotherms at 298 K

298 K					
CO_2		CH_4		N_2	
Pressure (kPa)	Loading (mol/kg)	Pressure (kPa)	Loading (mol/kg)	Pressure (kPa)	Loading (mol/kg)
0.061	0.003	0.061	0.000	0.526	0.000
2.077	0.332	2.077	0.053	20.505	0.013
5.088	0.613	5.088	0.117	50.212	0.029
7.020	0.756	7.020	0.147	70.084	0.038
10.061	0.919	10.061	0.194	100.259	0.053
15.055	1.110	15.055	0.262	150.373	0.076
25.015	1.353	25.015	0.364	250.333	0.118
40.010	1.586	40.010	0.466	400.393	0.172
60.005	1.796	60.005	0.555	600.152	0.232
80.014	1.955	80.014	0.617	800.072	0.282
99.997	2.087	99.997	0.664	1000.126	0.326
119.959	2.202	119.959	0.699	1199.992	0.363
159.986	2.393	159.986	0.746	1599.966	0.418
199.922	2.559	199.922	0.770	1999.538	0.462

Table C.28 Sorption data for CoBTTBAZPY CO_2, CH_4 and N_2 isotherms at 298 K

298 K									
CO_2				CH_4				N_2	
Pressure	Loading	Pressure	Loading	Pressure	Loading	Pressure	Loading	Pressure	Loading
(kPa)	(mol/kg)	(kPa)	(mol/kg)	(kPa)	(mol/kg)	(kPa)	(mol/kg)	(kPa)	(mol/kg)
0.366	0.000	1500.206	5.851	0.513	0.000	1600.300	3.457	0.660	0.000
1.916	0.014	1099.819	5.457	2.331	0.012	1200.473	3.124	2.170	0.005
20.505	0.277	850.159	5.125	20.786	0.159	800.380	2.633	20.799	0.024
41.112	0.710	549.865	4.546	40.497	0.303	600.300	2.282	40.310	0.053
60.436	1.106	400.246	4.100	60.102	0.433	400.099	1.808	60.369	0.084
80.494	1.482	200.246	3.040	80.040	0.549	200.273	1.122	80.548	0.116
100.299	1.807	99.765	1.946	100.567	0.668	100.326	0.641	100.660	0.146
150.453	2.470	40.337	0.893	150.760	0.927	49.892	0.343	150.400	0.216
200.433	2.959	20.037	0.454	200.714	1.152	19.837	0.142	200.126	0.284
300.179	3.622			300.460	1.530			300.152	0.413
400.166	4.064			400.299	1.833			400.313	0.534
600.166	4.642			600.366	2.302			499.872	0.646
800.046	5.031			800.433	2.647			699.845	0.848
999.792	5.324			999.872	2.915			900.126	1.027
1299.739	5.665			1299.926	3.224			1099.845	1.185
1699.485	6.000			1699.926	3.529			1399.805	1.394
2000.060	6.198			1999.765	3.705			1699.618	1.572
								1999.886	1.729

Table C.29 Sorption data for ZnBTTBAZPY CO_2, CH_4 and N_2 isotherms at 298 K

298 K									
CO_2				CH_4				N_2	
Pressure	Loading	Pressure	Loading	Pressure	Loading	Pressure	Loading	Pressure	Loading
(kPa)	(mol/kg)	(kPa)	(mol/kg)	(kPa)	(mol/kg)	(kPa)	(mol/kg)	(kPa)	(mol/kg)
0.433	0.000	1600.153	4.724	0.567	0.001	1500.073	2.668	0.526	0.011
1.956	0.002	1199.992	4.490	2.558	0.018	1100.193	2.408	1.596	0.015
21.026	0.094	800.406	4.123	21.213	0.130	800.366	2.121	20.238	0.037
40.404	0.458	400.206	3.394	40.871	0.249	500.046	1.695	40.591	0.063
60.355	0.829	200.005	2.547	61.010	0.356	350.039	1.385	60.449	0.089
80.468	1.156	100.166	1.674	80.067	0.454	100.393	0.563	80.401	0.113
99.939	1.422	50.146	0.981	100.847	0.554	50.226	0.314	100.433	0.138
149.985	1.995	20.051	0.444	150.640	0.766			150.106	0.195
200.380	2.428			200.580	0.950			200.500	0.252
300.446	2.986			300.152	1.253			300.166	0.356
400.527	3.348			400.620	1.497			500.326	0.541
500.326	3.609			500.259	1.694			700.179	0.699
700.019	3.972			600.326	1.859			900.206	0.836
899.952	4.223			800.219	2.122			1100.139	0.956
1099.926	4.408			1000.059	2.323			1400.006	1.109
1399.698	4.616			1300.046	2.547			1699.752	1.239
1699.418	4.770			1699.886	2.766			1999.859	1.349
2000.019	4.892			1999.739	2.889				

Table C.30 Sorption data for CdBTTB and ZnBTTB H_2O isotherms at 298 K

CdBTTB			ZnBTTB		
%RH	Wt%	Con(mol/kg)	%RH	Wt%	Con(mol/kg)
0.000	0.000	0.000	0.000	0.000	0.000
11.267	5.559	3.089	11.251	1.116	0.620
20.953	6.780	3.766	20.946	2.355	1.309
30.647	8.008	4.449	30.648	3.651	2.029
40.359	9.537	5.299	40.370	4.784	2.658
50.045	14.279	7.933	50.040	6.189	3.438
59.710	18.435	10.242	59.735	7.925	4.403
69.430	20.084	11.158	69.407	11.096	6.164
79.100	23.616	13.120	79.109	15.780	8.767
88.797	26.033	14.463	88.759	21.599	12.000
79.117	25.338	14.077	79.110	20.699	11.499
59.722	23.376	12.987	59.723	18.357	10.198
40.344	20.052	11.140	40.348	15.382	8.545
20.949	15.964	8.869	20.962	11.677	6.487
0.000	5.294	2.941	0.000	3.715	2.064

Table C.31 Sorption data for ZnBTTBDC and NiBTTB H_2O isotherms at 298 K

ZnBTTBBDC			NiBTTB		
%RH	Wt%	Con(mol/kg)	%RH	Wt%	Con(mol/kg)
0.000	0.000	0.000	0.000	0.000	0.000
11.269	1.729	0.961	11.261	0.292	0.162
20.949	2.761	1.534	20.942	0.525	0.292
30.665	3.656	2.031	30.663	0.737	0.409
40.361	4.483	2.490	40.365	0.828	0.460
50.043	5.291	2.939	50.063	0.934	0.519
59.725	6.139	3.411	59.731	0.976	0.542
69.441	7.132	3.962	69.409	1.030	0.572
79.108	8.258	4.588	79.114	1.117	0.620
88.803	9.322	5.179	88.795	1.204	0.669
79.109	8.982	4.990	79.127	1.156	0.642
59.721	8.231	4.573	59.741	1.033	0.574
40.358	7.140	3.967	40.370	0.875	0.486
20.961	5.526	3.070	20.957	0.645	0.358
0.000	1.876	1.042	0.000	0.000	0.000

Table C.32 Sorption data for CoBTTBBPY and ZnBTTBBPY H_2O isotherms at 298 K

CoBTTBBPY			ZnBTTBBPY		
%RH	Wt%	Con(mol/kg)	%RH	Wt%	Con(mol/kg)
0.000	0.000	0.000	0.000	0.000	0.000
11.274	0.098	0.055	11.264	0.585	0.325
20.951	0.172	0.096	20.945	1.058	0.588
30.653	0.248	0.138	30.646	1.567	0.871
40.359	0.332	0.185	40.361	2.459	1.366
50.039	0.425	0.236	50.040	4.025	2.236
59.715	0.538	0.299	59.722	15.380	8.544
69.430	0.687	0.382	69.417	18.183	10.101
79.108	0.965	0.536	79.102	19.877	11.043
88.787	2.671	1.484	88.780	22.131	12.295
79.118	2.200	1.222	79.119	20.632	11.462
59.711	1.664	0.925	59.731	18.026	10.015
40.356	1.214	0.674	40.353	10.873	6.041
20.947	0.756	0.420	20.932	7.359	4.088
0.000	0.181	0.101	0.000	1.890	1.050

Table C.33 Sorption data for CoBTTBAZPY and ZnBTTBAZPY H_2O isotherms at 298K

CoBTTBAZPY			ZnBTTBAZPY		
%RH	Wt%	Con(mol/kg)	%RH	Wt%	Con(mol/kg)
0.000	0.000	0.000	0.000	0.000	0.000
11.264	0.585	0.325	11.287	0.347	0.193
20.945	1.058	0.588	20.967	0.597	0.332
30.646	1.567	0.871	30.640	0.933	0.518
40.361	2.459	1.366	40.360	2.324	1.291
50.040	4.025	2.236	50.024	6.921	3.845
59.722	15.380	8.544	59.731	15.827	8.793
69.417	18.183	10.101	69.413	17.547	9.748
79.102	19.877	11.043	79.118	18.564	10.313
88.780	22.131	12.295	88.797	19.373	10.763
79.119	20.632	11.462	79.109	18.742	10.412
59.731	18.026	10.015	59.712	15.648	8.693
40.353	10.873	6.041	40.381	6.802	3.779
20.932	7.359	4.088	20.958	2.063	1.146
0.000	1.890	1.050	0.000	0.449	0.249

Table C.34 Sorption data for MOF-14 H_2O isotherms at 298K

MOF-14		
%RH	Wt%	Con(mol/kg)
0.000	0.000	0.000
11.265	1.792	0.995
20.948	2.462	1.368
30.658	3.053	1.696
40.348	3.426	1.903
50.057	3.792	2.107
59.723	4.025	2.236
69.410	4.610	2.561
79.134	4.832	2.685
88.779	5.395	2.997
79.093	5.336	2.965
59.737	5.141	2.856
40.346	4.840	2.689
20.959	4.189	2.327
0.000	1.420	0.789